Poly(3,4-ethylenedioxypyrrole) and Composites for Electrochromic and Supercapacitor Applications

B. NARSIMHA REDDY

A Dissertation Submitted to the
Indian Institute of Technology Hyderabad
In Partial Fulfillment of the Requirements for
Doctor of Philosophy

भारतीय प्रौद्योगिकी संस्थान हैदराबाद
Indian Institute of Technology Hyderabad

Department of Chemistry

July, 2014

Declaration

I declare that this written submission represents my ideas in my own words, and where others' ideas or words have been included, I have adequately cited and referenced the original sources. I also declare that I have adhered to all principles of academic honesty and integrity and have not misrepresented or fabricated or falsified any idea/data/fact/source in my submission. I understand that any violation of the above will be a cause for disciplinary action by the Institute and can also evoke penal action from the sources that have thus not been properly cited, or from whom proper permission has not been taken when needed.

_____

(Signature)

_____

(B NARSIMHA REDDY)

(CY10P003)

Approval Sheet

This thesis entitled **"Poly(3,4-ethylenedioxypyrrole) and Composites for Electrochromic and Supercapacitor Applications"** by B. Narsimha Reddy is approved for the degree of Doctor of Philosophy from the Indian Institute of Technology Hyderabad.

12/11/14

External Examiner
Prof. R. Dhamodharan
Department of Chemistry
Indian Institute of Technology Madras
Chennai- 600036, India

External Examiner
Prof. Anil Kumar
Department of Chemistry
Indian Institute of Technology Bombay,
Mumbai - 400076, India

12-11-2014

Internal Examiner
Dr. Ch. Subrahmanyam
Department of Chemistry
Indian Institute of Technology Hyderabad
Yeddumailaram - 502205, India

12/11/2014

Adviser
Dr. M. Deepa
Assistant Professor
Department of Chemistry
Indian Institute of Technology Hyderabad
Yeddumailaram - 502205, India

12/11/2014

Chairman
Dr. V. Siva Rama Krishna
Department of Electrical Engineering
Indian Institute of Technology Hyderabad
Yeddumailaram - 502205, India

Acknowledgements

I would like to express my sincere gratitude and appreciation to my advisor, Dr. Melepurath Deepa, for her constant encouragement and for supporting me all the way through the Ph.D. She provided me the freedom to work, which brought out the best in me.

I am very much thankful to our HOD, Prof. Faiz Ahmed Khan for his insightful suggestions and advice.I express my gratitude to my doctoral committee members: Dr. Ch. Subhramanyam and Dr. G. Satyanarayana, for their generous motivation and encouragement thoughout my course work and Ph.D.

I would like to thank Prof. U.B. Desai, Director, IIT Hyderabad, for providing me with such a vibrant environment for pursuing research.

I thank my group members: S. Rambabu, P. Naresh Kumar, A. Bhaskar and N. Remya,for without their camaraderie, this research would not have been possible.

This research would not have been possible without the financial assistance from IIT Hyderabad and the Department of Science & Technology (DST) and I express my gratitude to the institute and DST.

I would like to thank my family for supporting me throughout my life.

Contents

Abstract

In this thesis, poly(3,4-ethylenedioxypyrrole) or PEDOP and it's composites were synthesized wherein the polymer films were grown by electropolymerization and an appropriate moiety was integrated with the polymer to achieve enhanced electrochemical response for electrochromic and/or supercapacitor applications. Improvements in electrochromic and redox switching capability for PEDOP films were attained by use of reduced graphene oxide functionalized with an ionic liquid (RGO/IL) as a dopant/counter ion. Further, the variation in localized nanoscale conduction / work function profile of PEDOP, when doped with an intr1insically conducting charge balancing counter ion such as functionalized carbon nanotubes was compared with the nanoscale behavior of same polymer doped with insulating counter ions and correlated to the significantly increased electrochromic switching by using a combination of electrochemical tools and microscopy probes. Electrochromic devices usingPEDOP andpoly(5-cyano-indole) or PCIND as cathodic and anodic electrochromes with a novel ionic liquid based polymeric electrolyte were assembled, and the performance attributes of the device were examined in detail, to ultimately demonstrate the suitability of the PEDOP-PCIND device for smart window applications.Electrically conductive composites of Sb_2S_3 nanorods enwrapped by PEDOP were prepared and used as electrodes in asymmetric supercapacitors; structure-property correlation with an emphasis on the ability of Sb_2S_3 to serve as electron conduits was evaluated. A PEDOP-Au@WO_3 hybrid dual function electrochromic supercapacitor electrode capable of optically modulating solar radiation while simultaneously storing/releasing charge was constructed for the first time and the concurrent electrochromic cum pseudocapacitive roles of this hybrid was established and assessed with respect to pristine PEDOP and WO_3 films. The ability of PEDOP to enhance the photoelectrochromic response of a V_2O_5 nanobelts based film, using a PEDOP/V_2O_5 hybrid was shown. In this thesis, the remarkable potential of PEDOP and it's composites for high performance electrochromic devices, supercapacitors, electrochromic supercapacitors and as electrodes in self-powered photoelectrochromic devices is unambiguously demonstrated.

Chapter 1

Conducting polymers: Background and applications

1.1 Introduction

Chemical species that can be reversibly switched between two or more optical states by application of voltage or current are known asElectrochromic materials [1]. Electrochromism results from the generation of different visible region electronic absorption bands, on switching between redox states.The color change is commonly between a transparent bleached state and a colored state, or between two colored states. Applications of electrochromic materials include their use in controllable light-reflective or light-transmissive devices for optical information and storage, anti-glare rear-view mirrors, sunglasses, protective eyewear for military, controllable aircraft canopies, glare-reduction systems for offices and smart windows for use in cars and in buildings [2-6]. Of these, electrochromic rear-view mirrors for cars have already achieved considerable commercial success [5]. These safety devices prevent mirror-reflected glare which causes an ‘after image’ to stay on the eye’s retina. Whilst many types of chemical species exhibit electrochromism, only those with favorable electrochromic performance parameters are potentially useful for commercial applications.Thus, most applications require electrochromic materials with a high contrast ratio, large coloration efficiency (absorbance change/charge injected per unit area), prolonged cycle life, and write-erase efficiency (% of originally produsedcolor that may be subsequently electro-bleached). While displays need fast response times, by contrast, smart windows can tolerate response times of up to several minutes. Digital photographs of electrochromic devices (ECDs) in dark and transparent states are shown in Figure

1.1. The level of coloration in an electrochromic device is controlled by an applied voltage or current.An ECD has the configuration of an electrochemical cell: it has a cathode, an anode and an electrolyte that separates the two electrodes.

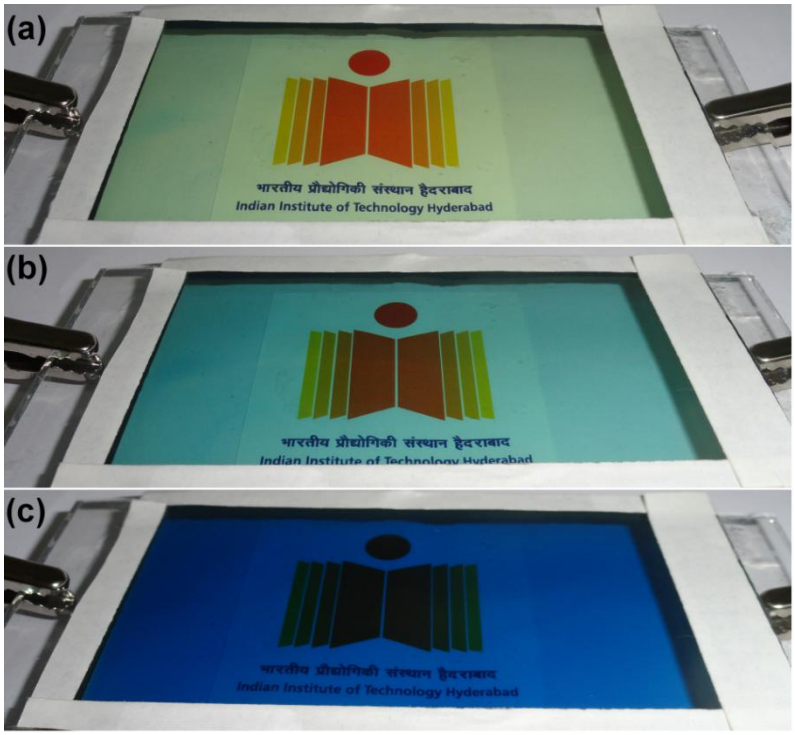

Figure 1.1: Electrochromic devices for smart window and rearview mirror applications developed at IIT Hyderabad in (a) transparent, (b) semi-transparent and (c) fully colored states.

1.2 Basic principles of electrochromism and classification

Color changes in an ECD occur by charging/discharging the electrochemical cell on application of an electrical potential. After the resulting pulse of current has decayed, and the color change has been effected, the new redox state persists, with little or no input of power, due to the so-called 'memory effect'. The electrochromic electrode, which can work in the reflective or transmissive mode, comprises of a glass coated with an electrically conducting film such as fluorine doped tin oxide (FTO) onto which the electrochromic material is deposited.

Alternatively, if one or both redox states are soluble, the electrochromic material may be dissolved in the electrolyte solution. In variable light transmissive devices, the counter electrode substrate is also a transparent FTO glass, with the counter electrode chemical species being either colorless in both its redox forms or being electrochromic in a complementary mode to the primary electrochromic material. For applications, that are designed to operate in the reflective mode, such asdisplays, the counter electrode can be of any material with a suitable reversible redox reaction. Upon applying a suitable potential, the ECD darkens, and in this colored state, the device inhibits visible radiation from passing through; solar radiation corresponding to wavelengths above 700 nm is transmitted (Figure 1.2a). Upon reversing the applied bias, the ECD acquires the transparent/bleached state, and it allows visible radiation to pass through (Figure1.2b). The phenomena can be repeated over a large number of cycles. In this manner, the ECD functions as a modulator of visible radiation.

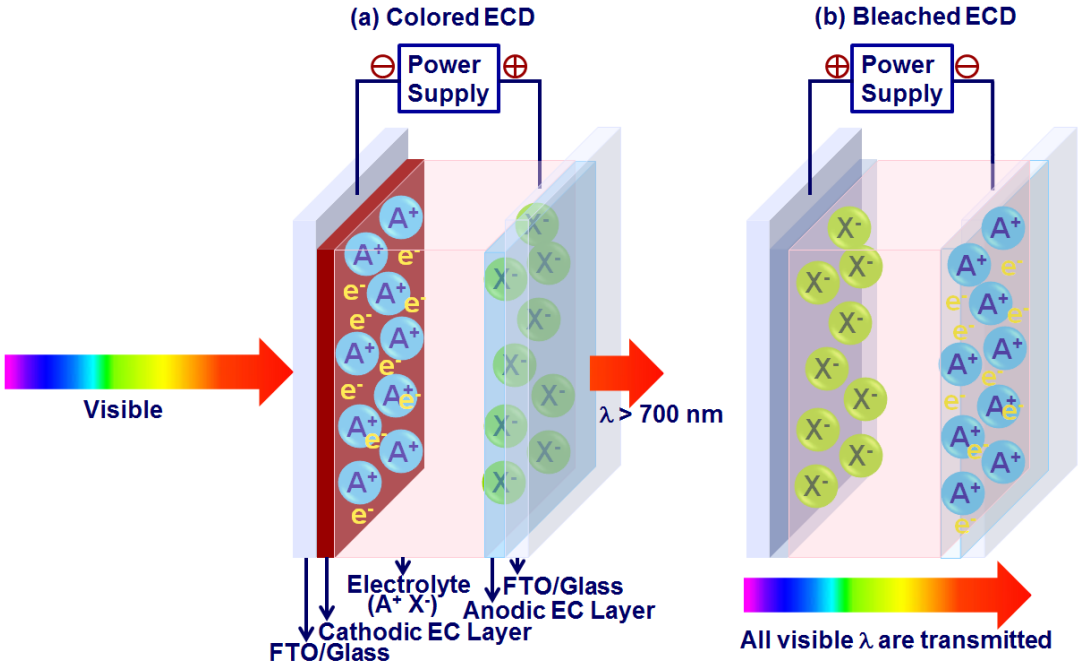

Figure 1.2: Schematic of a complementary electrochromic device, showing how electron and ion insertion during (a) coloration and (b) bleaching is accompanied by visible radiation modulation.

Some important examples of electrochromic materials which can be cathodically or anodically coloring are listed below.

- ✓ Transition metal oxides
- ✓ l,l'-Disubstituted-4,4'-bipyridylium salts (viologens)
- ✓ Metallopolymers
- ✓ Metal phthalocyanines
- ✓ **Conducting polymers (CPs)**

1.2.1 Conducting polymers (CPs)

All carbon based polymers were thought to be insulators about 30 years ago. However, in the last two decades, afield emerged on the basis of the ability of certain polymers to conduct charge. Alan Heeger, Alan MacDiarmid, and Hideki Shirakawa were awarded with The Nobel Prize in Chemistry for their discovery and elaboration of electronically conducting polymers in 2000 [7]. The three scientists found that polymer can be made to conduct electricity if carbon atoms are linked via alternating single and double bonds, and electrons are either removed through oxidation or introduced through reduction. The Chemical or electrochemical oxidation of numerous resonance stabilized aromatic molecules including pyrrole, thiophene, aniline, furan, carbazole, and azulene and indole (Figure 1.3) produces novel electronically conducting polymers.

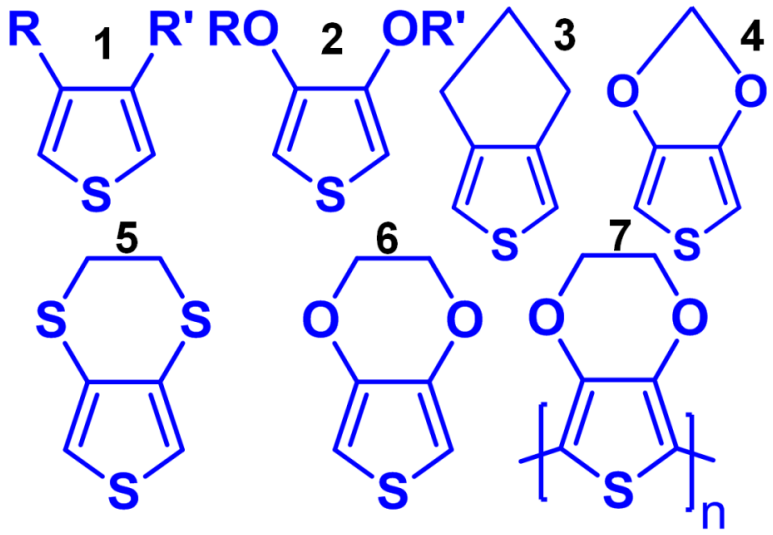

Figure 1.3: Monomers: 1: 3,4-dialkylthiophene,2: 3,4-dialkoxythiophene, 3: 3,4-propylenethiophene, 4: 3,4-methyldioxythiophene, 5: 3,4-ethylenedithiothiophene, 6: 3,4-ethylenedioxythiophene or 3,4-EDOT and polymer:7: poly(3,4-ethylenedioxythiophene) or PEDOT.

1.2.2 Electronic structure controls optical properties

The broad spectrum of functional properties of CPs stems primarily from the conjugation prevalent in these polymers; the presence of alternate single and double bonds across the polymer. The electrons in the π-bonds are weakly bound, and are easily delocalized which is responsible for the remarkably high electronic conductivities of conducting polymers. Since, single and double bond lengths are unequal and the Peierl's instability (i.e., C–C bonds are longer than C=C bonds) splits this band into 2 sub-bands, a completely filled valence band (VB, highest occupied molecular orbital or HOMO level) and an empty conduction band (CB, lowest unoccupied molecular orbital or LUMO level), separated by an energy gap. The conducting polymer is therefore akin to a semiconductor. The magnitude of the band gap controls the intrinsic properties of the polymer, such as optical properties, as shown below for **poly(3,4-ethylenedioxypyrrole) or PEDOP**, under different values of applied bias in a liquid electrolyte

(Figure 1.4). Optical absorption of PEDOP is pronounced in the visible region in the colored state and the NIR absorption dominates in the bleached state.

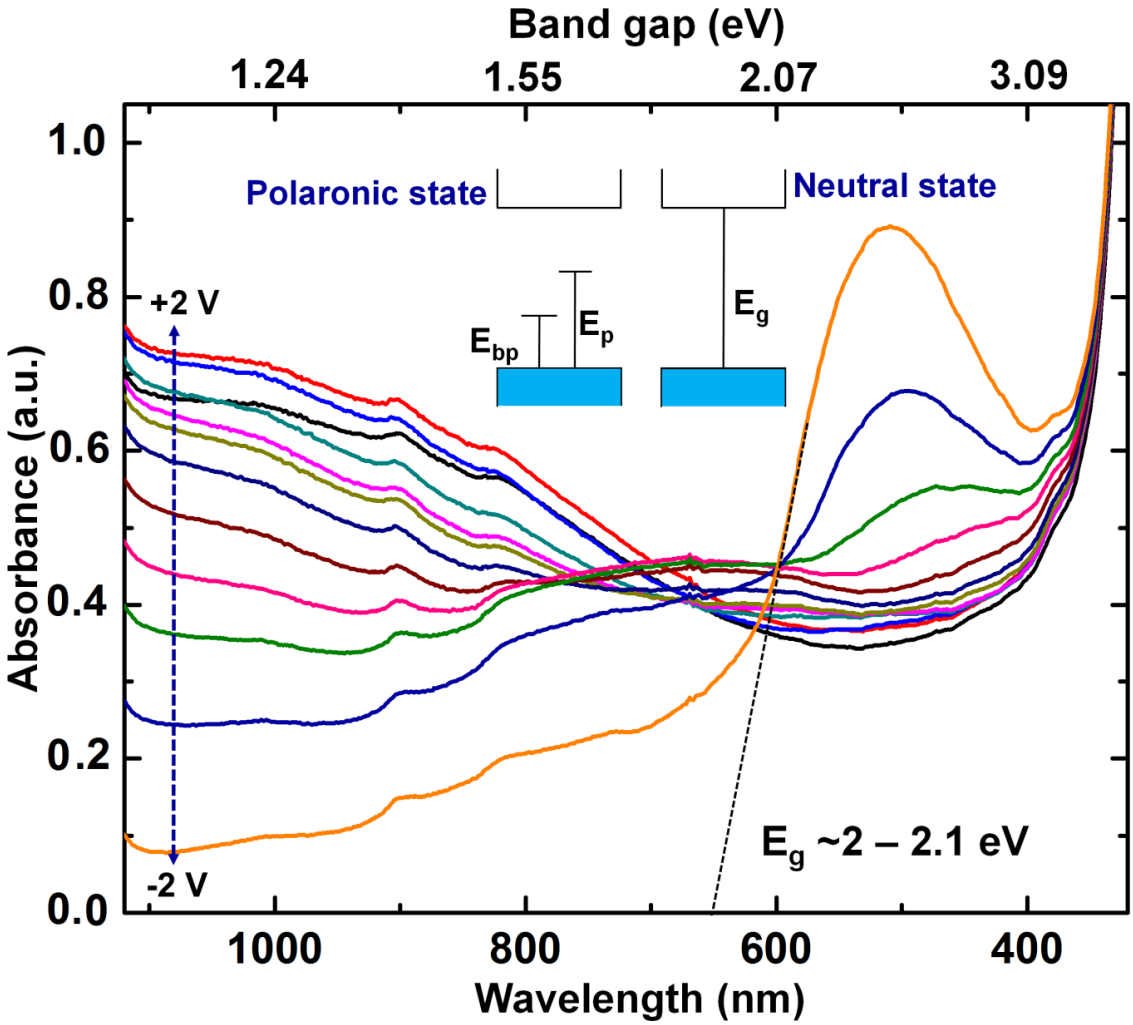

Figure 1.4: Optical absorbance spectra of a PEDOP film in a liquid electrolyte: 1 M $LiClO_4$ in propylene carbonate with Pt as the counter electrode, under varying potentials which lie between –2 and +2 V.

Oxidation and reduction or neutralization of conducting polymers is referred to as doping and dedoping respectively. During oxidation, anions from the electrolyte are inserted into the polymer backbone and simultaneously electrons are removed thus resulting in electron deficiency or “p-doped” state. During reduction, anions are removed from the polymer backbone

and electrons are inserted into the polymer, thereby, leading to either a neutral state or an excess of electrons called the "n-doped" state. The π-electrons are delocalized over the polymer backbone. The p- and n- doping processes are expressed through the following equation.

$$CP^{m+}:[D^-]_m \underset{-n[E^-],+ne^-}{\overset{Oxd\ +n[E^-],-ne^-}{\rightleftharpoons}} CP^{(m+n)+}:[D^-]_m:[E^-]_n \quad (1)$$

Charges are introduced into the polymer (insertion or extraction of electrons) during redox processes which are responsible for conduction. The charge in the polymer chain is stabilized by altering the conjugation over several monomers. The charge along with the distortion of the structure of the polymer is denoted as a polaron and can be either negative or positive. When two polarons form a couple, a bipolaron is generated with a charge of +2 or –2 (Figure 1.5).

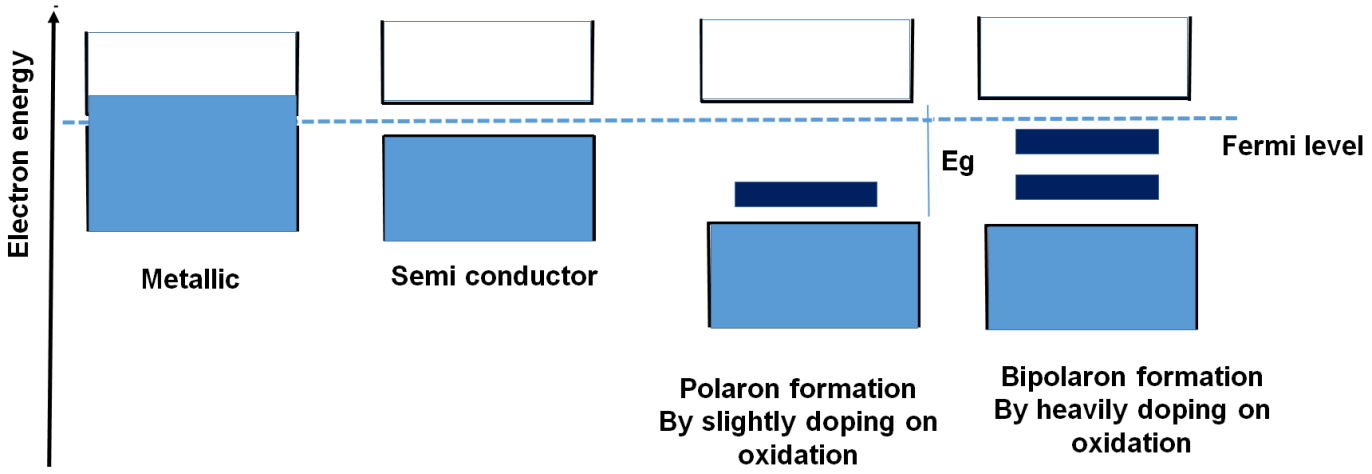

Figure 1.5: Schematic illustrating conduction and valence bands in metals and semiconductors and formation of polarons and bipolarons in CPs.

1.2.3 Doping/de-doping and coloration in CPs

Chemical or electrochemical doping increases the number of free charge carriers for conduction. The dopant, usually an anion, stays in the film and balances the positive charge of

the polymer. Upon doping, the charge carriers alter the structure of the polymer by increasing the length of the double bonds and shortening the single bonds, thus giving a more quinoidic character. As the doping level increases, the number of states within the band gap increases. At high doping levels, the states within the band gap start to overlap and create bands of bipolaronic states, as shown in Figure 1.5.

Several conjugated polymers have a band gap that lies within the visible light range of 1.7 to 3.2 eV. Relative band gaps and oxidation potentials of some CPs are displayed in Figure 1.6. Conducting polymers can therefore absorb and/or emit light in the visible region. The band gap energy is the minimum energy required for transition in an undoped polymer, by absorption. In the doped state, however, the electronic states introduced by polarons or and /or bipolarons permit absorption at lower photon energies, which changes the absorption spectrum of the polymer dramatically. As the doping level is raised, the original absorption peak diminishes at the cost of new polaronic and bipolaronic peaks. If the change in absorption occurs within the visible range, the human eye will interpret this as a change of color. The color of the polymer can be reversibly controlled via doping and de-doping by an electric voltage or current.

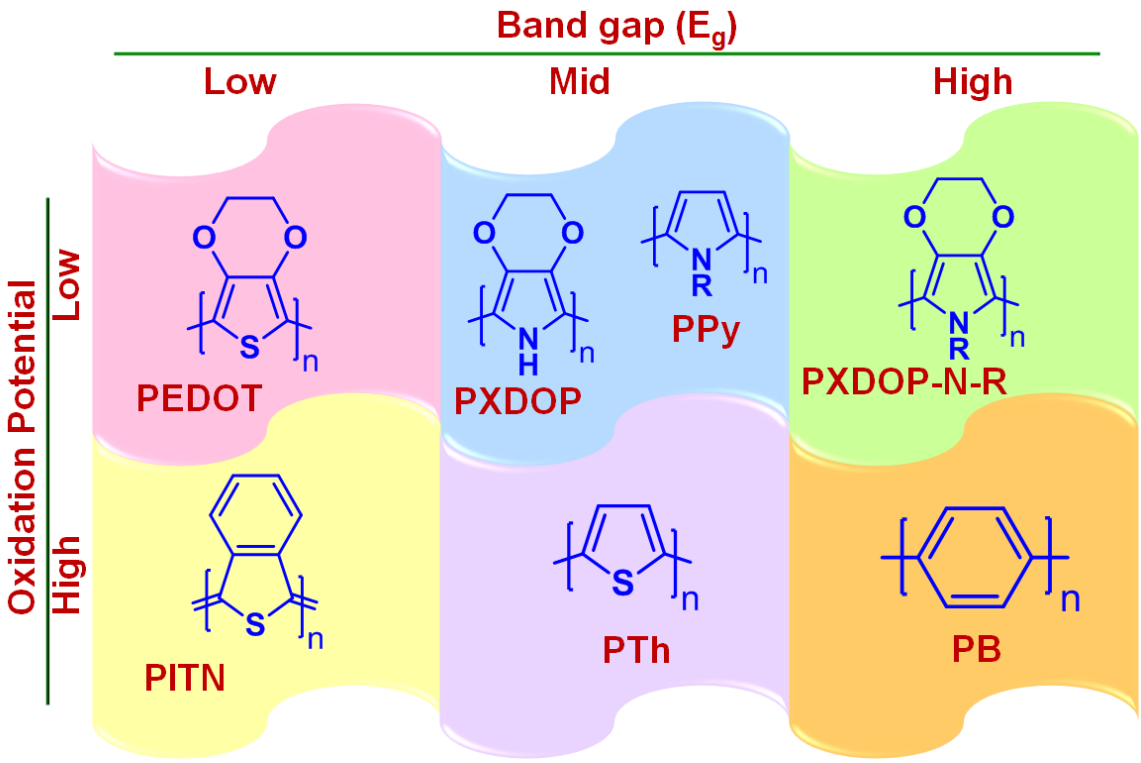

Figure 1.6: Relative oxidation potentials and band gaps of some conducting polymers, (PXDOP/T is poly(alkylenedioxypyrrole or thiophene), PPy is poly(pyrrole), PITN ispoly(isothianaphthene), Pth is poly(thiophene) and PB is poly(benzene)).

Electron-rich conjugated polymers which can be switched between their oxidized (doped) and charge-compensated (neutral) states rapidly over many redox cycles are useful for many applications like electrochromic devices and supercapacitors. Of the many useful properties afforded by these polymers (high conductivity, mechanical actuation, chemical sensing, etc.), molecular manipulation of conjugated systems can yield electrochromic materials with a range of colors, a high degree of switching stability, and striking color contrasts between absorptive and transmissive forms. For a cathodically coloring polymer like poly(3,4-ethylenedioxythiophene) or PEDOT, the oxidized or the p-doped state is characterized by a transmissive sky blue hue [8]. In the reduced neutral state, PEDOT is characterized by a deep blue hue. The oxidation and

reduction processes in PEDOT are reversible and therefore it can undergo thousands of sky blue ↔ deep blue transitions (as shown in Figure 1.7a) without incurring any significant loss in the electrochromic contrast, thus rendering it to be suitable for smart window applications [9]. The oxidized state is conducting with a conductivity of 8 S cm^{-1} for PEDOT doped with perchlorate ions owing to delocalization of electrons whereas the neutral state is almost insulating. Among anodically coloring polymers, poly(pyrrole) or PPy is yellow/green in the undoped insulating state and black in the doped conductive state[10] and poly(aniline) or PANI is green or blue in the doped state and yellow in the undoped state [11] (Figure 1.7c)and these two polymers have been studied extensively in the past. Incorporation of the ethylenedioxy bridge at the 3 and 4 positions in PPy yields the poly(alkylenedioxypyrroles) like poly (3,4-(ethylenedioxypyrrole) or PEDOP which is red in the neutral state and has a pale blue-black transmissive state in the oxidized state[12] (Figure 1.7b).

Figure 1.7: Electrochromism cum redox switching in (a) PEDOT, (b) PEDOP and (c) PANI films; PS, ES and LB are acronyms for pernigraniline, emeraldine salt and leucoemeraldine base respectively.

1.3 CPs in supercapacitors

Since CPs insert and release charge by undergoing oxidation and reduction reactions, upon application of external bias, in the presence of an electrolyte, they, in principle, permit energy storage in the form of charge. Thus they can be used for supercapacitor applications. Supercapacitors are divided into three families, based on electrode design.

i. Electrical double-layer capacitors (EDLCs) – with carbon electrodes or derivates with high electrostatic double-layer capacitance.

ii. Pseudocapacitors – with metal oxide or CP electrodes with a large amount of electrochemical pseudocapacitance.

iii. Hybrid capacitors – capacitors with asymmetric electrodes, one of which exhibits dominantly electrostatic and the other predominantly electrochemical capacitance (e.g. Li-ion capacitors).

Today, a plethora of supercapacitors are being manufactured worldwide for applications that require rapid recharging, high power output, and repetitive cycling. Within this dissertation, cells based on redox pseudocapacitance will be referred to as supercapacitors, a term which will be used interchangeably with electrochemical capacitors or pseudocapacitors. The classification of capacitors is provided in Figure 1.8.

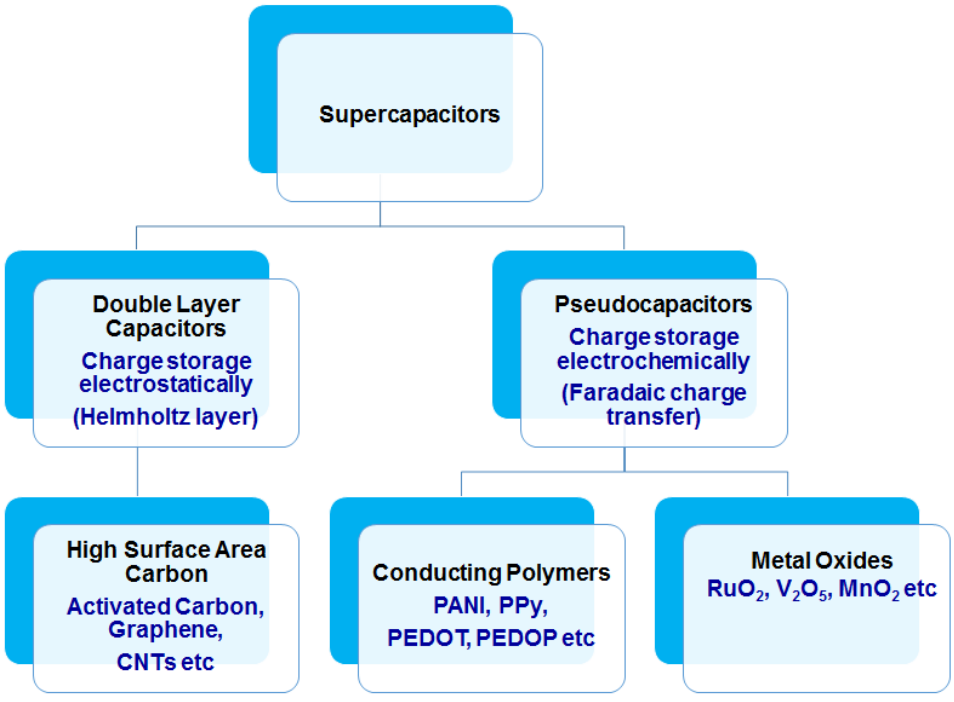

Figure 1.8: Classification of supercapacitors

1.4 Electrode materials for supercapacitors

1.4.1 Carbon

Carbon has been a popular choice for EDLCs due to its low cost, abundance, and long term history of use. It is imperative for carbon materials to have high surface areas of the order of 1000 m^2 g^{-1} and good intra- and inter- particle conductivity to be optimal for modern supercapacitors [13]. Charge is stored in the pores or at the interface between the active carbon material and the electrolyte (Figure 1.9). The conductivity of carbon electrodes also contributes to the power density of EDLCs. A balance between the pore- size and distribution which can enable easy access of electrolyte ions, high specific surface area for high capacitance, and optimal particle size for good conductivity are essential for desirable performance [14]. Nanoporous carbon electrodes which are typically utilized in EDLCs, take the shape of foams, fibers, nanotubes, sheets [15,16]. EDLCs constructed with carbon based electrodes employing aqueous or organic electrolytes have demonstrated capacitances ranging from a few Farads to several thousand Farads per cell [17,18].

1.4.2 Metal oxides

Metal oxides are suitable for electrochemical supercapacitors owing to high specific capacitance and low resistance [19]. Metal oxides store charge by undergoing oxidation and reduction reactions, upon application of external bias, in the presence of an electrolyte. Although the high cost of ruthenium prevents its large-scale use, one of the best capacitances reported to date is 840 F g^{-1} (energy density of 200 Wh kg^{-1}) and 500 mF cm^{-2} for a hydrous ruthenium oxide electrode in an aqueous sulfuric acid electrolyte solution. It also shows excellent reversibility with a cycle life over several hundred-thousand cycles [20]. Current academic

efforts emphasize on lower cost, less toxic metal oxides such as oxides of manganese or vanadium for practical supercapacitors.

1.4.3 Conducting polymers (CPs)

Electronically conducting polymers are promising for the realization of high performance supercapacitors, as they are characterized by high specific capacitances. The charge/discharge process involves the whole polymer mass and is not confined not only to the surface (Figure 1.9), as in the case of double-layer carbons. Thus, devices with low series resistance and high specific energy and power can be fabricated using CPs. CPs can provide large conductivity, flexible morphologies, wide voltage windows, high storage capacity, porosity, and reversibility. Moreover, CPs are inexpensive. But they are less stable than RuO_2, due to swelling and shrinking during oxidation and reduction. Despite this shortcoming, their low cost coupled with their cyclability over thousands of charge/discharge cycles without severe deterioration renders them attractive for electrochemical supercapacitors or psuedocapacitors [21].

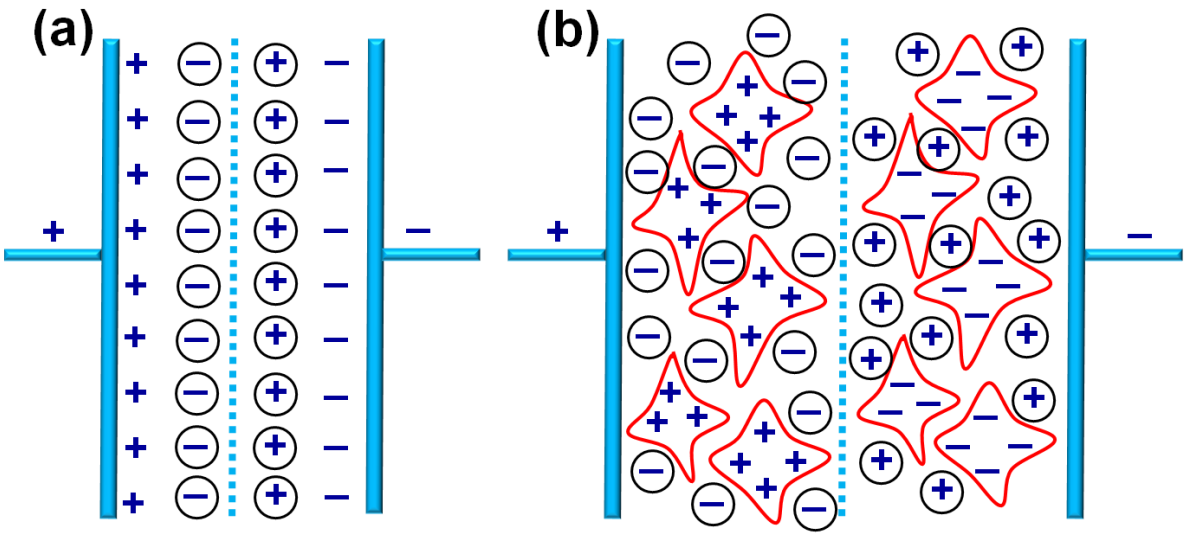

Figure 1.9: Schematic of (a) EDLCs (Carbon based electrodes) and (b) pseudocapacitors (metal oxides and CP based electrodes). The dashed line represents the electrolyte soaked in a separator.

1.4.4 Supercapacitors *versus* batteries/fuel cells

A graphical comparison of power density and energy density performance characteristics of batteries, supercapacitors and fuel cells, also known as the "Ragone plot" is shown in Figure 1.10 [22]. While energy density is the amount of energy stored per unit mass or volume of the system, power density is the energy transfer time per unit mass or volume. Batteries are generally high energy, low power devices, whereas electrolytic capacitors are higher power density devices with limited energy storage capabilities. Fuel cells show high energy storage, but their power output is limited. Electrochemical capacitors fill the gaps in terms of desired performance characteristics of energy storage devices. They can store more energy than traditional capacitors and deliver more power than batteries. They are usually used in combination with batteries, especially to provide a surge of power for a short duration of time, for applications like backup power for actuators [23].

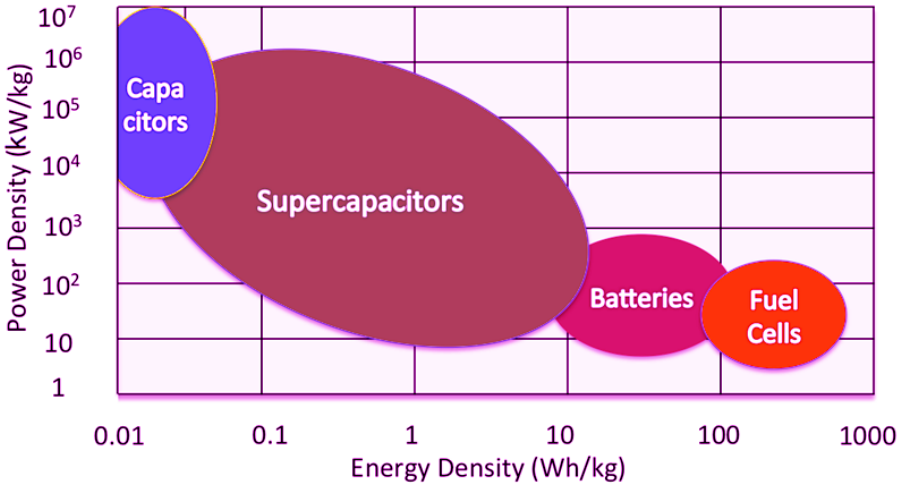

Figure 1.10: Ragone plot showing power density *versus* energy density of different energy storage devices. Adapted fromChem. Rev. 104(2004) 4245–4245, Copyright (2014) American Chemical Society [22].

1.5 Milestones and recent developments in CPs for electrochromics and supercapacitors

Although for more than four decades, electrochromic devices have been regarded forerunners for energy saving "smart windows" for buildings and vehicles, and there are a few companies across the globe which do produce electrochromic devices like windows and mirrors on a commercial scale. But there is an intensive quest for materials which can deliver an optimal balance between cost and performance (contrast, speed and cycle life). CPs, and mainly PEDOT and its' derivatives do meet this challenge to some extent, as they are highly cost effective and can offer large optical contrasts in short time spans, but researchers continue to grapple with two major issues, namely, durability and scalability. Similarly, in the field of pseudocapacitors, CP composites with carbon nanostructures are attractive, owing to large electrical conductivity, cyclability and high capacity [13]. Some notable research efforts in PEDOT or PEDOP based electrochromic films / devices or supercapacitors developed in the last few years are summarized here.

With a highly conducting, almost transparent, stable doped state, a narrow optical band-gap of ~1.6 eV and a particularly low oxidation potential when compared to its unsubstituted poly(thiophene) parent, neutral deep blue PEDOT shows a relatively stable and highly transmissive sky blue oxidized state as demonstrated in the pioneering work of Inganas et al., who described the first electrochemically prepared PEDOT-based ECDs[24]. Considering the onset of the optical absorption of neutral PEDOT lying in the near-IR region of the electromagnetic spectrum, along with the minimal tailing in the visible of its charged carrier transitions produced on electrochemical oxidation, the excellent transmissivity of PEDOT arousedconsiderable interet as illustrated by the reports of Jonas, Heinze and Inganas and co-workersand has been the focus of a significant number of publications since then [25-28].

In a notable study, a requisite technological component of a chameleonic fabric was fabricated with reflective-type electrochromic devices using stretchable, conductive fabric electrodes [29]. Lycra spandex fabric was impregnated with a conducting polymer (PEDOT:poly(styrene sulfonate) or PSS) and devices were assembled. The time taken for the electrochromic polymer to switch between colored states in devices prepared using PEDOT:PSS loaded Lycra (conductivity ~0.1 S cm^{-1}) was a few seconds. The electrochromic spandex functioned in solution while being stretched. In addition, stenciled devices were built. Such fabric electrochromic devices represent a critical step toward the realization of totally chameleonic fabric.

In another report, complex devices with conjugated polymers deposited onto metalized porous membranes were constructed. A 2 × 2 pixel type array device consisting of two conjugated polymers which displayed unique visible absorptions (blue and red) in the neutral state while maintaining the ability to switch to a very transmissive oxidized state was fabricated. PEDOT and PBEDOT-$B(OR)_2$ were electrodeposited onto the porous membrane and then switched with a bias voltage of 1 V. At a bias of 1 V, PEDOT is blue while PBEDOT-$B(OR)_2$ is red. When the bias is reversed and both polymers are fully oxidized, both polymers switch to a highly transmissive state, exposing the reflective gold surface [30].

The optimization of the capacitive behavior of PEDOT films as polymeric electrodes in flexible, electrochemical supercapacitors (ESCs) utilizing ionic liquid (IL) and organic gel electrolytes was accomplished recently [31]. The PEDOT/IL devices were found to be highly stable over hundreds of thousands of cycles and could be reversibly charged/discharged at scan rates between 500 mV s^{-1} and 2 V s^{-1} depending on the polymer loading. The efficacies of these PEDOT ESCs were assessed by using them as a power source for a high-contrast and fast-

switching electrochromic device, demonstrating their applicability in small organic electronic-based devices. In this study [31], the cycling stability of an ESC-360/IL (fabricated and tested in air) was monitored over 4,00,000 cycles between 0 and 1.0 V at 100 mV s^{-1} (Figure 1.14a). After 400 000 cycles, the device managed to retain 80% of the initial capacitance. The improved stability was in part attributed to lower volume changes reported for electroactive polymers when using solvent-free electrolytes. An ECD was constructed using a ProDOT-based polymer and a colorless dioxypyrrole-based polymer on the counter electrode for charge balance. To power the ECD, a fully charged ESC was then connected to the ECD. Starting with a fully charged ESC and the ECD in its colored state, as shown in Figure 1.14b, connecting the working electrodes leads to current flowing from the ESC to the ECD. Discharging the ESC and in the process, switches the ECD from its colored to its colorless state, as shown in Figure 1.14c. Upon reverse-bias, current flows from the ECD to the ESC causing the ECD to switch back to the colored state while partially recharging the ESC, thus illustrating a functional supercapacitor powered electrochromic device.

In another report, the formation mechanism of a coaxial MnO_2/PEDOT nanowire was elucidated by performing electrodeposition of MnO_2 and PEDOT on Au-sputtered nanoelectrodes within the 200 nm diameter pores of an anodized aluminum oxide (AAO) template. The formation of coaxial nanowires was shown to be a result of simultaneous growth of core MnO_2 and shell PEDOT by an analysis of the current density resulting from electrochemical deposition. A potential of 0.70 V was found to be the most favorable condition for synthesis of MnO_2/PEDOT coaxial nanowires, resulting in a high specific capacitance of 270 F g^{-1} [32], thereby demonstrating that combining nanostructures of pseudocapacitive-oxide and a CP leads to superior charge storage capacities.

1.6 Poly(3,4-ethylenedioxypyrrole) or PEDOP

CPs are excellent electrochromes, as they can offer multiple colors, have medium to low oxidation potentials, are extremely cheap compared to transition metal oxides, are easy to process and are easily scalable too when used in the form of films in ECDs [28]. In PEDOT, the 3,4-alkylenedioxy substitution pattern facilitates electrochemical polymerization by lowering the monomer oxidation potential and directing polymerization through the 2- and 5- positions, yielding regiosymmetric polymers with a low degree of main chain imperfections [33]. This is not the case with PPy, which exhibits structural defects arising from αβ, ββ couplings, resulting in conjugation breaks. Substitution of pyrrole at the β-positions prevents these unwanted couplings, leading to more regular materials. At the same time though, PPy exhibits a quite low oxidation potential (–0.2 V *versus* saturated calomel electrode or SCE) and can be formed as highly conductive (near metallic) and stable films. It is evident that combination of the electron-rich pyrrole heterocycle with a 3,4-alkylenedioxy substituent in 3,4-ethylenedioxypyrrole (EDOP) should provide a stable conducting polymer [34] (Figure 1.11).

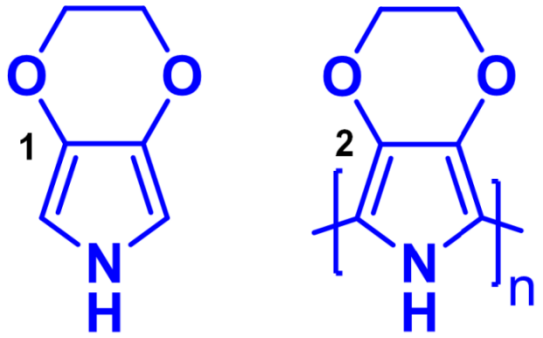

Figure 1.11: (1) Monomer 3,4-EDOP and (2) the corresponding polymer PEDOP.

The first report on this CP encompassed a study of an organic electrolyte-based electropolymerization of EDOP and the unique electrochromic properties of the resultant PEDOP films [12]. PEDOP is characterized by one of the lowest half wave potentials ($E_{1/2}$) for

p-type doping of any conjugated polymer reported to date [12]. This polymer switches between a bright red neutral form and a highly transmissive blue-gray doped/conducting form. Comparable to the preparation of EDOT derivatives, the synthesis of the monomer EDOP involves a multi-step process which is complicated by the necessity of protecting the pyrrole nitrogen as reported by Merz et al [35]. Starting from the precursor: dimethyl-*N*-benzyliminodiacetate, a five-step synthetic procedure afforded the monomer EDOP in 20% overall yield [36].

The presence of the 3,4-ethylenedioxy substituent on the pyrrole ring raises the position of the effective HOMO level of the conjugated polymer, PEDOP, and thus decreases the band gap (regarded as the onset of π-π* transition peak) considerably, compared to PPy, by 0.65 eV to a value of 2.05 eV. The spectrum for reduced PEDOP (–0.9 V) shows it to have a pronounced π-π* transition, especially in comparison to that observed for PPy. This illustrates the regiosymmetry imposed by the 2,5-linkages. The π-π* transition is fully depleted upon oxidation, and a strong lower energy peak centered at about 0.75 eV in the near-infrared region is observed. At approximately –0.4 V, the band in the near-infrared region acquires its maximum intensity. This further establishes the ease with which PEDOP can be transformed to its oxidized state. The low oxidation potential of PEDOP further ensures that the electroactivity induced by redox processes are not affected by air and moisture and re-affirm the formation of a very stable conductor.

Other notable developments included the preparation of a series of new poly(3,4-alkylenedioxypyrrole)s (PXDOPs) wherein some of the lowest oxidation potentials (if not the lowest) were obtained for the said CP [36]. This increased the stability of the doped state to ambient reduction when compared to regular PPy. The PXDOPs showed outstanding electrochemical stability and were able to endure potentials up to 2 V. As electrochromes, the

PXDOPs were shown to switch thousands of times between their red or orange neutral state and a light blue/gray doped state with high contrast in less than 200 ms. Furthermore, their low oxidation potentials allowed their use over a wide potential window (at least −1.5 to +1.3 V), thus making them compatible with numerous polymers in dual polymer electrochromic devices [36]. Yet another article by the same group, elaborated on the synthesis and materials properties of PXDOPs and showed how their flexible and adaptable repeat unit structure, high bandgap, high conductivities, biocompatibility, and low half-wave potential, $E_{1/2}$, made them powerful materials deemed to fit into the frontier of conducting polymers research [34]. In another study, the same group demonstrated a new and high yielding synthetic route towards 3,4-alkylenedioxy-functionalized pyrroles achieved by performing tandem Mitsunobu reactions on diethyl 1-benzyl-3,4-dihydroxypyrrole-2,5-dicarboxylate using a variety of 1,2-alkanediols or 1,3-alkanediols [37].

Another article focused on synthesis of three monomers of 3,4-bis(alkylthio)pyrroles and preparation of the corresponding polymers, by anodic electropolymerization and/or chemical oxidation using $FeCl_3$ as oxidant [38]. The monomers possessed significantly lower oxidation potentials than unsubstituted pyrrole due to the substitutions of electron donating alkylthio groups at 3- and 4-positions, which resulted in high *in-situ* conductivities and large contrasts for the polymers [38].

In a previous report, a film of N-ethyl substituted PEDOP, displayed multicolor electrochromism as it switched between green, violet, and grey hues. The highest transmittance change of this device was attained at 529 nm and amounted to 35.2% transmission contrast accompanied by a coloration efficiency of 428 $cm^2 C^{-1}$ [39].

Another set of studies focused on unraveling the charge-transport phenomena, redox switching and electrochromism of neat poly(3,4ethylenedioxypyrrole) (PEDOP) films and films embedded with Au and Ag nanoparticles [40,41]. Films were electropolymerized in an ionic liquid: 1-Butyl-1-methylpyrrolidinium bis(trifluoromethylsulfonyl)imide and Au and Ag nanoparticles were adsorbed by immersion of the CP films in the respective colloids to yield PEDOP-Au or PEDOP-Ag films. Films were characterized by electron microscopy and X-ray photoelectron spectroscopy. Electrochromic devices were constructed and they were characterized by spectroelectrochemistry, cyclic voltammetry [40,41]. A summary of PEDOP based ECDs reported in literature are listed in Table 1.1.

Table 1.1: Performance metrics of PEDOP films/devices.

Cathode	Anode	Electrolyte	Electrochromic / ion storage (ISC) properties	Ref.
PEDOP	Pt	0.1 M $LiClO_4$/PC	ISC = 50 mC cm^{-2} ΔT_{max} = 53% (λ = 510 nm)	[12]
PEDOP	Pt	0.1 M LiClO4/PC	ΔT_{max} = 59% (λ = 537 nm)	[36]
PEDOP	Pt	$TBABF_4$/PC	σ = 83 S cm^{-1} ΔT_{max} = 59% (λ = 537 nm)	[34]
PEDOP	Pussian Blue	CH_3CN +PC+PMMA+Li[N($SO_2CF_3)_2$]	η = 185 $cm^2 C^{-1}$ (λ = 448 nm) ISC = 0.8 mC cm^{-2}	[40]
PEDOP-Ag	Prussian blue	CH_3CN+PC+PMMA +Li[N($SO_2CF_3)_2$]	η = 220 $cm^2 C^{-1}$ (λ =445 nm) ISC = 1.9 mC cm^{-2}	[40]
PEDOP-Au	Prussian blue	CH_3CN +PC+PMMA+Li[N($SO_2CF_3)_2$]	η = 270 $cm^2 C^{-1}$ (λ = 458 nm) ISC = 4.7 mC cm^{-2}	[40]

$TBABF_4$ is tetrabutylammonium tetrafluoroborate, PMMA is poly(methylmethacrylate), η is coloration efficiency,ΔT is transmission modulation, ISC is ion storage capacity and σ is conductivity.

It is apparent from the above survey, that contrary to its' exhaustively investigated thiophene analogue PEDOT (>1000 articles), the number of reports on PEDOP despite a lower oxidation potential, excellent electrical conductivity and a capability to switch between red and blue hues (contrasting with PEDOT's switch between monochromic blue hues) are astonishingly very few, which too provided the motivation to work on PEDOP and its' composites, and evaluate their potential for ECDs and pseudocapacitors.

1.7 Objectives of the present work

The objectives of the work described in present thesis are summarized here.

i. To synthesize PEDOP films by electropolymerization and to study the effect of counterion on structure, electrochromism and electrochemical properties.

ii. To analyze the nanoscale conduction behavior and surface potentials of PEDOP films (doped with a range of either insulating or conducting anions) by Conducting atomic force microscopy (C-AFM) and Kelvin probe force microscopy (KPFM) and correlate the same with their electrochromic and electrochemical characteristics.

iii. To assemble prototype electrochromic devices using PEDOP films and poly(5-cyano indole) or PCIND films as cathode and anode respectively with an ionic liquid based electrolyte and explore their suitability for smart window applications.

iv. To explore the possibility of using cheap but equally effective alternates to multiwalled carbon nanotubes (MWCNTs, a popular choice for preparing CP composites) and to prepare PEDOP composites with highly conductive antimony sulfide (Sb_2S_3) nanorods and evaluate their performance for quasi solid-state supercapacitors.

v. To demonstrate a PEDOP/fibrous metal oxide hybrid based electrochromic pseudocapacitor and furnish an insight into the mechanistic aspects of charge transport

and transfer in the hybrid and how these phenomena differ from the pristine polymer or the oxide.

vi. To demonstrate a photoelectrochromic device based on a nanostructured PEDOP/metal oxide belts electrode and show how PEDOP improves (a) the electrochromic contrast of the oxide and (b) the efficiency of a photovoltaic cell.

To meet the above-described aims, PEDOP based films were prepared by using a variety of solutions containing appropriate components on conducting glass substrates via electropolymerization route. The effect of using reduced graphene oxide functionalized with an ionic liquid (RGO/IL) as a dopant/counter ion on microstructure, electrochromic response and redox behavior of PEDOP-RGO/IL films relative to pristine PEDOP (doped with IL) films is discussed in **Chapter 3**. In **Chapter 4**, how the localized nanoscale conduction / work function profile of PEDOP, when doped with an intrinsically conducting charge balancing counter ion such as functionalized carbon nanotubes, is dramatically different from that of the same polymer doped with insulating counter ions, and how this difference leads to a significantly improved redox switching performance in PEDOP-(MWCNT)SO_3^-) composite films is demonstrated. In **Chapter 5**, PEDOP doped with a fluoroalkylphosphate ionic liquid, in combination with a PCINP film were used for fabricating electrochromic devices and the performance attributes of the device were examined in detail, to ultimately demonstrate the suitability of the PEDOP-PCIND device for smart window applications. Electrically conductive composites of Sb_2S_3nanorods enwrapped by PEDOP were synthesized and used as electrodes in asymmetric supercapacitors; their structure-property correlation form the crux of **Chapter 6**. A PEDOP-Au@WO_3 hybrid dual function electrochromic supercapacitor electrode capable of optically modulating solar radiation while simultaneously storing/releasing charge was constructed and the

concurrent electrochromic cum pseudocapacitive roles of this hybrid were established and assessed with respect to pristine PEDOP and WO_3 films in **Chapter 7**. In **Chapter 8**, the ability of PEDOP to enhance the photoelectrochromic response of a V_2O_5 nanobelts based film, using a PEDOP/V_2O_5 hybrid is shown. Different instrumentation techniques which have been used to characterize PEDOP films and composites such as atomic force microscopy (AFM) with C-AFM, KPFM modes, UV-visible spectroscopy, electrochemical techniques such as cyclic voltammetry (CV), linear sweep voltammetry (LSV), chronoamperometry and electrochemical impedance spectroscopy (EIS), scanning electron microscopy (SEM), transmission electron microscopy (TEM), X-ray photoelectron microscopy (XPS) and Fourier transform infrared (FTIR) and Raman spectroscopies, X-ray diffraction (XRD) and thermogravimetric analysis (TGA) are described in the following **Chapter 2**.

References

[1] J. Platt, J. Chem. Phys. 34 (1961) 862–863.
[2] H. Jia, J. Wang, X. Zhang, Y. Wang, ACS Macro Lett. 3 (2013) 86–90.
[3] K. Wang, H. Wu, Y. Meng, Z. Wei, Small 10 (2013) 14–31.
[4] B. Weng, S. Ashraf, P. C. Innis, G. G. Wallace, J. Mater. Chem. C 10 (2013) 7430–7439.
[5] R. Gracia, D. Mecerreyes, Poly. Chem. 4 (2013) 2206–2214.
[6] D. Gupta, M. M. Wienk, R. A. J Janssen, Adv. Energy Mater. 3 (2013) 782–787.
[7] C. K. Chiang, C. R. Fincher, Y. W. Park, A. J. Heeger, H. Shirakawa, E. J. Louis, S. C. Gau A. G. MacDiarmid, Phys. Rev. Lett. 39 (1977) 1098–1101.
[8] L. Groenendaal, F. Jonas, D. Freitag, H. Pielartzik, J. R. Reynolds, Adv. Mater. 12 (2000) 481–494.
[9] A. Kumar, D. M. Welsh, M. C. Morvant, F. Piroux, K. A. Abboud,J. R. Reynolds, Chem. Mater. 10 (1998) 896-902.
[10] P. R. Somani, S. Radhakrishnan. Mater. Chem. Phys.1 (2003) 117–133.
[11] F. Carpi, D. D. Rossi, Optics. Laser Tech. 4 (2006) 292–305.
[12] C. L. Gaupp, K. Zong, P. Schottland, B. C. Thompson, C. A. Thomas, J. R. Reynolds, Macromolecules 4 (2000) 1132–1133.
[13] Y. Zhu, S. Murali, M. D. Stoller, K.J. Ganesh, W. Cai, P. J. Ferreira, A. Pirkle, R. M. Wallace, K. A. Cychosz, M. Thommes, D. Su, E. A. Stach, R. S. Ruoff, Science 332 (2011) 1537–1541.
[14] L. L. Zhang, X. S. Zhao, Chem. Soc. Rev. 9 (2009) 2520–2531.
[15] P. J. Mahon, G. L. Paul, S. M. Keshishian, A. M. Vassallo, J. Power Sources 91 (2000) 68–76.

[16] K. Leitner, A. Lerf , M. Winter, J. O. Besenhard, S. Villar-Rodil, F. Suarez-Garcıa, A. Martınez-Alonso, J.M.D. Tascon, J. Power Sources 153 (2006) 419–423.
[17] S. Roldán, M. Granda, R. Menéndez, R. Santamaría, C. Blanco, J. Phys. Chem. C, 115 (2011) 17606–17611.
[18] B. W. Ricketts, C. Ton-That, J. Power Sources 89 (2000) 64–69.
[19] P. Simon, Y. Gogotsi, Nat. Mater. 7 (2008) 845–854.
[20] A. Burke, J. Power Sources 91(2000) 37–50.
[21] M. Mastragostino, A. Catia, S. Francesca, J. Power Sources. 97 (2001) 812–815.
[22] M. Winter, R. J. Brodd, Chem. Rev. 104 (2004) 4245–4270.
[23] R. Kötz, M. Carlen, Electrochim. Acta 45(2000) 2483–2498.
[24] O. Inganas, I. Lundstrom, J. Electrochem. Soc. 131 (1984) 1129–1132.
[25] G. Sonmez, H. B. Sonmez, C. K. F. Shen, F. Wudl, Adv. Mater. 16 (2004) 1905–1908.
[26] R. Kiefer, D. G. Weis, J. Travas-Sejdic, G. Urban, J. Heinze, Sensors Actuators B: Chemical, 123 (2007) 379–383.
[27] Q. Pei, G. Zuccarello, M. Ahlskog, O. Inganäs, Polymer, 35 (1994) 1347–1351.
[28] P. M. Beaujuge, J. R. Reynolds, Chem. Rev. 110 (2010) 268–320.
[29] M. A. Invernale, Y. Ding, G. A. Sotzingacs, ACS Appl. Mater. Interfaces 2 (2010) 296–300.
[30] A. A. Argun, P. H. Aubert, B. C. Thompson, I. Schwendeman, C. L. Gaupp, J. Hwang, N. J. Pinto, D. B. Tanner, A. G. MacDiarmid, J. R. Reynolds, Chem. Mater. 16 (2004) 4401–4412.
[31] A. M. Österholm, D. E. Shen, A. L. Dyer, J. R. Reynolds. ACS Appl. Mater. Interfaces 5 (2013) 13432−13440.
[32] R. Liu, J. Duay, S. B. Lee, ACS Nano 5 (2011) 5608–5619.
[33] L. Groenendaal, G. Zotti, P. H. Aubert, S. M. Waybright, J. R. Reynolds, Adv. Mater. 15 (2003) 855–879.
[34] R. M. Walczak, J. R. Reynolds, Adv. Mater. 18 (2006) 1121–1131.
[35] A. Merz, R. Schwarz, R. Schropp, Adv. Mater. 4 (1992) 409–411.
[36] P. Schottland, K. Zong, C. L. Gaupp, B. C. Thompson, C. A. Thomas, I. Giurgiu, R. Hickman, K. A. Abboud, J. R. Reynolds, Macromolecules 33 (2000) 7051–7061.
[37] K. Zong, L. B. Groenendaalc, J. R. Reynolds, Tetrahedron Lett. 47 (2006) 3521–3523.
[38] H. Li, C.Lambert, R. Stahl, Macromolecules 39 (2006) 2049–2055.
[39] A. Kraft, M. Rottmann, H. D. Gilsing, H. Faltz, Electrochim. Acta 52 (2007) 5856–5862.
[40] A. Kharkwal, M. Deepa, A. G. Joshi, A. K. Srivastava, ChemPhysChem 12 (2011) 1176–1188.
[41] M. Deepa, A. Kharkwal, A. G. Joshi, A. K. Srivastava, J. Phys. Chem. B 115 (2011) 7321–7331.

Chapter 2

Materials and experimental techniques

This chapter provides details about various materials and techniques that were utilized during the synthesis and subsequent characterization of PEDOP or composite films.

2.1 Materials

Different chemicals which were used during experiments done in this thesis with their details are listed in Table 2.1.

Table 2.1: List of various chemicals used in the experimental work.

S.No.	Chemicals used	Company	Empirical/Molecular formula
MONOMERS			
1	3,4-Ethylenedioxypyrrole or EDOP (2% w/v solution in tetrahydrofuran)	Aldrich	$C_6H_7O_2N$
2	Aniline (M.W.~ 93 g/mol)	Merck	$C_6H_5NH_2$
3	3,4-ethylenedioxythiophene (EDOT)	Aldrich	$C_6H_6O_2S$
4	5-Cyano indole	Alfa-Aesar	$C_9H_6N_2$
ANIONIC SURFACTANTS			
5	Sodium (polystyrene sulphonate) (M.W. ~ 70,000)	Aldrich	$[-CH_2CH(C_6H_4SO_3Na)-]_n$
6	Sodiumdodecylsulfate (M.W. ~288.38 g/mol)	Aldrich	$C_{20}H_{37}NaO_7S$
IONIC LIQUIDS			
7	1-Ethyl-3-methyl imidazolium bis(trifluoromethylsylfonyl)imide	Merck	$C_9H_{20}NCF_3SO_3$

8	Trihexyl(tetradecyl)phosphonium tris(pentafluoroethyl)trifluorophosphate	Merck	$[(C_{32}H_{68})P^{+}][(C_2F_5)_3PF_3^{-}]$
9	1-Butyl-1-methylpyrrolidinium bis(trifluoromethylsulfonyl)imide ([BMPY][$N(CF_3SO_2)_2$])	Merck	$C_{11}H_{20}F_6N_2O_4S_2$
10	1-Butyl-3-methyl-imidazolium tris(pentafluoroethyl)trifluorophosphate ($BuMeIm^{+}[(C_2F_5)_3(PF_3)]^{-}$)	Merck	$C_{14}H_{15}F_{18}N_2P$
11	1-Butyl-3-methyl imidazolium trifluoromethanesulfonate or triflate ([BmIm][CF_3SO_3])	Merck	$C_9H_{15}F_3N_2O_3S$
SALTS			
12	Lithium perchlorate (M.W.~ 106.39 g/mol)	Aldrich	$LiClO_4$
13	Lithium trifluoromethanesulfonate (M.W. ~ 156.01 g/mol)	Aldrich	$LiCF_3SO_3$
SOLVENTS			
14	Dimethyl sulfoxide (M.W. ~ 78.13 g/mol)	Merck	C_2H_6OS
15	Methanol (M.W.~32 g/mol)	Merck	CH_3OH
16	Propylene carbonate (M.W. ~ 102.09 g/mol)	Merck	$C_4H_6O_3$
17	Poly(ethyleneglycol) (PEG-400) (M.W.~ 380 g/mol)	Merck	$HO(C_2H_4O)_nH$
18	Ethanol (M.W.~ 46 g/mol)	Merck	C_2H_5OH
19	Acetone (M.W.~ 58.08 g/mol)	Merck	CH_3COCH_3
20	Dimethylformamide (M.W.~73.10 g/mol)	Merck	C_3H_7NO
21	Toluene (M.W.~ 92.14 g/mol)	Merck	$C_6H_5CH_3$
22	Isopropanol	Merck	C_3H_8O

23	Acetonitrile (ACN)	Merck	C_2H_3N
24	Ethylene glycol	Merck	$C_2H_6O_2$
MISCELLANEOUS			
25	Graphite platelets (Width: 50 – 250 nm and Length: 0.5 to 5 μm)	Aldrich	C_n
26	Poly(vinylalcohol) (M.W. ~85,000-146,000)	Aldrich	$[-CH_2CH(OH)-]_n$
27	Hydrogen tetrachloroaurate (M.W.~ 393.83 g/mol)	Alfa-Aesar	$HAuCl_4.3H_2O$
28	Potassium hexacyanoferrate (M.W.~ 329.26 g/mol)	Merck	$K_3[Fe(CN)_6]$
29	Tetraoctylammoniumbromide (M.W.~ 546.81 g/mol)	Merck	$C_{32}H_{68}BrN$
30	Sodium borohydride (M.W ~37.83 g/mol)	Merck	$NaBH_4$
31	Sodium sulfate (M.W.~ 142.04 g/mol)	Merck	Na_2SO_4
32	Ferric chloride (M.W.~162.21 g/mol)	Merck	$FeCl_3$
33	Sodium nitrite (M.W. ~ g/mol)	Merck	$NaNO_2$
34	Potassium permanganate	Merck	$KMnO_4$
35	Nitric acid	Merck	HNO_3
36	Sulfuric acid	Merck	H_2SO_4
37	Hydrochloric acid 35%	Merck	HCl
38	Hydrazine	Merck	N_2H_4
39	Ammonia	Merck	NH_3
40	Multiwalled carbon nanotubes (MWCNTs) (90%) outer diameter: 10-15 nm, inner diameter: 2-6 nm and length 0.1-10 μm	Aldrich	

41	Sulphanilic acid	Merck	$C_6H_7NO_3S$
42	Ammoniumperoxydisulphate	Merck	$(NH_4)_2S_2O_8$
43	Azobisisibutyronitrile (AIBN)	Merck	$C_8H_{12}N_4$
44	Poly(vinylidenefluoride-co-hexafluoropropylene) pellets (PVdF-HFP, M_W = 455000)	Merck	$(-CH_2CF_2-)_x[-CF_2CF(CF_3)-]_y$
45	Oxalyl chloride	Merck	$C_2O_2Cl_2$
46	Poly(methylmethacrylate) (PMMA, M.W. 996000)	Aldrich	$C_5O_2H_8)_n$
47	m-Amino benzenesulfonic acid	Merck	$C_6H_7NO_3S$
48	Hydrogen peroxide 30%	Merck	H_2O_2
49	Sulfur	Aldrich	S
50	Antimony chloride	Alfa-Aesar	$SbCl_3$
51	Tri-sodium citrate	Merck	$Na_3C_6H_5O_7$
52	Tungsten metal powder	Alfa-Aesar	W
53	Sodium vanadate	Alfa-Aesar	Na_2VO_4
54	Sodium Chloride	Merck	NaCl

Ultrapure water (resistivity ~18.2 MΩ cm) was obtained through Millipore Direct-Q3 UV system. SnO_2:F (FTO) coated glass substrates with a sheet resistance of about 14 Ω sq^{-1} were procured from Pilkington, washed with soap solution, flushed with copious amounts of distilled water and cleaned with acetone prior to use. A carbon fiber cloth of 3 mm thickness was purchased from Alibaba Pvt. Ltd and used as the substrate for flexible

supercapacitors in Chapter 6. A 3M acrylic tape of 500 μm thickness was employed as the spacer, which was also used for accommodating the electrolyte, thus enabling construction of ECDs and supercapacitors.

2.2 Characterization techniques

2.2.1 Electrochemical methods

In chronoamperometry, a fixed potential is applied to the working electrode and current produced in the cell is monitored as a function of time. The resultant graph is plot of current *versus* time. In this thesis, CA has been used for (a) synthesis of films of CPs and composites/hybrids and (b) determination of charge density during coloration and bleaching of an electrochromic film with an Autolab PGSTAT 302N Potentiostat/Galvanostat coupled with a NOVA 1.9 software.

A generic method for synthesizing PEDOP films involves the preparation of a clear solution of the monomer 3,4-EDOP and a salt like $LiClO_4$ (or any ionic species) in an organic medium like acetonitrile. Alternately, the monomer in the same strength (0.1 M) can be dissolved in an ionic liquid (IL) or an IL/solvent mixture wherein, the IL serves as the dopant and as well as the solvent (if used alone) for electropolymerization. If only water was employed as the solvent for preparing PEDOP films, a surfactant like sodium poly(4-styrene sulfonate) is added to the bath for dissolving the monomer. A three electrode electrochemical cell comprising of a working electrode (FTO coated glass), a counter electrode (Pt rod/sheet or FTO coated glass) and a reference electrode (Ag/AgCl/KCl) was used (Figure 2.1). The electrodes were immersed in the solution containing the monomer. PEDOP films were deposited onto the working electrode by oxidative electropolymerization at room temperature by chronoamperometry. A fixed potential (chosen from a range between +1.2 to +2 V) was applied to the working electrode for a fixed

duration of time (typically between 1-10 min.). Light blue colored PEDOP films were obtained which were washed in deionized water or an organic solvent, dried in air and stored in air. Equation in Figure 2.2 represents the formation of polymer.

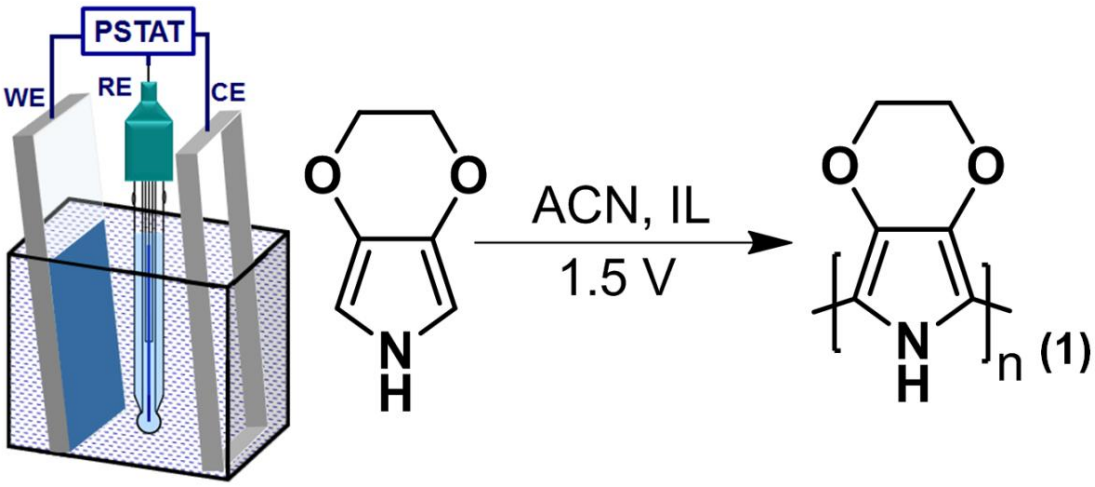

Figure 2.1: Schematic of the three electrode cell showing formation of PEDOP; the bath contains 3,4-EDOP, IL and ACN.

Chronopotentiometry is a constant current experiment wherein a current step is applied across an electrochemical cell and potential response is plotted as a function of time. Here this technique has been used for measuring galvanostatic charge-discharge characteristics of CP and composite films by applying different current densities (in A g^{-1}), typically in two electrode configurations with the working electrode being a CP film and the counter electrode being Pt or FTO coated glass or graphite coated glass. These measurements were done either on a battery testing unit (Arbin Instruments, BT 2000) or on an Autolab PGSTAT 302N Potentiostat/Galvanostat. Specific capacitances (SC, F g^{-1}) of the polymer or composite were calculated from the slopes of the charge or discharge curves by using the following equation (unless mentioned otherwise).

$$SC = I \times \Delta t / \Delta V \times m \quad (1)$$

SC is the specific capacitance, I is the current applied for charge or discharge, Δt is the time in seconds for charge or discharge, ΔV is voltage window and m is mass of active material of the

CV has been utilized (a) to discern the redox processes of CPs and composites in three electrode or two electrode configurations, (b) to characterize electrochromic or supercapacitor devices and (c) to determine cycling stability of films or devices;all with an Autolab PGSTAT 302N Potentiostat/Galvanostat coupled with a NOVA 1.9 software.CVmeasures current (A) or current density (A cm^{-2}) as a function ofapplied voltage, which is swept at a constant rate, $\upsilon = dV/dt$; it can be therefore used for determining capacitance. The capacitance of a capacitor is given as $C = dQ/dV$, where dV the voltage difference between the parallely placed electrodes associated with accumulation of charge Q on each electrode. Since charge is the integration of current over time range, it can be determined using $Q = \int I\, dt$ equation. The capacitance can be calculated using the following equation.

$$C = dQ/dV = \int I\, dt / dV = I\, \Delta t/\Delta V = I / \upsilon \qquad (2)$$

In LSV, the potential applied to the working electrode is swept on one direction and only once, from a start potential E_1 to an end potential E_2 at a fixed scan rate and the current generated at electrode is plotted as a function of swept potential, to yield a I-V or a J (current density)-V curve. In this thesis, the LSV technique has been employed (a) to study the I-V or J-V characteristics of polymer electrolytes, (b) to determine the electrochemical potential stability window of polymer electrolytes and (c) conductivity of CPs / composites with an Autolab PGSTAT 302N Potentiostat/Galvanostat coupled with a NOVA 1.9 software. From the straight-line fits, within the voltage windows in which the I-V response was almost linear, ambient temperature

conductivities were determined by using equation (4), wherein d is the thickness of the sample and a is the area of the sample.

$$\sigma_{RT} = (I/V) \times (d/a) \quad (3)$$

2.2.2 Spectroelectrochemistry and other spectroscopic methods

In the present thesis, absorbance or transmittance spectra of conducting polymer films/devices/ solutions were recorded on a Shimadzu UV-Visible-NIR 3600 spectrophotometer either in an *in-situ* manner under dc potentials of different magnitudes (applied for a fixed duration of time, e.g. 60 s) or in the as-fabricated state without applying any bias. Absorption spectra of solutions were measured in quartz cuvettes of 1 cm path length using the same instrument. A decisive performance metric of an electrochromic film/device is the coloration efficiency (η), which connects its optical density change (ΔOD) at a given wavelength to the charge density Q/A (C cm^{-2}) required to induce the change.

$$\eta(\lambda) = \Delta OD(\lambda) / Q/A = \log (T_b(\lambda)/T_c(\lambda))/Q/A \quad (4)$$

T_c and T_b are the transmittances of the film or device in colored and bleached states respectively. The optical density and/or transmittance of devices/films were measured under different potentials, each applied for a fixed time period. The charge Q/A or charge density values at each potential were determined by chronoamperometry, as discussed in an earlier section.

The time required for an electrochromic film (such as CP or composite films) or device to color from its bleached state or vice versa is termed as its response time. For most films/devices, response or switching time is of the order of a few seconds and is extremely useful for judging the suitability of a film for an electrochromic application. Electrochromic switching response of devices/films were measured under a square wave potential of fixed magnitude (e.g. ± 2 V) applied to the working electrode (CP film or composite), at a fixed monochromatic wavelength

such as λ_{max} of the CP or an appropriate wavelength at which high contrast is observed, using the same spectrophotometer, in kinetic mode. These measurements were done in a two electrode configuration either with a film as the working electrode and Pt as counter electrode in conjunction with a liquid electrolyte or in the device configuration with two complementary electrochromic films as working and counter electrodes. Step times or half-cycle times ranged between 1 to 5 s. The color-bleach kinetic plot is a graphical representation of absorbance or transmittance *versus* time, under a square wave bias from which switching times of CP or composite films/ devices were deduced. All *in-situ* spectrophotometry measurements of films colored/ bleached in electrolytes were implemented in a quartz cell. Devices based on CPs were directly inserted in the sample compartment during measurements.

In this thesis, EIS was employed to unravel the redox phenomena of CP and composite films/devices by superimposing different dc potentials over ac potentials of a small magnitude between 5-20 mV. The measurements were performed on an Autolab PGSTAT 302N Potentiostat/Galvanostat/Frequency Response Analyzer coupled with a NOVA 1.9 software.The measurements were done either in two electrode configurations (using the CP film as the working electrode and Pt or FTO/glass as the counter electrode) or in three electrode configurations, wherein a Ag/AgCl/KCl was the third (reference) electrode. EIS has also been used to measure conductivities of electrolytes (at room temperature and different temperatures) from the Z"*versus* Z' plots, wherein the onset of the curve on the real axis corresponds to the resistance (R) of the electrolyte. Measurements were done between two Pt electrodes.

$$\sigma\,(T) = (1/R) \times (l/a) \qquad (5)$$

In (9), a is the area of cross section of the two Pt electrodes and l is the distance between them.

FTIR spectra of CP films / composites and precursor materials / non-aqueous solutions were measured either in KBr pellets or pressed onto an IR transparent ZnSe crystal (10 mm^2 in dimensions) using a Bruker37Tensor FTIR spectrometer equipped with OPUS^{TM} software in the frequency range of 3000-500 cm^{-1}.

ABruker Senterra Dispersive Raman Microscope spectrometer was used in the present work for recording the Raman spectra of CP films, composites and other precursor materials or solutions. The instrument integrates a multi laser Raman spectrometer onto the confocal optical microscope. The spectrometer part is integrated in between the base and the binocular of the microscope. The confocal Raman microscope wasequipped with three excitation lasers (532 nm, 633 nm,785 nm) and a computer controlled xyz stage allowingincrement stepping down to 0.1 μm in all directions. A laser wavelength of 785 nm was used and samples were mounted on a microslide glass plates for the measurement. The usable wavelength range is 100-4000 cm^{-1}. The Raman spectrum is a plot of absorbance or transmittance *versus* chemical shift (cm^{-1}).

2.2.3Atomic force microscopy (AFM)

AFM (multimode) is a high-resolution imaging tool for complete surface characterization of properties like topography, elasticity, friction, adhesion, and electrical/magnetic fields. AFM operates in contact, intermediate (tapping), and non-contact modes. In contact mode operation, the AFM tip touches the sample surface, and the tip-sample repulsive force deflects the tip-cantilever [1]. The cantilever deflection is monitored and used as a feedback signal. In intermediate and non-contact modes, the cantilever is externally oscillated at, or close to, it's resonance frequency. The tip-sample interaction is altered as the tip-sample distance changes, leading to a change in oscillation amplitude (intermediate mode) and resonance frequency (non-contact mode). These amplitude and frequency changes, with respect to the reference amplitude

and frequency, are used as feedback signals to obtain the topography of the sample surface. Therefore, intermediate mode and non-contact modes are referred as amplitude modulation (AM) and frequency modulation (FM) operation, respectively. In intermediate and non-contact mode AFM, the tip-sample interaction is perturbed by attractive and repulsive forces, causing amplitude or frequency changes in the oscillation of the AFM tip, as illustrated schematically in Figure 2.2. In AM mode AFM, changes in the oscillation amplitude provide the feedback signal for imaging.

As seen in Figure 2.2a, the amplitude of oscillation increases as the tip-sample distance increases, due to the decrease in tip-sample interaction. The amplitude change is monitored and regulated by a feedback system to keep the tip-sample distance constant at a pre-determined set-point. The dependence of amplitude change on the tip-sample interaction can be described analytically, based on the harmonic oscillator model, and the amplitude change is generally accepted to be dependent on the force between the tip and sample. Therefore, AM mode measurements represent the direct force between the tip and sample. In FM mode AFM, changes in the oscillation frequency provide information about tip-sample interactions. The cantilever oscillation frequency changes due to the tip-sample distance variation, as illustrated in Figure 2.10b. A feedback system regulates the frequency change to keep the set-point frequency constant, allowing the topography of the sample surface to be acquired. The changes in oscillation frequency are dependent on the force gradient between tip and sample when the restoring force of the cantilever that is associated with tip oscillating energy is large compared to the interaction force between the tip and sample surface. In this thesis, AFM was used for studying the topography of CP and composite films and also to determine thickness of these films by constructing a sharp step of CP or composite on FTO coated glass and allowing the tip

(made of Pt/Ir) to run over the step, whilst simultaneously imaging the same. The height profile provided the film thickness. All AFM, C-AFM and KPFM data were recorded using a Veeco, Multimode 8 with ScanAsyst (Nanoscope 8.10 software) microscope.

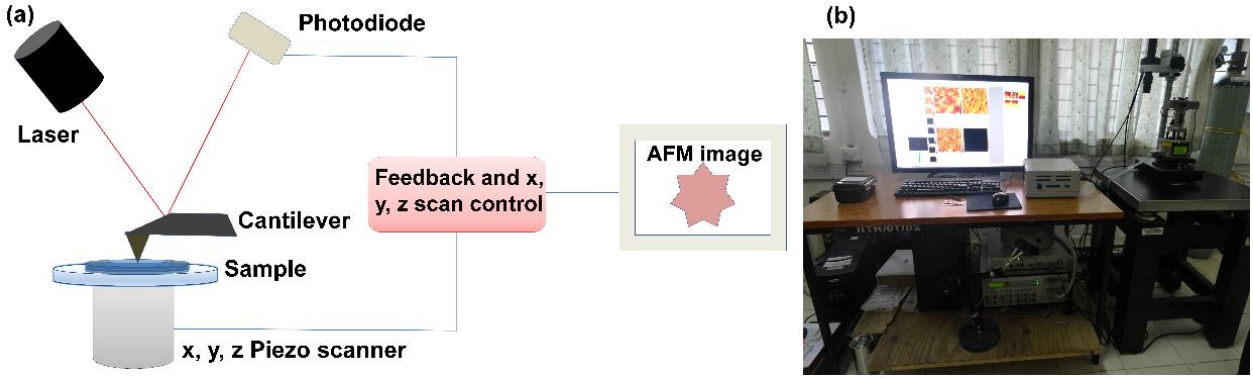

Figure 2.2: (a) Schematic of an AFM and (b) a photograph of a Bruker (formerly Veeco) atomic force microscope.

C-AFM is a secondary imaging mode derived from contact AFM that measures conductivity variations across medium- to low- conducting and semiconducting materials. C-AFM performs general-purpose measurements, and has a current range of 2 pA to 1mA. C-AFM employs a conductive probe tip. Typically, a dc bias is applied to the tip, and the sample is held at ground potential. While the z feedback signal is used to generate a normal contact AFM topography image, the current passing between the tip and sample is measured to generate the conductive AFM image (Figure 2.3). C-AFM images were recorded for CP films/ composites. For C-AFM, cantilevers made of antimony doped silicon (n-doped; resistivity ~0.01 - 0.025 Ω cm) and coated with Pt/Ir or Co/Cr (20 nm) on the front and backside were obtained from Veeco. Spring constant of tip was 0.2 N cm^{-2}.The current sensitivity was 1 nA V^{-1} and a load force of 49 nN was maintained between the tip and the sample. The sample deposited on FTO coated glass, (area ~10 mm^2) was attached to a stainless steel support with a conducting carbon tape. An even

coat of silver paste was applied from the surface of the conducting polymer film, along the edge of the conducting glass substrate to the stainless steel plinth, and the topography, current images and point contact I-V profiles were recorded at room temperature. A crack free, pinhole free strip of silver paste was obtained upon drying, which was used for taking electrical contacts. The contact tip is scanned in contact with the sample surface. The z-feedback loop uses the dc cantilever defending a signal to maintain a constant force between the tip and the sample to generate topography images. Concurrently, a dc bias of 50 mV or in the same range was applied to the tip. The sample or tip is held at ground potential. The built-in pre-amplified scanner head measures the current passing through the tip and sample and images the current profiles.

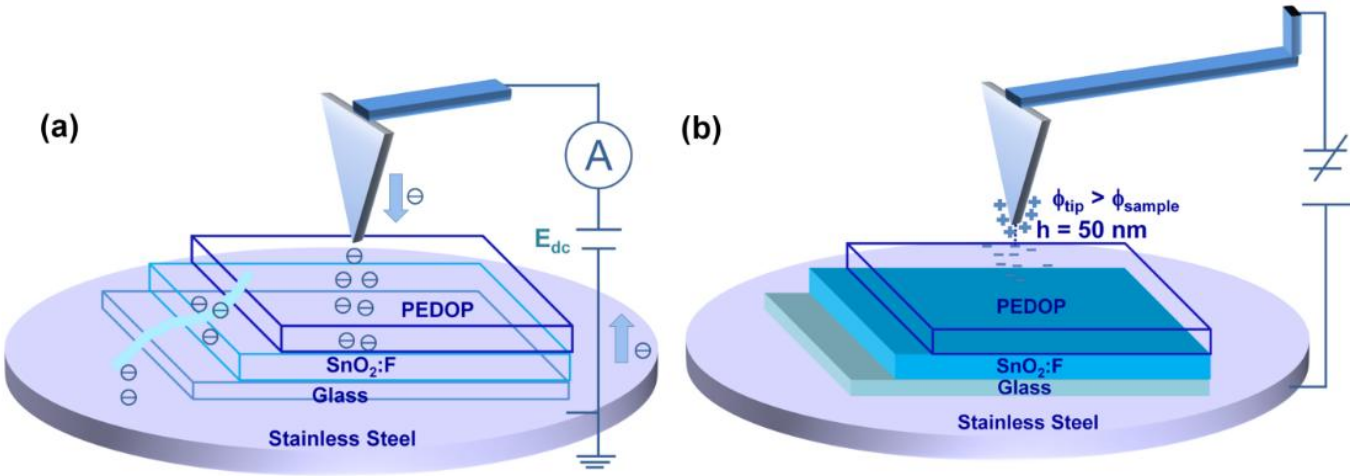

Figure 2.3: Schematics of (a) C-AFM and (b) KPFM modes.

KPFM, also known as surface potential microscopy, is a noncontact variant of atomic force microscopy (AFM), and was invented in 1991 [2]. With KPFM, the work function of surfaces can be observed at atomic or molecular scales. The map of the work function produced by KPFM gives information about the composition and electronic state of the local structures on the surface of a solid. The work function is the minimum energy (or work, usually measured in eV),

needed to remove an electron from a solid, to a point immediately outside the solid surface (or energy needed to move an electron from the Fermi level into vacuum). When two different conductors are brought into electrical contact, for example, via an external wire contact, electrons will flow from the one with lower work function to the one with higher work function, equalizing the Fermi energies. If they are made into a parallel plate capacitor, equal and opposite charges will be induced on the surfaces. The potential established between these two surfaces is called the contact potential difference (V_{CPD}), contact potential, or surface potential, which equals the work function difference of the two materials. Measuring the $V_{CPD,}$ is thus quite simple. An external potential (also called the backing potential) is applied to the capacitor until the surface charges disappear. At this point, the external potential equals the V_{CPD}. KPFM can measure V_{CPD}, and therefore work functions, in the nanometer regime.

In the present work, surface potential maps of CP and composite films were measured by employing cantilevers made of antimony doped silicon and with a metallized apex of Co/Cr or Pt/Ir on the front and the back side of the tip. The spring constant of tip was 1-5 N cm^{-2} cantilevers (Veeco, resonant frequency of ~70 kHz, spring constant ~ 2 N/m, lever thickness 2.8 μm, lever length 240 μm, lever width 30 μm). The tip height is 14 μm, and the tip radius is ~30 nm. The height data or topography was measured in tapping mode during the first pass, for every scan line. In the second pass, the tip lifts above the surface to an adjustable lift height, which was fixed at a value between 20-200 nm (for each sample), and scans the same line, while following the height profile recorded in the first pass. Potential maps are taken in interleave mode. An ac bias (V_{ac}) is applied to the tip and as a consequence an electrostatic force is generated between the tip and sample. This is the V_{CPD} and now an external dc voltage of the same magnitude (V_{dc}) but opposite sign is applied by the instrument to nullify V_{CPD}, and this potential is equal to the

work function difference between the sample and the tip (Figure 2.3). The force acting along the z axis is given by the following expression.

$$F(z) = 1/2\ V^2\ (dC/dz) \quad (6)$$

$$V = V_{dc} - V_{CPD} + V_{ac}\sin(\omega t) \quad (7)$$

C is the entire capacity between the tip and the sample surface. As V_{dc} is acquired at each point on the sample surface, the resultant image is a map of surface potentials or work function of the area under study. We performed KPFM measurements by bringing the tip in proximity (at a fixed hight above the sample) with respect to the top surface of the active film. No dc bias was applied to the sample during the measurement and a sinusoidal ac voltage of 5 V was applied to the tip during surface potential imaging.

2.2.4 Structural studies

For all SEM studies, a Carl-Zeiss Supra 40 field emission-SEM (FE-SEM) with EDX (energy dispersive X-ray analysis)was utilized for obtaining topographic images. A carbon double sided conductive tape (PELCO Tabs™) were used to place the films onto the sample holder and conducting carbon paint (EM Graphite Conductive Adhesive 154) was applied to the edges of the films to enhance the adhesion. An acceleration voltage of 6 kV was selected for examining the samples.X-ray diffractograms were recorded for CP/composites and precursor materials on a XRD, PANalytical, X'PertPRO instrument with Cu-Kα (λ = 1.5406 Å) radiation.High resolution HRTEM Tecnai G2 F30 STWINwas used for studying graphene oxide based samples in this thesis.

XPS was carried out on a Perkin Elmer 1257 model operating at a base pressure of ~4.2×10^{-8} Torr (100 Watt, 15 KV) with a non-monochromatized Mg Kα line at 1253.6 eV, an analyzer

pass energy of 60 eV, and a hemispherical sector analyzer capable of 25 meV resolution. The overall instrumental resolution was about 0.3 eV. The core level spectra were deconvoluted using a non-linear iterative least squares Gaussian fitting procedure. For all fitting multiplets, the FWHMs were fixed accordingly. Corrections due to charging effects were taken care of by using C(1s) as an internal reference and the Fermi edge of a gold sample. A Jandel Peak FitTM (version 4.01) program was used for the analyses.Thermal stability of electrolytes was determined by TGA in this thesis. TGA data for the samples were collected on a Q600, TA instruments in nitrogen atmosphere.

References

[1] P. West, Introduction to atomic force microscopy: Theory, practice, applications, www. AFMUniversity.org.
[2] M. Nonnenmacher, M. P. OBoyle, H. K. Wickramasinghe, Appl. Phys. Lett. 58 (1991) 2921–2923.

Chapter 3

PEDOP enwrapped by reduced graphene oxide/ionic liquid composite: Nanoscale conduction and electrochromism

3.1 Introduction

CP composites, by use of an appropriate conductive nanstructured moiety enable (a) extended modulation of solar radiation from visible (or photopic) to near-infrared (or NIR) spectral regions, (b) improvment in redox cycling capability and (c) further amplification of the electrochromic contrast ratio and (d) reduction in switching times [1]. Graphene oxide (GO) is a viable alternate to CNTs for fabricating composites with CPs, owing to low processing temperatures, lower cost and ease of preparation [2-4]. GO can be easily processed by modified Hummers' method [5]. To recover the desirable properties of graphene such as low band gap (since graphene monolayer is a zero gap material), high electronic conductivity, extraordinary mechanical and chemical strengths and large effective surface area, strong chemical reduction of GO is imperative [6]. Reduced graphene oxide or RGO can be further functionalized with an ionic liquid (IL) to yield a RGO/IL composite. The IL, overrides the effect of oxygen moieties considerably, and the ionic liquid cation and anion are entrapped in reduced graphene oxide. RGO/IL is easily dispersed in organic solvents and after monomer (pyrrole or thiophene or aniline) addition, it can then serve as a counter ion for electropolymerization of the latter. In this chapter, we study the ability of IL functionalized RGO to completely alter the charge transport dynamics of PEDOP, by use of electron microscopy, C-AFM and electrochemical probes.

3.2 Experimental

3.2.1. Synthesis of reduced graphene oxide (RGO)

Graphite platelets (0.5 g) were dispersed in H_2SO_4 (11.5 mL) and $KMnO_4$ (0.5 g) was added gradually under continuous stirring; the temperature of the slurry was maintained at approximately 20 ^{0}C. The slurry was stirred at 35 ^{0}C for 2 h, followed by addition of deionized water (2 mL) and further stirred for 1 h. The reaction was terminated by addition of deionized water (70 mL). The suspension was washed repeatedly using a 1:10 (HCl : Water, v/v) solution to remove unwanted metal ions till the supernatant liquid showed a pH close to neutral. Graphene oxide (GO) was extracted by filtration and dried in oven at ~ 60 ^{0}C till a completely dry product was obtained. GO (0.5 g) was dispersed in deionized water (10 mL), hydrazine (0.6 mL) and ammonia solution (7 mL), and refluxed for 1 h in an oil-bath at 95 ^{0}C. The suspension was then washed thoroughly with deionized water and dried in oven at ~ 60 ^{0}C for a few hours. Hydrogen gas was purged through the solid for 10 minutes to yield reduced graphene oxide (RGO) and it was stored in a vacuum desiccator. RGO (0.08 g) was ultrasonicated with 1-ethyl-3-methyl imidazolium bis(trifluoromethylsulfonyl)imide (2 g) for 2 h and the resulting bucky gel was subjected to iterative washing with acetonitrile and filtration to remove the superfluous ionic liquid till a RGO/IL composite was obtained. The photographs of GO, RGO/IL bucky gel and suspensions formed from GO and RGO/IL in acetonitrile are shown as insets of Figure 3.1b.

3.2.2 PEDOP–RGO/IL and PEDOP-IL films

A colloidal suspension containing EDOP (0.1 M), the bucky gel of RGO/IL composite in acetonitrile (12 mL) and PEG400 (2 mL) was used for the preparation of the PEDOP–RGO/IL films (the photograph of the precursor is shown in the inset of Figure 3.1b). The solution was ultrasonicated prior to film deposition to minimize aggregation and settling down of particles. A clear solution of 1-ethyl-3-methyl imidazolium bis(trifluoromethylsulfonyl)imide (2 g) and

EDOP (0.1 M) in acetonitrile (12 mL) and PEG400 (2 mL) was used for synthesizing the control PEDOP-IL films (photograph of this formulation is shown in the inset of Figure 3.1a). A three electrode single compartment cell with a platinum sheet as counter electrode, Ag/AgCl/KCl as reference electrode, and a transparent conducting SnO_2:F coated glass substrate as the working electrode was utilized for film deposition. A constant potential of +1.5 V was applied to the working electrode which was immersed in EDOP-RGO/IL dispersion or EDOP-IL solution for 300 s at room temperature. The resulting bluish-black colored composite films of PEDOP–RGO/IL or control PEDOP/IL were immediately rinsed with acetonitrile and dried in air for 2 h and stored in air. Prussian blue films were fabricated from a solution of $K_3[Fe(CN)_6]$ (10 mM) and $FeCl_3$ (10 mM) in HCl (0.01 N) in galvanostatic mode by application of 10 μA cm^{-2} to a SnO_2:F coated glass substrate for eight minutes. Devices with following configuration: PEDOP-RGO/IL-PB and PEDOP-IL-PB with 1-ethyl-3-methyl imidazolium bis(trifluoromethylsulfonyl)imide electrolyte were fabricated [7]. Reaction schemes are shown in Scheme 3.1.

(a)

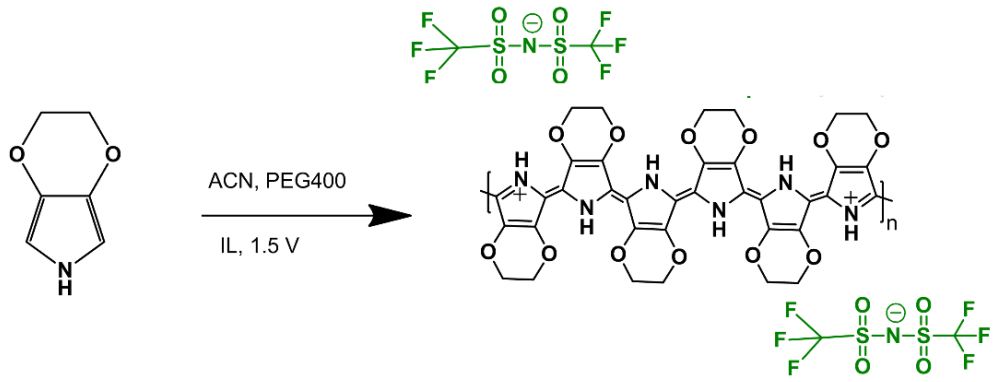

(b)

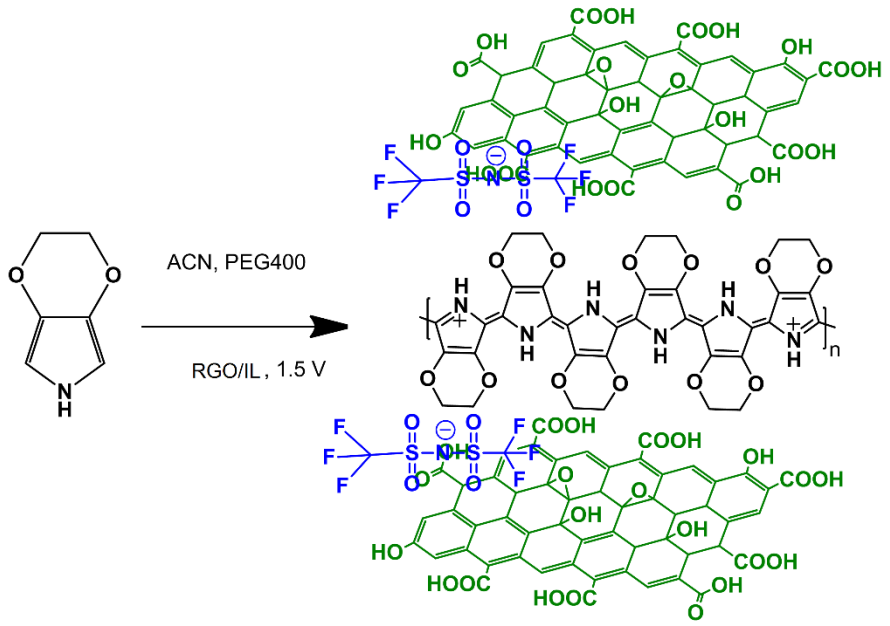

Scheme 3.1: Electropolymerization of (a) PEDOP/IL and (b) PEDOP-RGO/IL.

3.3Results and discussion

3.3.1 I-t plots and Electrogravimetry

The current-time transients recorded during electropolymerization from suspensions of (a) EDOP and IL and (b) EDOP and RGO/IL under a fixed dc potential of +1.5 V are shown in Figure 3.1a and b respectively. The initial spike followed by a plateau like response, observed for

the formation of both films is characteristic of (a) oxidation of monomer and (b) coupling of radical cations and precipitation of the oligomers onto the substrate to yield PEDOP nuclei. The plateau region commensurates with the PEDOP chain propagation. The corresponding charge involved during electropolymerization is also shown. For the control PEDOP-IL film, the Coulombic charge (Q) deposited increases almost linearly with time, and at the point of culmination of deposition time, i.e., at t = 300 s, Q was ~ 0.8 mC. A similar variation in current/charge with time was observed for potentiostatic synthesis of PEDOT doped by perchlorate ions [8]. In contrast for the PEDOP-RGO/IL, the Q *versus* t plot (Figure 3.1b) shows a linear dependence from t = 0 s to t = 80 s, and at this juncture, Q is 0.13 mC; thereafter Q saturates and does not vary much till the end of the deposition duration (t = 300 s). The magnitude of Coulombic charge deposited on the substrate from the EDOP-RGO/IL dispersion, is obviously smaller as compared to the charge deposited from the EDOP-IL solution. This difference may be attributed to the bulkier nature of the RGO/IL flakes, which are only dispersed and not dissolved as the ionic liquid anion or cation are, in the EDOP-IL solution. As a consequence, the movement of RGO/IL nanosheets, which serve as counterions for charge compensation onto the radical cations formed on PEDOP is sluggish and therefore lesser charge is deposited. The corresponding Δf *versus* time plots (Figure 3.1c and d) obtained from electrochemical quartz crystal microbalance (EQCM) analysis, for the two samples reveal a larger frequency decrease in the growing PEDOP-IL film as compared to the PEDOP-RGO/IL system, which also indicates a higher amount of polymer deposited in the former case. The corresponding mass deposited onto substrate is also considerably higher for the control PEDOP-IL film (Figure 3.1c) as compared to the PEDOP-RGO/IL composite. The Sauerbrey equation was employed for determination of mass, where Δf is the resonant frequency of the quartz

crystal, f_o is the fundamental frequency, ρ is the density of the quartz crystal (2.648 g cm^{-2}), μ is the shear modulus of quartz (2.947×10^{11} g cm^{-1} s^{-2}) and n is the harmonic number of oscillation (~1) and C_f is the sensitivity factor (Hz $cm^2 \mu g^{-1}$).

$$\Delta f = -2f_o^2 mn / (\rho\mu)^{1/2} = -C_f m \quad (1)$$

A direct comparison between the masses of the two samples is not justified, as in the case of the PEDOP-IL film, the mass deposited includes the mass of the solvent as well, for the ILcation/anion is highly solvated in solution, and therefore migrates as a whole onto the growing film. In contrast, for the formation of PEDOP-RGO/IL, the counter ion is least likely to be solvated and therefore the mass involved is significantly lowered. In an earlier report, a similar, almost linear variation for polymer mass per unit surface *versus* time was obtained for a PEDOT-ClO_4 system [9]. However, despite a higher mass/charge, the electropolymerization process seems to be more efficient in PEDOP-RGO/IL, as the maximum charge that can be deposited onto the substrate at a given time, is attained in a much shorter time span.

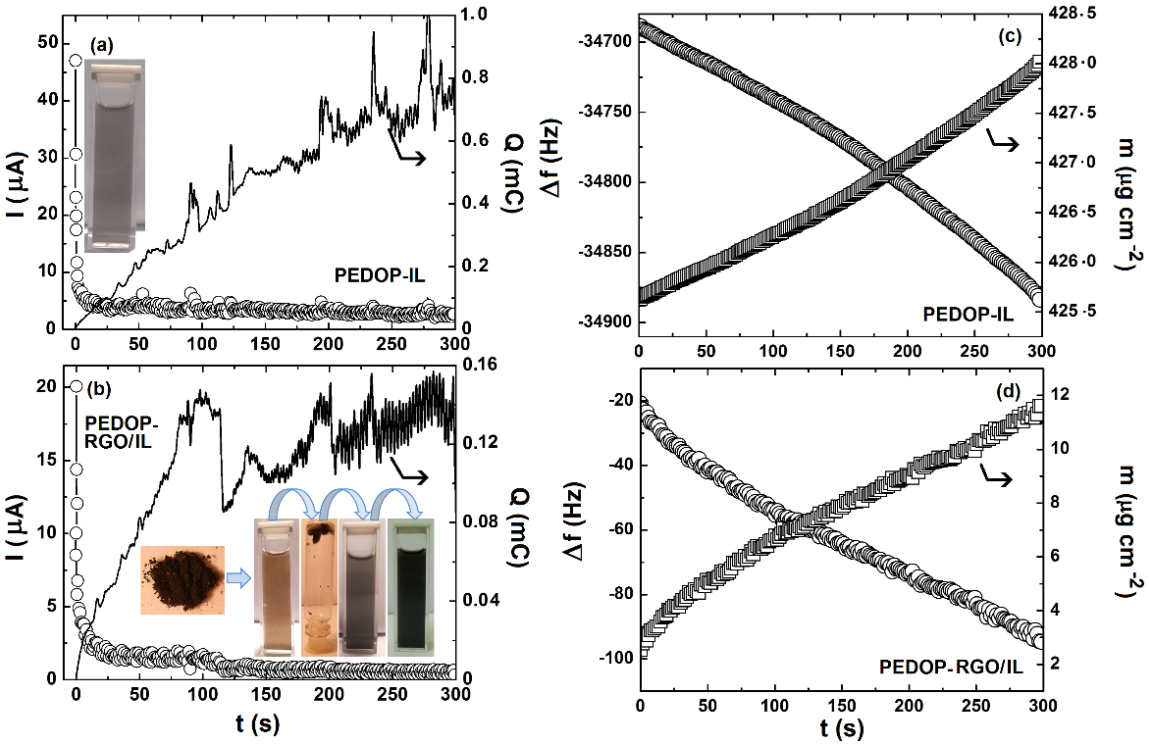

Figure 3.1: Current (○) / Charge (—) *versus* time transients for oxidative electropolymerization of (a) 0.1 M EDOP in ionic liquid solution (photograph of solution in inset) and (b) EDOP in a RGO/IL dispersion under a constant dc potential of +1.5 V. Inset of (b) from left to right shows photographs of GO powder, GO in acetonitrile, RGO/IL bucky gel, RGO/IL in acetonitrile, and EDOP-RGO/IL in acetonitrile. Frequency change (○) / polymer mass per unit surface area (□) *versus* time plots recorded during electropolymerization of (c) 0.1 M EDOP in neat ionic liquid and (d) 0.1 M EDOP in a RGO/IL dispersion, in chronoamperometric mode.

3.3.2. Raman spectra

Raman spectra of GO and RGO are shown in Figure 3.2. Both spectra show the D and the G bands. For neat GO, the G peak is seen at 1591 cm^{-1} and after reduction it shows a blue shift to 1584 cm^{-1}. The D band observed at 1353 cm^{-1} in pristine GO, which is ascribed to surface defects, smaller sized graphene layers and indicates the presence of other functionalities, also shows a blue shift to 1348 cm^{-1} upon reduction. The G peak is due to the in-plane vibration of sp^2 hybridized carbon atoms, which is the doubly degenerate zone center E_{2g} mode [10,11]. The intensity of both D and G bands decreases ongoing from GO to the reduced sample, indicating a

fewer defect density upon reduction. Similar hypsochromic shifts were also registered by authors for reduced GO products in previous works [10,12,13]. The 2D overtone band, which is visibly of a lower intensity as compared to the corresponding D band, is at 2697 cm^{-1} in neat GO and downshifts to 2674 cm^{-1} in the reduced sample. Such a shift has been observed previously ongoing from exfoliated GO to reduced graphene [14].

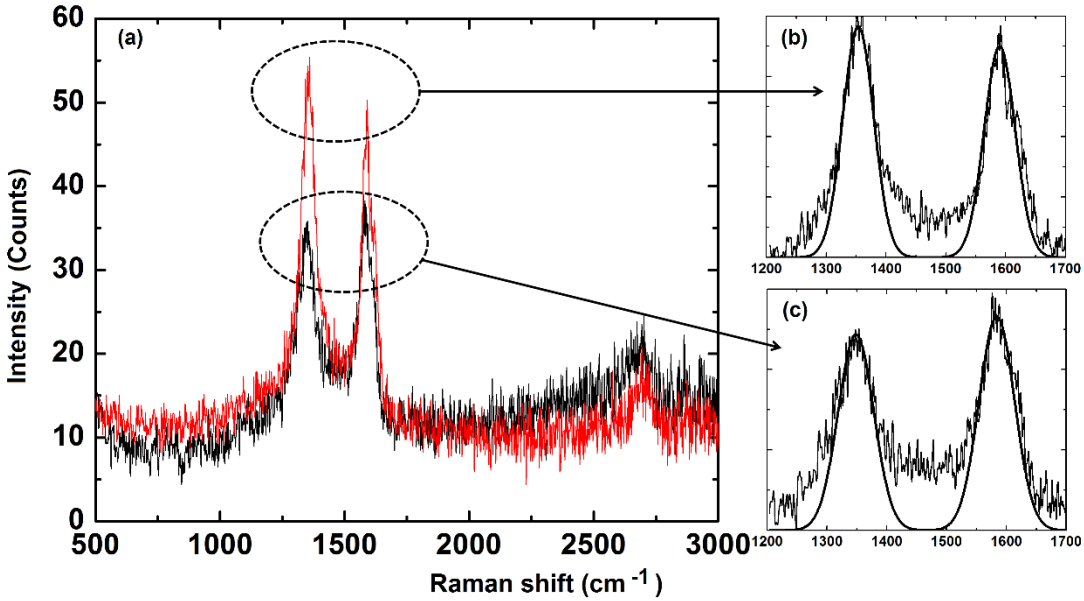

Figure 3.2: Raman spectra (solid scan, excitation wavelength = 785 nm) of (a) reduced GO (black line) and neat GO (red line), (b) and (c) are the Gaussian fits of D and G bands from (a).

3.3.3 SEM studies

The low magnification SEM image of GO (Figure 3.3a) shows large intertwined micron sized agglomerates and the corresponding high magnification image (Figure 3.3b) shows wedge shaped particles clumped together. The SEM image of RGO/IL (Figure 3.3c) however, shows a wrinkled sheet like structure, and in the corresponding high magnification image (Figure 3.3d), one such stack of sheets folded upwards is clearly seen. Agglomerated particles are also seen to be embedded in the silk like sheets (Figure 3.3c) and these could be due to the structure modified

by the ionic liquid and also due to the defects that are incurred by the exfoliated graphene sheets when subjected to rigorous chemical treatment. The individual graphene layers are not visible. The images reveal that the reduced graphene oxide sheets tend to stack together. The SEM micrographs of the control PEDOP-IL film (Figure 3.3e and f) reveal a globular morphology, a consequence of three dimensional nucleation and subsequent evolution into cauliflower like shapes 0.6 to 2.2 μm in size, a feature, typical of conducting polymer films. Although a good surface coverage of the substrate by a homogeneous network of globules is achieved along lateral dimensions of about several microns, but the polymer particles are separated or connected by pores. The inset of Figure 3.3f shows the presence of pores varying from 50 to 120 nm in dimensions. The SEM image a PEDOP-RGO/IL film (Figure 3.4a) displays an interconnected ensemble of globules and pores albeit a single distinctive difference. A closer inspection of the cauliflower shaped globules shows them to be decorated by "ribbon like shapes" approximately 100 – 500 nm in width. A high magnification image of one such globule, shown in Figure 3.4b, shows it to be almost entirely covered by the ribbon like shapes. These ribbons are entangled and curled up in some regions. They show a disordered growth with no particular orientation and they appear to be spewing from the protuberant globules. It is obvious that this effect on the structure is induced by the RGO/IL dopant, for control PEDOT-IL film was completely devoid of any such unusual artifact. The ability of the RGO/IL nanosheets in the electropolymerization suspension to orchestrate the formation of such elongated ribbon like strands is evident. In some regions of the same film, flake like structures (Figure 3.4c) and flattened irregular shapes (Figure 3.4d) were also observed. The flaky structure is an indicator of RGO/IL nanosheets stacking in a haphazard, disordered manner, under the influence of an electric field.

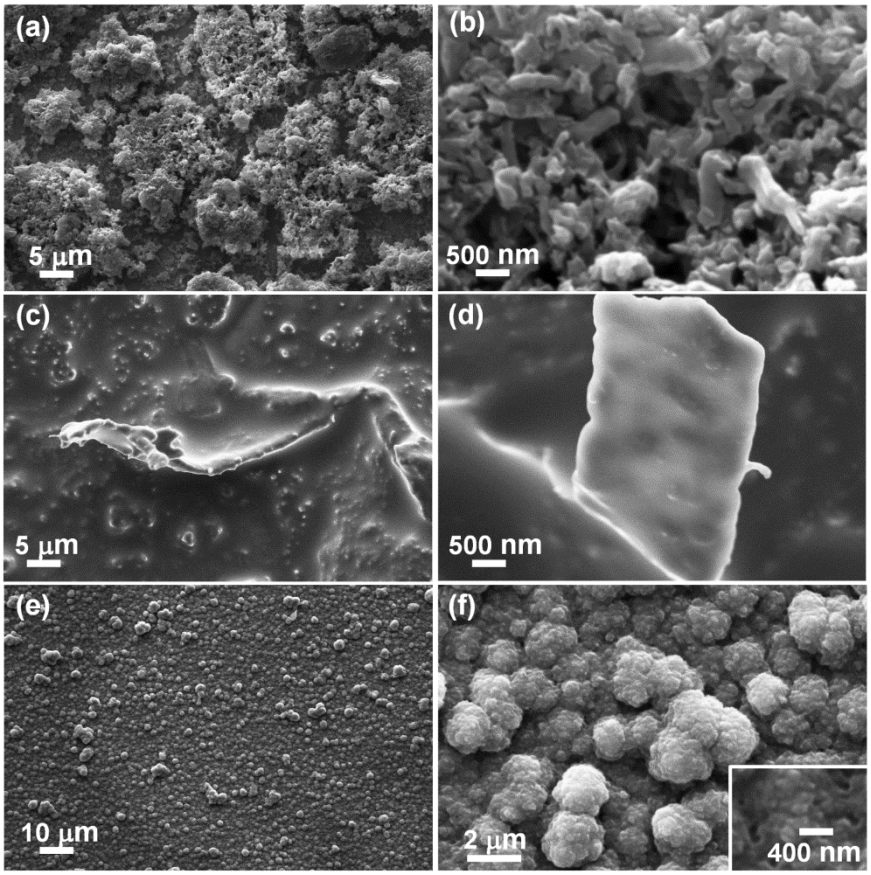

Figure 3.3: (a) Low and (b) high magnification images of neat GO, (c) low and (d) high magnification images of RGO/IL showing a wavy, crinkled sheet like structure, (e) low and (f) high magnification images of control PEDOP-IL showing the cauliflower-like morphology; inset of (f) shows the pores interspersed with the grains in the film.

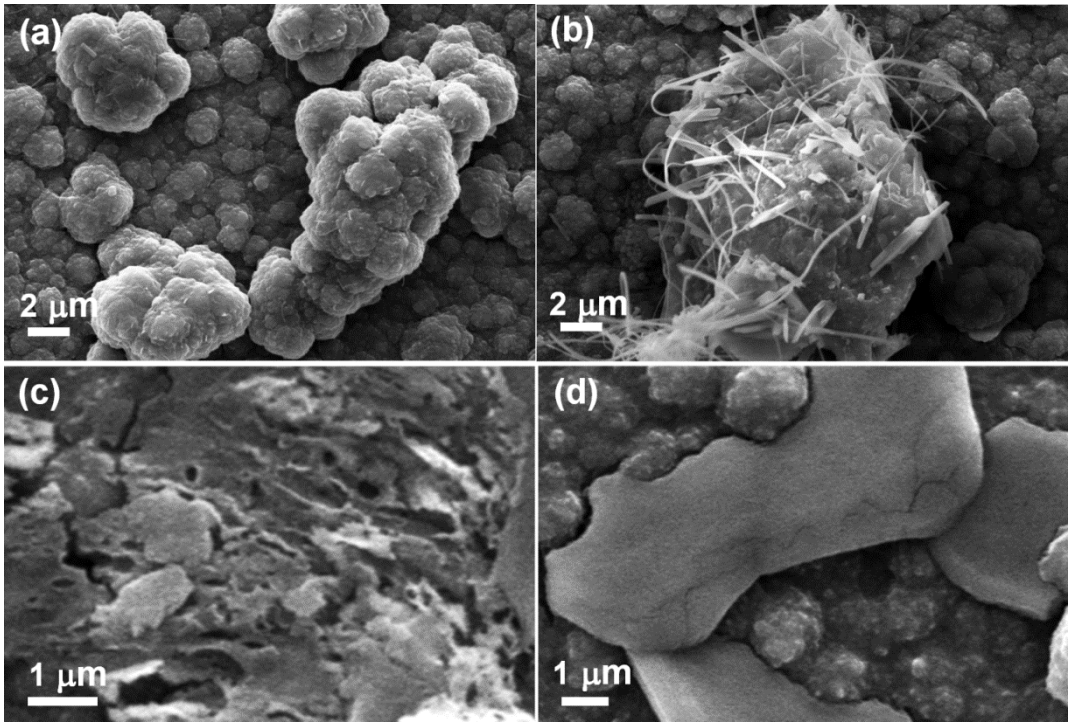

Figure 3.4: (a) Low and (b) high magnification images of PEDOP-RGO/IL showing the globular structure of the polymer decorated with elongated strands of RGO/IL, (c) in some regions of PEDOP-RGO/IL, stacked layers of RGO/IL flakes were identified and (d) featureless flat shapes originating from RGO/IL and embedded in the polymer in PEDOP-RGO/IL.

3.3.4 HRTEM analyses

The HRTEM image of neat RGO/IL shown in Figure 3.5a reveals crumpled silk veil like waves of RGO/IL nanosheets with a lateral size of about a few hundred nanometers. The undulations on the nanosheets are due to defects (caused by excessive sonication) and the region enclosed by a rectangle in Figure 3.5b shows the point where two nanosheets overlap. The folds and a rather high density of edge dislocations produce the wavy structure in RGO/IL (Figure 3.5c). Fast Fourier transformation (FFT) performed on the same, yielded the electron diffraction pattern (EDP) which is shown as an inset of Figure 3.5c. The inter-fringe spacing determined from the EDP, is ~0.15 nm. A blown-up view of a small region from this image is extracted onto Figure 3.5d. The separation between the two fringes is ~0.14 nm and it is close to the value

determined from EDP. Our value agrees well with that previously reported for a single layer of graphene prepared by micro mechanical cleavage [15]. Regions in RGO/IL, where the quasi-hexagonal lattice could be perceived are encircled in ellipses in Figure 3.5e. A magnified view of one such region from Figure 3.5e, is shown in Figure 3.5f; it distinctively illustrates the atomic level resolution attained in a RGO/IL layer and also concurs well with a reported TEM view for a graphene membrane [15]. HRTEM of the control PEDOP-IL film, shown in Figure 3.6a, shows an amorphous structure, a usual feature of CPs [16]. Low magnification image (Figure 3.6b) of the PEDOP-RGO/IL composite, again reveals compactly packed crumpled sheets, folded and curled up in many regions. This image shows that the polymer particles are adsorbed onto the surface of RGO/IL nanosheets and the predominant dark hues in the image indicate that almost a full use of the large specific area of RGO/IL nanosheets has been made. RGO/IL nanosheets act as scaffolds firstly for the adsorption of the monomer and later for the growth of the polymer chains, upon anodic oxidation, via formation of radical cations compensated by the negatively charged imide and carboxylate functionalities flanked to GO. The lattice fringes for two different layers of RGO/IL labeled as layers I and II and in direct contact with the polymer can be perceived in Figure 3.6c. Further magnification of the same yielded Figure 8d, which shows a distinct interface (shown with a dashed line) formed between the disordered polymer (seen in the right portion of the panel) and the structural ordering of the crystalline RGO/IL nanosheet structure is visible on the left side. The structure of RGO/IL continues to be preserved even in the PEDOP–RGO/IL composite, as dark and light fringe patterns could be identified in some portions of the film as well (Figure 3.6e). The separation between two similar lines was ~0.32 nm, which is close to a lattice constant of 0.34 nm attained for graphene films, grown by chemical vapor deposition [17,18].FFT on the Figure 3.6e is shown as an inset, and this too,

conforms to a d-spacing of 0.34 nm. The increase in the layer spacing on going from neat RGO/IL to PEDOP-RGO/IL could be due to the incorporation of the polymer. The corrugated structure of RGO/IL interspersed with defects (the latter evident from the curved and discontinuous line pattern in Figure 3.6f) in contact with the featureless polymer is also seen. Such a structure made of PEDOP chains sandwiched between RGO/IL layers has a large active surface area, which is favorable for charge transport.

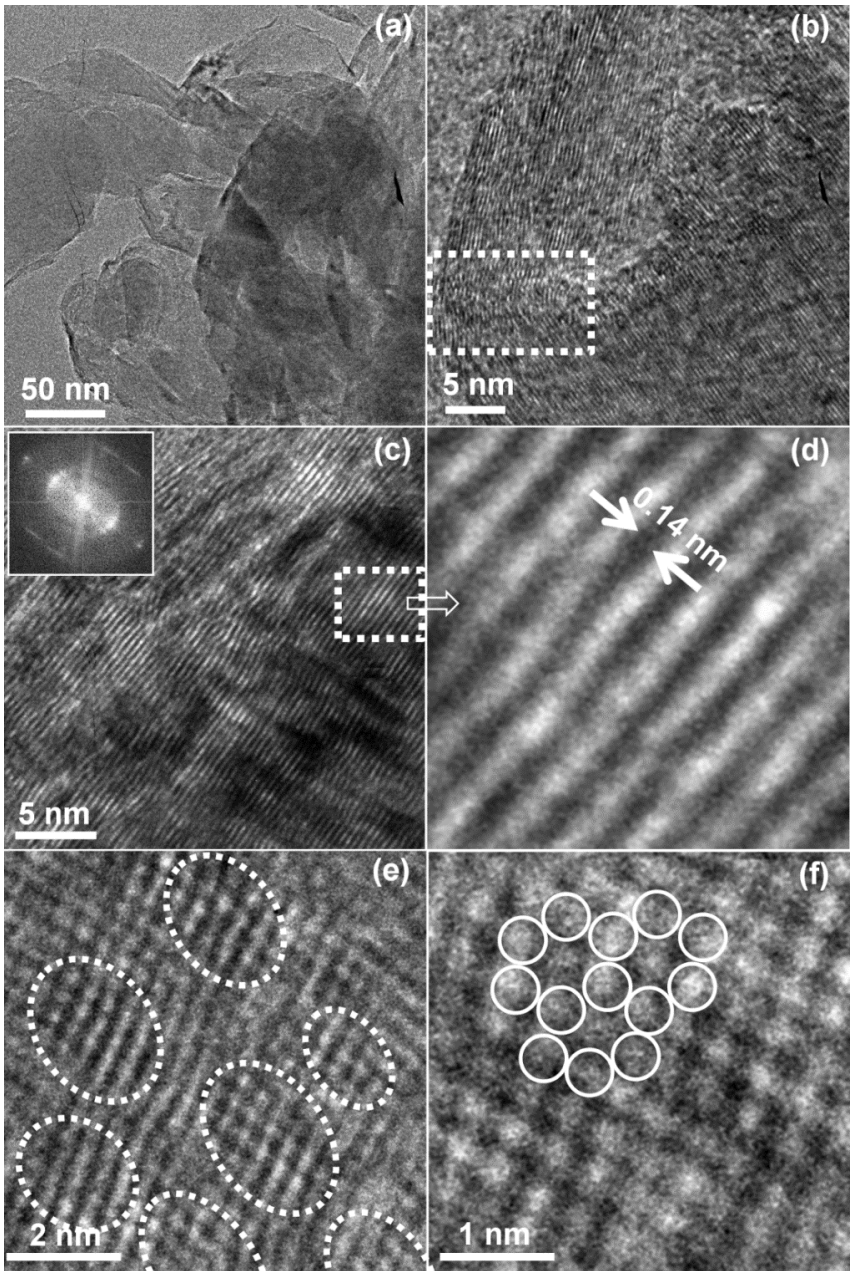

Figure 3.5: (a) TEM image of wrinkled pristine RGO/IL nanosheets, scrolled up in some regions, HRTEM images of (b) RGO/IL nanosheets juxtaposed on one another; the block encapsulated by dotted lines, reveals the defects in the structure, (c) wavy lattice fringes in overlapping nanosheets of RGO/IL and inset shows the corresponding spotty EDP generated by FFT, (d) is a blown up view of a small defect free region from (c) and shows the fringe separation, (e) shows the quasi-hexagonal lattice in RGO/IL as indicated from the regions enclosed by ellipses and (f) is an atomic resolution image derived from (e).

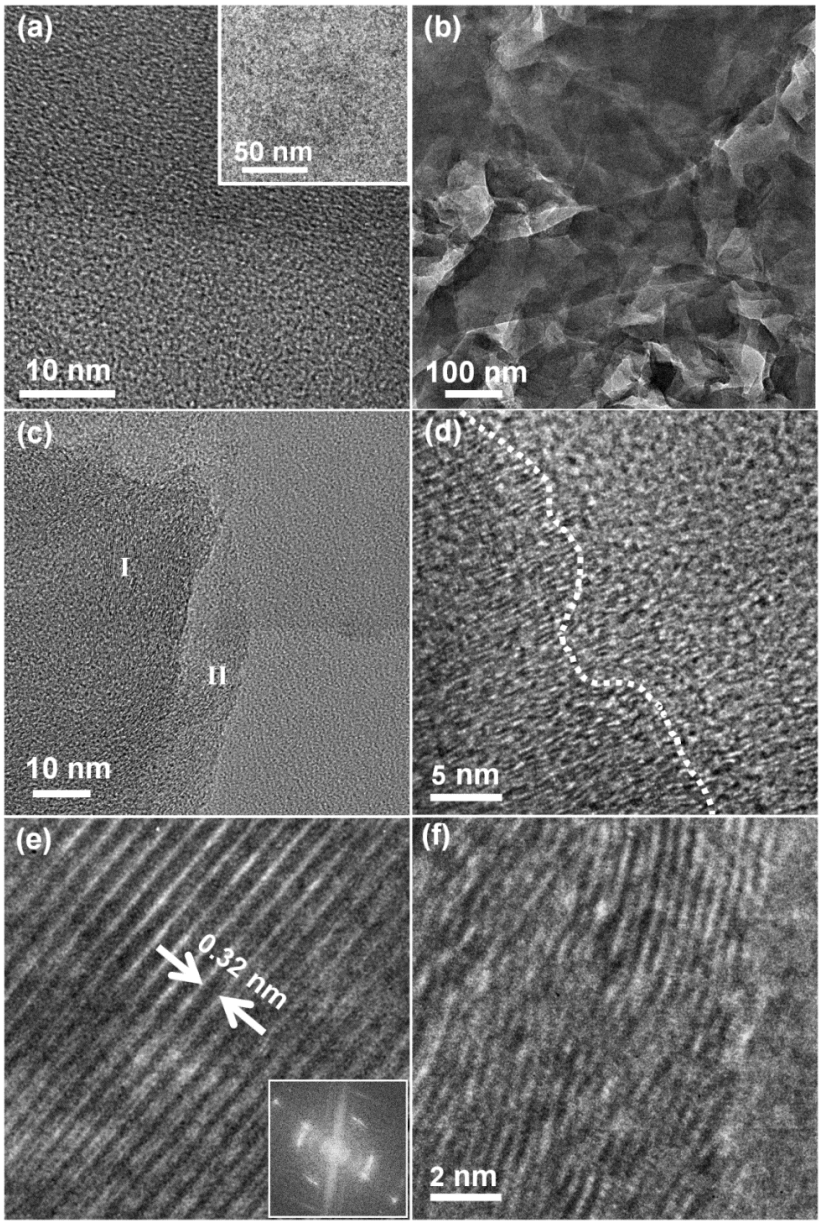

Figure 3.6: HRTEM images of (a) amorphous, featureless structure of control PEDOP-IL film, inset is the corresponding low magnification view, (b) multiple layers of RGO/IL nanosheets enwrapped PEDOP in the composite PEDOP–RGO/IL, (c) one nanosheet (I) of RGO/IL overlying on another nanosheet (II) in PEDOP-RGO/IL, (d) a clear interface formed between the amorphous polymer and the ordered structure of RGO/IL; represented by a dotted line, (e)an inter-fringe spacing of 0.32 nm achieved in a high quality crystallite of RGO/IL retained in PEDOP-RGO/IL; inset shows the corresponding speckled EDP produced by FFT and (f) corrugated sheets of RGO/IL in direct contact with the amorphous polymer.

3.3.5 XPS studies

The deconvoluted C1s and O1s core level spectra of GO and RGO are shown in Figure 3.7. Consistent with Gao et. al's C1s spectrum of hydrophilic GO produced by a modified Hummers' method [5,11], here we also obtained two separated peaks in the C1s spectrum (Figure 3.7a), a consequence of a high concentration of oxygen functionalities. The two peaks were resolved into six components (FWHM = 1.75 eV) at 284.7, 286.5, 288.2, 293.6, 295.3 and 296.8 eV attributable to C-C, C-OH (hydroxyl), C(O)C (epoxy), C-O-C (ether), C=O (carbonyl) and COO- (carboxylate) groups. The deconvolution of the slightly asymmetric O1s peak yielded two components at 532.4 and 533.8 eV (FWHM = 2.0 eV) ascribable to C-O and C-OH links (Figure 3.7d). The broadness of C1s peak is considerably reduced and the two peaks now appeared as one, in the RGO/IL sample (Figure 3.7b). A similar transition from a highly asymmetric to an almost non-asymmetric C1s signal was observed previously ongoing from GO to RGO by Stankovich et. al [19]. Here, the single dominant C1s peak peak observed for RGO indicates a good degree of restoration of the C=C network, after chemical reduction. The spectrum shows four components at 284.7, 286.6, 288.9 and 291.1 eV, after fixing the FWHM at 1.92 eV, corresponding to contributions from C-C, C-N, C-O and C=O linkages (Figure 3.7b). The additional C-N component shows that oxygen removal is accompanied by nitrogen incorporation in graphene during reduction. A similar signal for carbon bound to nitrogen has been observed by Yang et al. [20] and Dreyer et al. [21] for graphene functionalized with an amine terminated IL and for graphene reduced by hydrazine. Also notable is the reduction of the intensity of the O1s signal to about 34% of its original, ongoing from GO to RGO/IL, which is suggestive of the removal of oxygen containing groups (Figure 3.7e). This signal is again resolved into two components at 531.5 and 533.5 eV (FWHM = 2.55 eV) due to C-O and C-OH. The N1s peak of

RGO/IL (Figure 3.7c) was deconvoluted into main components at 399.2 and 401.65 eV; the former from the S-N of the imide ion and the latter arises from C-N (of the imidazolium cation and between carbon of GO and N generated during hydrazine treatment). A similar split of the N1s signal for the pure ionic liquid 1-butyl-3-methyl imidazolium cation and imide anion has been observed earlier [22]. Here, the FWHM was 1.88 eV and whilst the I(S-N) was 0.41, the I(C-N) was 0.59. The S2p spin-orbit doublet in RGO/IL (Figure 3.7f) with the $S2p_{3/2}$ and $S2p_{1/2}$ at 163.3 and 167.58 eV (FWHM = 2.93 eV) and a peak separation of about 1.2 eV, shows an intensity ratio of ~3:1, which agrees reasonably well with the reported values for the S2p components.[23] This sulfur signal is attributable to the sulfur on the imide anion. Similarly, the F1s signal inset of (Figure 3.7f) with FWHM of 2.3 eV was symmetric and peaked at 690.4 eV; this peak arises from the C-F linkages of the $-CF_3$ groups on the imide anions. The distinct signals due to N, F and S in the RGO/IL sample, affirm the inclusion of both the imidazolium ion and the imide anion within the RGO layers. The incorporation of RGO/IL in PEDOP in the composite and IL in control PEDOP was confirmed from the core level spectra of the control and composite. These spectra are shown in Figure 3.8 and 3.9.

For neat GO (prior to IL incorporation and reduction), the $I_{(C\text{-}C)(C1s)} / I_{(Ctotal)}$ ratio was 0.31, which is the proportion of GO that remains de-oxygenated. For the same sample, the $I_{(C\text{-}O)(C1s)} / I_{(Ctotal)}$ is 0.69, which is a measure of the degree of oxygenation prevalent in GO. A high value for this ratio is suggestive of a high oxygen content in GO. Subsequent to treatment with the IL and hydrazine reduction, for the RGO/IL sample, the $I_{(C\text{-}C)(C1s)} / I_{(Ctotal)}$ ratio increased from 0.31 to 0.64, indicating a fairly high restoration of the sp^2 bonded pristine carbon framework. The successful elimination of oxygen functionalities was also reflected in the low but nearly equivalent ratios of $I_{(C\text{-}O)(C1s)} / I_{(Ctotal)}$ and $I_{(C\text{-}N)(C1s)} / I_{(Ctotal)}$. The value was ~0.36 for neat RGO/IL,

as opposed to a rather large value of ~0.69 ($I_{(C-O)(C1s)}$ / $I_{(Ctotal)}$), observed for neat GO. For control PEDOP-IL, the dopant level, which is measure of the imide ion loading in the polymer, was estimated from the $I_{(S=O)(O1s)}$ / $I_{(Ctotal)}$ ratio, and it was found to be ~0.37. From the N1s spectrum of the same sample, the $I_{(S-N)(N1s)}$ / $I_{(Ctotal)}$ ratio was deduced to be ~0.32. Since the two values are not far apart, it is a reasonably good estimate of the doping percentage in the control PEDOP-IL. From the N1s of control PEDOP-IL, the $I_{(C-N)(N1s)}$ contribution was found to be quite high, ~0.43, which is as anticipated, as it is predominantly arising from C-NH links on the PEDOP chains. Most striking was the ratio of the $I_{(S-N)(N1s)}$ / $I_{(C-N^+)(N1s)}$ ratio; this is a ratio of the imide ion to imidazolium ion content in the film. It was ~1.28, indicating that the proportion of imidazolium cation incorporated in the polymer is only slightly lower than the proportion of imide ion included in the polymer. This ratio clearly indicates the incorporation of the imidazolium cation alongwith the anion in the control PEDOP-IL film, a feature which is absent in CP films doped by conventional anions [24]. In PEDOP–RGO/IL composite, from the O1s spectrum, the $\{I_{(S=O)(O1s)} + I_{(C-OH)(O1s)}\}/ I_{(Ctotal)}$ ratio was found to be ~0.41, which is a measure of the doing level of RGO/IL in PEDOP. For the same sample, from the N1s spectrum, the $I_{(S-N)(N1s)}$ and $I_{(C-N^+)(N1s)}$ values were ~ 0.11 and 0.15 respectively. Since the imidazolium ion was found to be in a higher proportion than the imide ion here, it is apparent that the imidazolium ion has greater affinity for GO than imide. Again, the S-N or $C-N^+$ proportions are lower in contrast to their values in control PEDOP-IL for here, the IL is flanked by GO and is not the sole counter ion during electropolymerization of PEDOP. A schematic showing the interactions that prevail in the PEDOP–RGO/IL composite is shown in Figure 3.10.

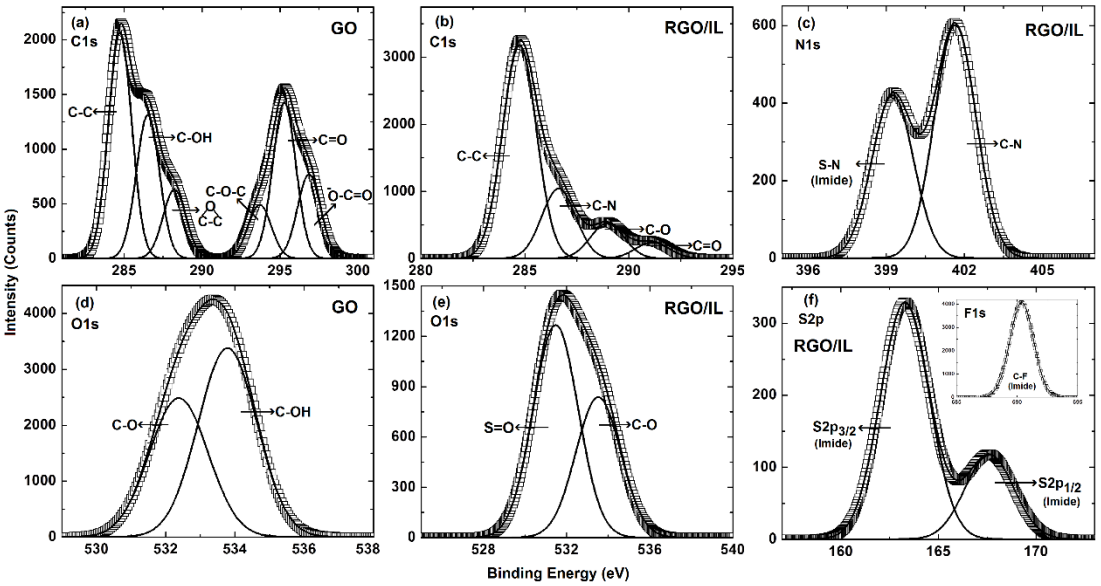

Figure 3.7: Deconvoluted core level spectra of (a) C1s and (d) O1s for GO before reduction, (b) C1s, (c) N1s, (e) O1s and (f) S2p of RGO/IL composite. Inset of (f) shows the F1s peak from RGO/IL.

The deconvoluted C1s, O1s, N1s and S2p core level spectra of control PEDOP-IL and PEDOP-RGO/IL composite films are shown inFigure 3.8 and 3.9. The deconvoluted C1s spectrum of control PEDOP-IL shows four components due to C-C, C-N, C-O and C-F groups (Figure 3.8a). The C-N contribution is prominent, as it arises from the C-NH groups on the pyrrole backbone and also from the two nitrogens: C-N/C-N^+ of the imidazolium ring, which happens to be the dopant ion in the control PEDOP-IL film. The C-F component also originates from the imide ion. In contrast, the C1s spectrum of the PEDOP-RGO/IL composite (Figure 3.9a) shows multiple components due to C-C, C-N, C-OH/C(O)C, C=O, C(O)O and C-F groups. The C-O groups could be resolved in the PEDOP-RGO/IL composite as the C1s is more asymmetric as compared to its counterpart in the control PEDOP-IL film. The deconvoluted O1s spectra, shown in Figure 3.8b and 3.9b of both control PEDOP-IL and PEDOP-RGO/IL composite are almost similar, with the two components due to S=O (from imide) and C-O (from the ethylenedioxy bridge on PEDOP or from oxygen attached to the carbon network in RGO)

and an additional high energy C-OH component (observed only in case of PEDOP-RGO/IL). The deconvolution of N1s spectrum, for control PEDOP-IL (Figure 3.8c) yielded three components at 399, 401.3 and 402.3 eV ascribable to S-N (from imide ion), C-N (from NH on the polymer / neutral C-N on the imidazolium ring) and C-N^+ (from the N^+-alkyl chain on the imidazolium), thus confirming the inclusion of both the imidazolium and imide ions in control PEDOP-IL. The C-NH assignment for PEDOP, in our case concurs with the C-NH signature reported for a polypyrrole sample[23]. The N1s signal owing to a greater asymmetry, in PEDOP-RGO/IL (Figure 3.8c) could be resolved into four components at 397.5, 398.5, 400.7 and 402 eV due to S-N (imide), =N– (imine linkages in PEDOP), C-NH (PEDOP) and C-N^+ (imidazolium) groups. The S2p deconvolution for both films (Figure 3.8d and 3.9d) yielded the expected spin-orbit split, $S2p_{1/2}$ and $S2p_{3/2}$ components. The results ratify that both RGO and IL are inherent parts of the PEDOP-RGO/IL and not superfluous entities.

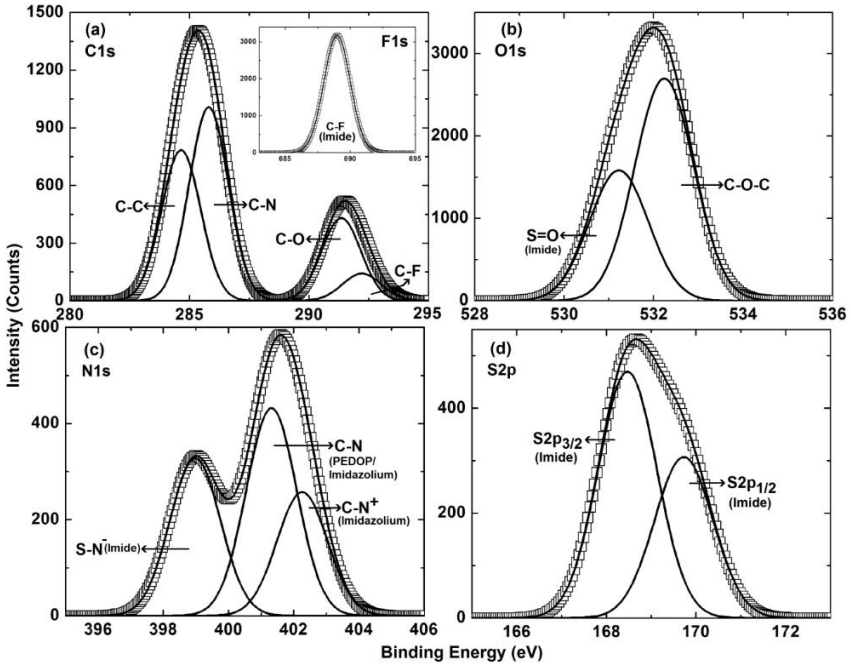

Figure 3.8: Deconvoluted core level spectra of (a) C1s, (b) O1s (c) N1s and (d) S2p of control PEDOP-IL film. Inset of (a) is the F1s core level spectrum from control PEDOP-IL.

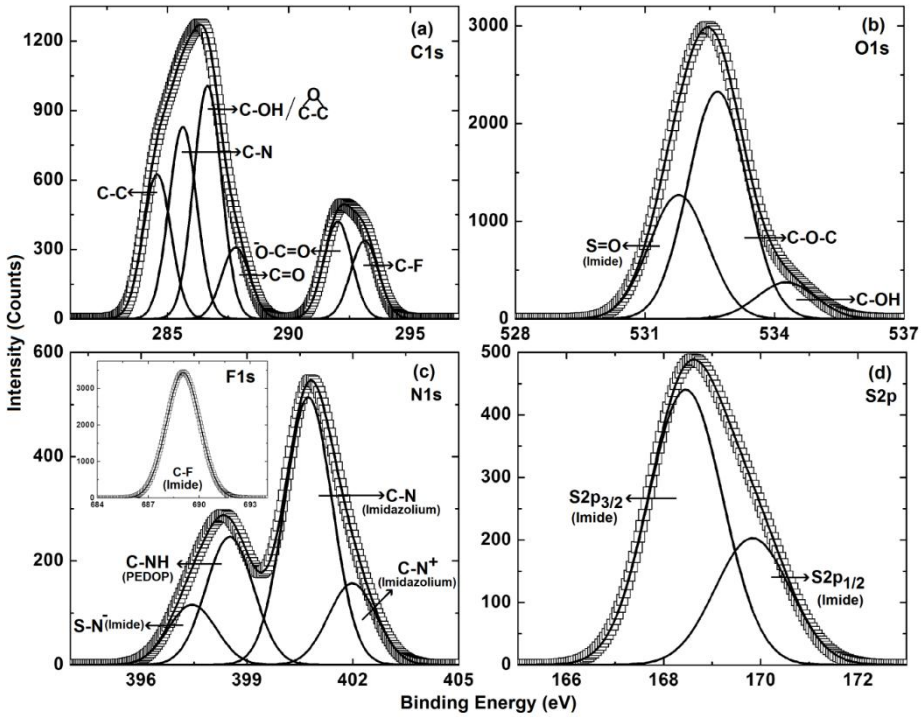

Figure 3.9: Deconvoluted core level spectra of (a) C1s, (b) O1s, (c) N1s and (d) S2p of PEDOP-RGO/IL composite film. Inset of (c) is the F1s core level spectrum from PEDOP-RGO/IL.

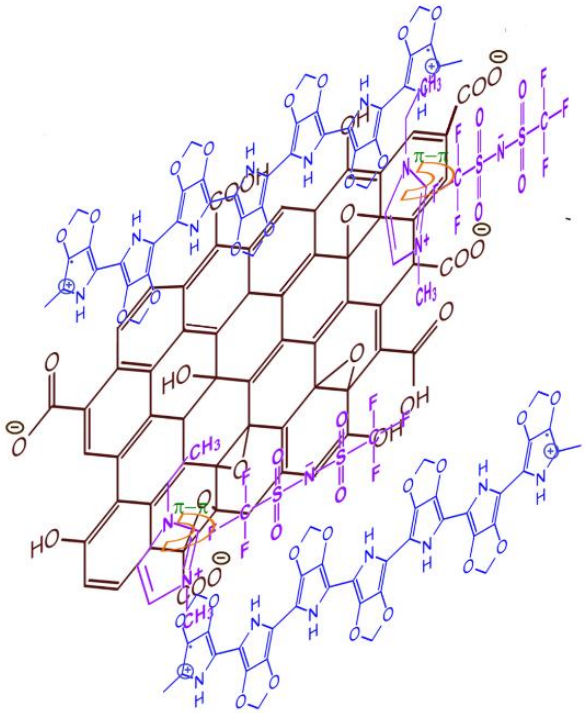

Figure 3.10: Schematic showing the interactions in the PEDOP–RGO/IL composite film.

3.3.6 Valence band spectra

The experimental photoemission spectra of the valence band region for neat GO, neat RGO/IL, control PEDOP-IL and PEDOP-RGO/IL are shown in Figure 3.11. The density of states (DOS) at the Fermi level (E_F, corresponding to a zero binding energy) is finite for all samples. The DOS in the vicinity of E_F has a larger magnitude (inferred from a higher intensity of the signal in the inset of Figure 3.11a) in RGO/IL as compared to GO. In an earlier report [14], a similar increase in DOS was observed as the level of hydrogenation (or reduction) was increased in graphene. Authors [14] postulated that the increase in DOS is caused by a change in the geometry, as the hydrogenated carbon atoms move out of the graphene plane, the lattice is distorted and the symmetry is broken, and as a result, more k points in the Brillouin zone contribute to DOS. The same line of reasoning can be used to explain the DOS increment ongoing from GO to RGO/IL. From the valence band diagrams, the E_F to valence band gap for GO was 2.05 eV and it reduced to 1.62 eV in RGO/IL, indicating the formation of a more conductive material upon reduction. For control PEDOP-IL, this gap was 1.76 eV and for the PEDOP–RGO/IL composite, it was 1.26 eV (Figure 3.11b); this narrowing of the energy gap could be due to the introduction of additional levels in the band gap by RGO/IL, thus enabling the formation of lower gap CP.

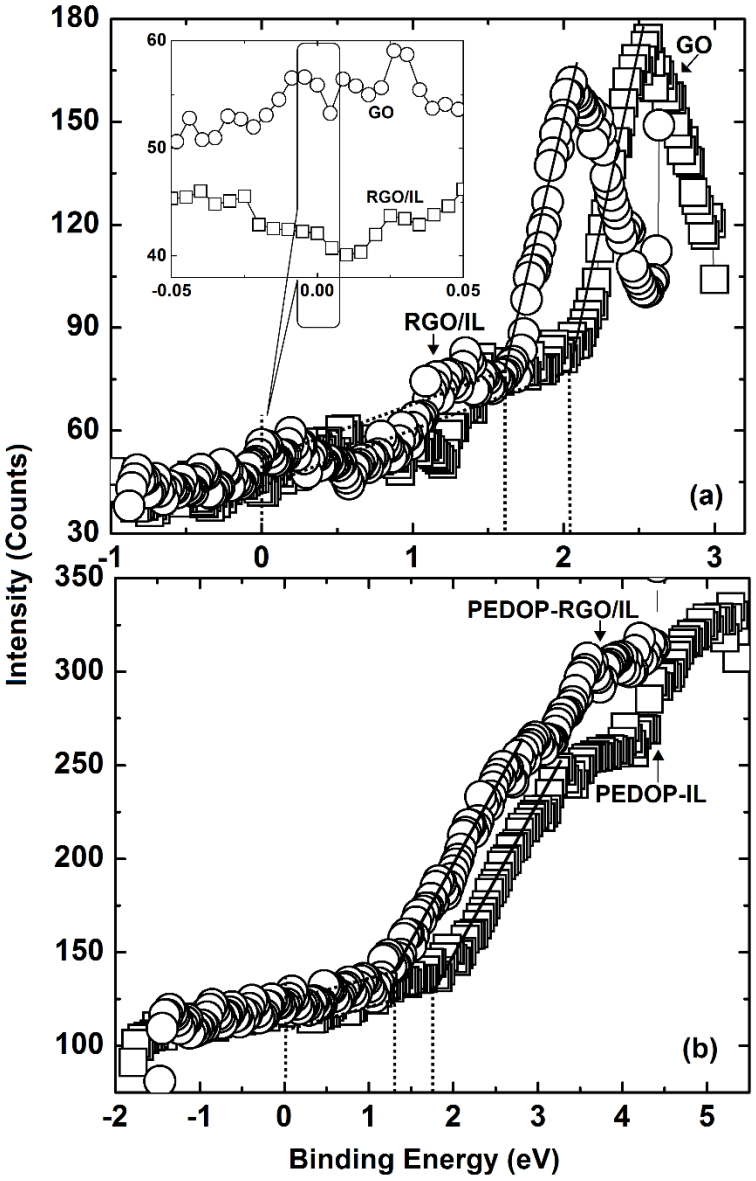

Figure 3.11: Valence band spectra of (a) (□) neat GO before reduction and (○) RGO/IL composite and (b) (□) control PEDOP-IL film and (○) PEDOP–RGO/IL composite film. Inset of (a) shows the difference in DOS between GO and RGO/IL at 0 eV. The dotted lines in (a) and (b) denote the valence band to Fermi level gaps.

3.3.7 C-AFM Studies

Typical current and the corresponding topographical images as well as the cross-sectional current profiles of control PEDOP and PEDOP–RGO/IL films are shown in Figure 3.12. Figure 3.13 shows the images and I-V trace of the neat SnO_2:F coated glass, which ratify that the plots

obtained in Figure 3.12 arise from the electroactive coating and not the underlying substrate. The current maps (Figure 3.12a and b) represent the current flowing vertically through the film, and these were imaged by applying a fixed voltage of 100 mV between the conducting tip and the substrate (on which the sample is mounted), whilst the tip simultaneously scans the surface of the film in a horizontal manner. The vertical current flowing through the film, as estimated by this method, is more relevant than the bulk dc conductivity determined by two/four-probe methods [25-27], for in most of the practical electronic devices, charge flows vertically through the electroactive material. In the current maps (Figure 3.12a and b), the bright regions are attributed to regions of high current, and the dark domains correspond to low currents. The maps are slightly noisy, and this originates from a rather high rms roughness of the films, as for control PEDOP-IL, it is 28 nm, and it is 16.2 nm for the PEDOP-RGO/IL film. The current map of the control PEDOP film (Figure 3.12a) shows the bright spots to be randomly scattered across the film, and these are surrounded by relatively large domains of dark regions. On the other hand, the current map of the PEDOP-RGO/IL nanocomposite film, shows very few dark domains, indicating that current tends to flow more uniformly across the surface of the PEDOP-RGO/IL film, as the conducting regions (denoted by bright regions) are enclosed by insulating dark domains to the extent as they are in the control PEDOP film. It is apparent that the RGO/IL dopant tends to connect the conducting polymer (PEDOP) grains by providing conducting pathways, thus maintaining a uniform current distribution. In contrast, in the control PEDOP film, the IL dopant is electronically insulating and therefore, the IL abundant regions in the film yield the dark regions and they obstruct the current flow. The maximum current flowing at the bright spots is about 2 nA in the control PEDOP film, which is significantly lower than a maximum current of 550 nA detected for the PEDOP-RGO/IL film, under the same bias voltage

of 100 mV. The role of RGO/IL in furnishing vertically pathways for charge percolation and propagation, thus improving the overall charge transport behavior of PEDOP is evident.

Further proof to support this claim, was obtained in the form of the point contact I-V characteristics of control PEDOP and PEDOP-RGO/IL films (Figure 3.12e and f), recorded from the bright regions (spots: A1 and B1) and the dark regions (spots: A2 and B2). Since current profiles recorded from different bright/dark regions from the current map of a given film, were roughly similar, only representative plots are shown here, chosen in a manner, so that they represent the average response of the film. For the control PEDOP sample, the current profile recorded from a bright spot A1, resembled that of a conventional semiconductor, in the potential range of –0.67 to +0.87 V. As can be seen from the figure, current saturates at ~12 nA, in the bright conducting spots, in the control PEDOP film. Although the response is non-linear, but assuming a linear behavior, the slope is ~15 nAV^{-1}, indicating poor conduction in the sample. The current response in the dark region shows an almost zero slope in the –0.7 to +0.7 V range, implying that very low or almost zero currents flow in the dark domains. Beyond this bias range, the response shows many current spikes, more dominant above +1.5 V and –1.5 V. A similar I-V curve, characterized by many spikes, has been observed earlier from the dark region of an electropolymerized polypyrrole film [24]. Authors [25,27], assigned such spikes to non-continouus density of states available for charge flow, which here, could be due to inhomogeneous distribution of the conducting PEDOP and the insulating IL dopant grains. In case of the PEDOP-RGO/IL film, the slope in the –0.25 V to +0.25 V region, was steep, and astonishingly, the traces were almost similar for both bright and dark spots, thus implying that insulating domains were rather scarce in this nanocomposite. As mentioned earlier, I-V traces were obtained from different bright and dark regions, and the current profile and the overall

magnitudes of currents were of the same order. The current was found to saturate at ~500 nA, in different regions of this film, thus suggestive of facile electron transport across the film. The slope of the curve was approximately 2000 nAV^{-1}, which is greater by two orders of magnitude as compared to the control PEDOP film. For highly doped PEDOT films, the slope estimated from C-AFM was found to be in the range of 3000 – 9000 nAV^{-1}. Here, since the response measured is for the as-fabricated films, and not for electrolytically oxidized films, the difference is accounted for.

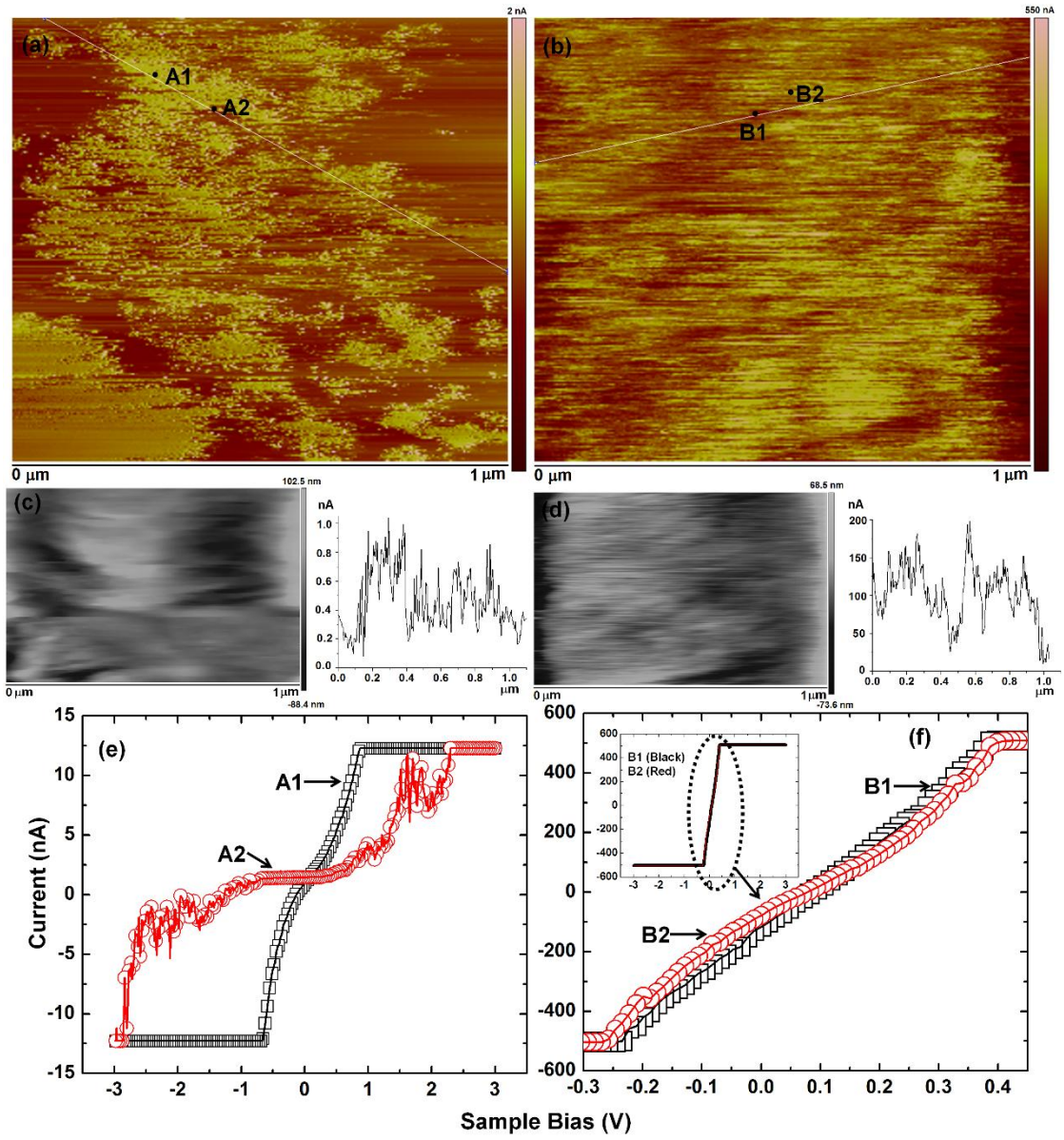

Figure 3.12: Representative current and topography images of control PEDOP-IL (a and c) and PEDOP-RGO/IL (b and d); adjoining (c) and (d) are the current cross-sectional profiles, measured along the lines shown in (a) and (b). I-V curves obtained from the points A1 and A2 in control PEDOP-IL (e) and from points B1 and B2 in PEDOP-RGO/IL nanocomposite (f): from –0.3 to +0.4 V and in (e) and inset of (f): from –3 to +3 V.

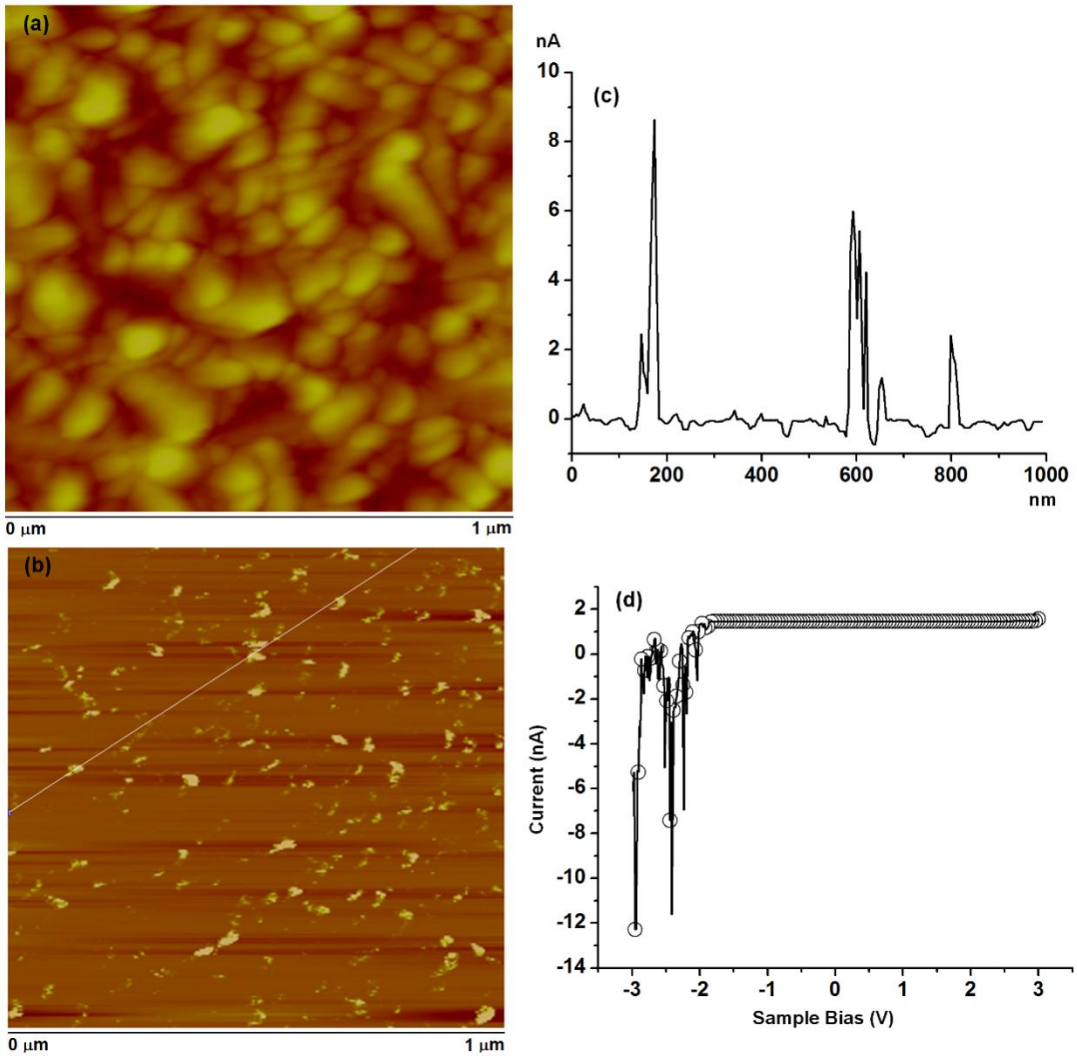

Figure 3.13: (a) Topography (height = 90 nm) and (b) current (height = 8 nA) images of neat SnO_2:F coated glass. (c) Cross-sectional current profile measured along the line shown in (b). Representative I-V plot (irrespective of bright or dark regions) measured from (b), showing the saturation of current in the –1.5 to +3 V range.

The enhanced conduction ability of PEDOP-RGO/IL was re-affirmed from the I-V characteristics of measured by linear sweep voltammetry method (Figure 3.14). The electronic conductivity of GO was deduced to be 0.08 S cm^{-1} and for RGO/IL, it was 0.11 S cm^{-1}. For the PEDOP-RGO/IL composite, the conductivity was 0.025 S cm^{-1} and for the control PEDOP-IL sample, it was 0.0007 S cm^{-1}. These values also complement the current sensing AFM results, as

RGO/IL increases the conductivity of PEDOP by two fold times, an attribute, which is of paramount significance for improving the redox response.

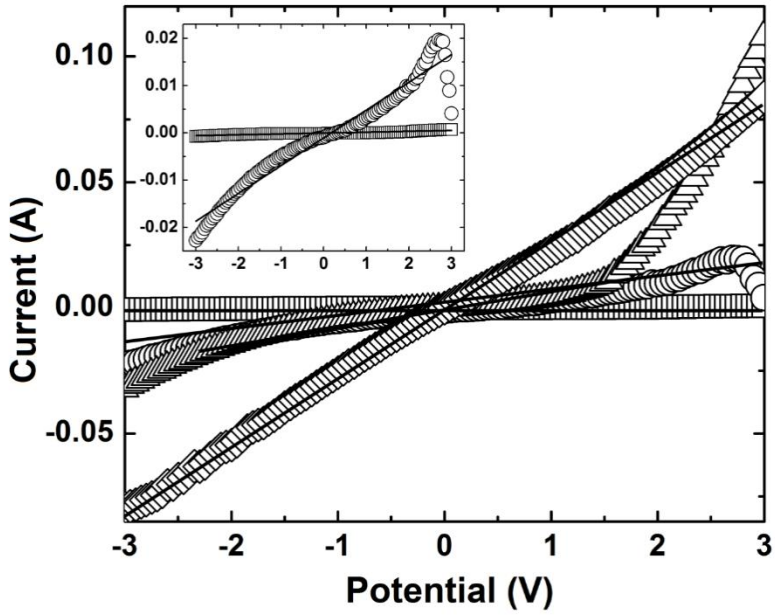

Figure 3.14: I-V characteristics of neat GO (△), RGO/IL composite (◇), control PEDOP-IL (□) and PEDOP-RGO/IL composite (○) recorded between stainless steel electrodes.Inset is a magnified view of polymer films.

The cyclic voltammogram of a control PEDOP-IL film recorded between +3 to –3 V (Figure 3.15a) shows twin oxidation peaks at –0.31 V, attributable to oxidation of PEDOP or polaron formation, followed by another peak at +0.5 V, which could be due to bipolaron formation. Subsequently, another set of two broad peaks are seen at +1.45 and +2.0 V, which in all likelihood, arise due to the over-oxidation of the polymer chain. PEDOP owing to the presence of the "ethylenedioxy" bridge has been shown to be less susceptible to over-oxidation as compared to poly(pyrrole) [28], which therefore explains the low heights of these two peaks. In the reverse branch, a broad cathodic wave, with peaks at –0.3 and –1.3 V are visible, the latter due to the conversion of polaron/bipolaron to neutral polymer and the former is due to charge trapping (when charged domains are embedded in the matrix of an insulating polymer [29]. The

ΔE_p or peak separation for the oxidation (polaron formation) ↔ reduction (neutral polymer formation) process was ~1 V. Since the polymer shows a reversible, clear redox process corresponding to anion ingress and egress with a narrow potential range, it is beneficial for improving the operational lifetime of the device. For the PEDOP-RGO/IL film (Figure 3.15d), the oxidation peak was observed at –0.63 V, followed by a relatively featureless anodic wave. In the cathodic branch, a sharp pre-peak at +0.9 V signified the incorporation of the positive charge in the polymer. This was followed by a peak at –0.46 V, attributable to the reduction of the oxidized polymer to the neutral form. The ΔE_p was ~0.17 V, which is much lesser than that observed for the control PEDOP-IL film. It is suggestive of a faster and a more reversible process in PEDOP-RGO/IL composite, in contrast to the PEDOP-IL film, again ratifying the superior current carrying ability of the composite, aided by the dopant RGO/IL.

The CV plots for the PEDOP-RGO/IL composite and control PEDOP-IL film recorded as a function of scan rate are shown Figure 3.15b and 3.16. For the PEDOP-RGO/IL composite, the voltammograms recorded at high scan rates (s ~50 – 100 mV s^{-1}), show a dominant capacitive behavior, indicating the high charge uptake capacity of the film. The high specific surface area of the composite, afforded by the RGO/IL nanosheets, allow a larger adsorption of imide ions from the electrolyte during redox switching. The comparison of the two films at a fixed sweep rate of 2 mV s^{-1} (Figure 3.15c), shows a weak oxidation peak at +0.5 V in the anodic sweep, followed by the reduction peak at –0.25 V in the reverse cathodic branch for the PEDOP-RGO/IL film. For the control PEDOP-IL film, only a single oxidation shoulder was seen at +0.36 V and no cathodic peak was observed. Further, the area under the voltammogram also shrank ongoing from the composite to the control film (at all scan rates). At a higher scan rate of 5 mV s^{-1}, the shape of the voltammogram changed (Figure 3.15e) and no peaks were observed for both films.

The response, at this juncture, was purely capacitive and the charge intercalation capacity was higher for the composite (PEDOP-RGO/IL: 13 mC cm^{-2} and PEDOP-IL: 1.2 mC cm^{-2}). Our charge insertion capacity is much greater than a value of 4 mC cm^{-2} reported for PEDOT in a dual conjugated polymer device [30] However, a digression from this response, was again observed at s = 100 mV s^{-1} (Figure 3.15f), wherein a weak shoulder at +0.03 V (in the oxidation cycle) and at –0.29 V (in the reduction cycle) were observed for the PEDOP-RGO/IL composite. The control PEDOP-IL film also showed similar behavior, but the potential values were different and area under the CV curve was smaller. But these studies do ratify the superiority of the composite by the virtue of (i) homogenity of current distribution (as seen from C-AFM), (ii) larger number of available electrochemically active sites and (iii) greater electrolyte permeation; both accorded by the larger surface area of the RGO/IL nanosheets and (iv) facile and efficient imide ion insertion and extraction, a manifestation of facile electron trasnport, possible in this film.

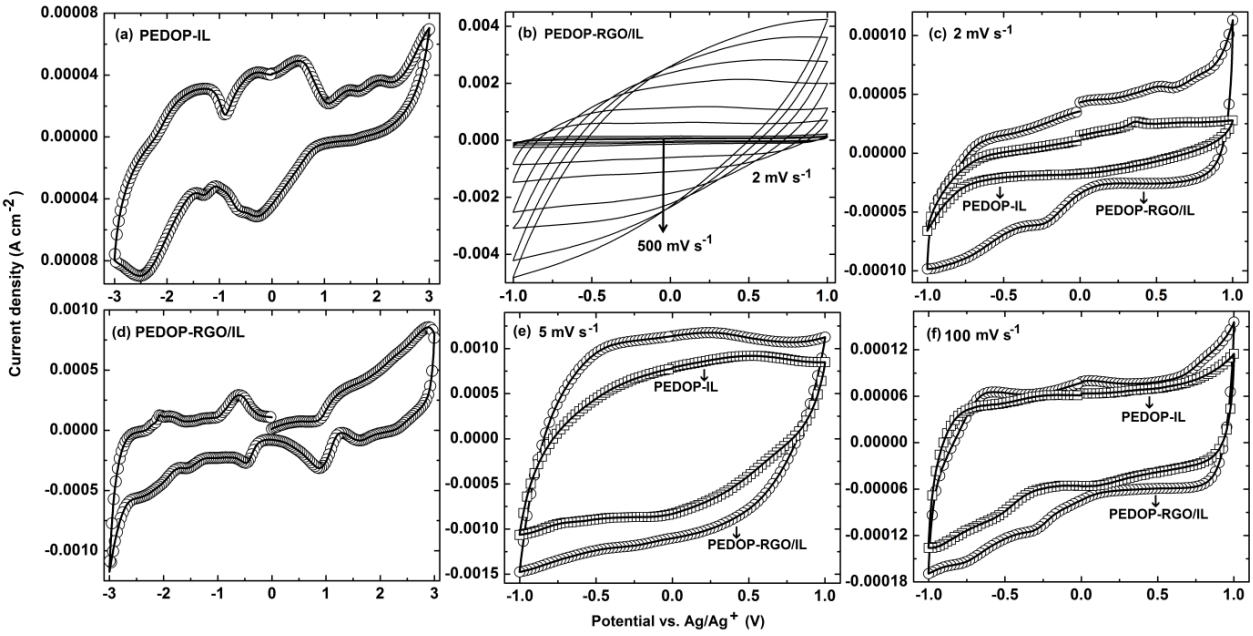

Figure 3.15: Cyclic voltammograms of (a) control PEDOP-IL film and (d) PEDOP-RGO/IL composite film recorded at a fixed scan rate of 10 mV s^{-1}, between +3 to –3 V, (b) PEDOP-RGO/IL composite film recorded as a function of scan rate: 2, 5, 10, 20, 50 100, 200, 300, 400 and 500 mV s^{-1} and comparison of voltammograms of control PEDOP-IL (□) and PEDOP-RGO/IL composite (○) at scan rates of (c) 2 mV s^{-1}, (e) 5 mV s^{-1} and (f) 100 mV s^{-1}.

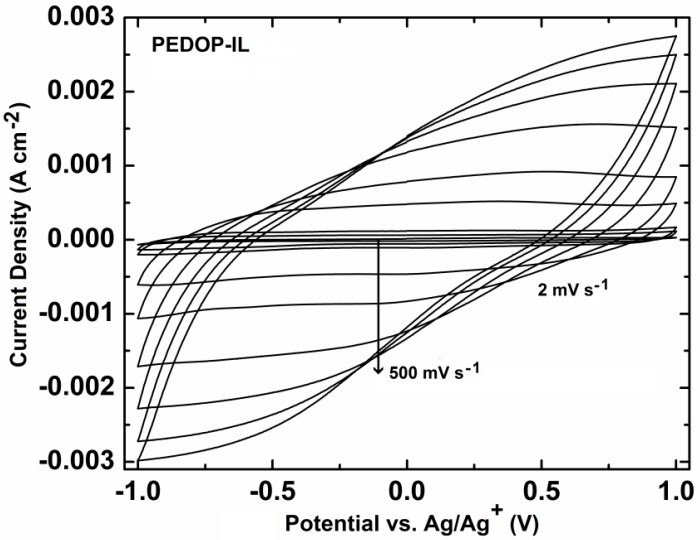

Figure 3.16: Cyclic voltammograms of control PEDOP-IL film recorded as a function of scan rate: 2, 5, 10, 20, 50 100, 200, 300, 400 and 500 mV s^{-1}.

3.3.8 Spectroelectrochemistry of PEDOP-IL and PEDOP-RGO/IL

The absorption plots of control PEDOP-IL and PEDOP-RGO/IL composite devices for oxidation potentials varied from +0.5 to +2.0 V (at intervals of +0.5 V) and reduction potentials from –0.2 to –3.0 V (at intervals of –0.1 V) are shown in Figure 3.17a and b. The reference potential for determining the optical density change at any given wavelength ($\Delta OD(\lambda)$) was fixed at +1.0 V for both devices. The bipolaronic peak observed in the oxidized state of the control PEDOP-IL in the 600 – 800 nm wavelength range paves way for the π-π^* absorption peak, observed under reduction potentials. The peak corresponding to π-π^* transitions is observed in the wavelength range of 490 - 495 nm, and it becomes predominant only at E > –2.0 V. But notable is the retention of a high but a rather flat absorption band in the 900 – 1800 nm wavelength region. This absorption in the near-infrared (NIR) region varies in a manner exactly similar to the bipolaronic peak, i.e., the intensity of this flat band decreases with increasing reduction potential, thus indicating the ability of the control film to modulate not only visible light, but also NIR radiation. For the PEDOP-RGO/IL composite (Figure 3.17b), the trends for optical density variation with wavelength/potential are akin to that of the control PEDOP-IL device, albeit a few differences. The π-π^* absorption peak, also tends to preponderate at E > –2.0 V, but it shows a bathochromic shift relative to the control PEDOP-IL, and it is seen in the wavelength range of 500 – 510 nm. The ΔOD_{max} ($\Delta OD_{max} = \Delta OD_{(-3.0\ V)} - \Delta OD_{(+1.0\ V)}$) in the visible region at λ_{max} ~ 500 nm for the PEDOP-RGO/IL composite was 0.94 and for the control PEDOP-IL, at a λ_{max} of 495 nm, ΔOD_{max} was 0.69. Our value for the composite is higher than a ΔOD of ~0.65 observed for a PEDOP film doped by ClO_4^- ions. In the PEDOP-RGO/IL device, a peak with a λ_{max} of ~733 nm was seen distinctly in the high reduction potential range of –1.9 to –3.0 V, with maximum intensity at E = –1.9 V. Furthermore, the intensity of the flat absorption

band in the NIR region (at $\lambda \geq 900$ nm), for the composite, showed the expected trend, i.e., it diminished with increasing reduction potential only in this narrow potential range of –1.9 to –3.0 V. For the remaining potentials of +0.5 to +2.0 V and –0.2 to –1.8 V and the trend was just the opposite, the absorption intensity of the flat band increased with increasing reduction potential. Although it is difficult to explain at this stage, but it is probably the RGO/IL nanosheets which cause the digression from the typical trend, as the control PEDOP-IL device does not show this unusual behavior.

Coloration efficiency (CE) plots of control PEDOP-IL and PEDOP-RGO/IL composite devices are shown in Figure 3.17c and d. For the control PEDOP-IL, a $CE_{max(visible)}$ of 263 cm^2 C^{-1}, in the visible region was attained under a potential of –2.7 V at a $\lambda_{max(visible)}$ of 467 nm. In addition to a $CE_{max(visible)}$ in the visible region, another $CE_{max(NIR)}$ was observed in the NIR region, and it was higher than its visible counterpart for applied reduction potentials of –1.8 to –3.0 V. For reduction potentials in the range of –0.8 to –1.7 V, $CE_{max(NIR)}$ was lower than $CE_{max(visible)}$. For the same film, under –2.7 V, at a $\lambda_{max(NIR)}$ of 1275 nm, a $CE_{max(NIR)}$ of 568 cm^2 C^{-1} was registered. For the PEDOP-RGO/IL composite, a remarkably high $CE_{max(visible)}$ of 477 cm^2 C^{-1} was achieved at a $\lambda_{max(visible)}$ of 509 nm, under a reduction potential of only –1.0 V. For the composite, in general, the $CE_{max(NIR)}$ was lower than $CE_{max(visible)}$, for nearly all values of applied potential under consideration. The CE_{max} in the photopic region, is higher for the composite as compared to the control film and it is also attained under a significantly lower value of applied potential, which implies that a fairly low injected charge density suffices to bring about a larger electrochromic contrast in the composite. This is most useful for increasing the cycling life of the device. The control PEDOP-IL is bereft of any such advantage, as the potential at which CE_{max} is obtained is much higher (E = –2.7 V). This is also augmented by the low CE

shown by the composite device at high negative potentials. Although the control film shows a higher $CE_{max(NIR)}$ as compared to the composite, but since, by and large, the primary function of electrochromic smart windows is to tune visible radiation, this function is far superior for the composite whilst simultaneously it also retains a fairly large coloring efficiency in the NIR region. In this manner, the composite achieves an optimal balance between visible and NIR coloring efficiencies and that too, at charge densities lower than that required for acquiring CE_{max} in the control PEDOP-IL. The PEDOP-RGO/IL composite, under a slightly lower reduction potential of –0.8 V, shows a $CE_{(visible)}$ of 459 $cm^2\ C^{-1}$ at a $\lambda_{max(visible)}$ of 532 nm, indicating the capability of the film to retain a fairly high CE, even at potentials less than –1.0 V. The RGO/IL nanosheets facilitate electron transport, as has been observed earlier by C-AFM, for there exist very few insulating domains in the composite,and therefore electron movement through the film is efficient and almost unhindered. On the other hand, in the control PEDOP-IL film, the prevelance of insulating regions in the absolute vicinity of the conducting regions, hinders electron transport. Greater the homogentiy of conducting areas, as in PEDOP-RGO/IL, easier it would be for electrons, to move out during oxidation and to move in during reduction through the cross-section of the film. For every electron ejected from the film, a charge compensating anion is inserted into the film from the electrolyte; so greater the ease of electron movement in the film, greater would be the number of ions adsorbed by the film from the electrolyte and thus larger would be the contrast and therefore the coloration efficiency. The CE results markedly reflect the role of RGO/IL nanosheets in enabling greater and easier access of the electrolyte ions to the electrochemically active sites in the composite. Although for PEDOP, the exact values of CEs are not highly reported, except in a previous study on a PEDOP-Au nanocomposite [6], wherein a CE of 270 $cm^2\ C^{-1}$ at λ = 458 nm was obtained. For PEDOP-RGO/IL, the CE is much

higher in the visible region. On comparing our values, with the thiophene analogue, i.e., PEDOT, we find that Gaupp et al. [31], achieved a CE of 206 cm^2 C^{-1}, at a λ_{max} of 585 nm, for 80% of the full switch. For another polychromic polymer, containing EDOT units, a CE of 680 cm^2 C^{-1} was reported at 535 nm [32]. For a poly(3,4-propylenedioxythiophene)-Et_2 film, a CE of 505 cm^2 $C^{-1}$was observed, which is slightly greater than our value for the composite [33].

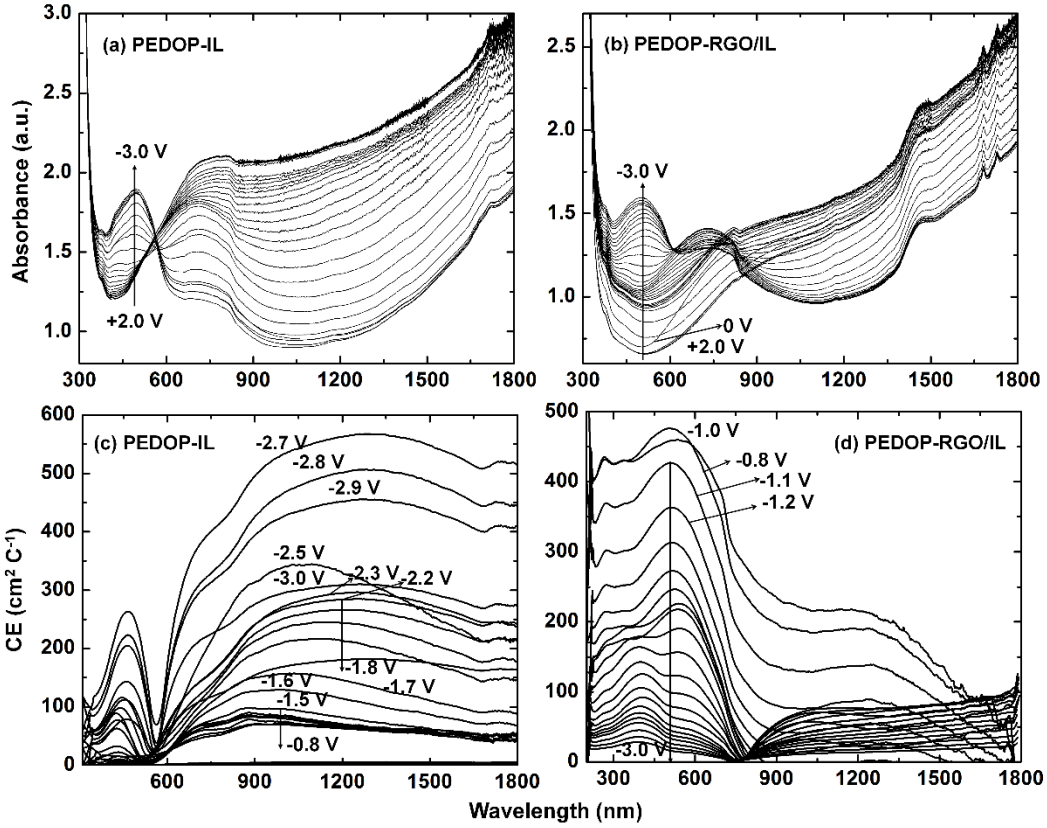

Figure 3.17: Absorption spectra of (a) control PEDOP-IL and (b) PEDOP–RGO/IL composite based devices under oxidation potentials of +0.5, +1.0, +1.5 and +2.0 V and under reduction potentials of –0.2 V to –3.0 V, in steps of –0.1 V in the 300 – 1800 nm wavelength range. CE*versus* wavelength plots for (c) control PEDOP-IL and (d) PEDOP–RGO/IL composite based devices, under reduction potentials of –0.8 to –3.0 V, in steps of –0.1 V. The absorption spectrum under +1.0 V has been chosen as reference in both cases.

Electrochromic switching response of the two devices, performed under a square wave potential of ±3 V, at a fixed wavelength of 500 nm, at 0.05 Hz, are shown in Figure 3.18a and c. The transmission modulation of the control PEDOP-IL is comparable to that of the composite PEDOP-RGO/IL, but the composite acquires a saturated hue in the bleached state in a lesser time span, as current propagation is more homogeneous in this film. Although our color-bleach times values are longer than the color and bleach times of 4.5 s shown for a copolymer of terthiophene and EDOP corresponding to a full switch [34], but since a good optical contrast (shown in Figure 3.18b and d) is acquired in about 10 s, the devices are conducive for transmissive electrochromic applications.

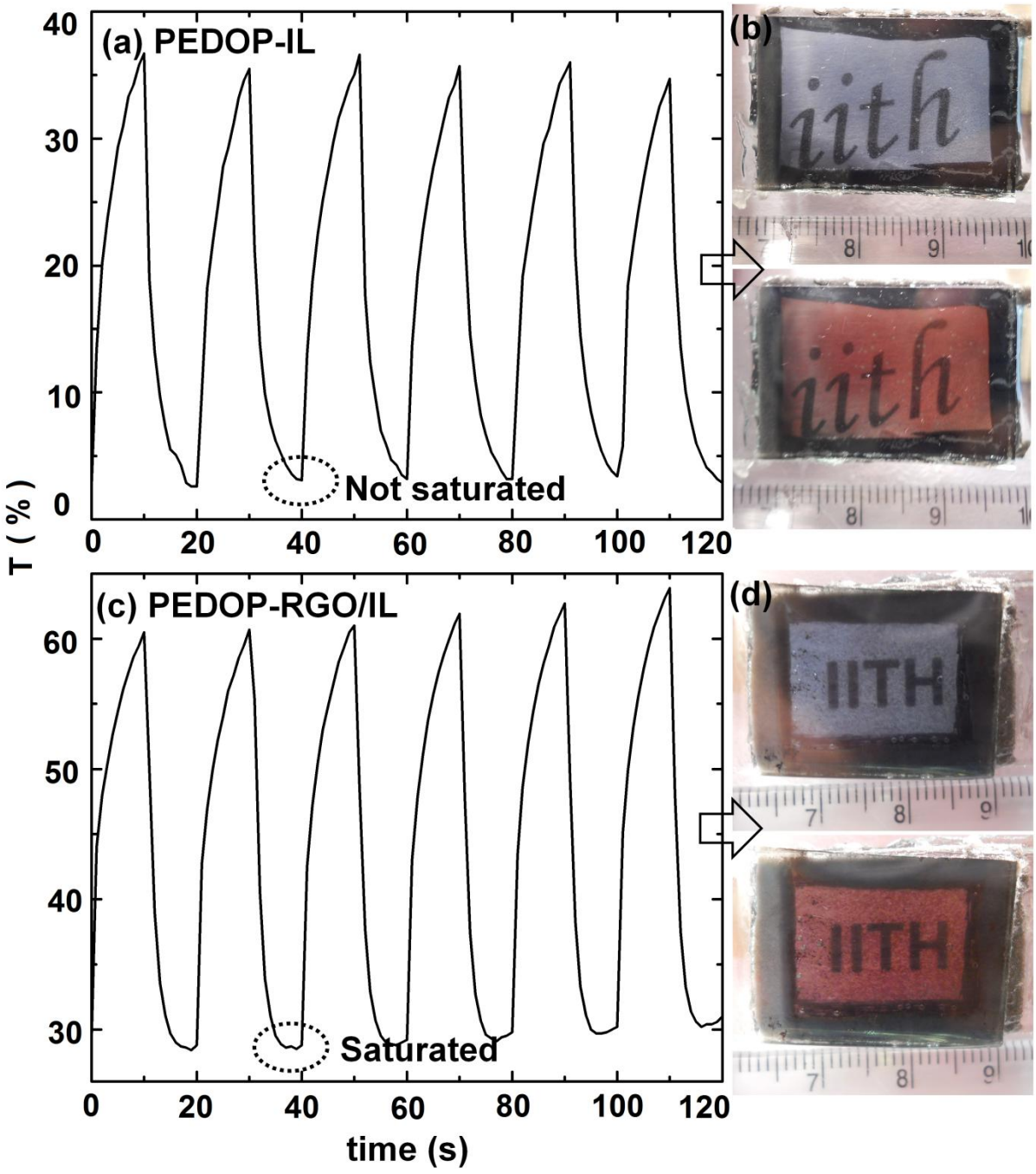

Figure 3.18: Transmision spectra of (a) control PEDOP-IL and (c) PEDOP-RGO/IL composite based devices under a square wave potential of ±3 V, at a monochromatic wavelength of 500 nm. Panels on right side show photographs of the devices of PEDOP-IL (b) and PEDOP-RGO/IL (d) in colored and bleached states.

3.4 Summary

Composites of RGO layers with PEDOP were prepared by an electrochemical method. We demonstrated the incorporation of RGO/IL in PEDOP by XPS, on the basis of new signals due to S, N and a completely altered C signal and by HRTEM which, revealed the composite to be composed of rippled sheets of RGO/IL encapsulating the polymer between the layers of RGO/IL and extending over several hundred squares of nanometers. An altered electronic structure for the composite, was also evidenced from the decreased valence band to fermi edge gap, ongoing from control PEDOP-IL to PEDOP-RGO/IL. C-AFM showed that the high current flowing regions dominate the surface of the PEDOP-RGO/IL composite, in stark contrast to control PEDOP-IL, wherein the conducting regions are predominantly flanked by insulating domains, which, obstruct electron propagation. RGO/IL in addition to serving as a dopant for forming the polymer film, also acts as an electron conduit connecting the PEDOP grains, thus leading to a homogeneous distribution of conducting regions in the PEDOP-RGO/IL composite. This was also supported by a two-fold increment in dc electronic conductivity, measured independently, and achieved in the PEDOP-RGO/IL composite. The benefit of less-hindered and more uniform current pathways available to the PEDOP-RGO/IL composite was clearly reflected in the improved optical contrast, as the ease of electron ingress and egress during reduction and oxidation of the electrochromic composite, allows higher ion uptake, thus imparting larger coloring efficiency in the visible region, faster bleaching rate and higher electrochemical ion-insertion-extraction capacity in comparison to the control PEDOP-IL film.

References

[1]C.G. Granqvist, Handbook of Inorganic Electrochromic Materials, Elsevier, Amsterdam, (1995)
[2] H. Chang, G. Wang, A. Yang, X. Tao, X. Liu, Y. Shen, Z. Zheng, Adv. Funct. Mater. 20(2010) 2893–2902.
[3] A. A. Green, M. C. Hersam, J. Phys. Chem. Lett. 1 (2010) 544–549.

[4] S. Park, R. S. Ruoff, Nature Nanotech. 4 (2009) 217–224.
[5] W. S. Hummers, R. E. Offeman,J. Am. Chem. Soc. 80 (1958) 1339-1339.
[6] A. Kharkwal, M. Deepa, A. G. Joshi, A. K. Srivastava, ChemPhysChem12 (2011) 1176–1188.
[7] S. Bhandari, M. Deepa, A. K. Srivastava, A. G. Joshi, R. Kant, J. Phys. Chem. B 113 (2009) 9416–9428.
[8] L. Pigani, A. Heras, A. Colina, R. Seeber, L.Palacois, J. Electrochem. Comm. 6 (2004) 1192–1198.
[9] I. Efimov, S. Winkels, J. W. Schultze, J. Electroanal. Chem. 499 (2001) 169–175.
[10] J. Lu, J. X. Yang, J. Wang, A. Lim, S. Wang, K. P. Loh, ACS Nano 3 (2009) 2367–2375.
[11] A. C. Ferrari, J. C. Meyer, V. Scardaci, C. Casiraghi, M. Lazzeri, F. Mauri, S. Piscanec, D. Jiang, K. S. Novoselov, S. Roth, A. K. Geim, Phys. Rev. Lett. 97 (2006) 187401–187404.
[12] W. Gao, L. B. Alemany, L. Ci, P. M. Ajayan, Nature Chem. 1 (2009) 403–408.
[13] W. Chen, L.Yan, Nanoscale, 2 (2010) 559–563.
[14] P. Chandrachud, B. S. Pujari, S. Haldar, B. Sanyal, D. S. Kanhere, J. Phys. Condens. Matter 22 (2010) 1–11.
[15] J. C. Meyer, A. K. Geim, M. I. Katsnelson, K. S. Novoselov, T. J. Booth, S. Roth, Nature 446 (2007) 60–63.
[16] S. Bhandari, M. Deepa, S. Pahal, A. G. Joshi, A. K. Srivastava, R. Kant, ChemSusChem 3 (2010) 97–105.
[17] A. Reina, A. Jia, J. Ho, D. Nezich, H. Son, V. Bulovic, M. S. Dresselhaus, J. Kong, Nano Lett. 9 (2009) 30–35.
[18] K. S. Kim, Y. Zhao, S. Y. Lee, J. M. Kim, J. H. Ahn, P. Kim, J. Y. Choi, B. H. Hong, Nature 457 (2009) 706–710.
[19] W. Gao, L. B. Alemany, L. Ci, P.M. Ajayan, Nature Chem. 1 (2009)403–408.
[20] S. Stankovich, D. A. Dikin, R. D. Piner, K. S. Kohlhaas, A. Kleinhammes, Y. Jia, Y. Wu, S. B. T. Nguyen, R. S. Ruoff, Carbon 45 (2007) 1558–1565.
[21] H. Yang, C. Shan, F. Li, D. Han, Q. Zhang, L. Niu, Chem. Comm. (2009) 3880–3882.
[22] D. R. Dreyer, S. Park, C. W. Bielawski, R. S. Ruoff, Chem. Soc. Rev. 39 (2010) 228–240.
[23] S. Caporali, U. Bardi, A. Lavacchi, J. Electron Spectr. Related Phen. 151 (2006) 4–8.
[24] S. Bhandari, M. Deepa, A. K. Srivastava, A. G. Joshi, R. Kant, J. Phys. Chem. B 113 (2009) 9416–9428.
[25] A. Jaramillo, L. D. Spurlock, V. Young, T. A. Brajter-Toth, Analyst 124 (1999)1215–1221.
[26] H. J. Lee, S. M. Park, J. Phys. Chem. B 108 (2004) 1590–1595.
[27] H. J. Lee, J. Lee, S. M. Park, J. Phys. Chem. B 114 (2010) 2660–2666.
[28] P. Schottland, K. Zong, C. L. Gaupp, B. C. Thompson, C. A. Thomas, I. Giurgiu, R. Hickman, K. A. Abboud, J. R. Reynolds, Macromolecules 33 (2000) 7051–7061.
[29] H. J. Ahonen, J. Lukkari, J. Kankare, Macromolecules 33 (2000) 6787–6793.
[30] J. Padilla, V. Seshadri, T. F. Otero, G. A. Sotzing, J. Electroanal. Chem. 609 (2007) 75–84.
[31] C. L. Gaupp, D. M. Welsh, R. D. Rauh, J. R. Reynolds, Chem. Mater. 14 (2002) 3964–3970.
[32] G. Sonmez, H. Meng, F. Wudl, Chem. Mater. 16 (2004) 574–580.
[33] C. L. Gaupp, D. M. Welsh, J. R. Reynolds, Macromol. Rapid Commun. 23 (2002) 885–889.
[34] H. Seol, H. Jeong, S. Jeon, J. Electroanal. Chem. 636 (2009) 107–112.

Chapter 4

Counter ion effect on nanoscale conduction and work function of PEDOP films

4.1 Introduction

For a CP to be utilized in an electrochromic or any similar device, a quantitative description of the conduction behavior of the polymer film with a spatial resolution at the nanoscale, can be of tremendous use, for the conduction aspects can be correlated to performance characteristics such as electrochromic contrast, switching kinetics, charge storage capacity and so forth. To this end, C-AFM technique, offers the possibility to probe the nano or molecular scale electronic transport properties and it also provides information about the homogeneity of the distribution of conducting domains in a given film. Likewise, Kelvin probe force microscopy (KPFM) also allows the qualitative determination of surface potentials of CPs, which is essential for discerning the functionality of CPs, when used in practical electrochemical cells. Previously, C-AFM measurements have been performed on polyaniline [1],polypyrrole [2], poly (methylthiophene) [3] and PEDOT or PEDOT:Poly(styrene sulfonate) or PSS [4–6]films. By employing C-AFM, Wu et al. examined the variation in electrical conductivity and evolution of band structures in polyaniline films after doping/dedoping the polymer at different potentials [5]. Since the redox switching in an electrochromic device relies predominantly on dynamic transport of charges, determination of localized work function of the CP at the nanometer scale and the variation of the same as a function of morphology or dopant content or type can be exploited to associate the electrochromic response with electron transport. Among many techniques such as KPFM, photoelectron spectroscopy, and SEM coupled with electron beam induced current

analysis that can be used for the measurement of work function, KPFM offers the ability to achieve surface potential maps of high resolution with relatively high energy sensitivity [7–9]. In an earlier study, Semenikhin et al. investigated the doping level distribution and surface morphology of anodically and cathodically doped poly-3-methylthiophene deposited on highly oriented pyrolitic graphite with KPFM as the probe [10]. In this chapter, we studied the effect of counter ion namely, (i) an intrinsically electron conducting dopant: functionalized multiwalled carbon nanotubes (MWCNTs) and insulating dopants such as (ii) a conventional salt anion: triflate and (iii) a surfactant based anion: dodecyl sulfate. On nanolevel conduction and work function of PEDOP films, obtained by electropolymerization.The effect of counter ion on conduction behavior of PEDOP was analyzed by C-AFM and KPFM and how their conduction/surface potential profiles influence electrochromism and electrochemical properties was unraveled.

4.2 Experimental

4.2.1 Functionalization of MWCNTs with benzyl sulfonate

A suspension of 25 g of $(NH_4)_2S_2O_8$ (87 mM) and 50 mg of MWCNTs (0.8 mM) in sulfuric acid(37 mL) was prepared and magnetically stirred for 3 hours at room temperature. To this dispersion, 1.4 g (1.6 mM) of benzene sulphanilic acid was added and stirring was continued for another 10 minutes. 0.55 g (1.6 mM) of $NaNO_2$ was added and this was followed by slow addition of 0.3 g of AIBN (0.4 mM). The resulting dispersion was refluxed at 80 ^oC for 3 h in an oil bath. The mixture was then transferred into 100 mL of ice cold water, washed repeatedly with deionized water, followed by washings in acetone and DMF. The product was dried at 60 ^oC in an oven for 12 h to yield a black solid of benzyl sulfonate functionalized MWCNTs.

4.2.2 Deposition of PEDOP films

An aqueous solution of 0.1 M EDOP and 0.1 M $LiCF_3SO_3$ was prepared in 10 mL of deionized water for deposition of PEDOP-$CF_3SO_3^-$ (triflate doped) films. A solution of 0.1 M EDOP and 0.1 M sodium dodecyl sulfate in 10 mL of deionized water was prepared for fabricating PEDOP-$(C_{12}H_{25})OSO_3^-$ (dodecyl sulfate doped) films. The precursor for PEDOP-MWCNT)SO_3^- films was a dispersion of 0.1 M EDOP and 1 mg/mL of sulfonate functionalized MWCNTs in deionized water (10 mL) prepared by ultrasonication for 10 minutes. Electropolymerization of the three films was performed in a three electrode configuration. FTO coated glass plates were employed as working and counter electrodes, and Ag/AgCl/KCl was used as the reference electrode. Bluish-black colored dodecyl sulfate doped PEDOP and triflate doped PEDOP films were deposited under potentiostatic conditions at room temperature in chronoamperometric mode by application of +1.8 V to the working electrode for 500 s. PEDOP films doped with (MWCNT)SO_3^- species, were obtained by applying +2.2 V for the same duration of time. All films were washed in deionized water, dried in air for 2 h and stored in air. Electropolymerization reactions are shown in Scheme 4.1.

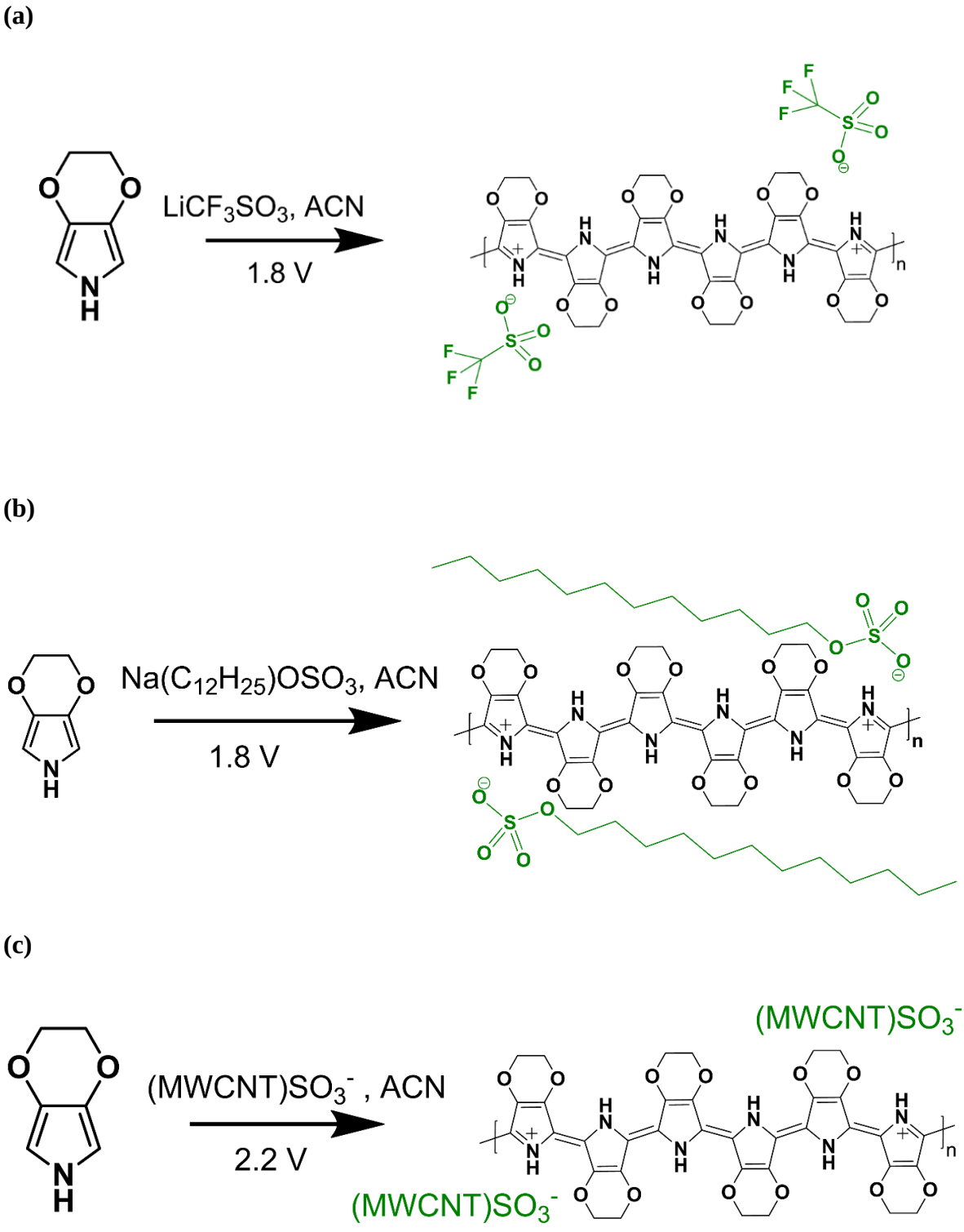

Scheme 4.1: Electrochemical synthesis of PEDOP-$CF_3SO_3^-$, PEDOP-$(C_{12}H_{25})OSO_3^-$ and PEDOP-MWCNT)SO_3^- films.

4.3 Results and discussion

4.3.1 I-t Transient curves

The I-t curves corresponding to the formation of films by oxidative electropolymerization, under potentiostatic conditions from precursor solutions containing the monomer EDOP and (a) $CF_3SO_3^-$, (b) $(C_{12}H_{25})OSO_3^-$ and (c) $(MWCNT)SO_3^-$ species are shown in Figure 4.1(a-c). The photograph of the precursor solution containing EDOP and sulfonated MWCNTs is shown in the inset of Figure 4.1c. A diluted aliquot of the same solution is also shown therein, to demonstrate that the sulfonated MWCNTs do not form precipitates, but remain dispersed in the solution phase. At t = 0 s, the current shows a spike for all the three cases which, is ascribed to electrical double-layer capacitance charging, and thereafter, it shows a steep decline. The domain wherein current is minimum, is attributed to the diffusion of monomer onto the electrode surface and formation of oligomers [11]. The ensuing slight current increase (observed only for films grown in triflate and dodecyl sulfate solutions), and the subsequent decay to acquire plateau-like response, in case of PEDOP doped with either dodecyl sulfate doped or with sulfonate functionalized MWCNTs is associated with nucleation and polymer growth [11]. For PEDOP films doped with triflate ions, current showed a steady decrease, and no plateau was seen; this could be due to the high resistance of the polymer layer deposit. But most striking is the initial difference in the current maximum values which, were ~ 0.195, 0.42 and 1.32 mA for PEDOP-$CF_3SO_3^-$,PEDOP-$(C_{12}H_{25})OSO_3^-$ and PEDOP-$(MWCNT)SO_3^-$ respectively. The magnitude of the initial current peak as well as the overall amplitude of current, during the processing of PEDOP-$(MWCNT)SO_3^-$ film, are much larger than the currents obtained in the $CF_3SO_3^-$ or $(C_{12}H_{25})OSO_3^-$ doped films.

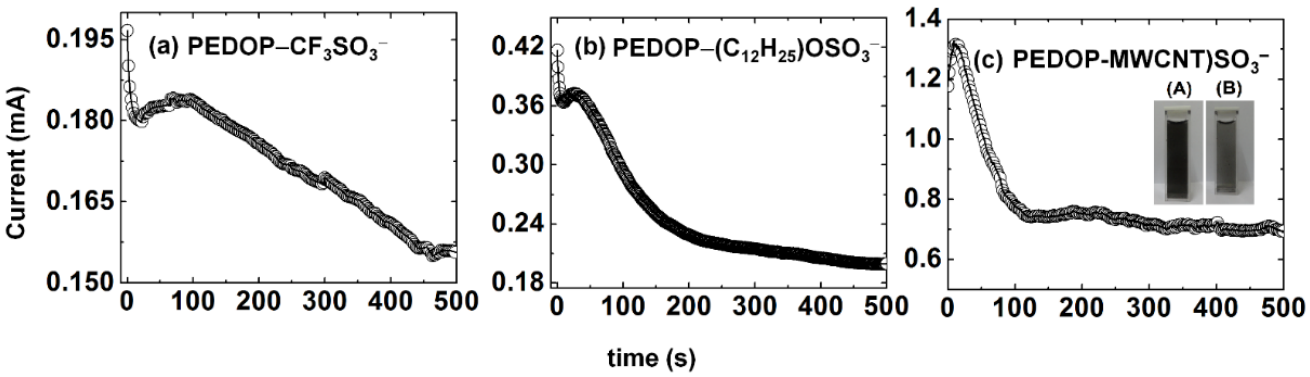

Figure 4.1: Current *versus* time transients recorded for the oxidative electro-synthesis of PEDOP films from solutions of 0.1 M EDOP with (a) $LiCF_3SO_3$, (b) $Na(C_{12}H_{25})OSO_3$ and (c) MWCNTs functionalized with C_6H_5-SO_3^- groups. Inset of (c) shows the digital photographs of the monomer-CNT dispersion used for fabricating PEDOP-(MWCNT)SO_3^- films.

4.3.2 Raman spectra

Raman spectra of PEDOP-$CF_3SO_3^-$,PEDOP-$(C_{12}H_{25})OSO_3^-$ and PEDOP-(MWCNT)SO_3^- films are shown in Figure 4.2a. Of particular importance is the strong peak at 1185 cm^{-1}, observed for the PEDOP-(MWCNT)SO_3^- film which, is ascribed to the S-O stretching mode, as it confirms the successful functionalization of MWCNTs with SO_3^- groups. This band is seen at 1189 cm^{-1} in PEDOP-$CF_3SO_3^-$ and PEDOP-$(C_{12}H_{25})OSO_3^-$ films, thus affirming the inclusion of triflate and dodecyl sulfate groups in these films. The C_β–C_β stretching mode arises from the pyrrole rings on the PEDOP chains, and the band is seen in the range of 1330-1350 cm^{-1}, in all the three spectra [12]. The symmetric stretching mode of C=C–O groups of PEDOP, shows a band at wavenumbers slightly above 1400 cm^{-1}. A smattering of low intensity peaks is observed in the 1200-1300 cm^{-1} region, and these originate from the C–N stretching of the pyrrole rings. A medium intensity band at ~715 cm^{-1} (PEDOP-(MWCNT)SO_3^-) possibly stems from the N–H out-of-plane bending mode and it is observed at ~711 cm^{-1}, in the other two films. An extremely strong broad peak extending from 1500 to 1600 cm^{-1}, is observed at 1608 cm^{-1} in the PEDOP-

(MWCNT)SO_3^- film and it is seen at 1617 cm^{-1}, in the other two films. This peak is due to the asymmetric stretching mode of C_α=C_β bonds of pyrrole. In PEDOP-(MWCNT)SO_3^- films, the D-band due to defects in CNTs, is expected at 1350 cm^{-1}, and the G-band is anticipated at 1578 cm^{-1} [13]. Since these overlap with the modes due to PEDOP, it is difficult to distinguish independent contributions. The radial breathing mode in single or double walled CNTs produces a sharp intense peak at ~202 cm^{-1} [14].Here, on enlarging the spectrum, in the low wavenumber region inset of Figure 4.2a, we observed a low intensity broad peak at 212 cm^{-1} only for the PEDOP-(MWCNT)SO_3^- film which, is an indicator of the prevalence of sulfonated CNTs in the CP matrix. The optical micrographs of the three films are shown in Figure 4.2b, c and d. While the PEDOP-(MWCNT)SO_3^- film appears to be composed of fiber like shapes, the PEDOP-$CF_3SO_3^-$ and PEDOP-($C_{12}H_{25}$)OSO_3^- films have a granular texture, with no distinct feature.

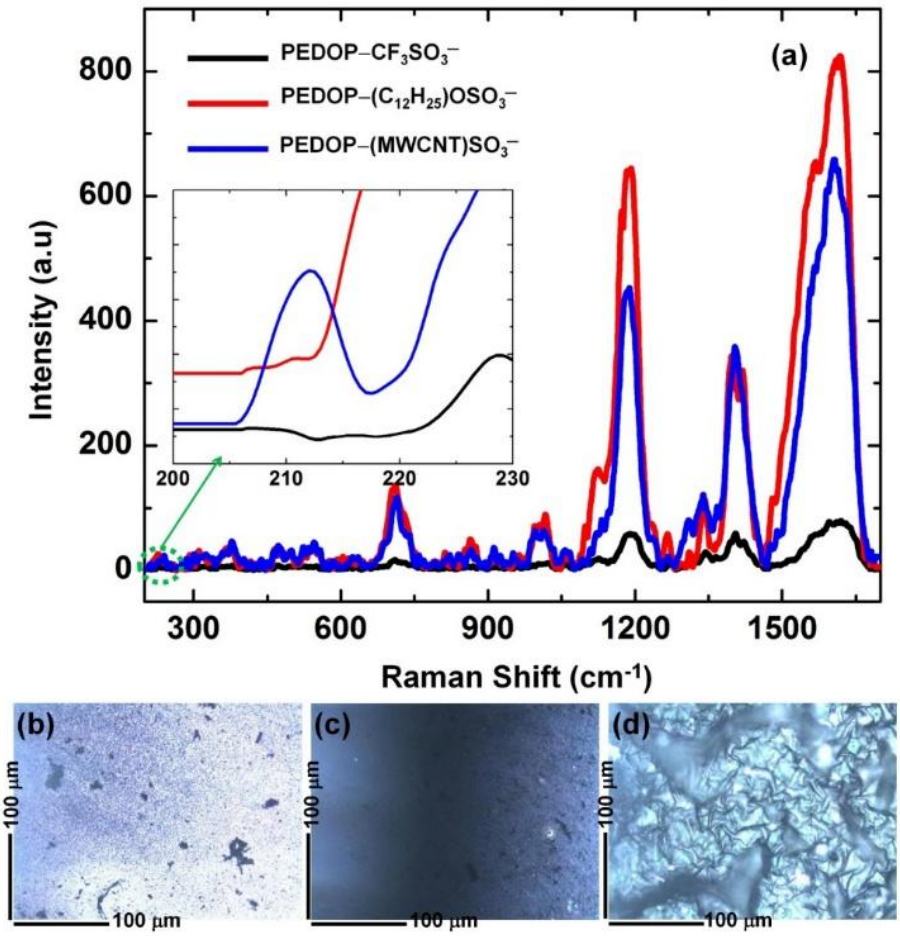

Figure 4.2:(a) Raman spectra of PEDOP-$CF_3SO_3^-$, PEDOP-$(C_{12}H_{25})OSO_3^-$ and PEDOP-(MWCNT)SO_3^- films in the 200 – 1600 cm^{-1} wavenumber range. Inset is an enlarged view of the low wavenumber region. Optical microscopy images of (b) PEDOP-$CF_3SO_3^-$, (c) PEDOP-$(C_{12}H_{25})OSO_3^-$ and (d) PEDOP-(MWCNT)SO_3^- films.

4.3.3 C-AFM studies

Figure 4.3 shows the topography and current images recorded concurrently for identical regions of as-fabricated films of PEDOP-$CF_3SO_3^-$, PEDOP-$(C_{12}H_{25})OSO_3^-$ and PEDOP-(MWCNT)SO_3^-; the scanned area was 3 µm × 3 µm for each film. The corresponding cross-section profiles recorded exactly along the middle of the images are shown in the insets of topography and current images. The topography of the PEDOP-$CF_3SO_3^-$ and PEDOP-

$(C_{12}H_{25})OSO_3^-$ films are almost alike (Figure 4.3a and d) and these films are composed of interconnected globular cauliflower like shapes. However, the surface morphology of the PEDOP-(MWCNT)SO_3^- film is conspicuously different from that of the PEDOP films doped by triflate or dodecyl sulfate ions. This film is constituted by elongated fibrillar shapes of PEDOP coated with the sulfonate functionalized MWCNTs. The root mean square roughness for PEDOP-$CF_3SO_3^-$,PEDOP-$(C_{12}H_{25})OSO_3^-$ and PEDOP-(MWCNT)SO_3^- films are 15.8, 17.8, 35.4 nm respectively. The higher roughness of the PEDOP-(MWCNT)SO_3^- film is advantageous, as it allows the film to adsorb more ions during electrochemical switching which, can effectively lead to high optical contrast [15]. The current images were obtained by contacting a conductive tip with the film surface and a small bias voltage of 50 mV was applied between the tip and the substrate. The magnitude of maximum currents can be seen from the color scaling in Figure 4.3b, e and h. Of the three films, the triflate doped PEDOP film is characterized by the least current carrying ability (I_{max} = 0.55 nA), whereas the film doped with sulfonated MWCNTs has the largest current carrying capacity (I_{max} = 25 nA). The distribution of the bright spots or domains in the PEDOP-$CF_3SO_3^-$ film is sparse. The distribution of the bright spots and the value of current maximum in the dodecyl sulfate doped PEDOP film are intermediate to that observed for PEDOP-$CF_3SO_3^-$ and PEDOP-(MWCNT)SO_3^- films; the I_{max} is 3 nA. In the films doped with triflate and dodecyl sulfate, the current flow is heterogeneous with localized regions of high electron conduction. In the PEDOP film doped with sulfonated MWCNTs, the homogeneity of the bright regions, characteristic of high electron conductance is better than that in the other two films. The current carrying capability of the PEDOP film doped with sulfonated MWCNTs, is 45-times greater than that of the PEDOP film doped with triflate ions, for the same value of applied bias. This is clearly illustrative of the extraordinary ability of the sulfonate functionalized

MWCNTs to increase the current carrying ability of PEDOP. The bright regions, in the current images represent the doping distribution, as well, for during oxidative electropolymerization, the counter ion is embedded onto the globular or the protuberant parts of the film, and consequently, these localized regions are highly conducting. In the PEDOP-(MWCNT)SO_3^- film, the tethering of the dopant ions, i.e., sulfonated MWCNTs to the PEDOP chains occurs at the molecular level, due to the single step potentiostatic deposition from a plating sol containing both the monomer and the sulfonated MWCNTs; the polymer is in direct contact with the MWCNTs, and therefore the flow of electrons through the bulk of the polymer deposit is facile as the sulfonated MWCNTs possess an intrinsic ability to conduct electrons. Such an unobstructed electron propagation through the bulk of the PEDOP film is not realized in the films doped by triflate or dodecyl sulfate ions as these are electronically insulating species, and therefore, not only is the highest current obtained for these films lower than that obtained in the PEDOP-(MWCNT)SO_3^- film but the localized spots characteristic of high currents, are also few.

In the triflate and dodecyl sulfate doped PEDOP films, the high current spots/islands are embedded in large insulating domains, as opposed to the PEDOP-(MWCNT)SO_3^- film, wherein the high current (bright) regions tend to dominate and also appear to be interlinked, thus improving the overall, lateral conduction of electrons in the film. The current section profile of the PEDOP-(MWCNT)SO_3^- film (Figure 4.3h) complements the imaging, as the span of crests corresponding to high currents, is significantly wider than the few troughs corresponding to low currents. It is apparent that localized electron conduction, is rather uniform across the PEDOP-(MWCNT)SO_3^- film. The exactly opposite response was obtained for the films doped by triflate ions, as fewer peaks corresponding to high currents were obtained. Point contact I-V curves were recorded at fifteen equidistant points on each current image, and the average I-V profile for each

film is shown (Figure 4.3c, f and i). A quasi-linear dependence of current on swept potential was confined to an unusually narrow voltage window of about –0.2 to +0.2 V for the PEDOP-$CF_3SO_3^-$, PEDOP-$(C_{12}H_{25})OSO_3^-$ and PEDOP-(MWCNT)SO_3^- films. From the straight-line fits, within the voltage windows in which the I-V response was almost linear, ambient temperature electronic conductivities were determined by using equation (1),

$$\sigma_{RT} = (I/V) \times (d/\pi r^2) \quad (1)$$

where *r* is the radius of the conducting tip and d is the thickness of the PEDOP film. The average electronic conductivities for the PEDOP-$CF_3SO_3^-$, PEDOP-$(C_{12}H_{25})OSO_3^-$ and PEDOP-(MWCNT)SO_3^- films were deduced from the ohmic regimes and were found to be 0.0002, 1.70 and 6.75 S cm^{-1} respectively. The ohmic region (slope ~ 1) is due to the thermally generated carriers. The substantially higher average nanoscale conductivity of the PEDOP-(MWCNT)SO_3^- film (higher by four orders of magnitude as compared to the film doped triflate ions!) shows that the sulfonated MWCNTs provide multiple conduction pathways for electron movement and thus enhance the conducting capacity of the polymer film. To explain the digression from the linear behavior in the high bias regimes, of the I-V plots in the three films, traps (type: deep or shallow or discrete) must be included, as charge carrier trapping in semiconductors (PEDOP is a p-type semiconductor in the doped state) can aid in understanding the complex current-voltage characteristics. The as-fabricated electrochemically polymerized PEDOP is oxidized and the non-degeneracy of such a poly(heterocyclic) compound causes the charge carriers to be polarons or bipolarons at high doping levels. These polarons and bipolarons form intra-gap states and therefore carrier transitions are facile and as a consequence conductivity is high. At high bias, either the holes in the interstate bands (due to polarons or bipolarons) are able to move freely due to the applied bias, or the movement of polarons in trap states are activated. The data was found

to exhibit the best fit when a model based on exponentially distributed trap states which, follows equation (2) was employed.

$$I(E) = A \exp(E^*/E)^{1/4} \quad (2)$$

A, is a temperature dependent pre-exponential factor, and E* is a critical field characteristic of the material. Exponential decay of log I as a function of $E^{-1/4}$, was obtained in the high positive potential regime for the PEDOP-$CF_3SO_3^-$ and PEDOP-$(C_{12}H_{25})OSO_3^-$ films. Insets of Figure 4.3c and f show these profiles. The I-V data of the PEDOP-(MWCNT)SO_3^- film was found to be highly fluctuating in the high potential regimes, and therefore did not fit in either discrete / exponential / Gaussian trap distributions.

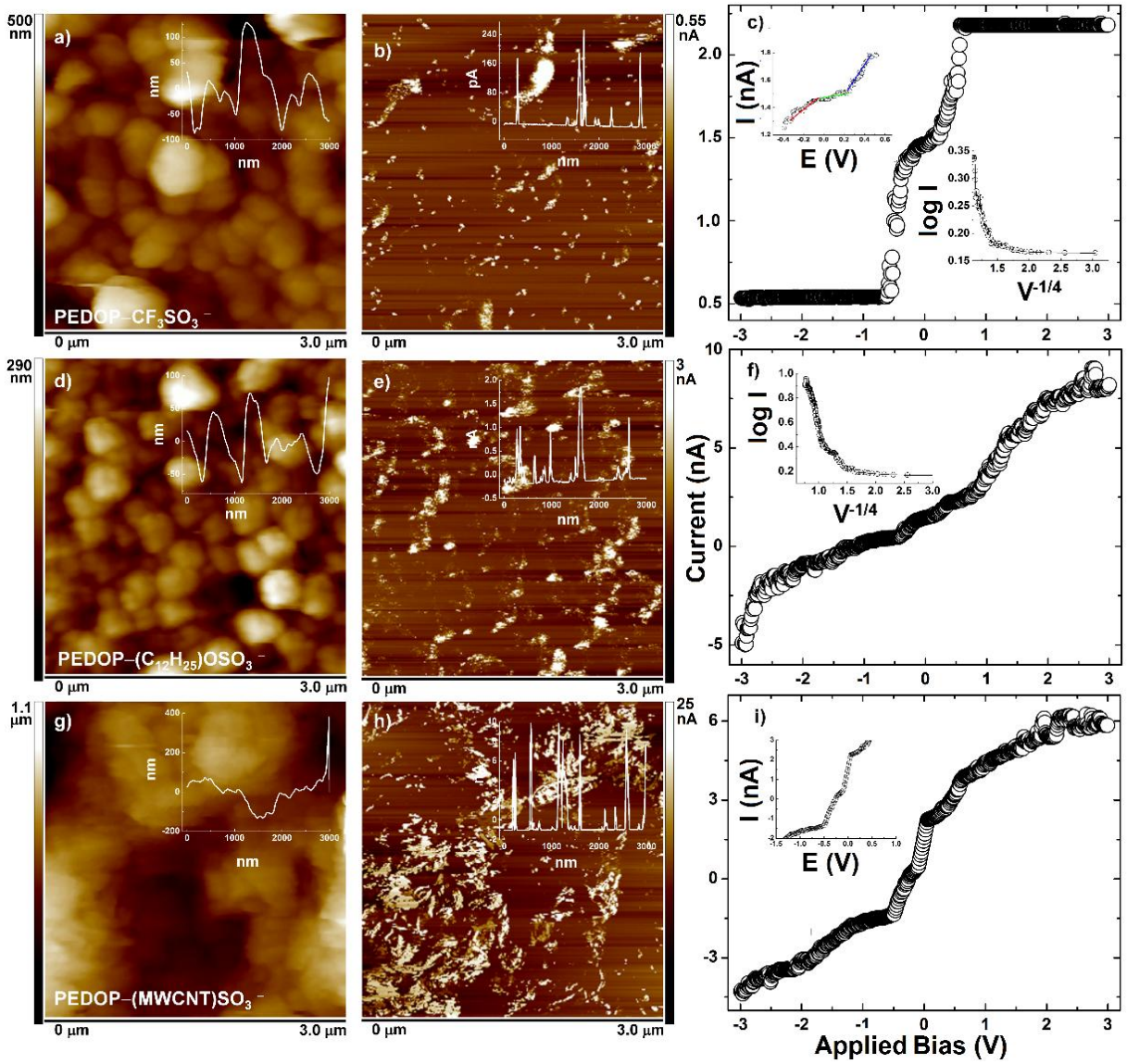

Figure 4.3: Concurrent topography (a,d,g) and current (b,e,h) images of PEDOP-$CF_3SO_3^-$, PEDOP-$(C_{12}H_{25})OSO_3^-$ and PEDOP-$(MWCNT)SO_3^-$ films recorded over a scanned area of 3 µm × 3 µm. Corresponding cross-sectional profiles are shown in the insets of the images. Resultant current-voltage curves of (c) PEDOP-$CF_3SO_3^-$, (f) PEDOP-$(C_{12}H_{25})OSO_3^-$ and (i) PEDOP-$(MWCNT)SO_3^-$ films. Each curve is averaged over 15 I-V curves recorded at 15 spots on each current image shown in b,e and h. Bottom inset of (c) and top inset of (f) are log I *versus* $V^{-1/4}$ plots derived from the corresponding I-V curves. Top insets of (c) and (i) are the corresponding enlarged views of I-V plots, to extract regimes corresponding to ohmic dependence.

Topography and current maps were also measured for the three films over a scanned area 1 μm × 1 μm and these are shown in Figure 4.4. The globules can be seen distinctly in the triflate and dodecyl sulfate doped films (Figure 4.4a and d), and the elongated mingling fibers of the PEDOP-(MWCNT)SO_3^- film (Figure 4.4g) are clearly visible in the high magnification image. The highest currents realized in PEDOP-$CF_3SO_3^-$, PEDOP-$(C_{12}H_{25})OSO_3^-$ and PEDOP-(MWCNT)SO_3^- films are 0.9, 3.0 and 23 nA respectively (see color scales in Figure 4.4b, e and h). In the corresponding I-V profiles (Figure 4.4c, f and i), averaged over fifteen points on each of the current maps, a linear dependence of current on external bias, was limited to voltage windows of –0.2 to +0.2 V, in the PEDOP-$(C_{12}H_{25})OSO_3^-$ film (top inset of Figure 4.4f) and from –0.15 to +0.2 V in the PEDOP-(MWCNT)SO_3^- film (top inset of Figure 5i). However, such an ohmic dependence of current on voltage was realized from ~ –2.9 to +1.5 V in case of the PEDOP-$CF_3SO_3^-$ film. For the latter film, at E > +1.5 V, the signal to noise ratio was rather low. For the PEDOP-$(C_{12}H_{25})OSO_3^-$ film, the deviation from the ohmic response was accounted for by using an exponential decline of log Ias a function of $E^{-1/4}$ (bottom inset of Figure 4.4f). For the PEDOP-(MWCNT)SO_3^- film a Mott-Gurney dependence was observed (bottom inset of Figure 4.5i), as a slope of approximately 2 was obtained for the log J *versus* log E plot. This is a trap-free space charge limited current (SCLC) in concordance with the Mott-Gurney Law [16],

$$j = 9/8 (\varepsilon_r \varepsilon_o \mu_{eff} V^2/L^3) \quad (3)$$

where ε_r is the dielectric constant of the film, μ_{eff} is the carrier mobility, ε_o is the permittivity of vacuum and L is the film thickness. The y-axis intercept (bottom inset of Figure 4.5i) can be represented as shown.

$$\log(9/16A\pi fZ'L^2) + \log(\mu_{eff}) = \text{y-axis intercept (log j)} \quad (4)$$

In (4), A is the surface area of the film and Z' and f are real contribution to impedance and f is the corresponding frequency, obtained from an impedance plot, which is shown in Figure 4.5. We deduced the charge carrier mobility to be 1.6×10^{-8} cm^2 V^{-1} s^{-1}, in the PEDOT-(MWCNT)SO_3^- film. Our value is close to that reported for a poly(phenylene vinylene) derivative (~1.5×10^{-7} cm^2 V^{-1} s^{-1}) but lower than that of poly(3-hexyl thiophene) which showed a μ of 8.3×10^{-5} cm^2 V^{-1} s^{-1}. Authors in [16] also used the Mott-Gurney dependence generated from a C-AFM plot to determine carrier mobilities. At higher potentials attributed to SCLC, the transport in this regime is governed by the injected holes due to space charge. But it must be recalled that the charge transport of PEDOP is not solely controlled by its electronic structure, and the counter ion, especially when it is sulfonated MWCNTs also influences carrier transport. In MWCNTs, percolation of carriers though the concentric cylinders of graphite allow delocalization of charge and promote fast electron movement.

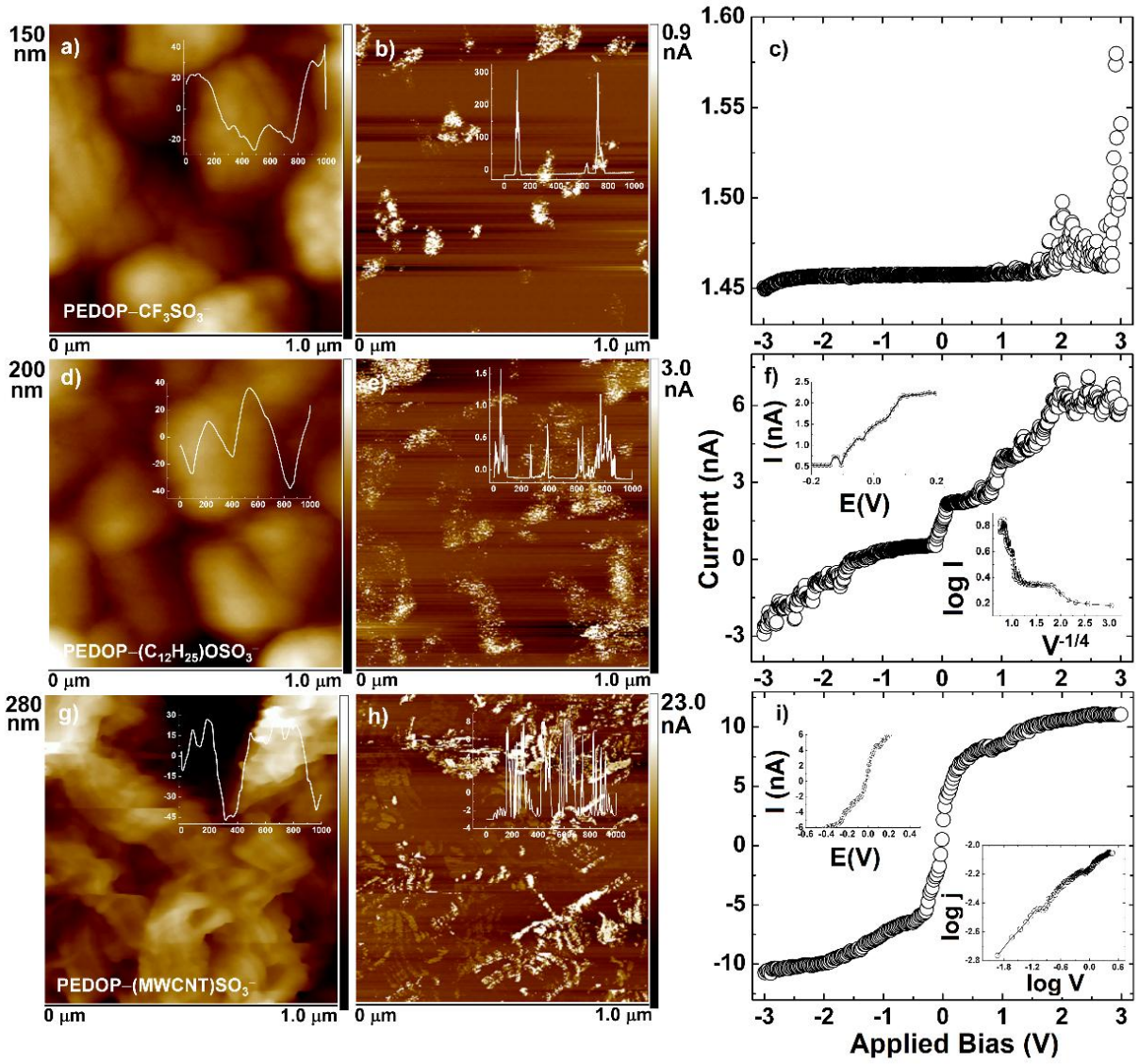

Figure 4.4: Simultaneous topography (a,d,g) and current (b,e,h) images of PEDOP-$CF_3SO_3^-$, PEDOP-$(C_{12}H_{25})OSO_3^-$ and PEDOP-$(MWCNT)SO_3^-$ films recorded over a scanned area of 1 μm × 1 μm. Corresponding cross-sectional profiles are shown in the insets of the images. Resultant current-voltage curves of (c) PEDOP-$CF_3SO_3^-$, (f) PEDOP-$(C_{12}H_{25})OSO_3^-$ and (i) PEDOP-$(MWCNT)SO_3^-$ films. Each curve is averaged over 15 I-V curves recorded at 15 spots on each current image shown in b,e and h. Top insets of (f) and (i) are the corresponding blown-up views of I-V plots, to extract regimes corresponding to linear dependence. Bottom inset of (f) is a log I *versus* $V^{-1/4}$ plot and bottom inset of (i) is a log j *versus* log V plot, both obtained from the corresponding I-V curves.

The PEDOP-(MWCNT)SO_3^- film shows Mott-Gurney dependence (bottom inset of Figure 4.4i) and equation (3) can be rewritten as:

$$\text{Log } j = \log (9/8\ \varepsilon_r\varepsilon_o\mu_{eff}/L^3) + 2 \log V \quad (5)$$

The y-axis intercept of the inset of Figure 4.4i can equated to the first part of equation (5) and μ_{eff} which is the carrier mobility can be determined.

However, in the equation (5), $\varepsilon_r$is unknown, and it was determined by recording an impedance spectrum of the same film using two gold coated spring contacts by applying an ac amplitude of 10 mV over a frequency range of 1 MHz to 0.01 Hz. No dc bias was applied to the assembly, during the measurement. By equating equations (6) and (7), $\varepsilon_r$was determined.

At the maximum of the semi-circle in the Z" *versus* Z' response,

$$C = 1/2\pi fZ' \quad (6)$$

where C is the capacitance of the film, f is the frequency and Z' the real component of impedance. Capacitance is also given by:

$$C = A\varepsilon_r\varepsilon_o / d \quad (7)$$

where A and d are the surface area and thickness of the film respectively.

$$\varepsilon_r = d/A2\pi fZ'\varepsilon_o \quad (8)$$

By substituting equation (8) in equation (5),

$$\log(9/16A\pi fZ'L^2) + \log(\mu_{eff}) = \text{y-axis intercept (log j)} \quad (9)$$

The *Z'* value was $1.14 \times 10^{-6}\Omega$, frequency at the maximum of the semi-circle was 4738 Hz, thickness of the film (L or d) was 620×10^{-7} cm, and by solving equation (9) we deduced the charge carrier mobility to be 1.6×10^{-8} cm^2 V^{-1} s^{-1}.

The dI/dV curves were generated from the I-V profiles recorded from current maps each with a scanned area of 1 μm × 1 μm (shown previously in Figure 4.4). The dI/dV curves were obtained from the I-V scans averaged over only the bright spots in each film (Figure 4.5a, b and c): for PEDOP-$CF_3SO_3^-$, PEDOP-$(C_{12}H_{25})OSO_3^-$ and PEDOP-$(MWCNT)SO_3^-$ films. Similarly, dI/dV plots were obtained by averaging the I-V scans recorded on the dark regions of the films (Figure 4.5a', b' and c'). The band gaps were estimated from the quasi-flat regions situated between the spikes in the dI/dV curves. For the PEDOP-$CF_3SO_3^-$ film, in the highly conducting domains (bright spots), the average band gap was ~3.8 eV, while for the PEDOP-$(C_{12}H_{25})OSO_3^-$ film, it was 0.81 eV and in case of the PEDOP-$(MWCNT)SO_3^-$ film, it was only 0.19 eV. Oxidized PEDOP doped by perchlorate anions, has a band gap of 2.05 eV [17]. Here, the much lower value can be explained by the fact that this in all likelihood represents the difference in the positions of the intra-gap states which, are introduced in the gap due to the polarons or bipolarons. We could not estimate a band gap from the dI/dV curve for the dark or less conducting regions in the PEDOP-$CF_3SO_3^-$ film, probably due to it's large magnitude but for the PEDOP-$(C_{12}H_{25})OSO_3^-$ and PEDOP-$(MWCNT)SO_3^-$ films, the band gaps determined from the flat regions are 2.31 and 0.58 eV respectively. It is noteworthy that the difference in the E_g values ongoing from the sole bright (highly conducting) to only dark (least conducting) domains in the PEDOP-$(MWCNT)SO_3^-$ film is not large (only from 0.19 to 0.58 eV). The narrow range of band gap corroborates that current or doping distribution in this film is homogeneous and is in

stark contrast to the triflate or dodecyl sulfate doped films wherein a large difference in E_g was observed (2.31-0.81 eV in PEDOP-$(C_{12}H_{25})OSO_3^-$). The PEDOP films doped by triflate or dodecyl sulfate can be visualized to be composed of conducting islands surrounded by a sea of insulating regions, while the PEDOP film doped by sulfonated MWCNTs predominantly comprises of interconnected conducting regions with high localized nanoscale electronic conductivity, juxtaposed with few insulating regimes. The average band gaps determined from the dI/dV curves recorded at both bright and dark spots were 3.65, 0.87 and 0.18 eV for the PEDOP-$CF_3SO_3^-$, PEDOP-$(C_{12}H_{25})OSO_3^-$ and PEDOP-$(MWCNT)SO_3^-$ films respectively and these curves are shown in Figure 4.6.

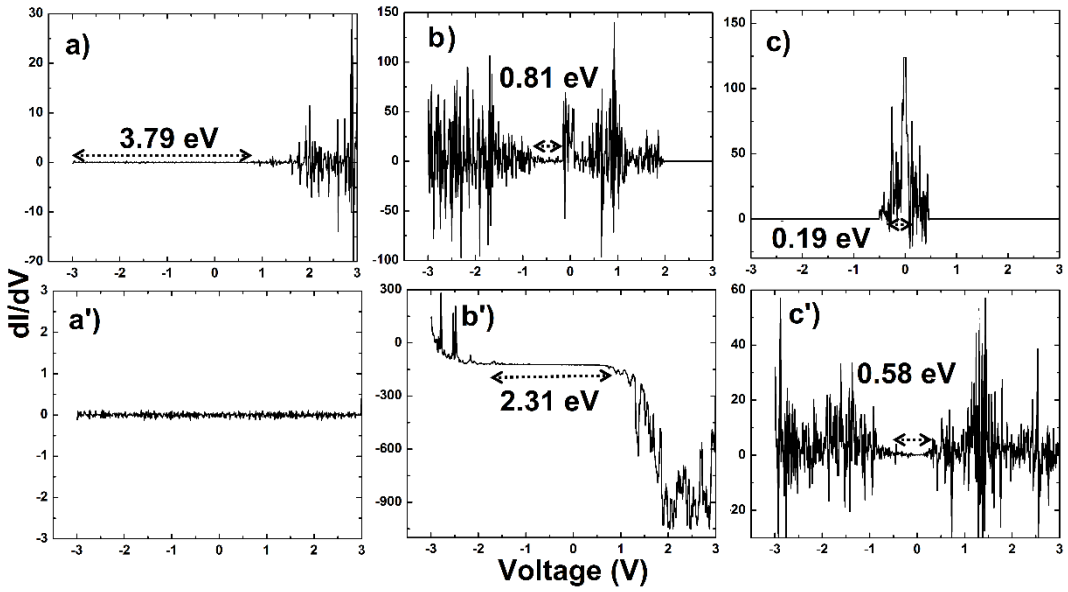

Figure 4.5: dI/dV *versus* applied bias (V) plots of (a,a') PEDOP-$CF_3SO_3^-$, (b,b') PEDOP-$(C_{12}H_{25})OSO_3^-$ and (c,c') PEDOP-$(MWCNT)SO_3^-$ films derived from the point contact I-V curves averaged over only bright and only dark spots of the current images shown in Figure 4.4.

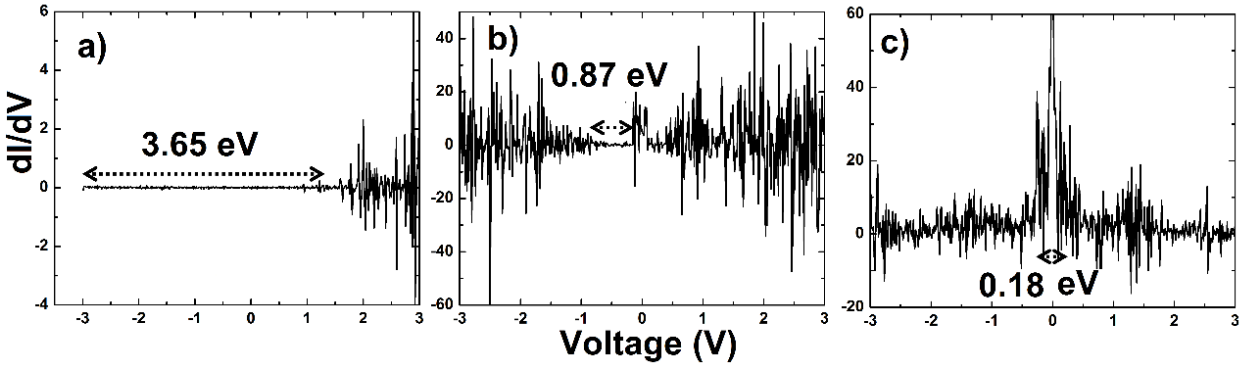

Figure 4.6: dI/dV *versus* applied bias (V) plots of (a) PEDOP-$CF_3SO_3^-$, (b) PEDOP-$(C_{12}H_{25})OSO_3^-$ and (c) PEDOP-(MWCNT)SO_3^- films derived from the point contact I-V curves averaged over 15 spots (inclusive of both bright and dark ones) in the current images shown in Figure 4.4**.**

4.3.4 Kelvin probe force microscopy

The Kelvin probe force microscope (KPFM) measures the contact potential difference between the conducting tip and the sample surface. The Fermi level of the tip aligns with that of the sample, upon electron tunneling between the sample and the tip. Both sample and tip are charged and contact potential difference (V_{CPD}) develops between the two and is given by equation (11).

$$V_{CPD} = (\Phi_{tip} - \Phi_{sample}) / e^- \quad (11)$$

Φ_{tip} is the work function of the conducting Co/Cr coated Si cantilever and it is about 4.9 eV and Φ_{sample} is the work function of the sample. In KPFM, the topography of the film surface is measured in tapping mode and the surface potential variation is measured with conducting tip simultaneously (Figure 4.8). The tip was held at ~50 nm above the film surface, and it is charged due to the applied ac potential. The sample surface is also charged since it is in the vicinity of the charged tip. The topography and the corresponding surface potential maps of PEDOP-$CF_3SO_3^-$, PEDOP-$(C_{12}H_{25})OSO_3^-$ and PEDOP-(MWCNT)SO_3^- films are shown in Figure 4.7. The cross-

sectional profiles and the potential height profiles were also measured along the mid-section of each image. The surface potentials of PEDOP-$CF_3SO_3^-$, PEDOP-$(C_{12}H_{25})OSO_3^-$ and PEDOP-(MWCNT)SO_3^- films are 110, 150 and 160 mV respectively which, were measured under exactly similar experimental conditions. The work functions determined from equation (11) are 4.89, 4.75 and 4.74 eV for PEDOP-$CF_3SO_3^-$, PEDOP-$(C_{12}H_{25})OSO_3^-$ and PEDOP-(MWCNT)SO_3^- films respectively. The bright regions in the surface potential maps correspond to higher doping levels, and the dark contours are characteristic of lesser dopant concentration [18,19]. Here, the surface potential map of the PEDOP-(MWCNT)SO_3^- film shows elongated shapes co-existing with globular grains and the bright contours are more dominant than the dark ones, indicating that the doping level is high which, implies that the sulfonated MWCNTs are uniformly distributed in the PEDOP film. The topography is also consistent with the surface potential variations. The change in surface potential, is mainly attributed to the variation in dopant distribution. As thickness of a given film increases during the course of electropolymerization, the dopant ions (be it triflate or dodecyl sulfate or sulfonated MWCNTs) tend to assemble onto the protuberant globules, and therefore the regions of high electrical current or potential are predominantly the grain tops. The work function of each film, can be approximated to its conduction band edge (E_{CB}). The band gaps (E_g) for bright/more conducting and dark/less conducting regions of a given film were estimated from the dI/dV curves (Figure 4.5), which yielded the VB positions (E_{VB}).

$$E_{VB} = E_g - E_{CB} \tag{12}$$

The energy band diagram illustrating the positions of CB, VB and band gap, in the highly conducting and less conducting domains of each film (PEDOP-$CF_3SO_3^-$, PEDOP-$(C_{12}H_{25})OSO_3^-$ and PEDOP-(MWCNT)SO_3^- films) with reference to the vacuum level fixed at 0 eV is shown in

Figure 4.8. The ease of reduction/oxidation is maximum for the PEDOP-(MWCNT)SO_3^- film and least for the PEDOP-$CF_3SO_3^-$ film, as in the PEDOP film doped by sulfonated MWCNTs, lesser energy is required to remove a charge carrier from the uppermost level of the potential well. In the bright regions, be it any film under study, the band gap is lower as compared to the corresponding gap in the dark domain.

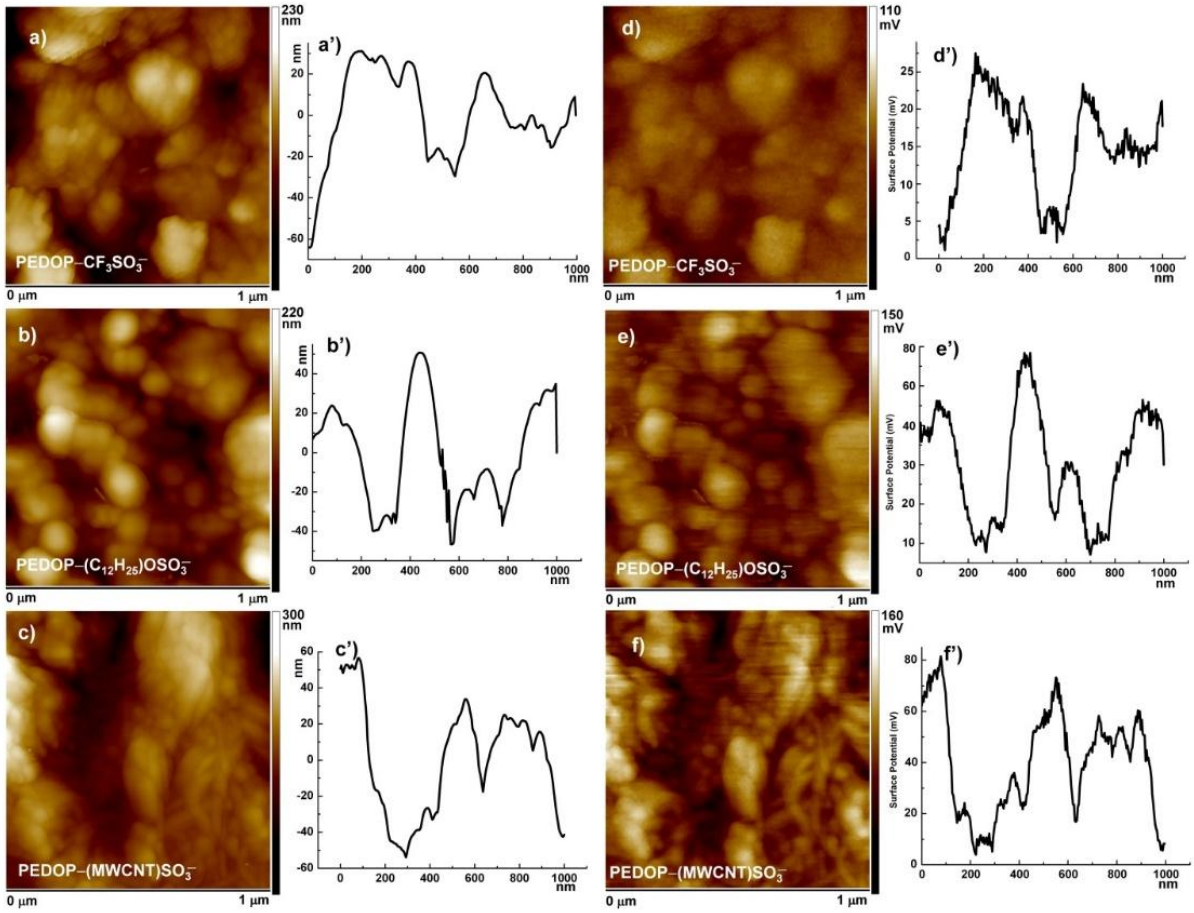

Figure 4.7: Topography and surface potential maps of (a,d) PEDOP-$CF_3SO_3^-$, (b,e) PEDOP-$(C_{12}H_{25})OSO_3^-$ and (c,f) PEDOP-(MWCNT)SO_3^- films recorded over a scanned area of 1 μm × 1 μm. Cross-sectional profiles of (a',d') PEDOP-$CF_3SO_3^-$, (b',e') PEDOP-$(C_{12}H_{25})OSO_3^-$ and (c',f') PEDOP-(MWCNT)SO_3^- films.

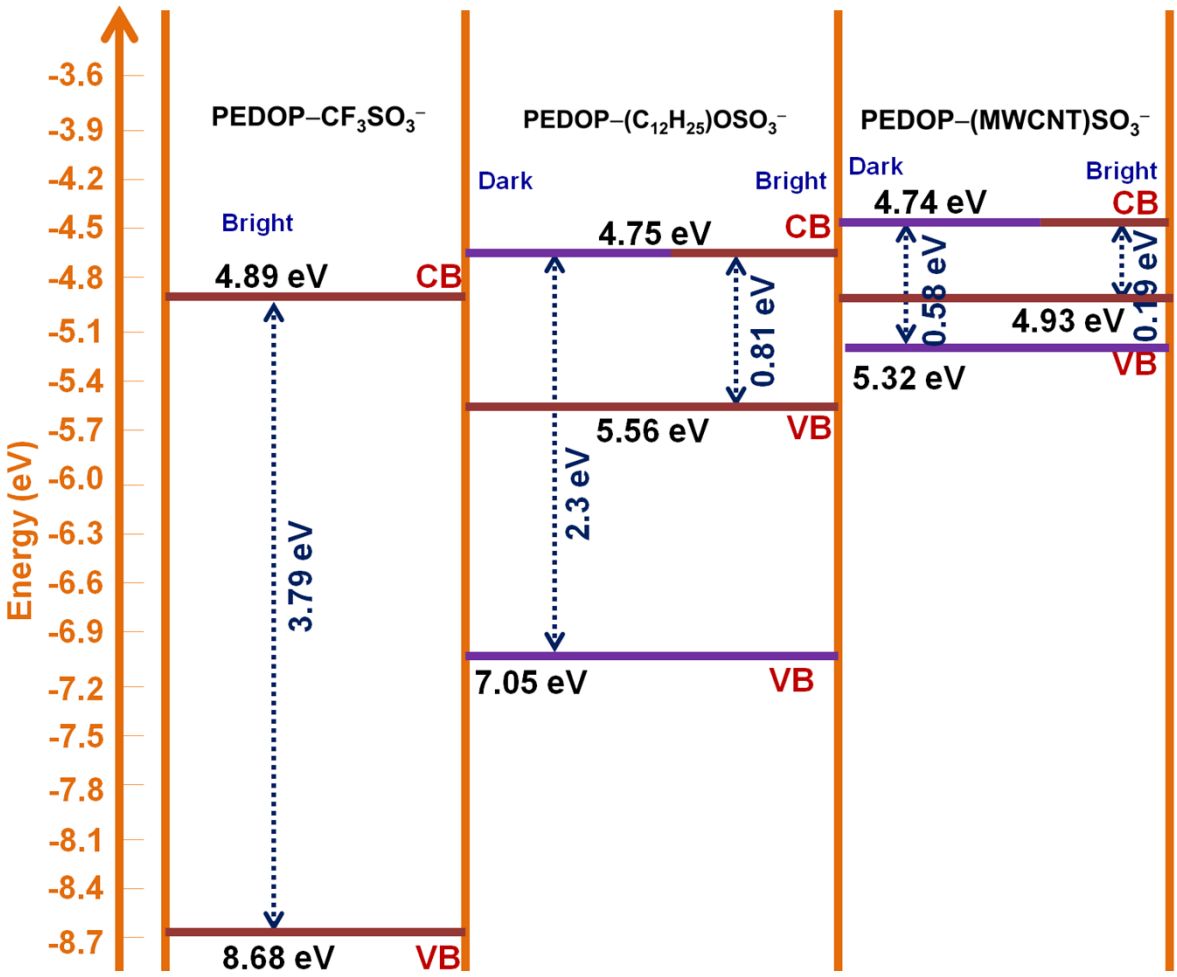

Figure 4.8: Energy band diagram of PEDOP-$CF_3SO_3^-$, PEDOP-$(C_{12}H_{25})OSO_3^-$ and PEDOP-(MWCNT)SO_3^- films.

4.3.5 Cyclic voltammetry

The redox activity of PEDOP-$CF_3SO_3^-$,PEDOP-$(C_{12}H_{25})OSO_3^-$ and PEDOP-(MWCNT)SO_3^- films were studied by cyclic voltammetry by the sweeping the potential between –1 V and +1 V at scan rates of 5 and 10 mV s^{-1} in 0.5 M $LiCF_3SO_3$ in PC. Irrespective of scan rate, the area under the voltammogram for the films, displayed in Figure 4.9a and b, was found to decrease in the following order: PEDOP-(MWCNT)SO_3^-> PEDOP-$(C_{12}H_{25})OSO_3^-$> PEDOP-$CF_3SO_3^-$. For the PEDOP-(MWCNT)SO_3^- film (Figure 4.9a), a small shoulder in the anodic branch was

observed at +0.7 V (j = 0.09 mA cm^{-2}), attributable to the oxidation of the neutral polymer to yield oxidized PEDOP. In the reverse sweep, a broad reduction peak is observed at –0.3 V (j = 0.08 mA cm^{-2}) corresponding to expulsion of triflate ions from the polymer. This was also preceded by a pre-peak at ~0.0 V which is possibly due to the release of cations from the polymer chain. A similar peak has previously been observed by Ahonen et al. [20] in an *in-situ* study of electrochemical doping/de-doping of PEDOT. For the remaining two films (Figure 4.9a), only broad cathodic peaks at ~ –0.2 and –0.46 V were observed for the $CF_3SO_3^-$ and $C_{12}H_{25})OSO_3^-$ doped films. The response however, acquires a highly capacitive character, at higher scan rates, especially for the PEDOP-(MWCNT)SO_3^- film and this can be judged by comparing the CV plots obtained at 5 mV s^{-1} (Figure 4.9b). The specific electrode capacitance of PEDOT films has previously been shown to increase by manifold times, when doped with carboxylate functionalized CNTs [21]. Authors propounded that the conducting polymer forms a uniform coating on the surface of MWCNTs and assist in forming a three dimensional network of the polymer and CNTs, when they are used as the charge balancing dopants during electro-synthesis. In addition, the porosity of the composite provides pathways for the propagation of ions and solvent molecules through the bulk of the films, resulting in improved electrochemical properties. The structures that prevail in the three films have been shown through a cartoon representation in Figure 4.9c. The charge balancing ions i.e., the triflate ions, dodecyl sulfate ions and the benzyl sulfonate functionalized MWCNTs (C_n-$C_6H_5SO_3^-$) are flanked to the PEDOP chains, at the molecular level, vis-à-vis electrostatic repulsions. Since the method of functionalization relied on exposing the MWCNTs to sulfuric acid, the possibility of a few carboxylate groups attaching to the carbon nanotubes cannot be ruled out. Therefore, we have also shown a few –COOH groups attached to the MWCNTs. CV plots acquire a highly

capacitive character for all the three films at high scan rates (especially at 100 mV s^{-1}), and these plots are shown in Figure 4.10.

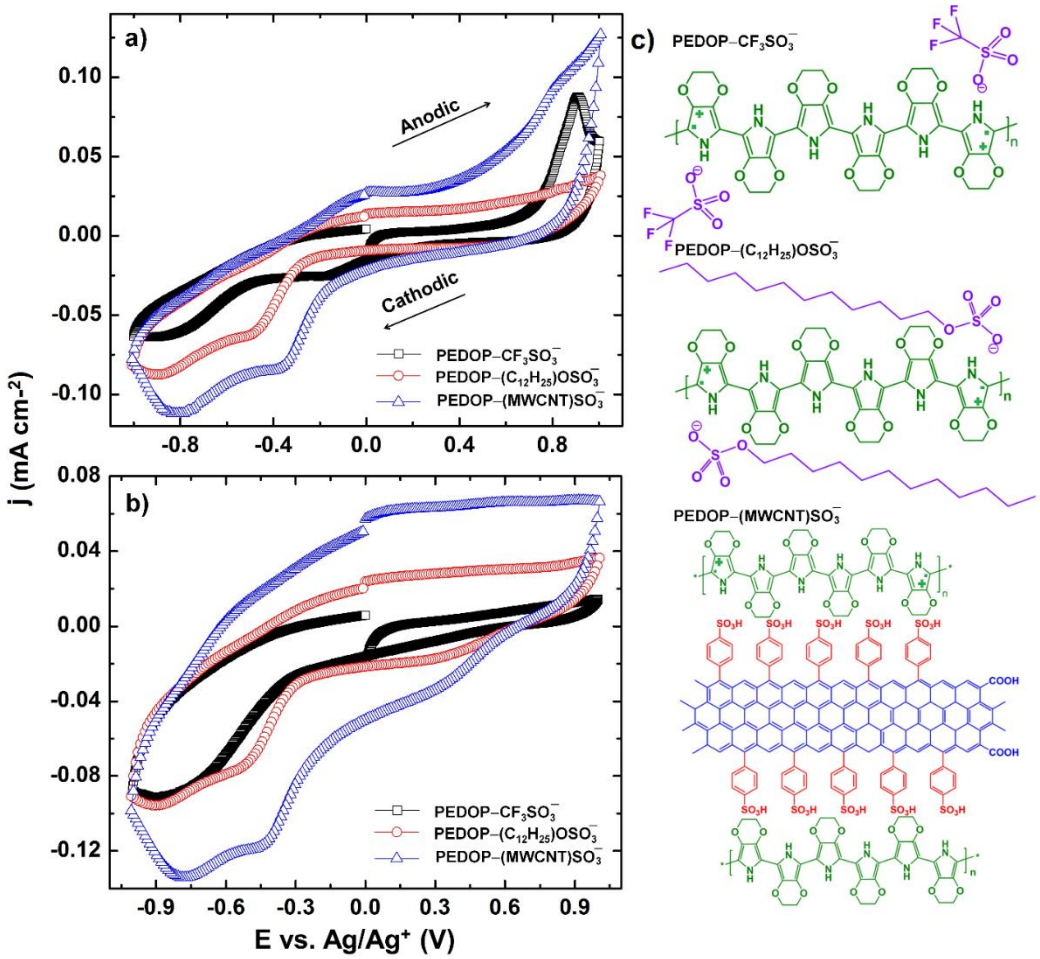

Figure 4.9: Cyclic voltammograms of PEDOP-$CF_3SO_3^-$ (□), PEDOP-$(C_{12}H_{25})OSO_3^-$ (○) and PEDOP-(MWCNT)SO_3^- (△) films recorded in a 0.5 M $LiCF_3SO_3$/PC electrolyte at scan speeds of (a) 5 mV s^{-1} and (b) 10 mV s^{-1}. (c) Schematic representation of the structures that prevail in the PEDOP-$CF_3SO_3^-$, PEDOP-$(C_{12}H_{25})OSO_3^-$ and PEDOP-(MWCNT)SO_3^- films.

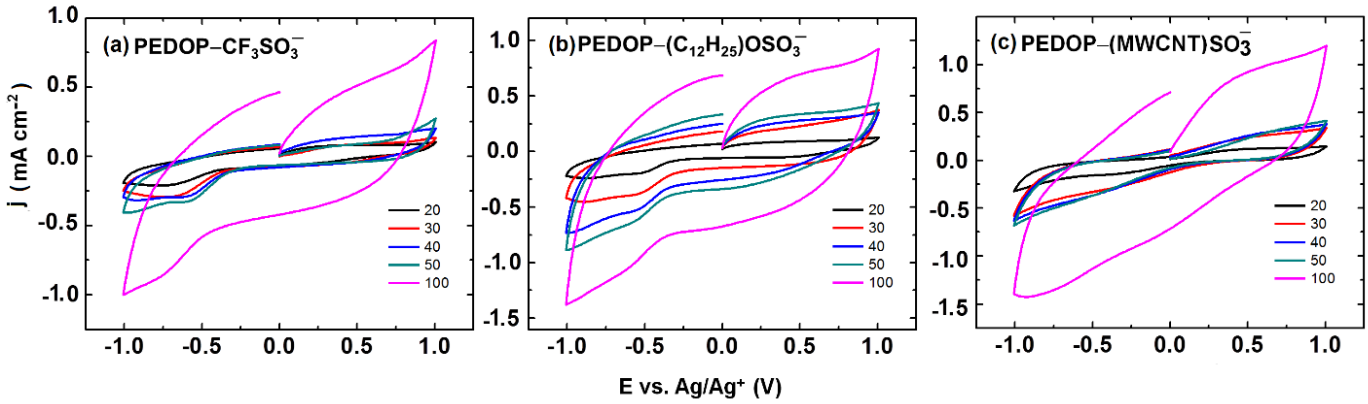

Figure 4.10: Cyclic voltammograms of (a) PEDOP-$CF_3SO_3^-$, (b) PEDOP-$(C_{12}H_{25})OSO_3^-$ and (c) PEDOP-(MWCNT)SO_3^- films recorded in a 0.5 M $LiCF_3SO_3$/PC electrolyte at scan speeds of 20, 30 40, 50 and 100 mV s^{-1}.

4.3.6. Spectroelectrochemistry of PEDOP films

Figure 4.11shows the *in-situ* absorbance plots of PEDOP-$CF_3SO_3^-$, PEDOP-$(C_{12}H_{25})OSO_3^-$, and PEDOP-(MWCNT)SO_3^- films recorded as a function of wavelength under different values of applied bias in the range of +0.5 V to –3.0 V. The reference voltage was fixed at +0.5 V for determining ΔOD (change in absorbance) values. The change in absorbance was defined as: ΔOD (λ_{max}) = OD (E = +0.5 V, λ_{max}) – OD (–x V, x = –0.5 to –3.0 V, λ_{max}). The bipolaronic transitions in oxidized PEDOP film produce a broad absorption in the NIR region and the intensity of this absorption decreases with increasing reduction potential. This trend is typical of PEDOP, and is independent of the counter ion, as the bipolaronic absorption (for PEDOP in the radical cation state) gives way to the π-π* transitions (characteristic of neutral reduced PEDOP). The λ_{max} positions for π-π* absorption are observed at 490 nm, 480 nm and 510 nm respectively for PEDOP-$CF_3SO_3^-$, PEDOP-$(C_{12}H_{25})OSO_3^-$ and PEDOP-(MWCNT)SO_3^- films. In the visible region ΔOD (λ_{max}) are 0.079, 0.12 and 0.54 for PEDOP-$(C_{12}H_{25})OSO_3^-$, PEDOP-$CF_3SO_3^-$ and PEDOP-(MWCNT)SO_3^- films respectively. The ability of PEDOP films doped with sulfonate

functionalized MWCNTs to show a larger optical modulation, for the same values of applied bias, clearly shows that the number of electrochemically active sites in the bulk of the polymer-CNT film exceeds that in the films doped by triflate or dodecyl sulfate. Further, since the polymer is in direct contact with MWCNTs, electron transfer and transport between the polymer and CNTs is facile as CNTs have high electronic conductivity. In the other two films, dodecyl sulfate and triflate groups are insulating and therefore, electron movement therein is not as facile as that realized in the PEDOP-(MWCNT)SO_3^- film. These two factors combinedly manifest in a higher electrochromic contrast and this advantage also extends to the NIR region. For a λ_{max} between 900-1000 nm, ΔOD values for PEDOP-($C_{12}H_{25}$)OSO_3^-, PEDOP-$CF_3SO_3^-$ and PEDOP-(MWCNT)SO_3^- films are 0.24, 0.29 and 0.55 respectively. The digital photographs of the PEDOP-$CF_3SO_3^-$and PEDOP-(MWCNT)SO_3^- films in reduced (red) and oxidized (pale blue) states are also shown in Figure 4.11. The higher contrast offered by the PEDOP-(MWCNT)SO_3^- film is evident for a deeper hue is acquired by this film in the neutral state in comparison to the triflate doped PEDOP film.

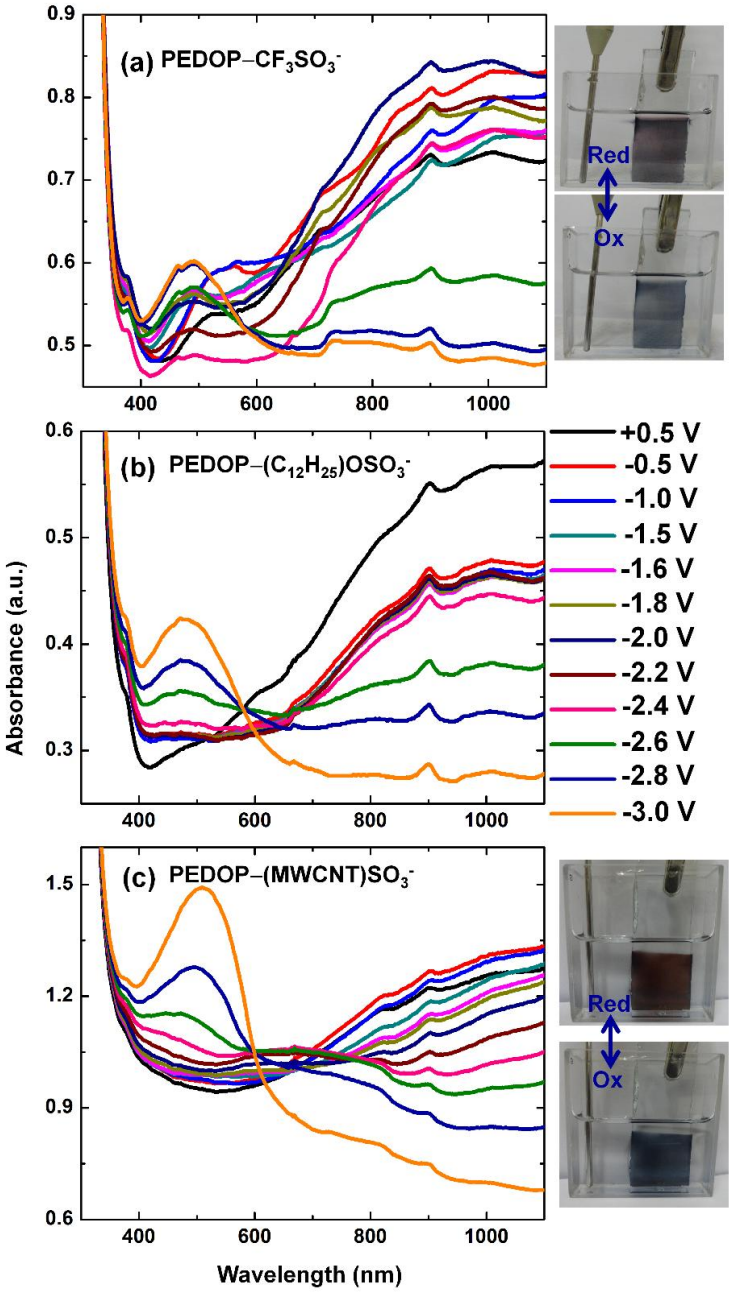

Figure 4.11: Absorption spectra of (a) PEDOP-$CF_3SO_3^-$, (b) PEDOP-$(C_{12}H_{25})OSO_3^-$ and (c) PEDOP-$(MWCNT)SO_3^-$ films recorded under different reduction potentials of –0.5 to –3.0 V and under an oxidation potential of +0.5 V in a 0.5 M $LiCF_3SO_3$/PC liquid electrolyte; the optical density response under +0.5 V has been taken as reference for determination of ΔOD values. Digital photographs of PEDOP-$CF_3SO_3^-$ and PEDOP-$(MWCNT)SO_3^-$ films in neutral and oxidized states have been shown in the adjoining panels.

Tramnsittance*versus* time transients at three monochromatic wavelengths ($\lambda = \lambda_{max}$, 550 nm and 1100 nm) for the PEDOP-$CF_3SO_3^-$, PEDOP-$(C_{12}H_{25})OSO_3^-$ and PEDOP-(MWCNT)SO_3^- films, when the potential of the film was switched from +3.0 V and –3.0 V are shown in Figure 4.12. The step time was fixed at 5 s. A wavelength of 550 nm was chosen, as it is the wavelength at which human eye is most responsive, and a λ = 1100 nm was also used, to determine the color-bleach kinetics in the NIR region. For an electrochromic layer to be employable in smart windows, the ability of the material to modulate NIR radiation is pertinent to this application. Coloration times (t_c, time to obtain a 10% to 90% increment in absorbance) and bleaching times (t_b, time to obtain a drop from 90% to 10% of total absorbance) were deduced for the three films. At λ_{max}, the color and bleach times for PEDOP-$CF_3SO_3^-$ were 2.14 and 1.37 s, for the PEDOP-$(C_{12}H_{25})OSO_3^-$ film, t_c and t_b were 3.26 and 3.81 s and for the PEDOP-(MWCNT)SO_3^- film: t_c and t_b were 5.18 and 1.14 s. Bleaching is faster than coloration for the PEDOP-(MWCNT)SO_3^- film. The optical response at λ = 1100 nm is discontinuous in the coloration cycle for both PEDOP-$(C_{12}H_{25})OSO_3^-$ and PEDOP-(MWCNT)SO_3^- films (Figure 4.12f and i). It is probably due to a two-step reduction process, the first one involving anion deintercalation and the second corresponding to cation insertion. Similar multi-step redox phenomena have been observed for PEDOT films in the past [22].

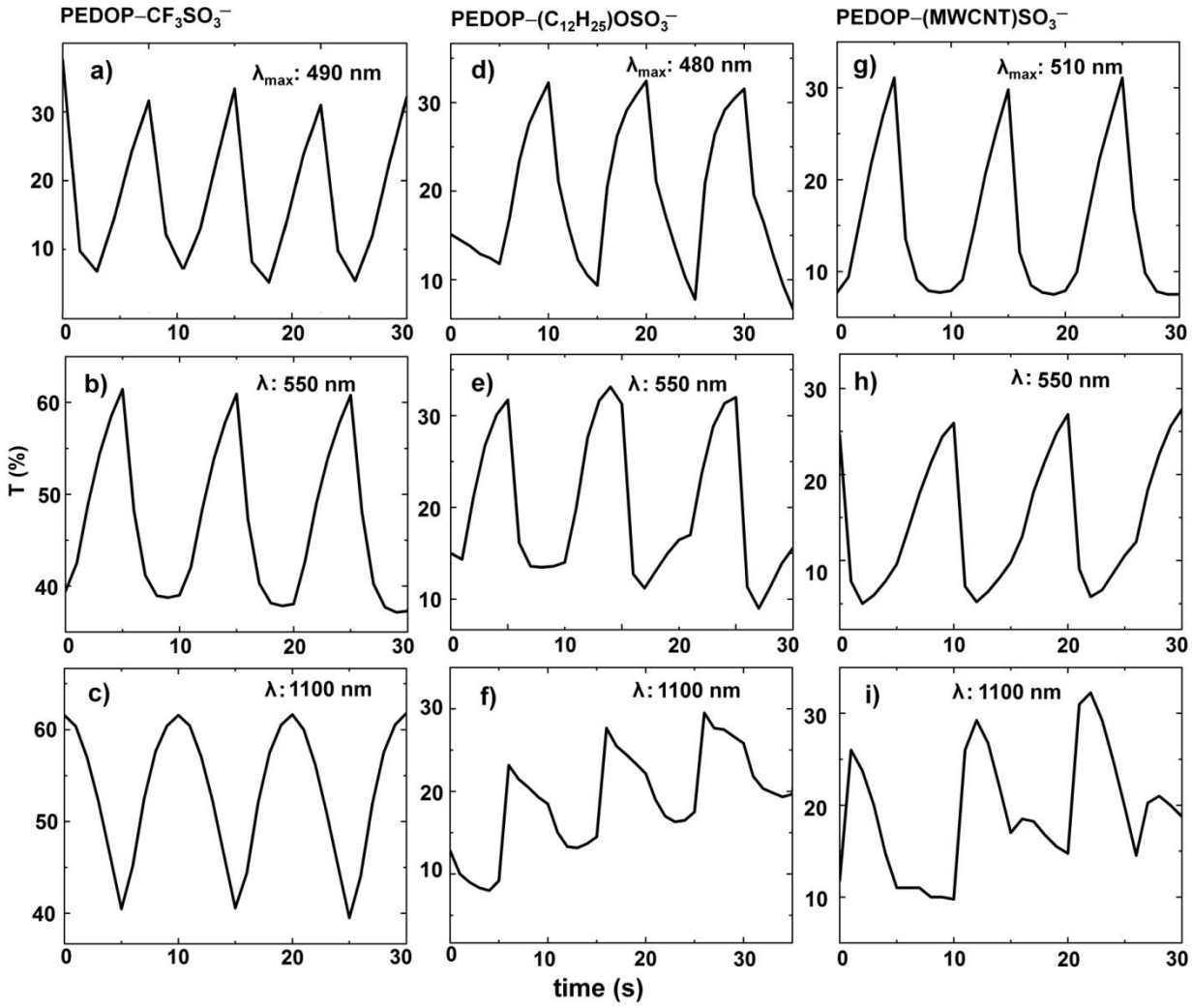

Figure 4.12: Variation of transmision as a function of time at monochromatic wavelengths for (a,b,c) PEDOP-$CF_3SO_3^-$, (d,e,f) PEDOP-$(C_{12}H_{25})OSO_3^-$ and (g,h,i) PEDOP-(MWCNT)SO_3^- films in a 0.5 M $LiCF_3SO_3$/PC electrolyte under a square wave dc potential of ±3.0 V at a frequency of 0.10 Hz.

4.4 Summary

The effect of counter ion in electropolymerized PEDOP films has been examined by simultaneously analyzing the topography and local current inhomogeneity and work function in the film. While PEDOP films doped by triflate and dodecyl sulfate ions can be visualized to be composed of segregated localized conducting domains embedded in a largely non-conductive

matrix, the PEDOP-(MWCNT)SO_3^- film is characterized by interlinked conducting regions with very few insulating domains juxtaposed within. An increase in the vertical electronic conductivity, greater by four orders of magnitude as compared to the PEDOP-$CF_3SO_3^-$ film, and a lower band gap achieved in the PEDOP-(MWCNT)SO_3^- film coupled with the lower work function of this film, are conducive for amplifying electrochromic response. By combining the local work function, obtained by KPFM and the superior current carrying capacity of the PEDOP-(MWCNT)SO_3^- film, the percolating pathways available for electron or ion transport, in the form of the concentric carbon nanotubes, clearly confirm how the dopant ion type and its distribution in the matrix of the CP, can by interaction with the polymer chains at the molecular level, alter the electronic structure of the CP. The effect of increased nanoscale surface potential, and the network of high current domains in the PEDOP-(MWCNT)SO_3^- film was reflected in the improved electrochromic contrast and kinetics.

References

[1] D. H. Han, S. M. Park, J. Phys. Chem. B 108 (2004) 13921–13927.
[2] H. J. Lee, S. M. Park, J. Phys. Chem. B 108 (2004)1590–1595.
[3] H. J. Lee, S. M. Park, J. Phys. Chem. B 108 (2004)16365–16371.
[4] D. H. Han, J. W. Kim, S. M. Park, J. Phys. Chem. B 110 (2006)14874–14880.
[5] S. C. L. Pingree, A. B. MacLeod, S. D. Ginger, J. Phys. Chem. C 112 (2008) 7922–7927.
[6] H. J. Lee, J. Lee, S. M. Park, J. Phys. Chem. B 114 (2010)2660–2666.
[7] W. Melitz, J. Shen, C. A. Kummel, S. Lee, Surf. Sci. Rev. 66 (2011) 1–27.
[8] A. Liscio, V. Palermo, P. Samor, Acc. Chem. Res. 43 (2010)541–550.
[9] H. Hoppe, T. Glatzel, M. Niggemann, A. Hinsch, M. Ch. L. Steriner, N. S. Sariciftci, Nano Lett. 5 (2005) 269–274.
[10] A. O. Semenikhin, L. Jiang, K. Hashimoto, A. Fujishima, Synthetic Met. 110 (2000) 115–122.
[11] H. Randriamahazaka and V. Noel, C. Chevrot, J. Electroanal. Chem.472 (1999) 103–111.
[12] S. Garreau, G. Louarn, J. P. Buisson, G. Froyer, S. Lefant, Macromolecules, 32 (1999) 6807–6812.
[13] S. A. Currana, A. V. Ellis, A. Vijayaraghavan, P. M. Ajayan, J. Chem. Phys. 120 (2004) 4886–4889.
[14] X. Zhao, Y. Ando, L. C. Qin, H. Kataura, Y. Maniwa, R. Saito, Chem. Phys. Lett. 361 (2002) 169–174.
[15]G. Sonmez, P. Schottland, J. R. Reynolds, Synth. Met. 155 (2005) 130–137.

[16] C. L. Gaupp, K. Zong, P. Schottland, B. C. Thompson, C. A. Thomas, J. R. Reynolds, Macromolecules 33 (2000)1132–1133.
[17] O. G. Reid, K. Munechika, D. S. Ginger, Nano Lett. 8 (2008) 1602–1609.
[18] K. Fesser, A. R. Bishop, D. K. Campbell, Phys. Rev. B 27 (1983) 4804–4825.
[19] H. T. Nicolai, G. A. H. Wetselaer, M. Kuik, A. J. Kronemeijer, B. de. Boer, P. W. M. Blorn, App. Phys. Lett. 19 (2010) 172107(1–3).
[20] H. J. Ahonen, J. Lukkari, J. Kankare, Macromolecules 33 (2000) 6787– 6793.
[21] C. Peng, J. Jin, G. Z. Chen, Electrochim. Acta 53 (2007) 525–537.
[22] M. Deepa, S. Bhandari, R. Kant, Electrochim. Acta 54 (2009) 1292–1303.

Chapter 5

A PEDOP-Poly(5-cyano indole) (PCIND) electrochromic device with a free standing ionic liquid based polymeric electrolyte

5.1 Introduction

In this chapter, the work on PEDOP was further extended by fabricating an all-conducting polymer based electrochromic device with Poly(5-cyano indole) or PCIND as the anodic electrochrome and PEDOP as the cathodic colorant. We used PCIND due to the following reasons: (a) due to the presence electron donating group (cyano), during electropolymerization the monomer oxidizes at lower oxidation potentials, (b) it is low band gap CP, (c) PCIND-PEDOP device is a unique combination for electrochromic device application. Both films were prepared by oxidative electropolymerization in a hydrophobic fluoroalkylphosphate (FAP) ion based ionic liquid: trihexyl(tetradecyl)phosphonium tris(pentafluoroethyl)trifluorophosphate. The reasons for preferring an ILs over a conventional salt solution as a medium for electropolymerization as well as for electrolyte synthesis are high ionic conductivity (> 10^{-3} S cm^{-1} at room temperature), large electrochemical window (>3 V) over which neither the electrolyte is oxidized or reduced), low volatility and high thermal stability (> 300 ^{o}C). Most importantly, the hydrophobic nature of the ILs employed herein, enabled the preparation of the films and electrochromic devices in air under ambient conditions without the use of any glove box or inert atmosphere. This is also supported in a previous pioneering report by Lu et al., wherein, enhanced cyclability and other performance attributes were realized for CPs like poly(aniline) prepared and generated in ILs [1]. Furthermore, since this IL contains the FAP ion; it offers an impressive electrochemical potential span of ~6 V and has a very low vapor pressure of 1 Pa [2], thus minimizing the susceptibility of PEDOP and PCIND films with FAP

counterions synthesized herein, towards electrochemical degradation. We followed the electrochemistry and electrochromism of PCIND and PEDOP films and devices prepared thereof using a self-supporting film of an IL based gel polymeric electrolyte with a large ionic conductivity, good thermal and electrochemical stability and high optical transparency. The IL being hydrophobic imparts a high hydrolytic stability to the polymer electrolyte, which limits moisture and oxygen uptake from the atmosphere during device operation or shelf storage. The outstanding electrochromic coloring efficiency and contrast shown by the two films were correlated with their nanoscale current carrying capabilities, which were measured by conducting atomic force microscopy. The energetics of the electrochromic device components were visualized by Kelvin probe force microscopy, by mapping localized surface potentials. In the prototype electrochromic devices fabricated herein, the performance attributes of PCIND and PEDOP films combine synergistically to manifest in a reversible bright red to a transmissive blue redox switch, via an intermediate green hue which is superior to that achieved in the individual electrochromes independently.

5.2 Experimental

5.2.1Polymerization of PEDOP and PCIND

Poly(5-cyano indole) and Poly(3,4-ethylenedioxypyrrole) films were prepared by electrochemical deposition on FTO coated glass substrates (2×5 cm^2 dimensions). Two separate monomer solutions of (i) 5-Cyano indole (0.01 M) and (ii) EDOP (0.01 M) were prepared in ACN and $[(C_{32}H_{68})P^+][(C_2F_5)_3PF_3^-]$ (0.01 M), was dissolved as a dopant ion source in each of the deposition baths. The deposition was carried out under potentiostatic conditions in a three electrode configuration with Pt as an auxiliary electrode, Ag/AgCl/KCl as the reference electrode and the FTO/Glass substrate served as the working electrode. A fixed dc potential of +1.5 V was

applied for 500 s to deposit the corresponding PCIND and PEDOP films. While PEDOP films were pale-blue in color, the PCIND films were yellow in color. The films were rinsed rigorously in multiple ACN baths, and dried in open air for a few hours. Polymerization reaction of both the monomers is shown in Scheme 5.1.

(a)

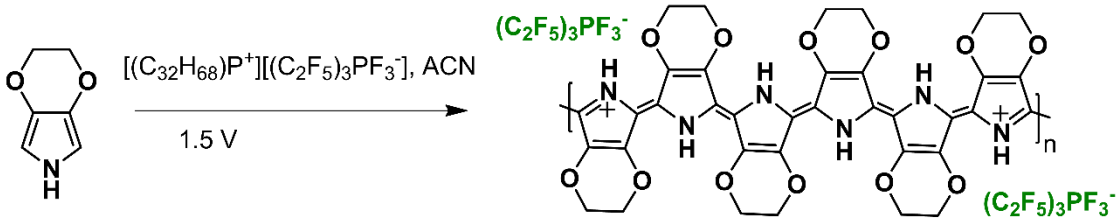

(b)

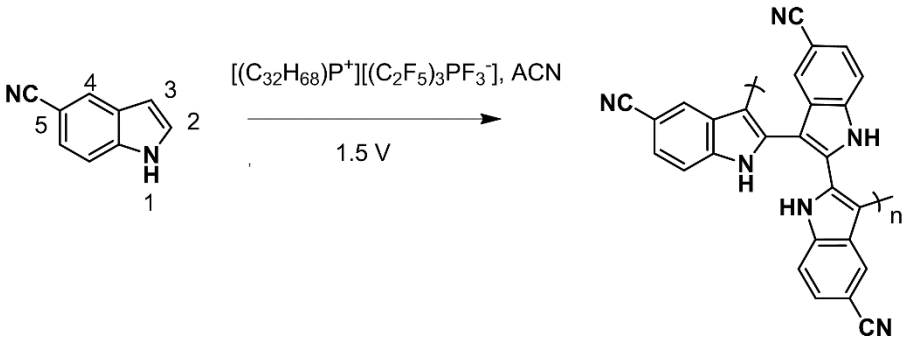

Scheme 5.1: Electropolymerization of PEDOP and PCIND**.**

5.2.2 Electrolyte preparation and device fabrication

For preparing the transparent gel polymeric electrolyte layer, to a clear solution of ([BMPY][$N(CF_3SO_2)_2$] (0.1 M) dissolved in propylene carbonate at room temperature, 15 wt.% of PVdF-HFP was added and the solution was magnetically stirred for 6 h at 70 ^oC. The resulting hot, homogeneous, transparent, viscous solution was immediately transferred into a

clean glass petridish and it was left undisturbed for 24 h. A transparent gel polymeric electrolyte film composed of: [BMPY][$N(CF_3SO_2)_2$]-PVdF-HFP-PC, was obtained which was extracted from the dish onto the electrode surface (PCIND, film facing the electrolyte) using tweezers and scalpel blade. A 3M acrylic tape of 500 μm thickness was employed as the spacer, to accommodate the electrolyte and to prevent the shorting of the two electrochromes. The counter electrode (PEDOP, film surface facing inwards) was applied onto the polymer electrolyte/PCIND configuration, and the whole assembly was sealed using an epoxy sealant. The device configuration was therefore as follows: PCIND-[BMPY][$N(CF_3SO_2)_2$]-PVdF-HFP-PC-PEDOP.

5.3 Results and discussion

5.3.1 Deposition curves

The current-time transient curves corresponding to the formation of PCIND and PEDOP films by oxidative electropolymerization, under potentiostatic conditions (E = +1.5 V) from their precursor solutions containing the monomer (5-cyano indole or 3, 4-ethylenedioxypyrrole) in the FAP ionic liquid: $[(C_{32}H_{68})P^+][(C_2F_5)_3PF_3^-]$ are shown in Figure 5.1. For polymerization of 5-cyano indole (Figure 5.1a), at t = 0, the current shows an abrupt spike, ascribable to the double layer capacitance charging, followed by a gradual decline. This depleting current region corresponds to the formation of monomer cation radicals. The radical cation ($R^{+\bullet}$) has a greater electron pair density at the α-position, and it dimerizes to yield a dication which can further lose two protons to yield the stable dimer, which concurs well with the mechanism proposed for the formation of poly(pyrrole) in a previous report[3,4]. The dimer further oxidizes to yield the oligomer and chain propagation continues to yield the polymer chain (a green colored PCIND deposit on the conducting substrate) with positive charges counter-balanced by the FAP anions.

The anodic polymerization of 3,4-EDOP (Figure 5.1b) involves three successive steps. In Figure 5.1b, the first one (region I) involves diffusion controlled oxidation of the monomer species and the second one (region II), when current reaches a minimum, corresponds to the deposition of the oligomeric clusters on the electrode surface and the final one (region III) is represented by the rise in current and acquisition of a current magnitude that varies monotonically with time. This region is attributed to the nucleation and growth of polymer chains (which are flanked by the charge compensating FAP ions) to yield the blue-black transparent film of PEDOP. Raman and FTIR spectral analysis also confirmed the inclusion of the FAP anion along the back bone of the polymer, in both PCIND and PEDOP films (Figure 5.2 and Table 5.1).

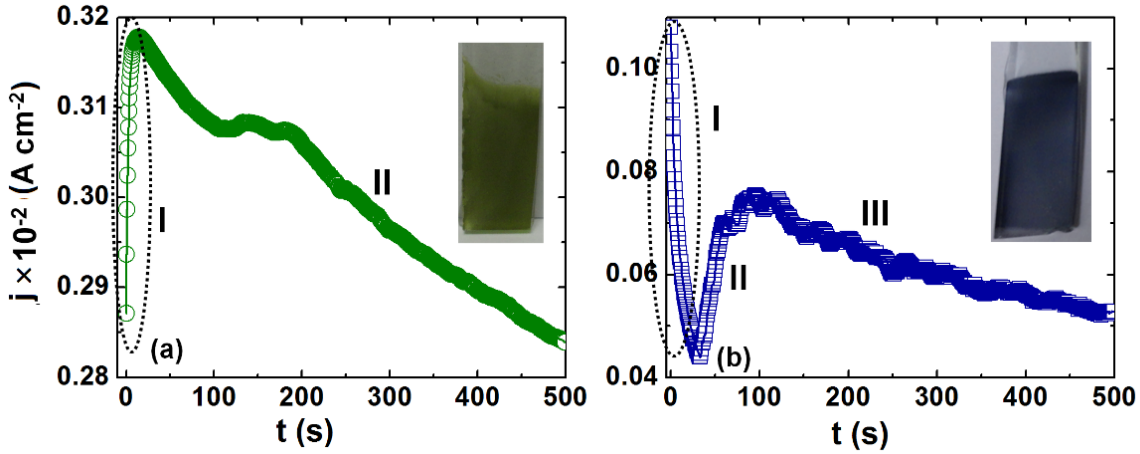

Figure5.1: Current density *versus* time transients recorded for the oxidative electro-synthesis of PCIND and PEDOP films from solutions of (a) 0.01 M 5-CIND and (b) 0.01 M 3,4-EDOP, both in AN and each containing the ionic liquid: 0.1 M ($[(C_{32}H_{68})P^{+}][(C_2F_5)_3PF_3^{-}]$). Digital photographs of the as-fabricated films are shown in the corresponding insets.

5.3.2 FTIR and Raman spectra

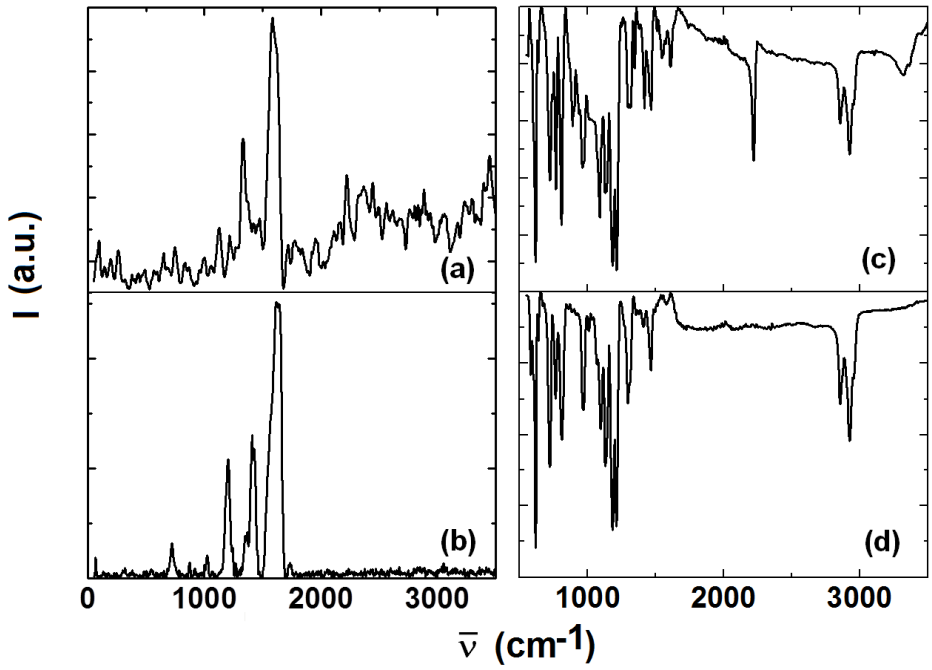

Figure 5.2: Raman spectra of (a) PCIND and (b) PEDOP films and FTIR spectra of (c) PCIND and (d) PEDOP films.

The assignments for various peaks observed for PEDOP and PCIND films are provided in Table 5.1 which confirms the formation of the two films.

Table 5.1:FTIR and Raman band positions and assignments for PCIND and PEDOP films.

PCIND		PEDOP		Description
FTIR (cm^{-1})	Raman (cm^{-1})	FTIR (cm^{-1})	Raman (cm^{-1})	
2926	–	2925	–	ν(C=C–H)
2856	–	2856	–	ν(-C–H)
2220	–	–	–	ν(C≡N)
1609	1650	–	1578	ν(C=C)
1380	1355	1310	1355	$\nu(C_\beta\text{-}C_\beta)$
1212	1230	1210	1290	ν(C-N)
–	–	1066	–	δ(C-O-C)
888	845	862	872	ν(P-F)
766, 722	–	762, 719	–	δ(C-N-C)
–	720	–	720	δ(N-H)

5.3.3. C-AFM and KPFM studies

Figure 5.3 shows the topography and current images recorded simultaneously over scanned areas of 1 μm × 1 μm for as-fabricated films of PCIND and PEDOP. The corresponding cross-section profiles recorded exactly along the middle of the images are shown in Figure 5.4. The topography images of the PCIND and PEDOP films shows the films to have smooth surfaces and this is also reflected in the rms roughness parameters, which are 30 and 17 nm, respectively (Figure 5.3a and b). The currents flowing through the PCIND and PEDOP films were mapped by applying a dc bias to the tip, whilst the tip ran horizontally over the surface (Figure 5.3c and d). The maximum current value registered for the PCIND film was 0.7 nA and for the PEDOP film, it was 24.6 nA. Since the two films have different compositions, the magnitudes of currents cannot be compared. The PCIND film is composed of sparsely distributed high current islands

capable of carrying electronic currents in the range of 0.6-0.7 nA which are embedded in a relatively low current phase. The low current phase can sustain currents of the order of 0.05 to 0.15 nA. The PEDOP film, on the other hand, is constituted by high current domains which are interconnected and have a rather homogeneous span across the film surface. The domains which are capable of sustaining large currents, in either of the two films (PCIND or PEDOP) play a significant role in improving (a) the charge transfer at the CP/electrolyte interface and (b) charge transport through the bulk of the film to/from the current collecting FTO contact. Since both films possess the localized high current regions, charge propagation is expected to be facile in the PCIND-PEDOP device. To determine the nanoscale conductivities of the films, point contact I-V curves were recorded at fifteen equidistant points on each current image, and the average I-V profile for each film is shown (Figure 5.3e and f). The I-V curves for each film can be spilt into two/three regions (marked as I, II and III in the plots), wherein a quasi-linear dependence of current on swept potential was observed. The straight-line fits, within the voltage windows in which the I-V response was almost linear, room temperature electronic conductivities were determined by using equation (1),

$$\sigma_{RT} = (I/V) \times (d/\pi r^2) \qquad (1)$$

In (1) r is the radius of the conducting tip and d is the thickness of the PCIND or PEDOP film. The average electronic conductivities for the PCIND and PEDOP film deduced from the ohmic regimes were 0.1 and 5.4 S cm^{-1} respectively. To the best of our knowledge, while the conductivity of PCIND has not been reported in the past, the conductivity of chemically polymerized film of PEDOP doped by anthraquinone-2-sulfonic acid was found to be 0.3 S cm^{-1}, which indicates the advantage of using an IL as a dopant, as done herein to improve electron conduction [5].

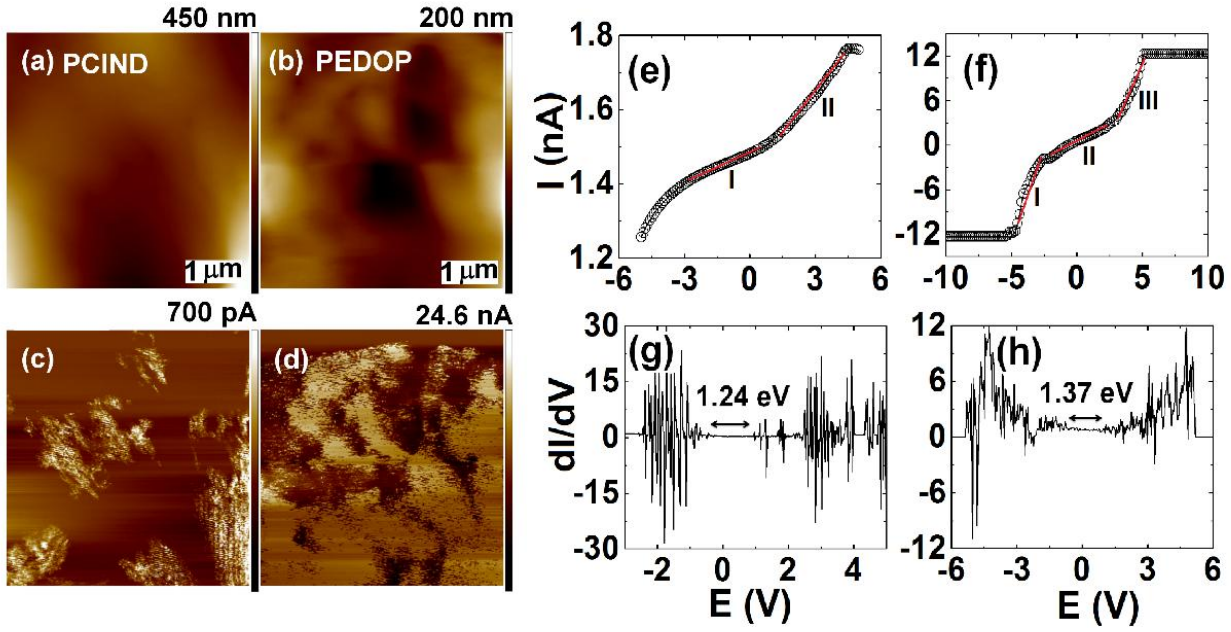

Figure 5.3: Concurrent topography and current images of (a,c) PCIND and (b,d) PEDOP films recorded over scanned areas of 1 μm × 1 μm. Resultant current-voltage curves of (e) PCIND and (f) PEDOPfilms. Each curve is averaged over 15 I-V curves recorded at 15 spots on each current image shown in c and d. dI/dV *versus* applied bias (V) plots of (g) PCIND and (h) PEDOPfilms.

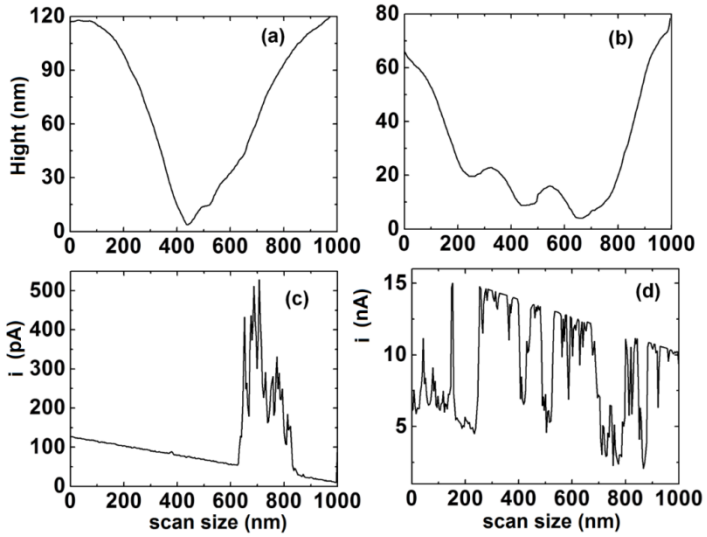

Figure 5.4: Cross-sectional profiles of topography (a,b) and current (c,d) images of PCIND and PEDOP derived from Figure 5.3.

In KPFM an ac bias is applied to a conducting Pt/Ir tip of a known work function, it scans the sample surface and the localized contact potential difference (V_{CPD}) that arises between the conducting tip and the sample surface, is used for generating the surface potential map, as shown in the following equation (2).

$$V_{CPD} = (\Phi_{tip} - \Phi_{sample}) / e^{-} \quad (2)$$

Φ_{tip} is the work function of the conducting Pt/Ir coated Si cantilever and Φ_{sample} is the work function of the sample, which can be approximated to its' Fermi level position. The work function of Pt/Ir tip was first calibrated with highly ordered pyrolytic graphite (HOPG) (Φ_{HOPG} = 4.6 eV) to convert the measured V_{CPD} to absolute surface work function [6]. The absolute surface work function of the sample was calculated with equation (3).

$$\Phi_{sample} = 4.6 \text{ eV} + V_{CPDHOPG} - V_{CPDsample} \quad (3)$$

The topography and the corresponding surface potential maps of PCIND and PEDOPfilms are shown in Figure 5.5. The cross-sectional profiles and the potential height profiles were also measured along the mid-section of each image and these are provided in Figure 5.6. The surface potentials of PCIND and PEDOPfilms are 130 and 30 mV respectively and the corresponding Fermi energy levels, determined from equation (3), are 4.87 and 4.97 eV. The bright regions in the surface potential maps represent higher doping levels, and the dark topological regions indicate lower dopant levels [7]. The change in surface potential, is mainly attributed to the variation in dopant distribution. As thickness of a given film increases during the course of electropolymerization, the tris(pentafluoroethyl)trifluorophosphate ions tend to assemble onto the protuberant globules, and therefore the regions of high electrical current or potential are predominantly the grain tops. The band gaps (E_g) of a given film were estimated from absorbance curves and conduction band positions were determined from oxidation potentials.

The band gaps of PCIND and PEDOP are 1.41 and 1.82 eV respectively. The reported band gaps of PEDOP and PCIND are 2.1 and 2.4 eV, wherein the dopant was ClO_4^- ions [8,9].Our values are lower than the reported values, owing to the use of different dopant anion. Lower band gaps are advantageous, for energy required to attain the conducting state is lesser. The energy band diagram illustrating the positions of CB, VB and band gap, in the PCIND and PEDOPfilms with reference to the vacuum level fixed at 0 eV is shown in Figure 5.5e.

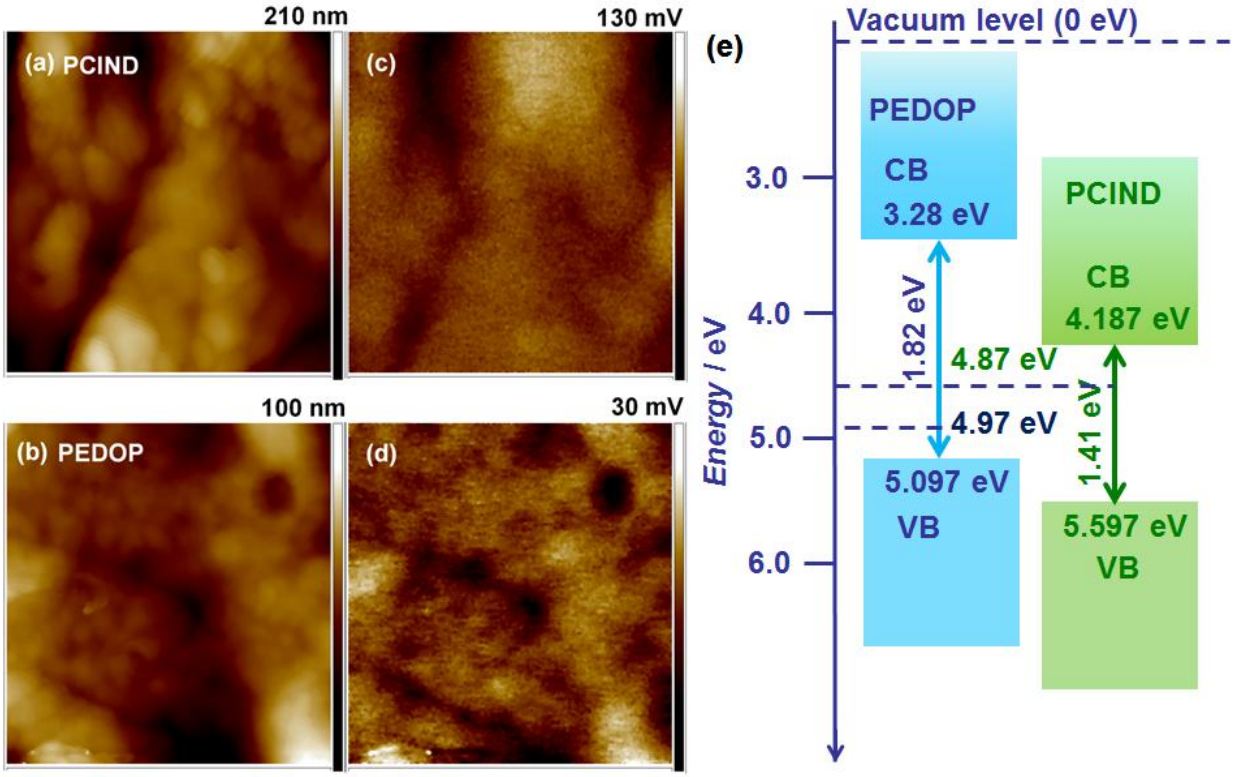

Figure 5.5: Topography and surface potential maps of (a,c) PCIND and (b,d) PEDOP films recorded over scanned areas of 1 µm × 1 µm and (e) energy band diagram of PCIND and PEDOP films.

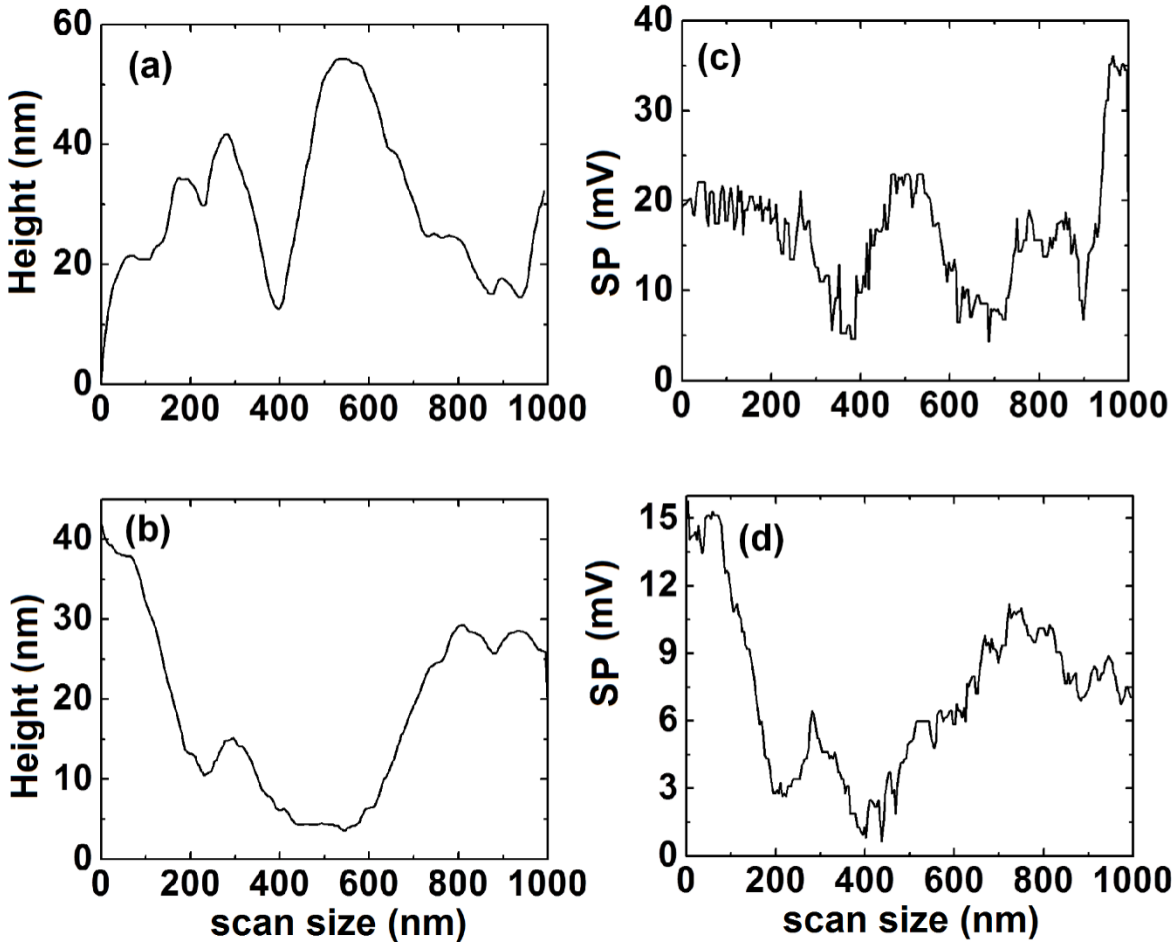

Figure 5.6: Cross-sectional profiles of topography (a,b) and surface potential (c,d) images of PCIND and PEDOP derived from Figure 5.4.

From the cyclic voltammograms of PEDOP and PCIND recorded at a sweep rate of 2 mV s^{-1} (Figure 5.11), the oxidation peaks were observed at potentials (E_O) of 0.9 V (*versus* Ag/Ag^+) and 0.4 V(*versus* Ag/Ag^+). The potential of reference electrode (Ag/Ag^+) was +0.197 V (*versus* NHE). The oxidation potential (*versus* NHE) corresponds to the highest occupied molecular orbital (HOMO) position or valence band position of the electroactive material. Therefore, the oxidation potential of PEDOP (*versus* NHE) will be: E_O = (0.6 + 0.197) V = 0.797 V. The oxidation potential of PCIND (*versus* NHE) will be: E_O = 0.9 + 0.197 V= 1.097 V. 0 V

(*versus*NHE) corresponds to 4.5 eV (w.r.t. vacuum level). The VB positions of PEDOP and PCIND are therefore 5.297 and 5.597 eV respectively.Band gaps (E_g) of PEDOP and PCIND: The absorption edge wavelengths were obtained by extrapolating the absorption spectra of PEDOP and PCIND (in their red and blue states respectively). Using $E_g = hc/\lambda$, where c is the speed of light, the band gaps of PEDOP and PCIND were 1.82 and 1.41 eV respectively.

5.3.4 Ionic liquid electrolyte properties

Figure 5.7a shows the variation of ionic conductivity of the [BMPY][$N(CF_3SO_2)_2$]-PVdF-HFP-PC gel film as a function of reciprocal absolute temperature. The ionic conductivities of the gel film at different temperatures were determined from the *Z*" *versus Z*' plots which were recorded for the gel sandwiched between two Pt electrodes, in combination with a reference electrode (Ag/AgCl/KCl). The Nyquist plots recorded at different temperatures are shown in Figure 5.9. The magnitudes of resistances were extracted from the curves, at a fixed frequency of 1100 Hz. The gel polymeric electrolyte exhibits a room temperature (RT ~ 25 ^oC) ionic conductivity of 1.196×10^{-3} S cm^{-1}, which is adequate for electrochromic device operation. A reasonably high ionic conductivity (in the range of 10^{-3} to 10^{-2} S cm^{-1}) in polymer electrolytes also acts to minimize the ohmic drop across the cell, and thus activates coloration and bleaching of the device, at lower potentials.

The thermal dependence of conductivity shows a distinct curved profile, which is typical of highly viscous amorphous polymeric electrolytes[10].Ionic conductivity for the [BMPY][$N(CF_3SO_2)_2$]-PVdF-HFP-PC gel electrolyte film increases as a function of increasing temperature, and the overall variance over the temperature range under consideration is about an order of magnitude. These studies clearly exemplified the suitability of this gel electrolyte film for electrochromic window applications, as a major prerequisite that an electrolyte must fulfill is

that conductivity should exhibit nominal variance over the operational temperature range of an electrochromic window (–20 to 80 ^{o}C) [11].

The thermal stability of the ionic liquids ($[(C_{32}H_{68})P^{+}][(C_2F_5)_3PF_3^{-}]$ and ([BMPY][$N(CF_3SO_2)_2$]) and the [BMPY][$N(CF_3SO_2)_2$]-PVdF-HFP-PC gel, was determined by TGA. To illustrate this fact, the TGA curves of the ILs and the polymer electrolyte were recorded and are shown in Figure 5.7b. The FAP IL, which was employed as a counter ion for deposition of PCIND and PEDOP films, exhibits a high thermal stability with a thermal degradation temperature, only above 380 ^{o}C. The [BMPY][$N(CF_3SO_2)_2$] ionic liquid, which was used for preparing the polymer electrolyte, was observed to undergo thermal decomposition at temperatures above 340 ^{o}C. The [BMPY][$N(CF_3SO_2)_2$]-PVdF-HFP-PC gel electrolyte which was used for fabricating prototype electrochromic devices, exhibited a wide thermal stability window, spanning from 25 to 250 ^{o}C. Such a large temperature stability window renders the electrolyte suitable for electrochromic window applications, as the observed upper limit is far above the operational limit of 80 ^{o}C for an electrochromic device. The electrochemical stability of the two ILs and the [BMPY][$N(CF_3SO_2)_2$]-PVdF-HFP-PC gel film was assessed from their linear sweep voltammetry (LSV) plots (Figure 5.7c-e). LSV was performed for the ILs and the gel polymeric electrolyte (at 25 ^{o}C) at a scan rate of 20 mV s^{-1} using Pt as working and counter electrodes and a reference electrode (Ag/AgCl/KCl) in a classical three electrode configuration. The voltammograms are linear within the voltage ranges of –3.5 to +2.4 V for the IL: $[(C_{32}H_{68})P^{+}][(C_2F_5)_3PF_3^{-}]$and between –2.8 to +2 V for the [BMPY][$N(CF_3SO_2)_2$] IL, and above these limiting potentials, the currents show a steep increase, indicative of decomposition reactions. The electrochemical potential stability window for the [BMPY][$N(CF_3SO_2)_2$]-PVdF-

HFP-PC gel is confined to –3 to +2 V, thus implying a voltage span of ~5 V, which is sufficient for electrochromic window applications.

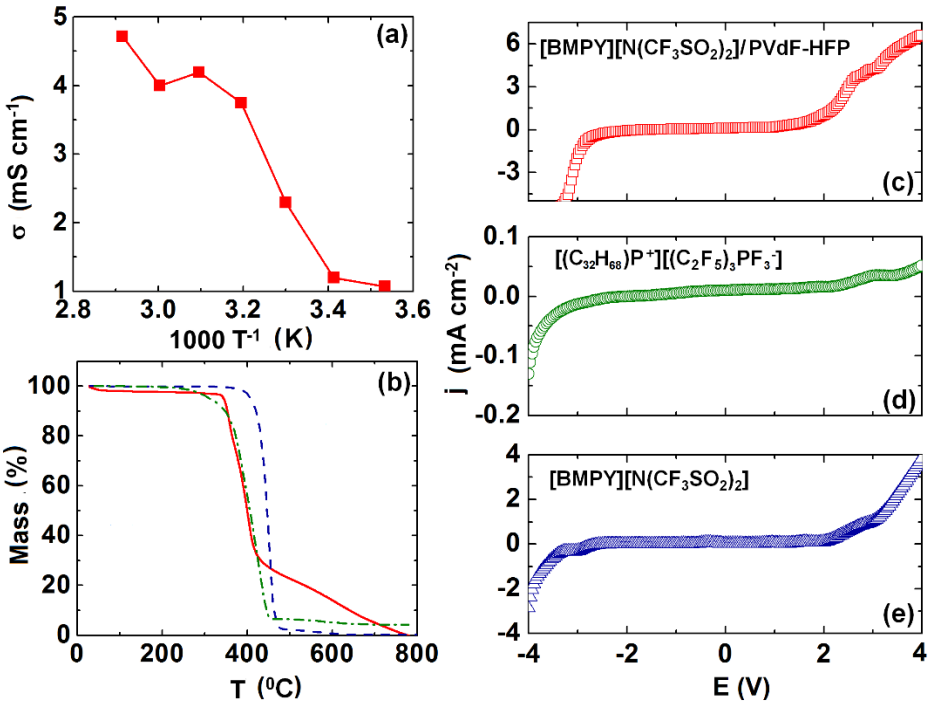

Figure 5.7: (a) Ionic conductivity *versus* reciprocal absolute temperature curve for the [BMPY][$N(CF_3SO_2)_2$]-PVdF-HFP-PC gel electrolyte, (b) TGA curves for the ILs: [$(C_{32}H_{68})P^+$][$(C_2F_5)_3PF_3^-$] (---) and [BMPY][$N(CF_3SO_2)_2$] (—) and the gel electrolyte:[BMPY][$N(CF_3SO_2)_2$]-PVdF-HFP-PC (— •) and LSV plots of (c) the gel electrolyte film and (d,e) the ILs, recorded at a scan rate of 20 mV s^{-1} between two Pt electrodes.

Electrochromic devices for "smart windows" aim at achievement of control over solar radiation flowing through a window, and therefore a primary condition that the electrolyte must fulfill, is that it should be transparent to visible radiation [12,13]. A transmission spectrum of the [BMPY][$N(CF_3SO_2)_2$]-PVdF-HFP-PC gel recorded in the 900 - 300 nm range is shown in

Figure8a. The percent transmission observed for this gel electrolyte is about 85% in the visible region (~ 400 - 750 nm), which renders it suitable for use in electrochromic windows.

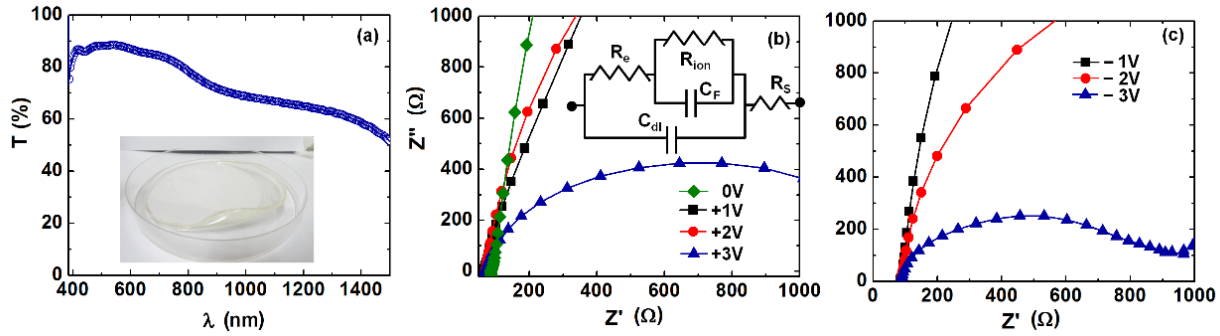

Figure 5.8: (a) Variation of transmittance as a function of wavelength for the [BMPY][$N(CF_3SO_2)_2$]-PVdF-HFP-PC gel electrolyte; inset of (a) shows the photograph of the gel electrolyte. Electrochemical impedance spectra of the PCIND-[BMPY][$N(CF_3SO_2)_2$]-PVdF-HFP-PC-PEDOP device recorded under dc potentials of (b) 0 (◆), +1 (■), +2 (●) and +3 (▲) V and (c) −1 (■), −2 (●) and −3 (▲) V, over a frequency range of 0.1 to 10^6 Hz; dc potential applied to PCIND as the working electrode. Inset of (b) shows the equivalent circuit used for fitting the experimental data.

5.3.5 Impedance analysis and cyclic voltammetry

To unravel the charge transport dynamics in the PEDOP-PCIND device, the electrochemical impedance response of the PCIND-PEDOP devices were recorded under a fixed ac amplitude of 5 mV with different dc potentials superimposed on the ac signal to perturb the set polarization conditions (Figure 5.8b and c). The Nyquist plot (Z" *versus* Z') obtained at zero dc potential (Figure 5.8b) is almost linear and it can be inferred that the PCIND film exhibits a highly capacitive character (C_{dl} = 9.8 and C_F = 12.4 μF cm^{-2}) as the impedance curve shows only a slight slant from the 90^o angle, which is characteristic of an ideal capacitor. This implies, that the film has a strong tendency (i) to promote the formation of an electrical double layer at the PCIND/gel electrolyte interface (C_{dl}) and (ii) to facilitate the oxidation of PCIND film, which

results in incorporation of imide ions from the electrolyte in the polymer chain (C_F, redox pseudocapacitance). The contribution of the resistive component to charge transfer and transport, becomes increasingly dominant upon raising the applied dc bias from 0 to +3 V in steps of +1 V. While the Z" *versus* Z' profile is almost a straight line (suggestive of fast charge transfer and transport at the PCIND/electrolyte interface) at 0 V, the same profile acquires a semi-circular shape under E = +3 V. The experimental data for the device was fitted in an equivalent circuit, which is shown as an inset of Figure 5.8b. R_e and R_{ion} are the resistances offered by the PCIND film to electron and ion-movement. This model has been successfully used in the past for the separating ionic and electronic resistances for a poly(pyrrole) film probed in a $NaClO_4$ electrolyte.[14]. Authors obtained an ionic conductivity of 0.5 mS cm^{-1} for poly(pyrrole) from impedance studies. Here, we deduced electronic and ionic conductivities of 0.6×10^{-4} and 0.6×10^{-6} S cm^{-1} for the PCIND film. The details pertaining to the model used are given in the next paragraph. These values were obtained from the Nyquist plot recorded for the sample, subjected to a zero dc bias. The increase in the resistive contribution ongoing to higher negative (reducing) or positive (oxidizing) potentials, as can be judged from the transformation of the Z" *versus* Z' profile from linear to an arc, could be perhaps due to the resistance offered by the oxidized PCIND polymer for further oxidation (as potential increases from +1 to +3 V) and similarly by the reduced PCIND polymer for further reduction (as potential increases from −1 to −3 V). This also indirectly indicates that the polymer structure and composition are conducive for facile ion-ingress and egress at low oxidation and reduction potentials. The PCIND-PEDOP device is therefore expected to exhibit a high electrochromic contrast.

Equations used for calculating R_e and R_{ion}:

$$1/(R_h - R_s) = 1/R_e + 1/R_{ion} \quad (4)$$

$$3(R_l - R_s) = R_e + R_{ion} \quad (5)$$

Rs is the solution resistance, which can be obtained from the impedance curve generated by using a bare FTO-coated glass substrate as the working electrode. The $R_h$is the value that is the high frequency real axis intercept minus R_s. R_l is the low frequency limiting real impedance. The $R_e$and $R_{ion}$are the electronic and ionic resistances of the films. These plots are shown in Figure 5.9. R_e and R_{ion} were determined by solving equations (4) and (5). σ, R, l and aare the conductivity, resistance, thickness and surface area (of the films) in equations (6) and (7).

$$\sigma_e = 1/R_e \times l/a \quad (6)$$

$$\sigma_{ion} = 1/R_{ion} \times l/a \quad (7)$$

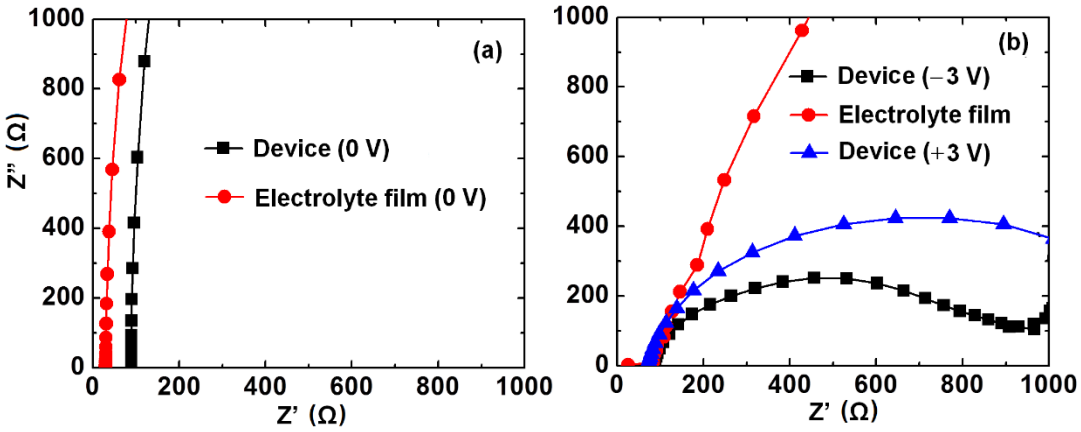

Figure 5.9: Electrochemical impedance spectra of (a) the [BMPY][$N(CF_3SO_2)_2$]-PVdF-HFP-PC electrolyte film (●) between two FTO coated glass substrates and the PCIND-[BMPY][$N(CF_3SO_2)_2$]-PVdF-HFP-PC-PEDOP device (■) recorded under a dc potential of 0 V and (b) for the device under +3 (■) and −3 (▲) V and for the electrolyte between two FTO coated glass substrates under 0 V (●), over a frequency range of 0.1 to 10^6 Hz.

Table 5.2: EIS parameters for the PCIND-[BMPY][$N(CF_3SO_2)_2$]-PVdF-HFP-PC-PEDOP device, under different potentials. Capacitances were obtained from the fits.

E (V)	σ_e (S cm^{-1})	σ_{ion} (S cm^{-1})	C_{dl} (μF)	C_F (μF)
0	0.6×10^{-4}	0.6×10^{-6}	9.82	12.4
+3	1×10^{-2}	1×10^{-3}	6.68	43.3
−3	1.5×10^{-3}	4×10^{-4}	10.2	77.2

The electrochemical behavior of the PCIND and PEDOP films was studied using cyclic voltammetry, in the [BMPY][$N(CF_3SO_2)_2$] IL (Figure 5.10). The cyclic voltammogram of the PCIND film, recorded at a scan rate (s) of 2 mV s^{-1} (Figure 5.10a), shows an oxidation peak at +0.9 V, and in the reverse sweep, a broad current plateau centered at +0.4 V is observed. The two peaks correspond to the insertion and extraction of the imide ($N(CF_3SO_2)_2^-$) ions into and from the film, according to the following equation (8).

$$\mathrm{PCIND^{m+}{:}[(C_2F_5)_3PF^-_3]_m} \underset{\text{Red}}{\overset{\text{Oxd}}{\rightleftharpoons}} \mathrm{PCIND^{(m+n)}{:}[(C_2F_5)_3PF^-_3]_m{:}[N(CF_3SO_2)^-_2]_n}$$

$$\text{Oxd: } +n[N(CF_3SO_2)^-_2],\ -ne^- \qquad \text{Red: } -n[N(CF_3SO_2)^-_2],\ +ne^- \tag{8}$$

However, upon progressively increasing the scan rate, from 2 to 50 mV s^{-1}, the oxidation peak current amplitude increases, and the peak shifts to a more positive potential of +1.04 V for the scan recorded at 50 mV s^{-1}). The peak shift towards higher voltage region could be due to the slowdown of the rate of insertion of the dopant imide ions into the PCIND film. For the PEDOP film, the CV plot recorded at 2 mV s^{-1} (Figure 5.10b), oxidation and reduction peaks are observed at +0.6 and +0.18 V respectively. These processes correspond to a reversible transition between conducting (oxidized) and the neutral, insulating (reduced) states of PEDOP, as illustrated through the equation (9).

$$PEDOP^{m+}:[(C_2F_5)_3PF^-_3]_m \underset{-n[N(CF_3SO_2)^-_2],\ +ne^-}{\overset{Oxd\ +n[N(CF_3SO_2)^-_2],\ -ne^-}{\rightleftharpoons}} PEDOP^{(m+n)}:[(C_2F_5)_3PF^-_3]_m :[N(CF_3SO_2)^-_2]_n \quad (9)$$

Red

At higher scan rates, due to the fast ion transport between the film and electrolyte, the peaks disappear, but the current density maxima increase as a function of scan rate. The charge storage capacities of PCIND and PEDOP films, deduced from the areas under the anodic branches of their voltammograms recorded at a scan rate of 50 mV s^{-1} are 2.21 and 1.28 mC cm^{-2}. The CV plots of the PCIND-PEDOP device encompassing the [BMPY][$N(CF_3SO_2)_2$]-PVdF-HFP-PC gel, obtained by using the PCIND film as the working electrode, are shown in Figure 5.10c.

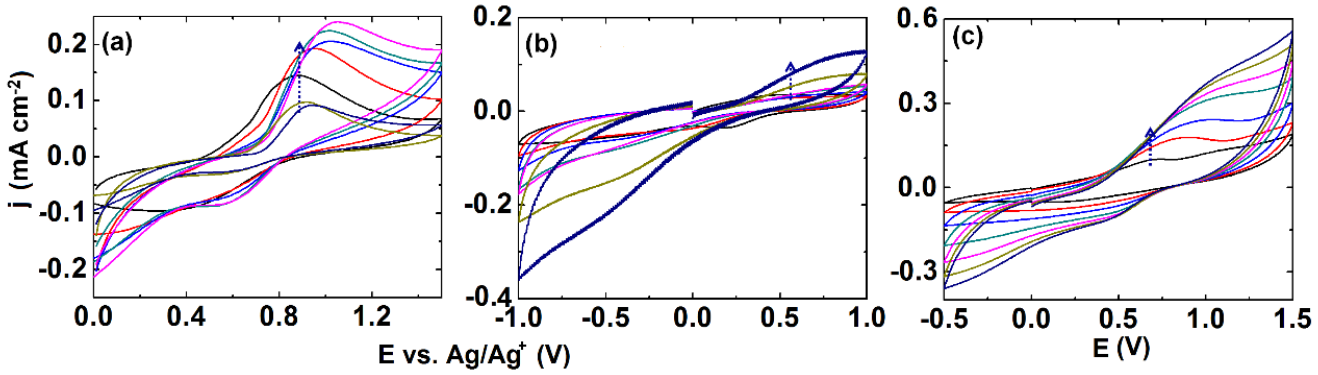

Figure 5.10: Cyclic voltammograms of (a) PCIND and (b) PEDOP films recorded in the ionic liquid: [BMPY][$N(CF_3SO_2)_2$] and (c) the PCIND-[BMPY][$N(CF_3SO_2)_2$]-PVdF-HFP-PC-PEDOP device; at scan speeds of 2, 5, 10, 20, 30, 40 and 50 mV s^{-1}. The arrow in each panel shows the direction of increasing scan rate.

A distinctive peak corresponding to the oxidation of PCIND is observed at +0.6 V, for a plot swept at 2 mV s^{-1}. A reduction peak is visible for the device in the plot recorded at 50 mV s^{-1}. The plots are relatively featureless, and oxidation/reduction peaks are not pronounced owing to

fast reaction rates. The charge storage capacity for the PCIND electrode (at s = 50 mV s^{-1}) in device configuration, is deduced to be 6.8 mC cm^{-2}, which is larger than the capacities delivered by the individual films.

The variation of absorbance of (i) a PCIND film (Figure 5.11a) subjected to applied bias in the range of – 1 V to +3 V and (ii) a PEDOP film (Figure 5.11b) subjected to applied bias in the range of +1 to −3 V, as a function of wavelength are shown. The measurements were performed in-situ in the IL: [BMPY][$N(CF_3SO_2)_2$], and the potential was varied in both cases, in steps of 0.2 V.ΔOD is defined as the optical density change at a monochromatic wavelength (~λ_{max}) as, ΔOD (λ)= [OD (λ, −3 V) – OD (λ, +1 V)] for the PEDOP film, and for the PCIND film, the expression takes the following form: ΔOD (λ) = [OD (λ, +3 V) – OD (λ, −1 V)]. For the as-fabricated PCIND film, a λ_{max} was observed at ~700 nm, corresponding to the polaronic transitions in the polymer and the film is yellow in color[15]. With increasing positive potentials (from +0.2 to +3 V), the intensity of this peak diminishes at the expense of another λ_{max}which is observed at 650 nm in the visible region. This peak arises from the transitions between the bipolaronic states corresponding to the formation of fully oxidized PCIND film and impart a dark green hue to the film, which transforms to blue at high positive potentials (as at E = +3 V). Digital photographs of the PCIND and PEDOP films in oxidized and reduced states are also shown in Figure 5.11. For the PEDOP film, the broad band observed in the NIR region for the film in the as-fabricated state and under low negative potentials originates from the bipolaronic transitions and when the film is fully reduced (at E = −3 V), the film acquires a neutral, insulating state and as a consequence the π-π* transitions, produce the λ_{max}peak observed at 490 nm. The PEDOP film has a transparent blue hue in the oxidized state and it is red in the reduced

form. The ΔOD_{max} values for the PEDOP and PCIND films were deduced to be 0.067 and 0.146 respectively at $\lambda_{max}$of 490 and 650 nm.

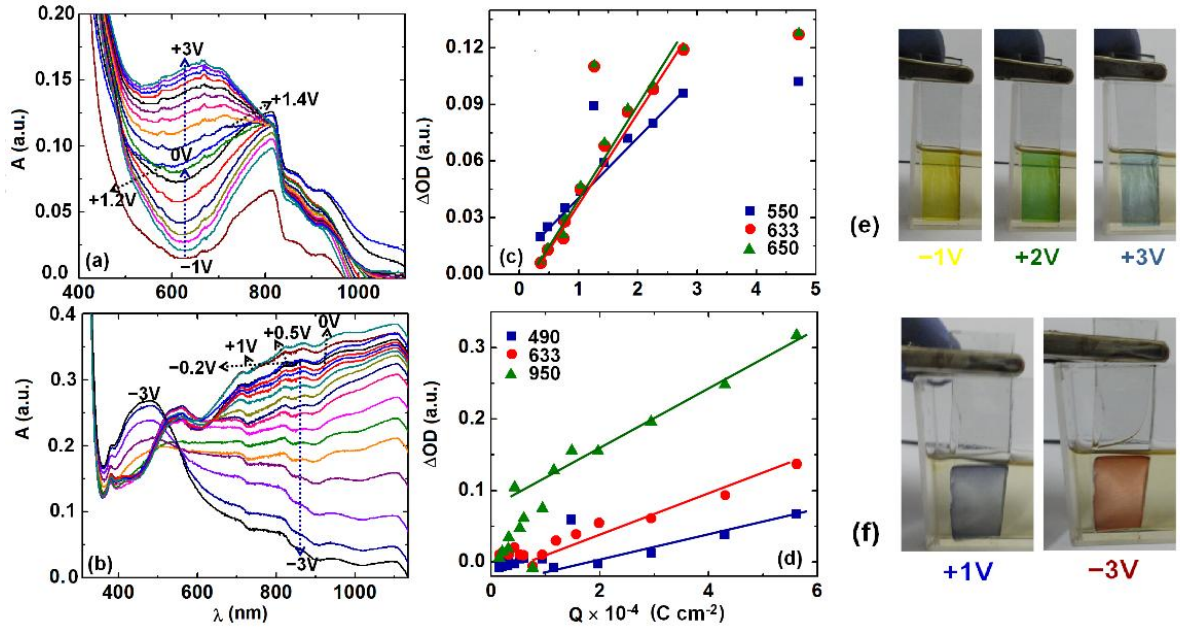

Figure 5.11:*In-situ* absorption spectra of (a) PCIND and (b) PEDOP films recorded under different potentials varying from: –1 to +3 V in (a) +1 to −3 V in (b); both measurements performed in the [BMPY][$N(CF_3SO_2)_2$] IL in steps of 0.2 V. ΔOD *versus* charge density plots at monochromatic wavelengths of (c) 550 (■), 633 (●) and 650 (▲) nm for PCIND film with OD response under −1 V in (a) as reference for determination of ΔOD and (d) 490 (■), 633 (●) and 950 (▲) nm for PEDOP film with ODresponse under +1 V in (b) as reference for determination of ΔOD. Digital photographs of (e) PCIND and (f) PEDOP films in neutral and oxidized states.

5.3.6 Spectroelectrochemistry of films and devices

Coloration efficiency at a monochromatic wavelength is defined as the optical density change induced in a film or device by the amount of charge intercalated (Q) per unit area (A) which is shown as equation (10).

$$CE\ (\lambda) = \Delta OD\ (\lambda)/Q/A \qquad (10)$$

The slope of ΔOD (λ) *versus* Q/A yields the CE value for a film or device. The ΔOD (λ) *versus* Q/A plots were generated for the PCIND and PEDOP films at different wavelengths and these are shown in Figure 5.11c and d. The CEs or η of the films and device are summarized in Table 5.3. Notably, for the PCIND film at a λ_{max} of ~650 nm, the CE was 449 cm^2 C^{-1}. The CE for the PEDOP film at λ_{max} of 490 nm, was 148.5 cm^2 C^{-1} and it was higher in the NIR region, as a value of 478 cm^2 C^{-1} was estimated for the same film at 950 nm. The CE is therefore anticipated to increase significantly on combining two electrochromes capable of delivering high contrast individually. This is also reflected in the absorbance plot shown in Figure 5.12. Figure 5.12a shows the absorbance *versus* wavelength plots for a PCIND-[BMPY][$N(CF_3SO_2)_2$]-PVdF-HFP-PC-PEDOP device recorded *in-situ* under applied potentials that were varied from –3 V to +3 V, in steps of 0.2 V. The measurements were performed with respect to PCIND as the working electrode. The device shows a broad λ_{max} in the visible region, which is centered at ~475 nm in the fully oxidized state (+3 V applied to PCIND film). In the fully reduced state (−3 V applied to PCIND film), it shows a broad absorption in the NIR region. The ΔOD *versus* charge density curves for the device are shown in Figure 5.12b. The coloration efficiency (determined from the slopes of the plots) of the device at 475 nm is 480 cm^2 C^{-1} which is greater than the CEs of the individual electrochromes in the photopic region. In the NIR region, theCE of the device was found to be substantially higher than that achieved in PCIND or PEDOP alone; for the device it was 796 cm^2 C^{-1} (at λ = 1100 nm). The coloration efficiency of the device is as expected, much higher than the CE values of the individual PEDOP and PCIND electrochromes, especially in the NIR region, thus indicating that these two films are most suitable for fabricating practical smart windows capable of modulating NIR (or heat) component of solar radiation. In the past, for a poly(indole-6-carboxylic acid) (PIn)-PEDOT device based on a conventional gel

electrolyte, a maximum CE of 510 cm^2 C^{-1} at 600 nm was obtained [16]. In another recent report [17], a device based on poly(5-cyanoindole-co-EDOT) and PEDOT with a traditional polymer electrolyte containing poly(methylmethacrylate) and tetrabutylammonium tetrafluoroborate showed a CE of 680 cm^2 C^{-1} at 630 nm and a response time of 0.8 s at 630 nm. But it must be noted that in these reports, CE was calculated using a single value of ΔOD and corresponding charge density, whereas we took all possible charge densities into consideration. While our visible coloration efficiency value is comparable to the reported values, the CE in the NIR region is significantly higher, as the optical modulation was not very high in the NIR region in these reports [16,17].Modulation of NIR radiation, along with visible radiation modulation is imperative for smart window applications. Previously, in a report on a nickel dithiolene-containing electropolymerized pendent indole units, NIR electrochromic switching at 800 nm was shown, but coloration efficiency was not provided [18]. For a neat PEDOP device with Prussian blue as the counter electrode in the past, a value of 185 cm^2 C^{-1} (λ = 448 nm) was obtained [19],which shows the efficacy of PCIND as a counter electrode in improving the device contrast.

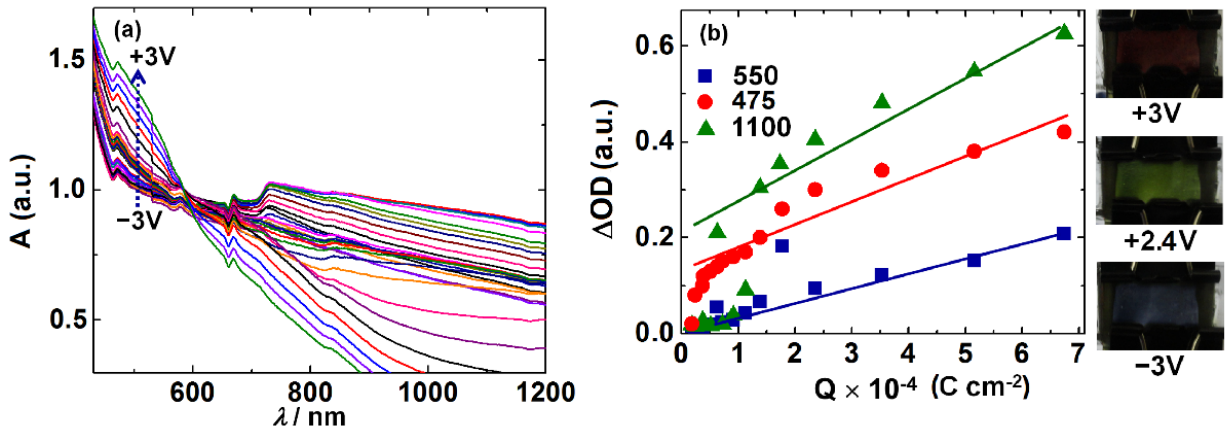

Figure 5.12: (a) *In-situ* absorption spectra of the PCIND-[BMPY][N(CF_3SO_2)$_2$]-PVdF-HFP-PC-PEDOP device recorded under different potentials varying from: –3 to +3 V (varied in steps of 0.2 V) and (b) ΔOD *versus* charge density plots at monochromatic wavelengths of 550 (■) , 475 (●) and 1100 (▲) nm for the PCIND-[BMPY][N(CF_3SO_2)$_2$]-PVdF-HFP-PC-PEDOP device, with the OD response under −3 V in (a) as reference, for determination of ΔOD. Photographs of the device under −3 V (fully reduced PCIND), +3 V (fully oxidized PCIND) and at an intermediate potential of +2.4 V (partially oxidized PCIND) are shown in the adjacent panel.

Table 5.3: CEs of the films and device at different monochromatic wavelengths deduced from the slopes of the ΔOD *versus* charge density profiles.

Sample description	CE (cm^2 C^{-1})	CE (cm^2 C^{-1})	CE (cm^2 C^{-1})
PCIND film	449 (λ = 650 nm)	327 (λ = 550 nm)	430 (λ = 633 nm)
PEDOP film	148 (λ = 490 nm)	212 (λ = 633 nm)	478 (λ = 950 nm)
PCIND-PEDOP device	480 (λ = 475 nm)	192 (λ = 550 nm)	796 (λ = 1100 nm)

The transmittance*versus* time curves for the PCIND and the PEDOP films and the PCIND-[BMPY][N(CF_3SO_2)$_2$]-PVdF-HFP-PC-PEDOP device, are shown in Figure 5.13, after equilibrating the films for a few cycles. The step time was chosen as 7.5 s and the films were subjected to a square wave potential of ± 3 V. The geometric active areas of the electrodes were 2 cm^2. Coloration and bleaching times for the PCIND films (at a $\lambda_{max}$of 650 nm) are 0.8 and 1.4 s respectively. Coloration and bleaching times are fast for the PCIND film, which re-affirms the

outcome of impedance study. Both insertion/oxidation and extraction/reduction of imide ions is facile in the PCIND film. Similarly, the color and bleach times for the PEDOP film were estimated to be 1.3 and 1.8 s respectively at a wavelength of 490 nm. In the past, color and bleach times of 16 and 20 s have been reported for a PEDOT based flexible device doped by triflate ions at a monochromatic wavelength of 650 nm [20]. For the device here, at a monochromatic wavelength of 475 nm, the coloration and bleaching times are 0.8 and 1.3 s respectively, and the magnitude of contrast is almost twice of that achieved in the individual electrochromes. The device was also subjected to repeated cycling between the colored and bleached states and the response of the device was recorded after 1000 cycles. The device retained ~85% of its' original total modulation and color and bleach times were almost unaffected, indicating that the device has potential for smart window applications. In an earlier report, the response required to attain 95% of total transmittance difference was found to be 2 s from the reduced to the oxidized state and 0.7 s from the oxidized to the reduced state for a PIn-PEDOT device [16]. In an earlier report on a nickel dithiolene-containing electropolymerized pendent indole units, response times of the order of few seconds were observed [18]. A PEDOT-nanotube based electrochromic device showed response times of the order of a few ms (in the range of 4-30 ms) for an active electrode area of less than 1 cm^2. Authors attributed the extremely fast kinetics to short diffusion pathways afforded by the nanotubular polymer morphology [21]. While switching times of the order of a few ms are a critical pre-requisite for display applications, for window applications, slow switching, even of the order of a few minutes is permissible [22]. Our values for switching times (for an area of 2 cm^2) are acceptable for electrochromic windows, as ultra-fast switching is generally not an absolute necessity for this application.

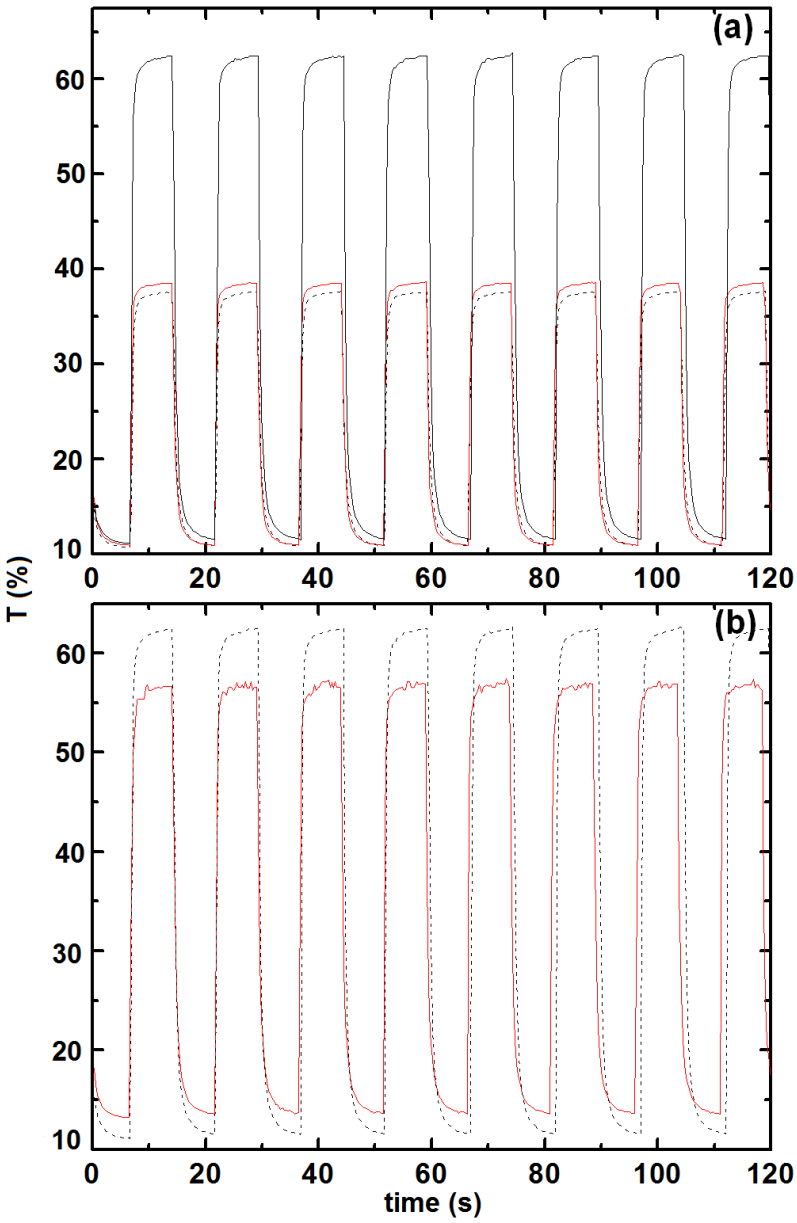

Figure 5.13: Transmitance versus time curves for (a) PCIND (—) atλ_{max} = 650 nm, PEDOP (….) at λ_{max} = 490 nm films recorded in the ionic liquid: [BMPY] [$N(CF_3SO_2)_2$] and the PCIND-[BMPY][$N(CF_3SO_2)_2$]-PVdF-HFP-PC-PEDOP device (— —) at λ_{max} = 475 nm and (b) for the device at 475 nm in the first few cycles(….) and after 1000 cycles (—) of coloration and bleaching; all measurements under a square wave dc potential of ±3.0 V at a frequency of ~0.066 Hz.

5.4 Summary

A fluoroalkylphosphate ion based hydrophobic IL: trihexyl(tetradecyl)phosphonium tris(pentafluoroethyl)trifluorophosphate was used for the first time, as the medium for electro-syntheses of poly(5-cyano indole) and poly(3,4-ethylenedioxypyrrole) films. Prototype electrochromic devices with PCIND and PEDOP as cathodic and anodic electrodes were fabricated; an IL based highly conductive, thermally and electrochemically stable and optically transparent gel was used as the polymer electrolyte. The device showed a remarkably large coloring efficiency of 480 cm^2 C^{-1} in the visible region and 796 cm^2 C^{-1} in the NIR region and demonstrated a reversible red to green to blue switch, and a charge storage capacity which was substantially higher than what could be achieved with the individual electrochromes. We correlate the device performance (high contrast and color tunability) to the synergy between various parameters such as: high nanolevel electronic conductivities of PCIND and PEDOP films (which facilitate electron transport and transfer), low charge transport resistances through the bulk of the individual films, low charge transfer resistances at the polymer/electrolyte interfaces and low work functions. Our studies demonstrate the potential of these scalable and inexpensive PCIND films as anodes for practical electrochromic smart windows.

References

[1] W. Lu, A. G. Fadeev, B. Qi, Smela, E. B. R. Mattes, J. Ding,; G. M. Spinks, J. Mazurkiewicz, D. Zhou, G. G. Wallace, D. R. MacFarlane, S. A. Forsyth, Forsyth, M. Science 297 (2002) 983–987.
[2] A. F. Ferreira, P. N. Simoes, A. G.M. Ferreira, J. Chem. Therm. 45 (2012) 16–27.
[3] S. Sadki, P. Schottland, N. Brodiec, G. Sabouraud, Chem. Soc. Rev. 29 (2000) 283–293.
[4] C. P. Andrieux, P. Audebert, P. Hapiot, J. M. Saveant, J. Phys. Chem. 95 (1991) 10158–10164.
[5] G. Sönmez, P. Schottland, K. Zong, J. R. Reynolds, J. Mater. Chem. 11 (2001) 289–294.
[6] W. Melitz, J. Shen, S. Lee, J. S. Lee, A. C. Kummel, R. Droopad, E. T. Yu, J. Appl. Phys. 108 (2010) 023711–023711.
[7] B. N. Reddy, M. Deepa, Electrochim. Acta 70 (2012) 228–240.
[8] C. L. Gaupp, K. Zong, P. Schottland, B. C. Thompson, C. A. Thomas, J. R. Reynolds, Macromolecules 33 (2000) 1132–1133.

[9] H. Talbi, D. Billaud, G. Louarn, A. Pron, Spectrochim. Acta A 56 (2000) 717–728.
[10] F.M. Gray, Polymer Electrolytes, RSC Materials Monographs, The Royal Society of Chemistry, UK, 1997.
[11] O. Bohnke, G. Frand, M. Rezrazi, C. Rousselot, C. Truche, Solid State Ionics 66 (1993) 105–112.
[12] M. Döbbelin, I. Azcune, M. Bedu, A. R. Luzuriaga, A. Genua, V. Jovanovski, G. Cabañero, I. Odriozola, Chem. Mater. 24 (2012) 1583–1590.
[13] S. A. Agnihotry, P. Pradeep, S. S. Sekhon. Electrochim. Acta. 44 (1999) 3121–3126
[14] X. Ren, P. G. Pickup, J. Electroanal. Chem. 420 (1997) 251–257.
[15] E.B. Maarouf, D. Billaud, E. Hannecart, Mater. Res. Bull. 29 (1994) 637–643.
[16] G. Nie, L. Zhou, Q. Guo, S. Zhang, Electrochem. Commun. 2010, 12, 160–163.
[17] W. Yu, J. Chen, Y. Fu, J. Xu, G. Nie, J. Electroanal.Chem. 700 (2013) 17–23.
[18] S. Dalgleish, N. Robertson, Chem. Commun., 39 (2009) 5826–5828.
[19] A. Kharkwal, M. Deepa, A. G. Joshi, A. K. Srivastava, ChemPhysChem 12 (2011) 1176–1188.
[20] D. Mecerreyes, R. Marcilla, E. Ochoteco, H. Grande, J. A. Pomposoa, R. Vergaz, J. M. Sánchez Pena, Electrochim. Acta. 49 (2004) 3555–3559.
[21] S. I. Cho, S. B. Lee, Acc. Chem Res. 41 (2008) 699–707.
[22] C. G. Granqvist, Nat. Mater. 5 (2006) 89–90.

Chapter 6

Highly conductive PEDOP enwrapped Sb_2S_3 nanorods for supercapacitors

6.1 Introduction

For supercapacitor applications, until now, most efforts have been devoted to creating CP nanocomposites with either electronically conductive carbon nanostructures such as graphene, carbon nanotubes, carbon fibers [1-3] or by use of complementary pseudocapacitive transition metal oxides like RuO_2, MnO_2, Co_3O_4, V_2O_5 and NiO [4-6]. In a carbon nano-moiety-CP composite, the synergy between the ability of the polymer to store and release faradaic charge by undergoing redox reactions and the capability of the carbon nano-moiety to function as an electron conduit, thereby allowing charge storage by electrical double layer formation, translates to high capacitance and therefore high power density. The need to develop new alternate materials capable of charge storage stems from the fact that supercapacitor designs using carbon nanostructures/CP composites have been exhaustively investigated and possibilities are often limited to the use of graphene or multi/single-walled carbon nanotubes or fibers. In the past, although graphene or multi/single-walled carbon nanotubes enwrapped CP composites have demonstrated excellent performance characteristics, when employed as electrodes in supercapacitors, but further improving the electrical conductivity of the composite at a low cost remains a formidable challenge. Among various desirable architectures for electrodes, one-dimensional nanostructures are attractive as they offer short diffusion lengths for ions and high charge/discharge rates.

By considering the above-mentioned factors which can boost supercapacitor performance, we fabricated, for the first time, electrodes of electrically conductive and economically viable, and less toxic antimony sulfide (Sb_2S_3) nanorods enwrapped by PEDOP. For growing a CP directly with tube or wire like morphologies, generally, templates such as anodized alumina are employed and the process is cumbersome and the scalability is poor [1]. To alleviate this issue, we grew electronically conducting Sb_2S_3 nanorods, using a template free, inexpensive one-pot approach. Further oxidative electropolymerization, from a medium containing the monomer and the nanorods allowed the CP chains to encapsulate the nanorods and deposit onto the current collector surface under a directed electric potential. The nanorods -like morphology and the excellent electronic conductivity of Sb_2S_3 allow this sulfide to play a role akin to carbon nanotubes in a CP composite. Sb_2S_3 nanorods offer the benefit of fast electron transfer at the nanorods /polymer interface, owing to the direct and intimate contact between the rods and the polymer. This is advantageous as the principal function of a supercapacitor is to deliver high power at a fast rate, when required. Solid state supercapacitor cells were fabricated by use of electrodes with three-dimensional networks of Sb_2S_3 nanorods enwrapped by PEDOP, an IL based gel as the electrolyte and electrophoretically deposited graphite as the counter electrode. The composite supercapacitor developed in the present study clearly outperforms the neat polymer based supercapacitor, thus furnishing a new approach for fabricating advanced supercapacitors with high performance, inherently safe operation and long lifetime. Herein, we also highlight the construction and the outstanding performance of a PEDOP-Sb_2S_3 electrode based flexible, lightweight supercapacitors cell, with a carbon-fiber cloth as the current collector, wherein the distensibility, low weight and the ultra-thin architecture of the cell demonstrates the

enormous practical significance of the composite, thus illustrating the promise the conductive Sb_2S_3 nanorods have as scaffolds for a plethora of electroactive materials.

6.2 Experimental

6.2.1 Synthesis of Sb_2S_3 nanorods

$SbCl_3$ (0.25 g) was dissolved in ultrapure water (30 ml) and stirred for 10 min, followed by addition of ethylene glycol (30 mL) at room temperature. After stirring for another 10 min, sulfur (0.1 g) and $NaBH_4$ (0.3 g) were added slowly. The mixture was stirred for another 30 min, transferred in to an autoclave of 100 ml capacity and heated for 12 h at 180 ^oC. A black precipitate was obtained, which was filtered and washed with deionized water then dried at 60 ^oC. The resulting Sb_2S_3 nanorods were stored in air.

6.2.2 Fabrication of electrodes and devices

EDOP (0.1 M) monomer solution was prepared in acetonitrile (30 mL) separately, 0.1 M 1-butyl-3-methyl-imidazolium tris(pentafluoroethyl)trifluorophosphate was used as the dopant ion source. SnO_2:F (FTO) coated glass or carbon fiber cloth (of area 1×2 cm^2) was employed as the working electrode and a Pt sheet was used as the counter electrode and Ag/AgCl/KCl was used as the reference electrode. Bluish-black PEDOP films were obtained under potentiostatic conditions at room temperature in chronoamperometric mode by application of +1.5 V to the working electrode for 500 s. The Sb_2S_3nanorods (1.5 g) were added to the monomer bath and the solution was sonicated for 30 min and the same procedure was repeated to yield PEDOP/Sb_2S_3 films. Electropolymerization reaction is shown in Scheme 6.1.

A dispersion of graphite (0.1 g) in ethanol (30 mL) was prepared by ultrasonication for 15 min and using a two electrode configuration with FTO coated glass or carbon fiber cloth, graphite coatings were obtained on one of the electrodes upon application of a constant potential

of 20 V for 5 min using a Tarsons MC-01 electrophoresis power supply. Graphite electrodes have been labeled as Gr in this study. A quasi-solid polymer electrolyte was synthesized by dissolving PMMA (1 g) in the IL: ($BuMeIm^+[(C_2F_5)_3(PF_3)]^-$) (4 g) by continuous stirring at 80 ^oC for 5-6 h till a transparent viscous gel was obtained which had little flow properties when cooled to room temperature. An acrylic tape of 0.5 mm thickness was employed as the spacer and was applied along the four edges of the active electrode, the electrolyte was filled in the cavity using a glass rod and heated in a vacuum oven at 50 ^oC till a bubble free electrolyte layer was obtained. The counter electrode (Gr) was then pressed upon this assembly and the whole configuration was held together using binder clips and placed in an online vacuum oven for 1 h. The edges were finally sealed with an epoxy. Asymmetric cells with either FTO coated glass or carbon fiber cloth as current collectors, were obtained with the following configurations: PEDOP-Gr and PEDOP/Sb_2S_3-Gr.

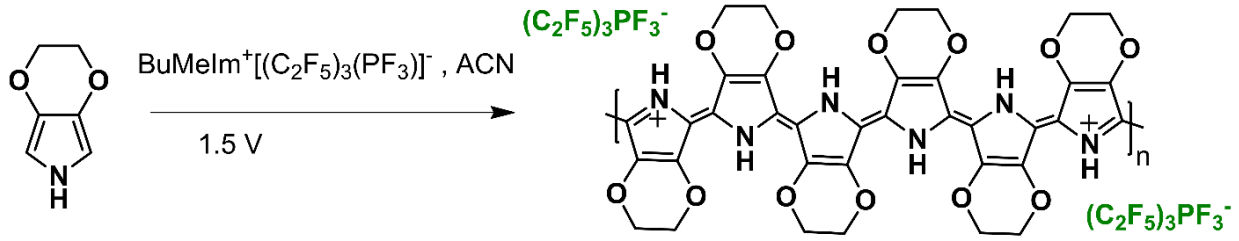

Scheme 6.1: Electropolymerization reaction of EDOP.

6.3 Results and discussion

6.3.1 Deposition curves

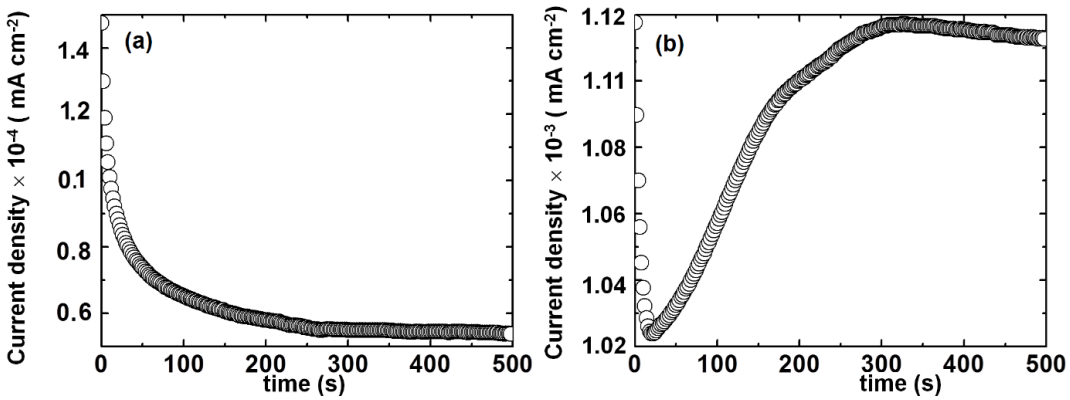

Figure 6.1: Current density *versus* time transients recorded for the oxidative electro-synthesis of PEDOP and composite PEDOP/Sb_2S_3 films from solutions of (a) 0.1 M 3,4-EDOP (b) 0.1 M 3,4-EDOP/ 1 mg Sb_2S_3 and both in AN and each containing the IL: 0.1 M 1-butyl-3-methyl-imidazolium tris(pentafluoroethyl)trifluorophosphate.

Current-time transients of PEDOP and PEDOP/Sb_2S_3 are shown in Figure 6.1. The initial spike followed by plateau behavior of EDOP in IL, represents oligomerization followed by polymer formation. For PEDOP/Sb_2S_3, a spike was followed by a sharp rise and a plateau which represents oxidation of monomer, oligomerization followed by polymerization.

6.3.2 Raman and XRD analysis

Sb_2S_3 nanorods show peaks at 174 and 269 cm^{-1} and a weak peak at 295 cm^{-1}. The peaks at 280 and 309 $cm^{-1}$are due to Sb_2S_3vibrational modes (Figure 6.2). Table 6.1 provides the vibrational band assignments for PEDOP films.

Table 6.1: Band positions and assignments for neat PEDOP film (ν: stretching mode).

PEDOP (cm^{-1})	Assignment
2095	ν(-C–H)
1641	ν(C=C)
1405	$\nu(C_\beta\text{-}C_\beta)$
1290	ν(C-S), ν(C-N)
820	ν(P-F) (from IL dopant)
733	ν(N-H)

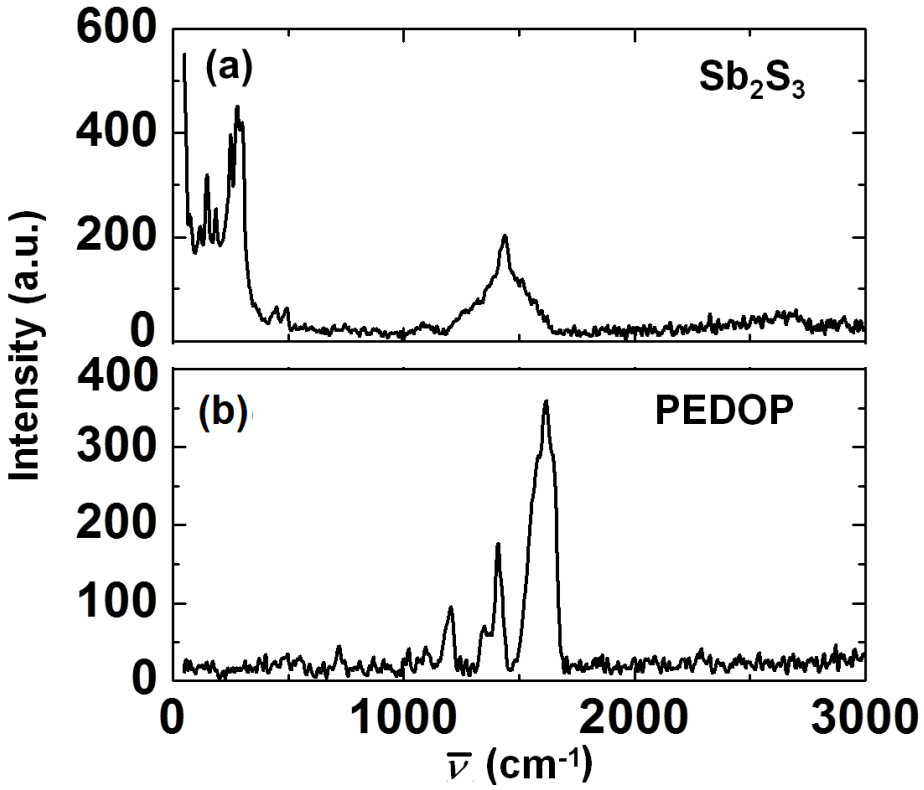

Figure 6.2: Raman spectra of (a) Sb_2S_3 nanorods and (b) neat PEDOP film.

The XRD pattern of Sb_2S_3 nanorods shows (Figure 6.3) main peaks at d = 7.86, 5.70, 4.97, 3.95 and 3.5 Å corresponding to the (020), (120), (220), (101) and (040) planes of orthorhombic Sb_2S_3, as per the JCPDS file number 42-1393. No peaks of any other phases were detected, indicating that the nanorods sample is a high-purity, single-phase sample.

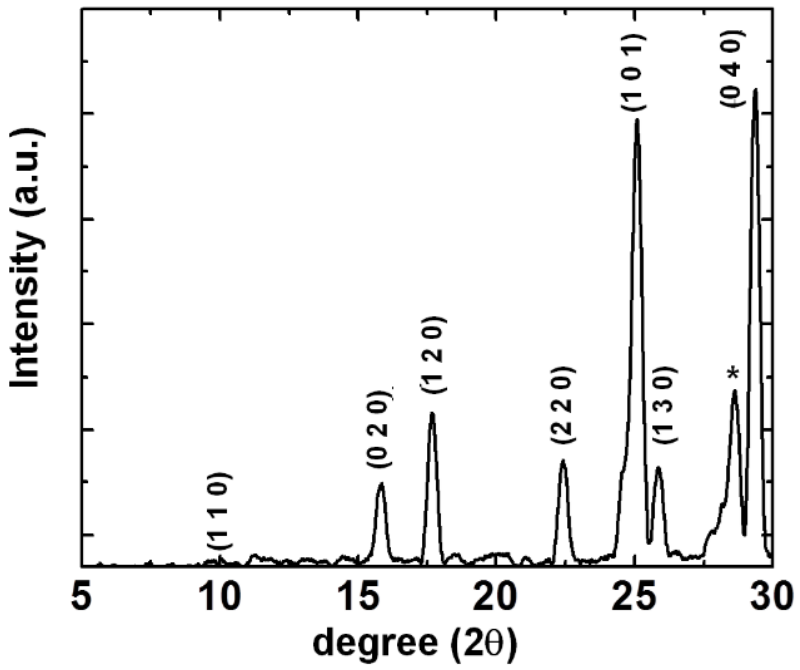

Figure 6.3: XRD pattern of Sb_2S_3 nanorods; the asterisk marked peak arises from the substrate.

6.3.3 Topography of electrodes

AFM images of pristine Sb_2S_3 nanorods are shown in Figure 6.4. The low magnification topographical images of neat Sb_2S_3 (Figure 6.4a and c) reveal a 3D network of interlinked but randomly oriented rods, with lengths varying from 1 to 3 μm and widths ranging from 50 to 150 nm. Since there are hardly any particulate shapes visible in the images, it is obvious that the synthetic process is quite efficient for producing homogenously distributed rectangular shaped nanorods. The high magnification image of pristine Sb_2S_3 nanorods shows that the rods have flattened surfaces and they tend to aggregate (Figure 6.4b). The thickness of the rod, which was measured from a cross-sectional profile is approximately 80 nm and upon stacking the thickness increased to about 300 nm (Figure 6.4d).

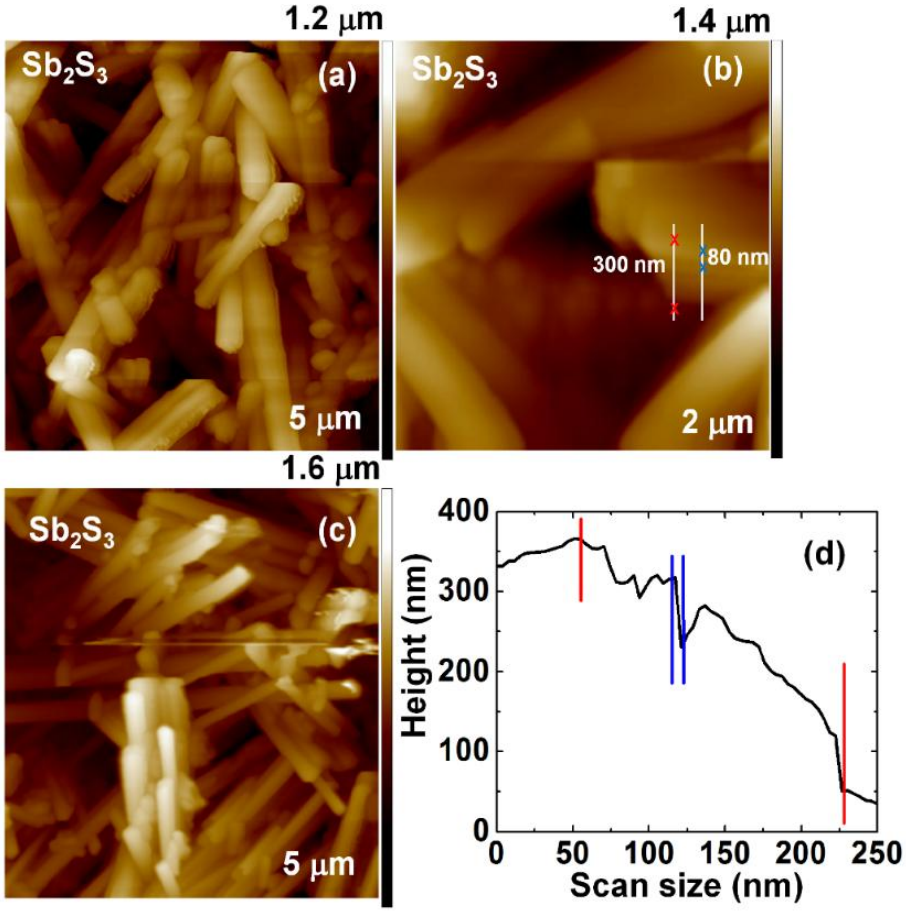

Figure 6.4: Topography images of (a,c) Sb_2S_3 nanorods over different regions of the same film with scan sizes of 5 μm × 5 μm, (b) over a scan size of 2 μm × 2 μm and (d) section profile of a stack of Sb_2S_3 nanorods from (b), showing the stack thickness of ~300 nm and an individual rod to have a thickness of ~80 nm.

The field emission SEM or FE-SEM images of pristine Sb_2S_3 nanorods, shown in Figure 6.5a and b, reveal the nanorods to be characterized by forest like growth, misaligned with respect to each other, but devoid of any branching. There are no particles or aggregates indicating that the sample is entirely made up of uniform nanorods having a smooth surface texture. The rods extend upto few microns in length and their diameters vary between 50 to 150 nm which concur with the AFM observations. The inset of Figure 6.5b shows a high contrast image of the rod, and

the rod width/thickness was 80 nm. The FE-SEM images of the PEDOP-Sb_2S_3 composite (Figure 6.5c and d) shows the Sb_2S_3 nanorods to be juxtaposed with the PEDOP grains, indicating a good mixing of the polymer with the rods, the particulate sheath formed on the rods stem from the polymer. The inset of Figure 6.5d shows the width of the rod to be 230 nm, which is greater than that of pristine Sb_2S_3 rods indicating the presence of polymer around the rod. Further, it is also noticed that the pristine rods have sharp edges whereas upon integration with the polymer, their edges are jagged, indicative of polymer incorporation. It is obvious that the inclusion of Sb_2S_3 nanorods in the polymer matrix affords high surface area to facilitate electrochemical reactions, in contrast to pristine PEDOP. The FE-SEM image of PEDOP is shown in Figure 6.6. The pristine CP film has a granular morphology typical of electropolymerized CPs.

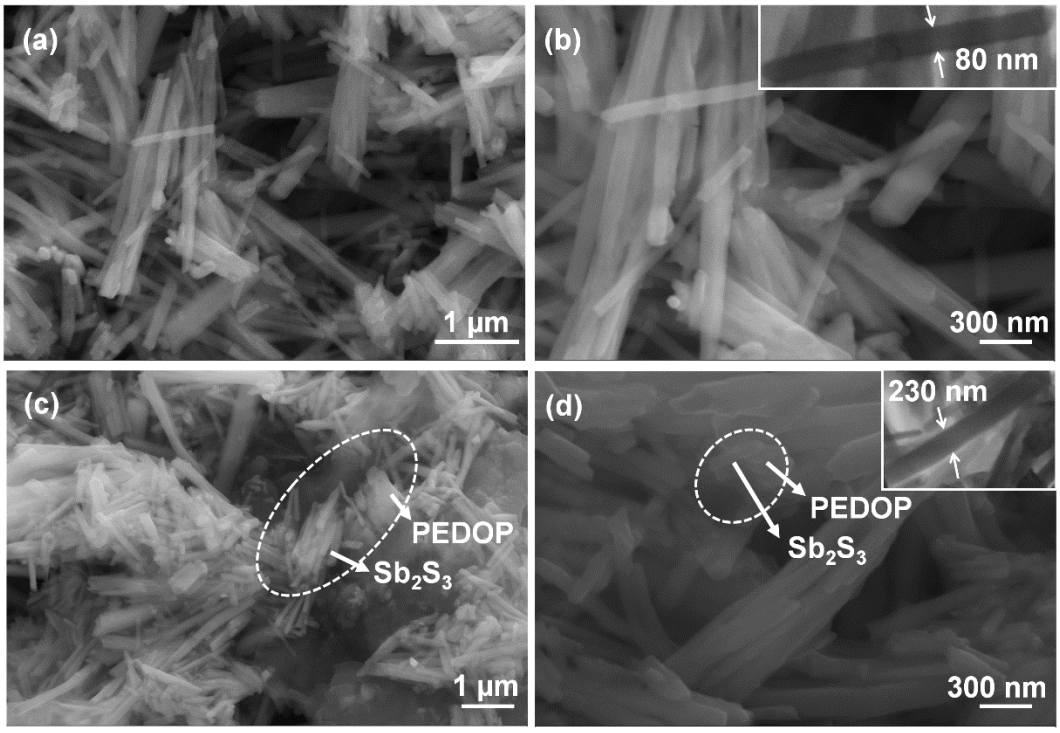

Figure 6.5: FE-SEM images of (a,b) Sb_2S_3 nanorods, (c,d) PEDOP/Sb_2S_3 films. Insets of (b and d) are enlarged high contrast images derived from the micrographs.

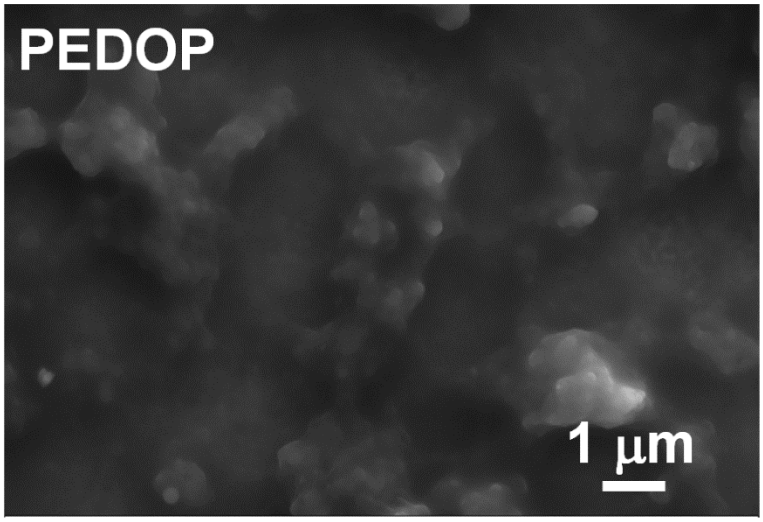

Figure 6.6: FE-SEM image of a pristine PEDOP film.

6.3.4 XPS studies of electrodes

The survey spectra of the PEDOP-Sb_2S_3 and pristine Sb_2S_3 films are shown in Figure 6.7. Signals from C1s, Sb3d, P2p, F1s, S2p and N1s levels are seen in survey spectrum of PEDOP, PEDOP-Sb_2S_3, and from Sb3d and S2p in Sb_2S_3. While the antimony and sulfur peaks indicate the inclusion of Sb_2S_3 quantum dots in the polymer matrix, the fluorine and phosphorous peaks imply the incorporation of the IL anion: $[(C_2F_5)_3(PF_3)]^-$ as the counter ion compensating the positive charge on the polymer (PEDOP) backbone. The deconvoluted C1s core level spectrum of PEDOP-Sb_2S_3 film (Figure 6.8a) consists of four components at 284.6, 286, 289.2 and 290.8 eV, which can be attributed to C-C, C-N, C-O and C-F linkages respectively. The N1s profile observed for the PEDOP-Sb_2S_3 film (Figure 6.8b) is asymmetric indicating that nitrogen prevails in two different chemical environments. The low energy peak at 399.5 eV arises from the -NH- bond of the pyrrole ring in the polymer and the high energy peak at 401.5 eV stems from the nitrogen of the 1-ethyl-3-methyl imidazolium cation. The insertion of the imidazolium cation along with the trialkylphosphate (FAP) anion in the polymer film, during oxidative electropolymerization, is not unusual, as has been observed in the past for PEDOT films doped

by IL functionalized graphene [7]. Since the charge on every imidazolium ion will be balanced by a charged FAP anion, the area under the $EtMeIm^+$ curve (denoted by I_{EtMeIm}^+) is a measure of the FAP counter-ion content in the polymer composite film. Therefore the ratio of I_{EtMeIm}^+ / $I_{N(total)}$ represents the doping level in PEDOP by the IL. The value of this ratio is 0.28, which is the doping level in PEDOP by FAP ions. Our value is close to a value of 0.3 reported in the past for PEDOT films doped by poly(styrene sulfonate) or PSS [8]. The atomic ratio of $I_{C(total)}$ / $I_{NH(pyrrole)}$ is ~ 7 for the PEDOP-Sb_2S_3 film, and is only slightly greater than the theoretical ratio of 6. A digression from the theoretical ratio of C:S, i.e., a value of 5:1 has been previously observed in films of PEDOT doped with dodecyl sulfate ions [9].The deconvoluted P2p spectra for the PEDOP-Sb_2S_3 film (Figure 6.8c) reveal two components at 135.5 and 134.2 eV due to the spin-orbit split, ascribable to $P2p_{1/2}$ and $P2p_{3/2}$ levels, and they originate from the PF_3 groups in the FAP anion [10]. The film also shows a single, intense, symmetric peak at ~689 nm arising from the F1s levels from the C-F and P-F bonds in the FAP anion. The twin peaks from Sb3d are clearly seen for the composite (Figure 6.8d), indicating the inclusion of Sb_2S_3.

The S2p core level spectrum of PEDOP-Sb_2S_3 consists of two peaks corresponding to the spin-split doublet: $S2p_{1/2}$ and $S2p_{3/2}$ at 163.8 and 162.3 eV respectively with a relative intensity of 1:2 (inset of Figure 6.8d). This doublet arises from sulfide in Sb_2S_3, as the polymer does not contain any sulfur. A crude estimate of the Sb_2S_3 content in PEDOP was also obtained from the ratio of the intensities of the split carbon peak's C-C component to the S2p peak; the I_{S2p}/ I_{C-C} was found to be 0.56.

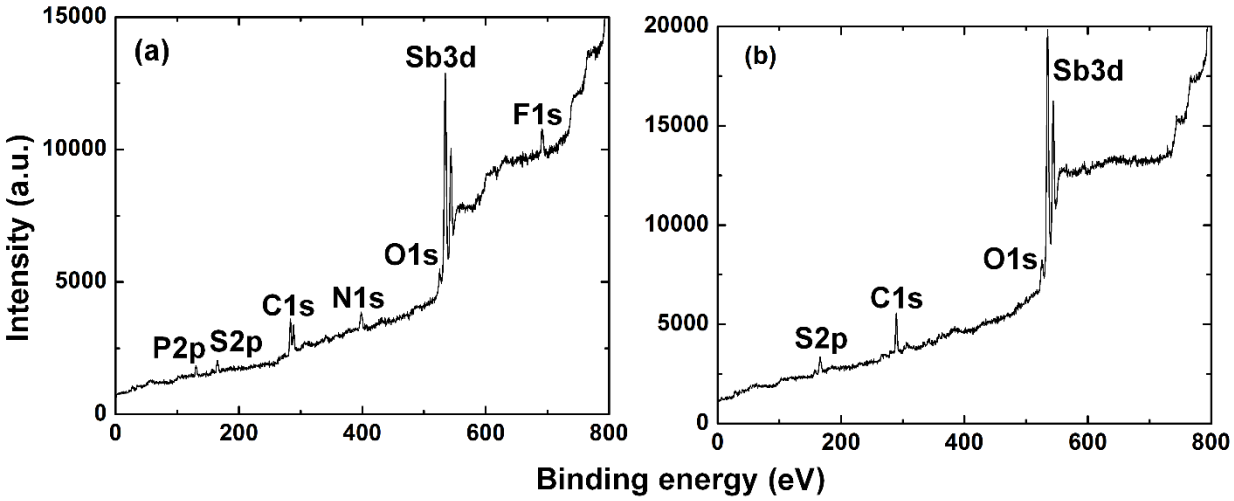

Figure 6.7: Survey spectra of (a) PEDOP-Sb_2S_3, (b) Sb_2S_3 illustrating the different elemental contributions in each sample.

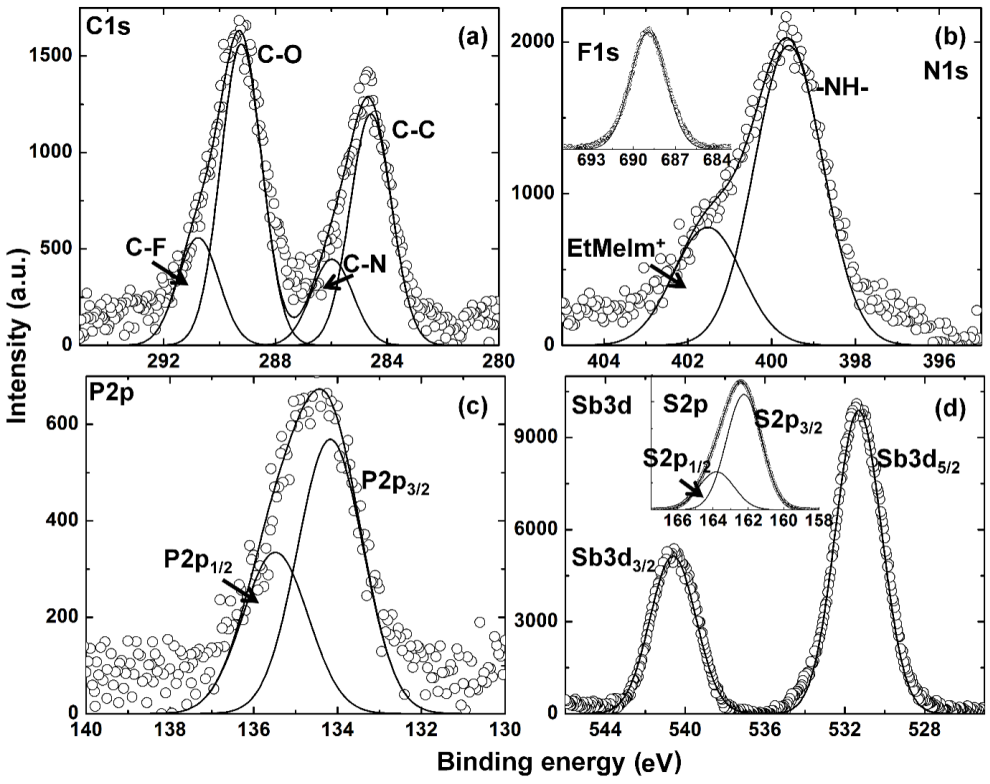

Figure 6.8: Deconvoluted core level spectra of (a) C1s, (b) N1s, (c) P2p and (d) Sb3d of a PEDOP-Sb_2S_3 film. Insets of (b) and (d) are the F1s and S2p core level spectra.

6.3.5 C-AFM studies on electrodes

Figure 6.9 shows the topography and current images simultaneously recorded for identical regions of Sb_2S_3 and PEDOP/Sb_2S_3 films; the scanned area was 5 μm × 5 μm for each film. The difference in the topography ongoing from Figure 6.4 to Figure 6.9 for the same samples (Sb_2S_3 and PEDOP/Sb_2S_3) arises from the different modes used for making the measurement. While contact mode is used in C-AFM, tapping mode is used for recording conventional topography images, and therefore the C-AFM images are slightly distorted. Here, the current images were generated by contacting a conductive tip with the film surface and a small bias voltage of 50 mV was applied. The current image of Sb_2S_3 nanorods shows uniformly distributed bright regions and an extraordinarily high current carrying capability, and as the maximum current flowing through the film is 1.1 μA. The maximum current the neat PEDOP film is capable of carrying is 12 nA and the number of high current bright domains are very sparse (Figure 6.11a and b). On incorporating Sb_2S_3 nanorods in the CP film, the current carrying capability of the polymer is considerably enhanced, which is also confirmed from a maximum current of 0.05 μA observed in the current image of PEDOP/Sb_2S_3. The current of the PEDOP/Sb_2S_3 film is 2 times greater than that of neat PEDOP film, for the same value of applied bias. In the PEDOP/Sb_2S_3 film, the enwrapping of the Sb_2S_3 nanorods by the polymer chains occurs at the molecular level, due to the single step potentiostatic deposition from a plating sol containing both the monomer and the Sb_2S_3 nanorods. The polymer is in direct contact with the Sb_2S_3 nanorods, and therefore the flow of electrons through the bulk of the composite is facile as the Sb_2S_3 nanorods possess an intrinsic ability to conduct electrons. Such an unobstructed electron propagation through the bulk of the neat PEDOP film is not realized, as it is relatively almost electronically insulating.

The current section profile of the composite film (Figure 6.10) complements the imaging, as the span of crests corresponding to high currents, is significantly wider than the (few) troughs corresponding to low currents. It is apparent that localized electron conduction, is rather uniform across the composite film. The exactly opposite response was obtained for the neat films, as very few peaks corresponding to high currents were observed (Figure 6.12). Point contact I-V curves were recorded at fifteen equidistant points on each current image, and the average I-V profile for each film is shown (Figure 6.9 c and f). A quasi-linear dependence of current on swept potential was confined to narrow voltage windows. From the straight-line fits, within the voltage windows in which the I-V response was almost linear, ambient temperature electronic conductivities were determined by using equation (1),

$$\sigma_{RT} = (I/V) \times (d/\pi r^2) \quad (1)$$

In (1) r is the radius of the conducting tip and d is the thickness of the film. The average electronic conductivities for Sb_2S_3 and PEDOP/Sb_2S_3 films were deduced from the ohmic regimes and were calculated to be 5 and 1.735 S cm^{-1} respectively. The nanoscale conductivity of neat PEDOP is determined to be 0.053 S cm^{-1}. The considerably enhanced average nanoscale conductivity of the composite film, 32 times greater than it's neat counterpart, shows that the Sb_2S_3 nanorods provide facile conduction pathways for electron movement and naturally enhance the conducting capacity of the polymer film.

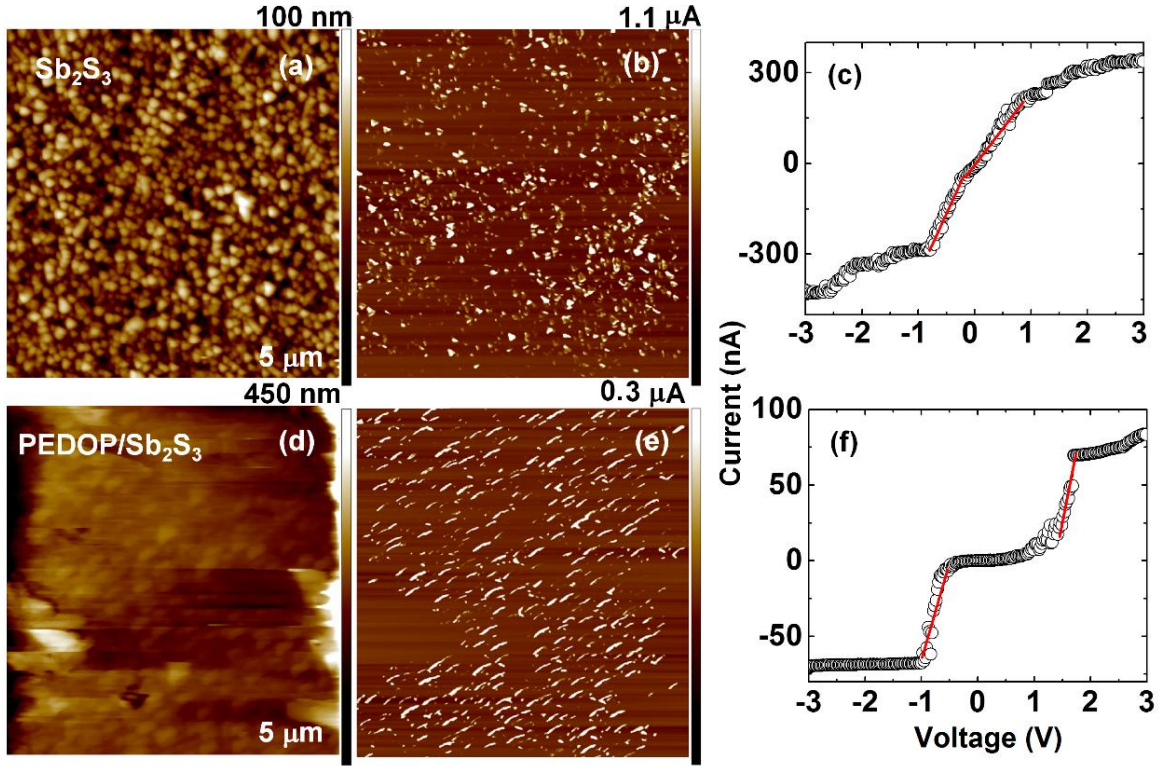

Figure 6.9: Concurrent topography and current images of (a,b) Sb_2S_3 nanorods, (d,e) PEDOP/Sb_2S_3, films recorded over scanned areas of 5 µm × 5 µm. Resultant current-voltage curves of (c) Sb_2S_3 nanorods, (f) PEDOP/Sb_2S_3, films. Each curve is averaged over 15 I-V curves recorded at 15 spots on each current image shown in b and e.

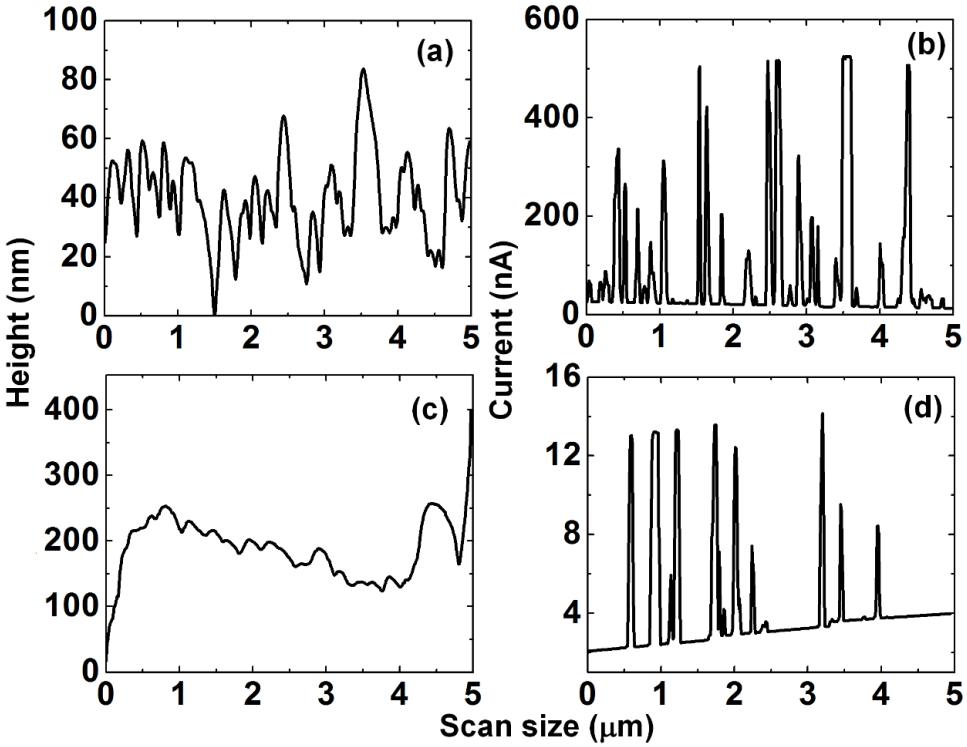

Figure 6.10: Cross section profiles of topography and current images of (a,b) Sb_2S_3 nanorods, (c,d) PEDOP/Sb_2S_3 (films recorded over scanned areas of 5 μm × 5 μm (corresponding to the images in Figure 6.9).

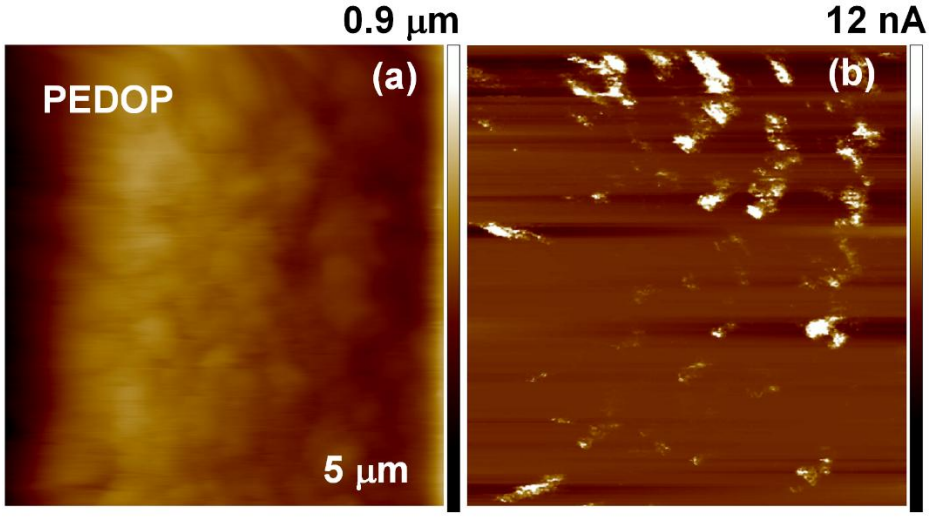

Figure 6.11: Simultaneous (a) topography and (b) current images of a neat PEDOP film.

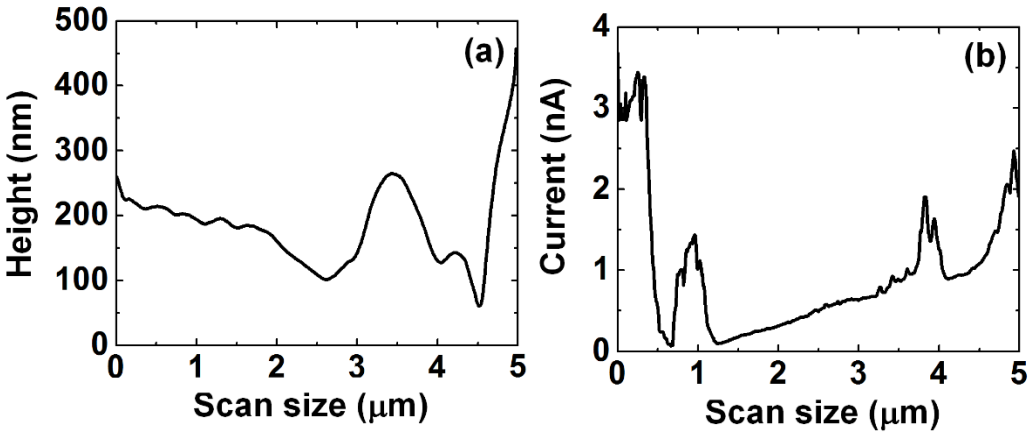

Figure 6.12: Cross section profiles of topography and current images of (a, b) neat PEDOP film recorded over scanned areas of 5 μm × 5 μm (corresponding to the images in Figure 6.11).

6.3.6 Cyclic voltammetric studies

Figure 6.13a show the comparison of cyclic voltammograms of neat films and their corresponding composites (PEDOP and PEDOP/Sb_2S_3), recorded at a constant scan rate of 50 mV s^{-1} in the potential range of 0 to +1 V. For the PEDOP/Sb_2S_3 composite, a quasi-rectangular voltammetric profile was observed, the slight undulations in the current density curve in the anodic scan, is a consequence of oxidation of the polymer. The polymer enwrapped Sb_2S_3 nanorods, have interconnected elongated tubular morphologies, and the FAP or $[(C_2F_5)_3(PF_3)]^-$ ions from the electrolyte percolate more easily and have better access to the electroactive sites as compared to the pristine polymer. The electrically conductive Sb_2S_3 nanorods are directly in contact with the PEDOP in the composite, which facilitate electron transport through the bulk of the composite and therefore improve the overall ion uptake capability of the electroactive electrode. Figure 6.13b displays the CV plots of the PEDOP/Sb_2S_3-Gr based supercapacitor cells recorded at different scan rates. All the curves retain an almost rectangular shape, even at a high scan rate of 100 mV s^{-1}, which is characteristic of low contact resistance of the supercapacitor. A similar observation was made for a graphene hydrogel-MnO_2 based supercapacitor in a previous

report [11].The increase in the redox current as a function of scan rate, observed for the composite cells, is suggestive of good rate capability.

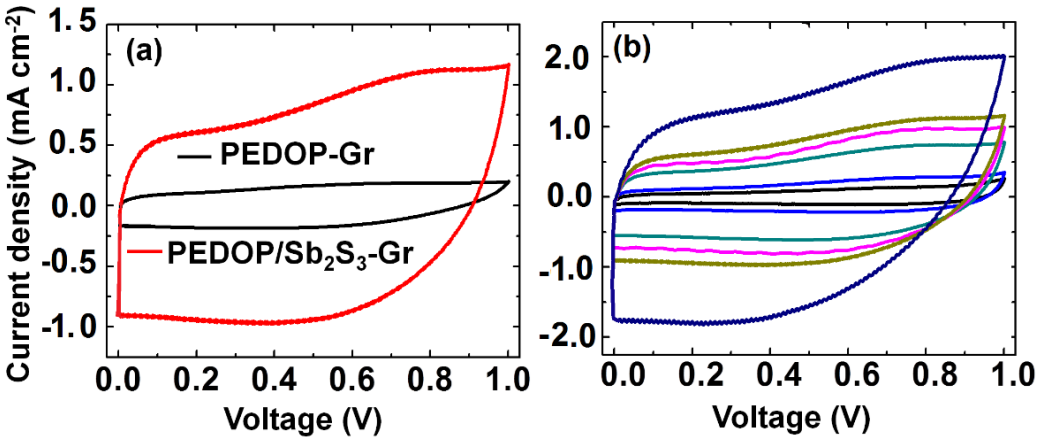

Figure 6.13: Cyclic voltammograms of (a) PEDOP-Gr, PEDOP/Sb_2S_3-Gr devices compared by recording at the same scan rate of 100 mV s^{-1} and (b) PEDOP/Sb_2S_3-Gr cells at different scan rates of 2, 5, 10, 20, 50 and 100 mV s^{-1}.

6.3.7 Charge-discharge characteristics of cells

The galvanostatic charge-discharge curves of PEDOP-Gr and PEDOP/Sb_2S_3-Gr cells (obtained at a fixed current density of 1 A g^{-1} using a potential window of 0 – 1 V) are shown in Figure 6.14a and b. Both cells show triangular shapes, implying that the potential of charge or discharge varies linearly with time, which is indicative of good reversibility. The charge/discharge times vary for different electrodes, for a fixed value of applied current density, thus indicating different specific capacitances. The specific capacitance was calculated from slope of the discharge curve and by using following equation.

$$SC = i \times \Delta t / \Delta V \times m \qquad (2)$$

In equation (2), SC is the specific capacitance, i is the current applied for discharge, Δt is the time in seconds for discharge, ΔV is voltage window and m is mass of active material of the working electrode.The specific capacitance for the PEDOP-Gr cell is 630 F g^{-1} in comparison to

a SC of 1008 F g^{-1} achieved for the composite, at the same current density of 1 A g^{-1}. The large difference in specific capacitance ongoing from the neat polymer to the corresponding composite, also points at the fact that the nanorods like morphology of Sb_2S_3 increases the anion intercalation capability of the polymer (by the virtue of large accessible surface area coated with the polymer). The higher accessible surface area to mass ratio achieved in the composites is responsible for the higher specific capacitances. The three-dimensional network of electrically conductive Sb_2S_3 nanorods serves as scaffold for the conducting polymers in the composites. In a previous report, Liu et. al. obtained a specific capacitance of 664 F g^{-1} for a composite PEDOT/RuO_2 hollow nanotube based cell [12]. In yet another study, a specific capacitance of 210 F g^{-1} was achieved for coaxial MnO_2/PEDOT nanowires [13]. Our values are comparable to literature values for CP nanostructured electrodes. The rate capability of the neat polymer and composite based cells was determined by recording the charge/discharge curves at different current densities of 0.2, 0.4, 0.6, 0.8 and 1 A g^{-1} (Figure 6.14b). The PEDOP/Sb_2S_3 composite retained 88% of its capacitance when the current density was increased from 0.2 to 1 A g^{-1}, thus indicating good rate performance. The rate performance of the neat polymer was abysmal, as the capacitance was only 630 F g^{-1} at a high current density of 1 A g^{-1}. The cycling stability of the PEDOP-Gr and PEDOP/Sb_2S_3-Gr cells was also compared. The variation of specific capacitance (obtained from the charge/discharge curves, at a current density of 1 A g^{-1}), as a function of galvanostatic charge/discharge cycles is shown in Figure 6.14c. At the end of 1000 charge/discharge cycles, while the PEDOP/Sb_2S_3-Gr cell retained 87% of its initial capacitance, the corresponding neat polymer cell maintained only 70% of its original capacitance. The greatly enhanced power density of the PEDOP/Sb_2S_3 composite supercapacitor (504 W kg^{-1}), relative to

315 W kg^{-1} for neat PEDOP cell is attributed to the fast charge-discharge rates effected by the lower ion-diffusion resistance offered by the composite.

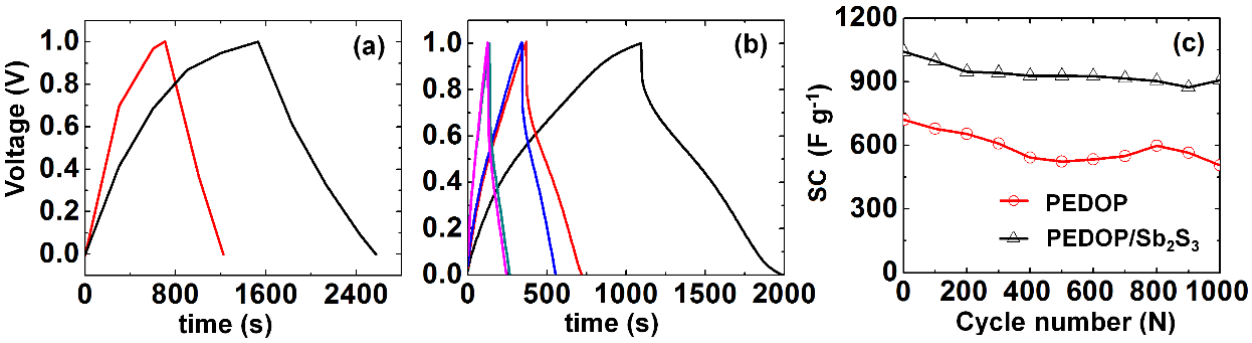

Figure 6.14: Galvanostatic charge-discharge curves of (a) PEDOP-Gr and PEDOP/Sb_2S_3-Gr cells at a fixed current density of 1 A g^{-1}, rate capability of (b) PEDOP/Sb_2S_3-Gr cell (at different current densities of 0.2, 0.4, 0.6, 0.8, 1.0 A g^{-1}) and cycling performance of (c) PEDOP-Gr and PEDOP/Sb_2S_3-Gr cells at a fixed current density of 1 A g^{-1}.

6.3.8 Electrochemical impedance spectroscopy

The Nyquist plots of PEDOP-Gr and PEDOP/Sb_2S_3-Gr cells recorded under an ac perturbation signal of 0.1 mV, in the frequency range of 0.01 to 1 M Hz are shown in Figure 6.15 and the related parameters are summarized in Table 6.2. Almost all the plots are composed of an arc followed by an inclined straight line. The undefined semicircle involves a parallel combination of interfacial resistance due to charge transfer (R_{CT}) and the corresponding electrical double layer capacitance (C_{dl}). The span of this arc is extremely small for both PEDOP/Sb_2S_3 composite as compared to the neat polymer. This indicates that the charge transfer resistance is small and the redox system is kinetically fast. The R_{CT} values are 296 Ω for PEDOP and 55 Ω for the PEDOP/Sb_2S_3 composite. The lower values of R_{CT} for the composites show that electron transfer from the composite to the underlying FTO electrode accompanied by anion transfer from the electrolyte to the composite are more facile relative to their rates in the neat PEDOP based cell. In the composite, the polymer coated Sb_2S_3nanorods allow the more number

of electrolyte ions to access redox active sites on the polymer easily. In the low frequency regime, the impedance plot increases steeply and becomes almost vertical for both the electrodes, characteristic of pure capacitive behavior. The extrapolation of the straight line, yields the x-axis intercept which is equal to $R_s + 1/3\ R_\Sigma$, where R_s is the uncompensated electrolyte resistance and R_Σ stands for ion diffusion resistance or an internal resistance (characteristic of the electrode material). The ion diffusion resistances were 240 and 9 Ω for the PEDOP and PEDOP/Sb_2S_3 composites.This implies that after the counterions are transferred from the bulk gel electrolyte to the PEDOP/Sb_2S_3 composite, ions can easily diffuse through this electrode comprising of the 3D network of polymer coated nanorods as compared to the neat electrode wherein ion-transport is hindered by the low electronic conductivity and also by the granular morphology. The EIS results reveal that the composite offers low resistance to ion diffusion in the electroactive phase and also to ion transfer at the electrolyte/film interface. The low internal resistance, for both electron and ion-movement in the PEDOP/Sb_2S_3-Gr composite based cell is responsible for the high capacitance attained by this cell even at a high charge-discharge rate. The fibrillar structures that prevail in the composite film afford short diffusion pathways thus improving the ion-transport properties of the composite. Such effects are not realized in the cells based on the neat PEDOP film and therefore the electrochemical performance is poor. The impedance plots for the PEDOP/Sb_2S_3-Gr cell before and after cycling have been compared in Figure 6.15b. After 1000 cycles, both ion-diffusion resistance and charge transfer resistance increase slightly, which is a manifestation of polymer swelling and shrinking upon repeated ion intercalation and de-intercalation.

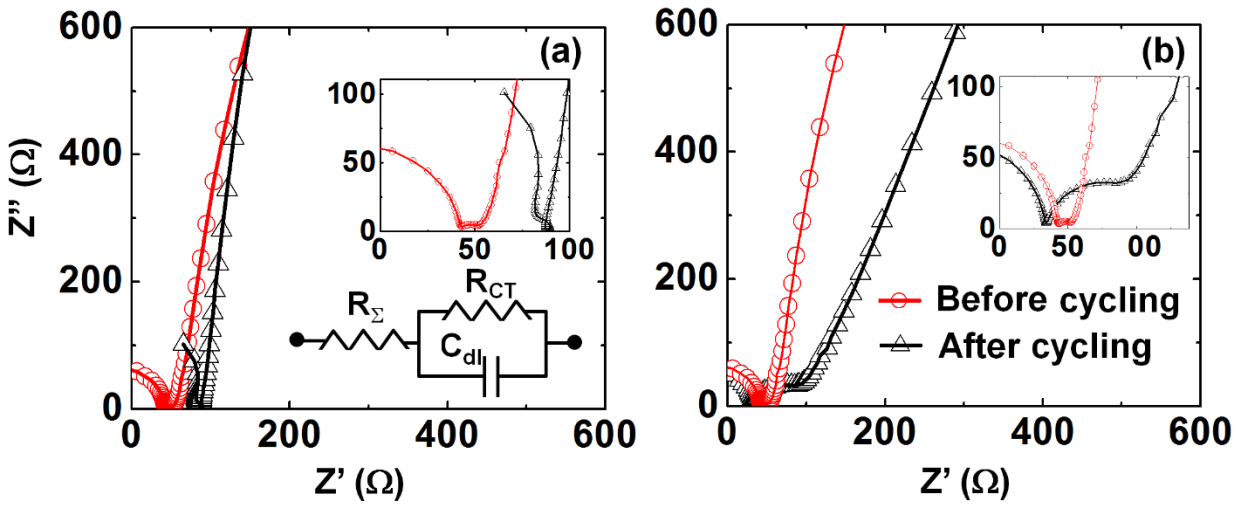

Figure 6.15: Nyquist plots of (a) PEDOP-Gr and PEDOP/Sb_2S_3-Gr cell, comparison of Z" *versus* Z' plots (b) before and after 1000 charge-discharge cycles of the composite based cell. PEDOP/Sb_2S_3-Gr all plots recorded in the frequency range of 0.01 Hz to 1 MHz. Corresponding insets show enlarged views of the same plots in the high frequency region. Inset of (a) shows the equivalent circuit used for fitting the experimental data.

Table 6.2: Impedance parameters for different working electrodes, with graphite as the counter electrode, determined from Figure 6.15.

Sample	R_{CT} (Ω)	R_{Σ}(Ω)	C_{dl} (μF)
PEDOP	296	240	51
PEDOP/Sb_2S_3	55	9	48
PEDOP/Sb_2S_3 (after 1000 cycles)	67	3	61

6.3.9 Flexible supercapacitor

The performance characteristics of the PEDOP/Sb_2S_3 motivated us to fabricate lightweight, flexible supercapacitors, using a carbon fiber cloth (sheet resistance ~ 2.7 Ω cm^{-2}, thickness ~ 3 mm, weight ~1.8 g cm^{-2}) instead of FTO coated glass. The cell was constructed with the following configuration: Carbon fiber cloth/PEDOP/Sb_2S_3-$EtMeIm^+$ $[(C_2F_5)_3(PF_3)]^-$/PMMA gel-Gr/Carbon fiber cloth, wherein, the graphite layer was electrophoretically deposited and the PEDOP/Sb_2S_3 composite was electropolymerized onto the carbon fiber cloth. The galvanostatic

charge-discharge plot recorded at a current density of 1 A g^{-1} and the CV plot of the cell recorded at 50 mV s^{-1} are shown in Figure 6.16. The specific capacitance was determined to be 150 F g^{-1}, which is comparable to the capacitance (150 F g^{-1} at 1 A g^{-1}) achieved for a flexible PEDOT based cell in a previous report [13]. A LED was also illuminated with this cell

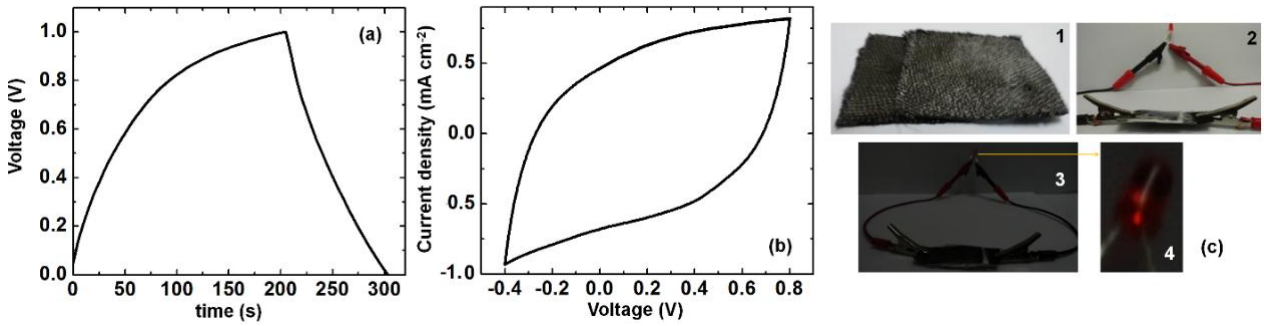

Figure 6.16: (a) Charge-discharge curve recorded at a current density of 1 A g^{-1} and (b) cyclic voltammogram (at 10 mV s^{-1}) of a flexible, thin quasi solid-state supercapacitor cell with the following configuration: Carbon fiber cloth/PEDOP/Sb_2S_3-gel electrolyte-Gr/Carbon fiber cloth. (c) Photographs of (1) flexible cell and (2-4) a LED being illuminated by the flexible cell.

6.4 Summary

Sb_2S_3 nanorods, extending in length to a few microns and 50-150 nm in width, and possessing unusually large bulk and nanoscale electronic conductivities were prepared by a hydrothermal method in a pre-step. A PEDOP/Sb_2S_3 composite electrode was electro-synthesized from a monomer-Sb_2S_3 nanorods' suspension. The enwrapping of Sb_2S_3 nanorods by PEDOP in the composite was ascertained by XPS and Raman studies. The high surface area afforded by the Sb_2S_3 nanorods steers the formation of PEDOP/Sb_2S_3 composite with fibrillar structures which is strikingly different from the conventional granular morphology achieved for the neat PEDOP film. C-AFM analyses also showed the presence of a large number of uniformly distributed high current domains in the composite in contrast to the neat polymer for which sparsely distributed high current spots embedded in largely insulating regions, spanning over a

few microns were observed. Further evidence for the effectiveness of Sb_2S_3 in serving as a 3D conductive scaffold, was obtained in terms of nanoscale conductivity of the PEDOP/Sb_2S_3 composite, which was 32 times higher in comparison to that obtained for the neat polymer. The role of Sb_2S_3 nanorods in greatly improving the ion uptake capability of PEDOP was reflected in the large specific capacitance of 1008 (at 1 A g^{-1}), good rate capability and repetitive cycling durability (88 and 85% capacitance retention after 1000 cycles) for asymmetric supercapacitors constructed with the composite and graphite as the electrodes. The greatly enhanced power density of the PEDOP/Sb_2S_3 composite supercapacitor (504 W kg^{-1}), relative to 315 W kg^{-1} for neat PEDOP cell is attributed to the fast charge-discharge rates effected by the lower ion-diffusion resistance offered by the composite. A practical demonstration of a LED illumination by use of a thin, lightweight, flexible supercapacitor constructed with PEDOP/Sb_2S_3 and graphite as the electroactive materials and a carbon-fiber cloth as the current collector, opens up possibilities for using this inexpensive facile approach for creating composites of conductive Sb_2S_3 nanorods with a plethora of other CPs as well for high performance supercapacitors.

References

[1] S. Cho, S. B. Lee, Acc. Chem. Res. 6 (2008) 699–707.
[2] A. Kumar, J. R. Reynolds, Macromolecules 29 (1996) 7629–7630.
[3] C. L. Gaupp, K. Zong, P. Schottland, B. C.Thompson, C. A. Thomas, J. R. Reynolds, Macromolecules 33 (2000) 1132–1133.
[4] B. N. Reddy, M. Deepa, A. G. Joshi, A. K. Srivastava, J. Phys. Chem. C 115 (2011) 18354–18365.
[5] B. N. Reddy, M. Deepa, Electrochim. Acta 70 (2012) 228–240.
[6] T. H. Perez, M. Morales, N. Batina, M. Salmona, J. Electrochem. Soc. 5 (2001) 369–375.
[7] A.P. Saxena, M. Deepa, A.G. Joshi, S. Bhandari, A. K. Srivastava, ACS Applied Mater. Interfaces3 (2011) 1115–1126.
[8] J. Hwang, F. Amy, A. Kahn, Org. Elec. 7 (2006) 387–396.
[9] N. Sakmeche, S. Aeiyach, J. J. Aaron, M. Jouini, J. C. Lacroix, P. C. Lacaze, Langmuir15 (1999) 2566–2574.
[10] I. Niedermaie, C. Kolbeck, N. Taccardi, P. S. Schulz, J. L, T. Drewello, P. Wasserscheid, H. P. Steinrück, F. Maier, ChemPhysChem 13 (2012) 1725–1735.
[11] H. Gao, F. Xiao, C. B. Ching, H. Duan, ACS Appl. Mater. Interfaces 5 (2012) 2801–2810.

[12] R. Liu, S. B. Lee, J. Am. Chem. Soc. 10 (2008) 2942–2943.
[13] S. Cho, D. H. Choi, S. H. Kim, S. B. Lee, Chem. Mater. 17 (2005) 4564–4566.

Chapter7

A PEDOP-gold nanoparticles-tungsten oxide based electrochromic pseudocapacitor

7.1 Introduction

Multifunctional hybrid materials based on CPs and inorganic transition metal oxides have sparked considerable research interest for the complementarity in their optical and electrical properties lead to devices that can outperform pristine polymer or oxide based devices. Such hybrid materials find use as active electrodes in diverse applications that include chemical sensors, supercapacitors, electrochromic devices, batteries and organic solar cells [1-5]. Among transition metal oxides, tungsten oxide (WO_3), due to a very high redox switching stability ($> 10^5$ cycles), large transmission modulation in the visible region corresponding to the colorless to deep blue transition, and good ion storage capacity is a versatile material useful for both electrochromic and supercapacitor applications [6]. Pseudocapacitors store energy by undergoing Faradaic charge transfer reactions [7] and electrochromic materials conserve energy by dynamically electro-modulating solar radiation by absorption [8].

A single material capable of performing both functions, undergoing charging (insertion of cations and deintercalation of anions) and coloration in tandem and on changing the polarity, discharging (removal of cations and insertion of anions) and bleaching simultaneously will permit the deduction of the charge storage level in the film, simply on the basis of its' color [9]. In a previous report, an electrochromic supercapacitor based on an ordered bi-continuous double-

gyroid V_2O_5 network with a specific capacitance of 155 F g^{-1} underwent a concurrent color change from green to yellow, which demonstrated the viability of using charge ingress/egress and color change together [10]. In another study, a poly(aniline) or PANI/WO_3 composite prepared by electropolymerizing aniline monomer onto a sol-gel based spin coated WO_3 film showed higher CE and specific capacitance compared to the pure components [11]. The complementary properties of the two materials, such as the high electrical conductivity of PEDOP can make the WO_3 matrix more conducting and the large surface area and the porous assembly afforded by the WO_3 fibers can serve as a scaffold for coating the polymer, to yield a fibrillar morphology as opposed to a granular one. The CE of the hybrid is expected to be higher than the individual electrochromes, as they will both undergo color change in response to the external stimulus. Both PEDOP and WO_3 are pseudocapacitive materials, as they undergo charge/discharge via reversible Faradaic charge transfer processes, and as a result the specific capacitance of the hybrid will be high, for it will include contributions from both of them. Further, pristine conducting polymers electrodes suffer from poor cycling stability due to their brittle texture and low mechanical strength [12,13]. Coupling PEDOP with WO_3, where WO_3 has excellent cycling lifetime and good mechanical strength is an effective approach to overcome the limitations posed by PEDOP.

7.2 Experimental

7.2.1 Preparation of WO_3, PEDOP and hybrid films

WO_3 powder was prepared by a hydrothermal process. Tungsten powder (1 g) was weighed in a 50 mL beaker and H_2O_2 (15 mL) was added gradually. The mixture was stirred for 20 min. and after the effervescence had subsided, the resulting colorless sol of peroxotungstic acid was

transferred to an autoclave of 50 mL capacity and heated for 12 h at 180 ^{o}C. A light yellow precipitate of WO_3 was obtained which was washed with deionized water repeatedly and dried at room temperature. WO_3 powder (0.1 g) and ethyl alcohol (20 mL) were taken in a 25 mL beaker and this mixture was sonicated for 15 min. A white suspension was obtained; two FTO/glass electrodes were immersed in the suspension and a dc potential of 10 V was applied for 5 min using a Tarsons electrophoresis power supply unit. A thin transparent layer of WO_3 was deposited onto one of the two FTO/glass electrodes. The WO_3 films were washed with deionized water, heated at 80 ^{o}C for 30 min. in an oven and subsequently annealed at 500 ^{o}C in a furnace for 1 h and stored in a desiccator.

Gold nanoparticles were prepared using a citrate reduction method [14]. An aqueous solution of auric chloride was prepared in a 50 mL beaker with $HAuCl_4$ (6 mg). In a separate beaker, a solution of tri-sodium citrate (4.4 mg) was prepared in ultrapure water (2 mL). The citrate solution was added drop-wise to auric chloride solution with constant stirring, over a period of 10 min. A deep pink colored colloid of Au nanoparticles was obtained and used without any further treatment.

The transparent WO_3 film was immersed in a gold colloid for 2 h to enable the Au nanoparticles to tether to the oxide vis-à-vis the electrostatic attraction between the carboxylate groups on citrate capped Au and the W^{+6} centers. The resulting WO_3@Au film was dried in air. A 0.1 M EDOP solution was prepared in 20 mL of acetonitrile and PSS (0.2 g) was dissolved in the solution. A three electrode electrochemical cell with a FTO/glass electrode as the counter electrode, Ag/AgCl/KCl as the reference electrode and an Au@WO_3 film as the working electrode was used for the oxidative electropolymerization of 3,4-EDOP. Upon application of a

dc potential of +1.4 V for 500 s to the working electrode, a PEDOP-Au@WO_3 hybrid film was obtained. Pristine blue-black colored PEDOP films were obtained when FTO/glass was employed was the working electrode (scheme 7.1). The films were washed in acetonitrile and dried in air.

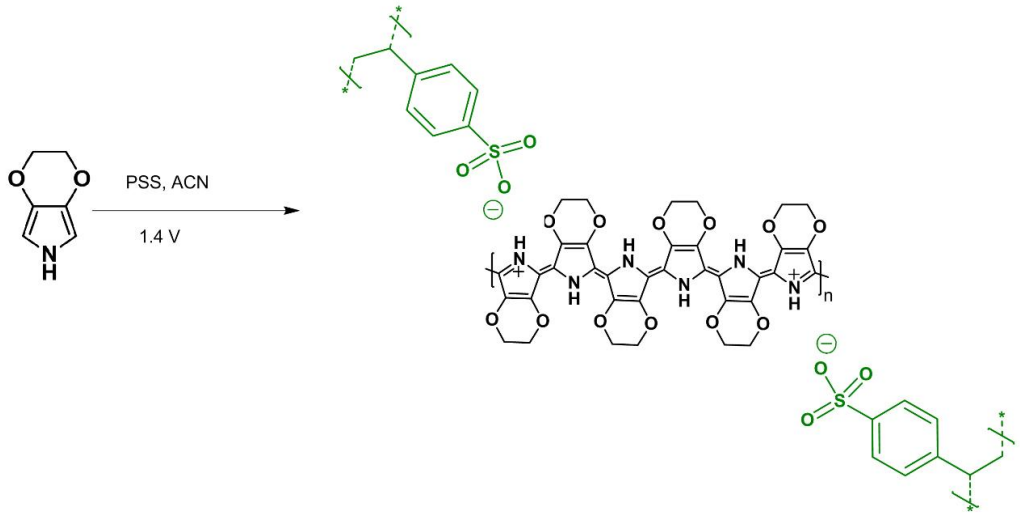

Scheme 7.1: Electrodeposition of PEDOP films.

7.3 Results and discussion

7.3.1 Deposition curves

The current-time transient curves corresponding to the formation of PEDOP on pre-cleaned FTO/glass or an Au@WO_3 film by oxidative electropolymerization, under potentiostatic conditions (E = +1.4 V) from a precursor solution containing the monomer EDOP and the dopant PSS are shown in Figure 7.1. In both cases, at the start, at t = 0 s, the current shows an abrupt spike, which is attributed to the double layer capacitance charging, and it is followed by a gradual decline. The depleting current regime corresponds to the formation of monomer cation

radicals which is followed by oligomerization and a coupling polymerization that terminates with the formation of a blue-black colored PEDOP deposit either on the neat conducting substrate or on the Au@WO_3 film to yield PEDOP and PEDOP-Au@WO_3 films respectively.

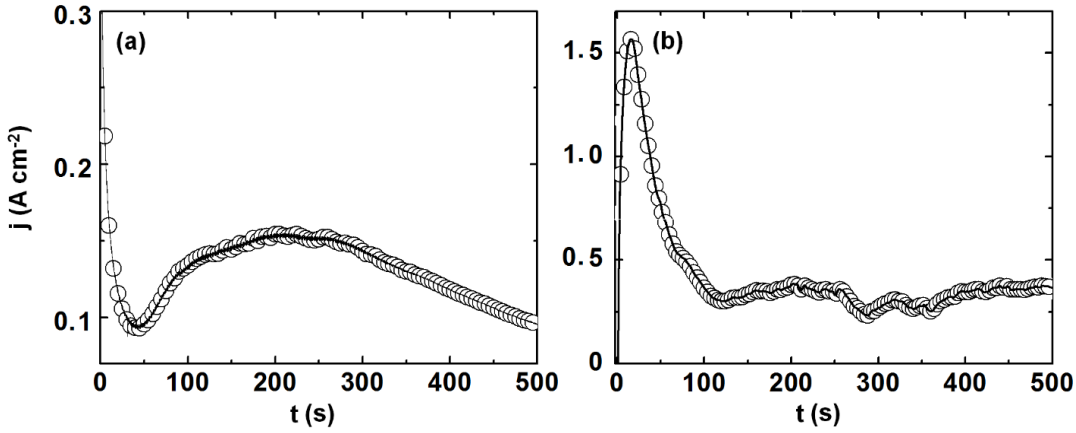

Figure 7.1: Current density *versus* time transients recorded for the oxidative electro-synthesis of (a) PEDOP and (b) PEDOP-Au@WO_3 hybrid films from a solution of 0.1 M 3,4-EDOP and 0.2 g PSS in acetonitrile.

7.3.2 Structural aspects

The X-ray diffractograms of Au nanoparticles, pristine WO_3, PEDOP and Au@WO_3 electrodes are shown in Figure 7.2(i). The XRD pattern of Au nanoparticles shows four prominent Bragg reflections at around 38.2°, 44.7°, 64.5° and 78.3° which match well with the d-values corresponding to the face centered cubic lattice of Au as per the JCPDS file no. 04-0784. The intensity of the (111) plane is much higher compared to the (200), (220) and (311) diffraction peaks, suggesting that the (111) plane is the predominant orientation. The XRD pattern of the PEDOP electrode shows a broad hump centered at $2\theta = 26^{o}$ and d = 1.76 Å, confirming the amorphous structure of the PEDOP:PSS electrode. The XRD pattern of WO_3 showed dominant peaks at d = 3.5, 3.36 and 3.35 Å, which were indexed to the monoclinic

crystal structure of WO_3 (ICDD-PDF2-2004 01-072-0677). These peaks were assigned to the (002), (020) and (200) planes of WO_3, respectively. The XRD pattern of Au@WO_3 showed the same cluster of three peaks corresponding to WO_3 and in addition, peaks at d = 2.3, 2.0, 1.4 and 1.2 Å were also observed, which match with the (111), (200), (220) and (311) reflections of Au with a fcc structure, thus indicating that Au nanoparticles are attached to WO_3, as expected.

The Raman spectra of WO_3, PEDOP, Au nanoparticles, Au@WO_3 and PEDOP-Au@WO_3 are shown in Figure 7.2(ii). For WO_3, the bands centered at 807 and 716 cm^{-1} arise from W–O stretching, and the two bands located at 327 and 273 cm^{-1} belong to the O–W–O bending modes. The Raman bands agree well with the reported bands for the δ-phase of monoclinic WO_3 [15]. For PEDOP, the C–C vibrational stretching mode is seen in the range of 1330–1350 cm^{-1} and it arises from the pyrrole rings on the polymer backbone [16]. The symmetric stretching mode of C–C–O groups of PEDOP produces a peak at 1400 cm^{-1}. A cluster of low intensity peaks is observed in the 1200-1300 cm^{-1} region, and these originate from the C–N stretching vibrations of the pyrrole rings. A medium intensity band at ~715 cm^{-1} is ascribed to the N–H out-of-plane bending mode and it is observed at ~711 cm^{-1} in the hybrid. Au nanoparticles shows peaks at 1380 and 1590 cm^{-1} corresponding to the symmetric and asymmetric stretching of C-O bond from the citrate cap [17]. The Au@WO_3 film shows peaks at 807, 716 cm^{-1} and 327, 273 cm^{-1} corresponding to W–O stretching and O–W–O bending modes. The PEDOP-Au@WO_3 film shows distinct peaks at 350and 1370, 1400 cm^{-1} due to lattice vibrational mode of Au, C-C and C-C-O stretching modes, thus confirming the inclusion of PEDOP and Au in the hybrid film.

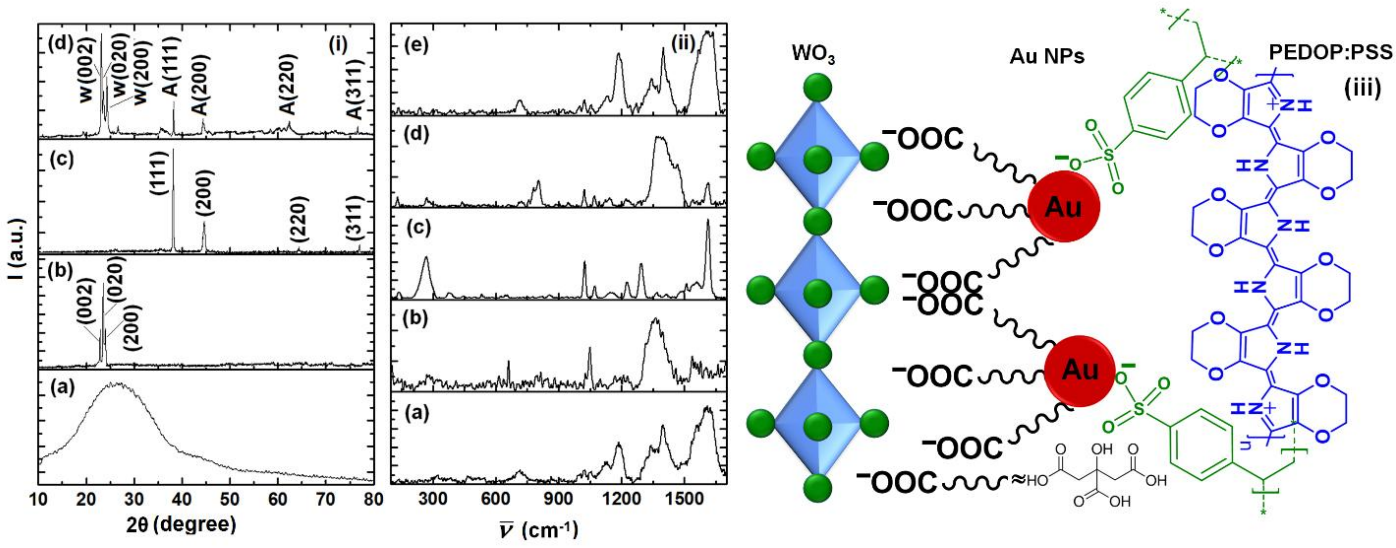

Figure 7.2: (i) XRD patterns of (a) PEDOP, (b) WO_3, (c) Au nanoparticles and (d) Au@WO_3 films, (ii) Raman spectra of (a) PEDOP film, (b) WO_3 film, (c) Au nanoparticles, (d) Au@WO_3 film and (e) PEDOP-Au@WO_3 hybrid film and (iii) schematic of WO_3-Au-PEDOP:PSS interactions in the hybrid film. W and A in (i) represent WO_3 and Au respectively.

7.3.3 Morphology and nanoscale conduction

The SEM micrographs and energy dispersive X-ray analysis (EDX) plots of WO_3, Au@WO_3, PEDOP and PEDOP-Au@WO_3 films are shown in Figure 7.3. The low and high magnification images of WO_3 reveal the presence of densely packed and interlinked network of fibrillar shapes with tapered ends. The morphology is akin to the topography seen in the corresponding AFM image (Figure 7.4), thus confirming that the film is composed of randomly organized but highly compact framework of WO_3 fibers with distinct grain boundaries. The fiber lengths vary between 100 to 250 nm. The WO_3 fibers acquire distorted shapes and appear as blobs, 50 to 200 nm in size when the film is coated with Au nanoparticles, as in the Au@WO_3 film (Figure 7.3c and d). The particles now have irregular shapes with indistinctive grain boundaries but continue to retain their mingling characteristic which is useful for ion and electron transport during

charge/discharge or color-bleach process. While the EDX pattern of WO_3 revealed distinct signals from W and O, the EDX of Au@WO_3 film shows signals from W, Au and O thus confirming the inclusion of Au in the film. The morphology of the pristine PEDOP film is relatively featureless, and the film appears to be composed of agglomerated polymer particles of no particular shape. Signals from C, N and O are seen in the corresponding EDX plot, which are the elements that constitute the backbone of the polymer. The PEDOP-Au@WO_3 hybrid film is composed of an interconnected framework of aggregated particles with indistinctive shapes. The film is highly porous and the pore sizes vary from 0.5 to 1 μm. The EDX pattern shows signals from C, N, O, Au and W, thus indicating the presence of the polymer and Au along with WO_3 in the hybrid, which is line with the rationale used for fabricating the hybrid. Since only the WO_3 morphology was distinctive, and the subsequent incorporation of Au or PEDOP led to relatively featureless morphologies, the AFM images of pristine WO_3 were recorded over different length scales (Figure 7.4). A 3D network of randomly oriented fibers, with lengths in the range of 50 to 200 nm and widths ranging from 20 to 60 nm was observed. In the low magnification image no irregular shaped particles of WO_3 were observed which implied that the fiber like morphology is uniform across the film.

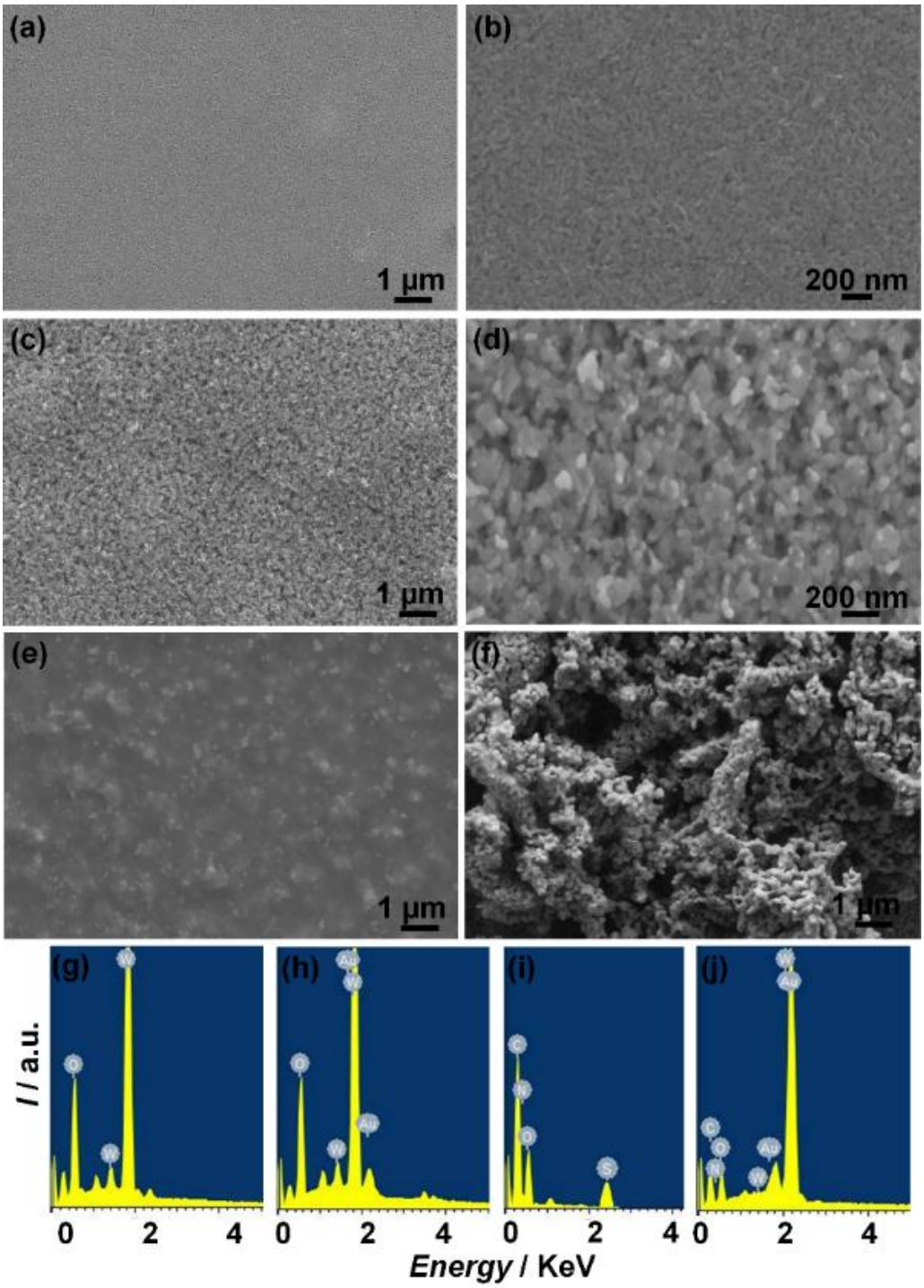

Figure 7.3: SEM micrographs of (a,b) WO_3, (c,d) Au@WO_3, (e) PEDOP and (f) PEDOP-Au@WO_3 films and EDX plots of (g) WO_3, (h) Au@WO_3, (i) PEDOP and (j) PEDOP-Au@WO_3 hybrid films.

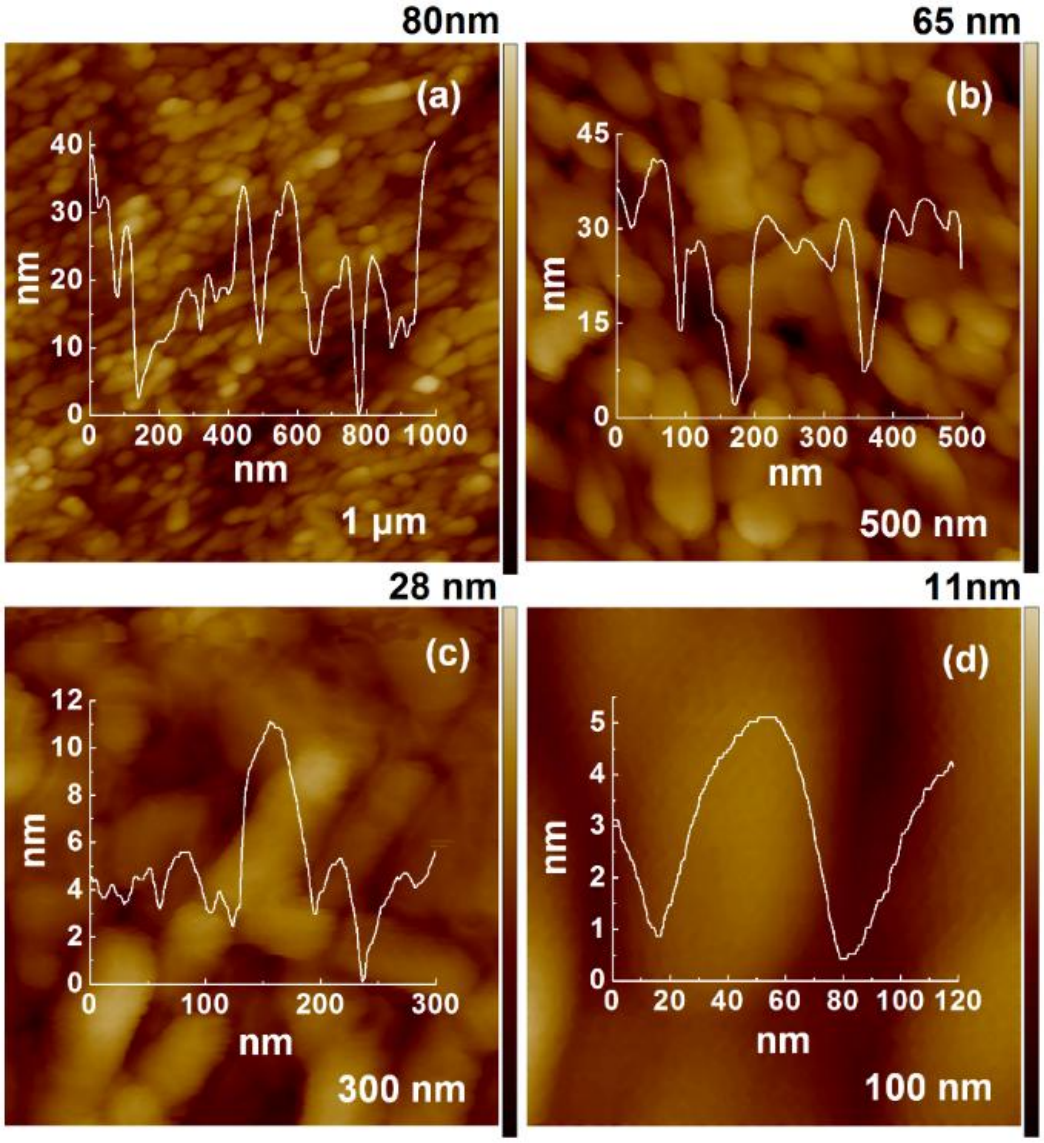

Figure 7.4: Topography images of WO_3 over different regions of the same film with scan sizes of 1μm × 1 μm, (b) 0.5 μm × 0.5 μm, (c) 0.3 μm × 0.3 μm and (d) 0.1 μm × 0.1 μm. Insets show the corresponding section profiles.

The topography and current images recorded concurrently over scanned areas of 1 μm × 1 μm for the WO_3, PEDOP and PEDOP-Au@WO_3 films are shown in Figure 7.5. The WO_3 electrode film comprises of elongated particles but the topography is distorted as in C-AFM, the tip contacts the surface which adversely affects the image. Both PEDOP and WO_3 showed

featureless topographies. The currents flowing through films were mapped by applying a dc bias (50 mV) to the tip, whilst the tip ran horizontally over the surface (Figure 7.5a, c and e). Their section profiles are shown in Figure 7.6.The maximum currents achieved for the WO_3, PEDOP, PEDOP-Au@WO_3 films were 0.03, 12 and 24 nA, thus indicating the hybrid film is capable of conducting higher currents relative to PEDOP or WO_3. Point contact I-V curves were recorded at fifteen equidistant points on each current image, and the average I-V profile for each film is shown (Figure 7.5c, f and i). The straight-line fits, within the voltage windows in which the I-V response was almost linear, room temperature electronic conductivities were determined by using equation (1).

$$\sigma_{RT} = (I/V) \times (d/\pi r^2) \qquad (1)$$

In (1), r is the radius of the conducting tip and d is the thickness of the film. The average nanoscale electronic conductivities of WO_3, PEDOP and PEDOP-Au@WO_3 films deduced from the ohmic regimes were 0.64, 0.015 and 0.88 S cm^{-1} respectively. The superior electronic conductivity of the hybrid compared to pristine polymer or oxide is expected to be advantageous for facilitating charge transport through the bulk of the film during oxidation and reduction. The presence of metallic gold nanoparticles in the hybrid is responsible for it's enhanced nanoscale conductivity.

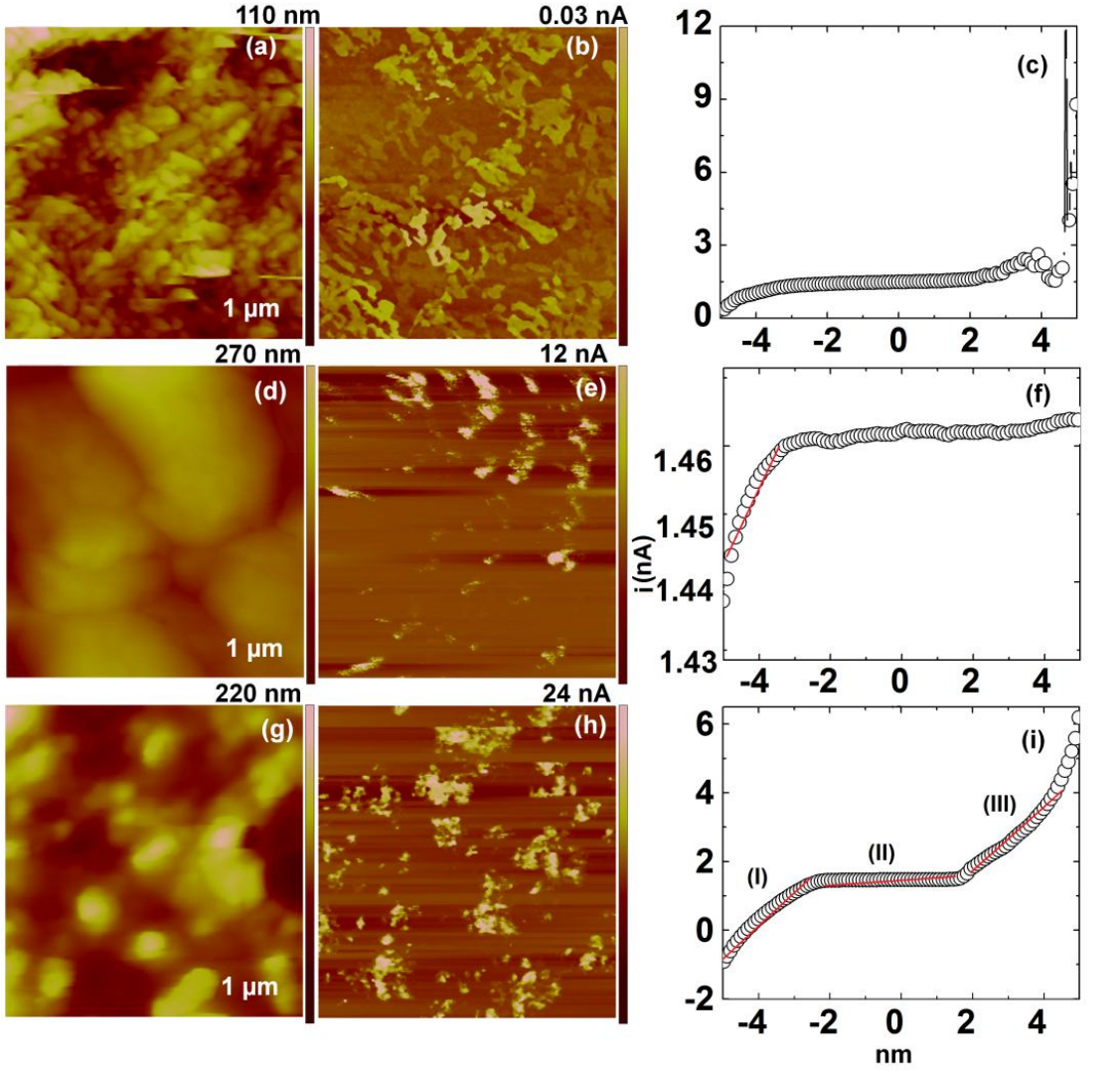

Figure 7.5: Concurrent topography and current images of (a, b) WO_3, (d, e) PEDOP, (g, h) PEDOP-Au@WO_3 hybrid films recorded over scanned areas of 1 µm × 1 µm. Resultant current-voltage curves of (c) WO_3, (f) PEDOP, (i) PEDOP-Au@WO_3 hybrid films. Each curve is averaged over 15 I-V curves recorded at 15 spots on each current image shown in b, e and h.

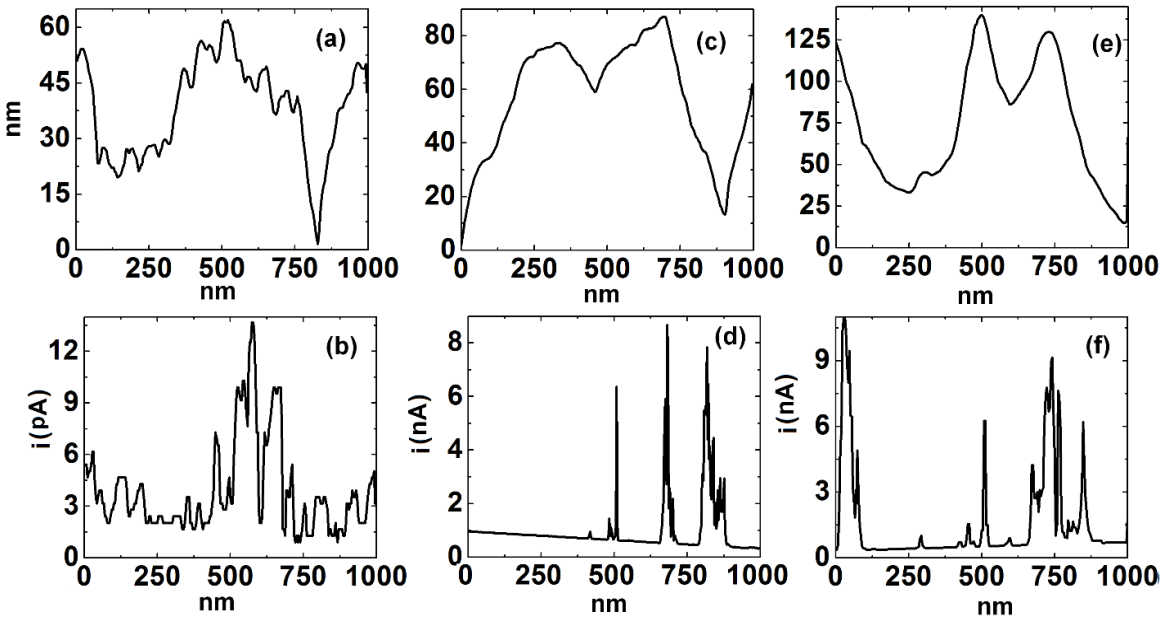

Figure 7.6: Cross section profiles of topography and current images of (a,b) WO_3, (c,d) PEDOP, (e,f) PEDOP-Au@WO_3 hybrid films(corresponding to the images (a,b), (d,e) and (g,h) respectively in Figure 7.5).

7.3.4 Electrochemical behavior

The cyclic voltammograms of WO_3, PEDOP and PEDOP-Au@WO_3 hybrid films recorded at different scan rates in the IL: 1-butyl-3-methyl imidazolium triflate with a Pt rod as the counter electrode are shown in Figure 7.7. The CV plot of WO_3 film recorded at a scan rate of 2 mV s^{-1} shows a broad oxidation peak –0.24 V in the anodic branch corresponding to de-intercalation of lithium ions and electrons from WO_3. This is followed by a shoulder at –0.46 V in the cathodic sweep signifying reduction involving concomitant intercalation of lithium ions from the electrolyte and electrons from the external circuit into the WO_3 film. The CV profile is retained as the scan rate is successively raised from 2 to 100 mV s^{-1}, albeit the fact that the cathodic shoulder is not perceptible scan rates above 30 mV s^{-1}. The reversible redox process operational

in WO_3 is shown in equation (2) and the CV curves observed by us are similar to the ones reported for sol-gel derived WO_3 films [18].

$$WO_3 + xe^- + x[BmIm]^+ \leftrightarrows [BmIm]_xWO_3 \quad (2)$$

The CV curve for PEDOP film is featureless in the cathodic branch, but two shoulders are observed at –0.2 and –0.43 V in the anodic sweep (at 2 mV s^{-1}). These peaks indicate the stepwise insertion of triflate ions and extraction of $[BmIm]^+$ ions from the neutral polymer to yield the oxidized PEDOP. The voltammograms do not exhibit well-defines anodic/cathodic peaks in the voltage range at any scan rate, and similar featureless curves have been observed for PEDOT doped by Szymanska etal., in the past [19]. The CV plot of the PEDOP-Au@WO_3 hybrid film recorded at 2 mV s^{-1} shows an oxidation peak at +0.33 V followed by a reduction peak at +0.11 V in the reverse sweep. Both the reduction and oxidation peaks shift to more negative potentials as a function of increasing scan rate. The reduction peak is observed at –0.11 V in plot recorded at 100 mV s^{-1}. The oxidation peak ceases to exist at scan rates above 30 mV s^{-1}, as it is seen at +0.17 V at 20 mV s^{-1}. The oxidation peak can be ascribed to conversion of PEDOP's state from neutral to radical cation state and transformation of tungsten oxide to tungsten bronze. The charge storage capacities obtained by integrating the area under the voltammograms recorded at 100 mV s^{-1} are 0.0032, 0.05 and 0.2 mC cm^{-2} for WO_3, PEDOP and PEDOP-Au@WO_3 hybrid films. The higher ion storage capacity obtained for the hybrid illustrates the combined enhancement in its ion uptake capability due to PEDOP and WO_3. The mechanism for charge storage in WO_3, PEDOP and PEDOP-Au@WO_3 films is by electrochemical oxidation and reduction or pseudocapacitance, and in the hybrid the charge storage capacity is increased as the WO_3 fibers by the virtue of their structure comprising of

elongated-shapes permit more ions to intercalate and the high electrical conductivity of PEDOP allows facile electron transport in the hybrid, an advantage which cannot be realized in pristine WO_3 films, which are largely ion conducting but electronically insulating. Although in PEDOP, the benefit of good electronic conductivity of PEDOP contributes to improving its' capacitance, but the ion intercalation-deintercalation capacity via electrochemical oxidation and reduction is adversely affected compared to the PEDOP-Au@WO_3 hybrid, owing to the regular granular morphology of the pristine polymer. In the hybrid, the polymer PEDOP is coated over the WO_3 fibers and is also linked to the oxide through the Au monolayer. The poly(styrene sulfonate) dopant in PEDOP flanks to the Au monolayer and this link is the interconnect between the two pseudocapacitive layers: WO_3 and PEDOP. As a consequence, the fibrillar morphology of PEDOP-Au@WO_3 hybrid allows for greater ion insertion compared to pristine granular PEDOP.

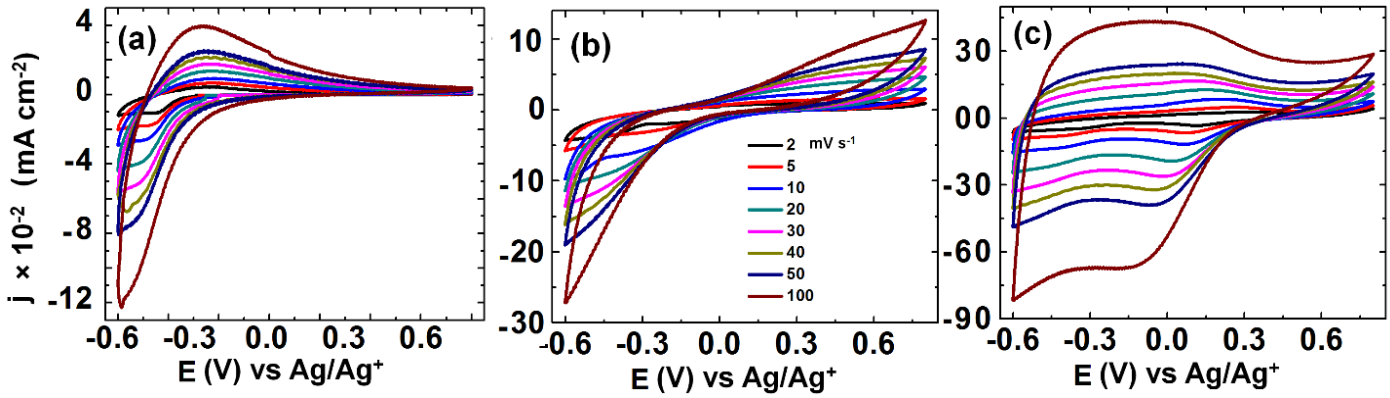

Figure 7.7: Cyclic voltammograms of (a) WO_3, (b) PEDOP and (c) PEDOP-Au@WO_3 hybrid films recorded at different scan rates of 5, 10, 20, 30, 40, 50 and 100 mV s^{-1}. Pt was used as counter electrode and the IL: 1-butyl-3-methyl imidazolium triflate was used as the electrolyte.

Galvanostatic charge-discharge curves (at 1 A g^{-1}) of the WO_3, PEDOP and PEDOP-Au@WO_3–PEDOP hybrid electrodes with 1-butyl-3-methyl imidazolium triflate as the electrolyte are displayed in Figure 7.8a. The polymer and WO_3 exhibit almost symmetric charge-

discharge curves and their specific capacitances are 14 and 30 F g^{-1} respectively. The PEDOP-Au@WO_3–PEDOP hybrid shows a SC of 130 F g^{-1}, which is 4 and 10 times greater than that attained for the WO_3 and polymer films. This excellent capacitive behavior of the PEDOP-Au@WO_3 film is attributed to the combined pseudocapacitances of WO_3 and PEDOP. An IR drop at the turning point of the charge-discharge line was observed only for the PEDOP-Au@WO_3, probably arises from Au nanoparticles, and the magnitude of IR drop was enlarged at the higher current density, as can be judged from the rate capability curves. The rate performance of the PEDOP-Au@WO_3 films was evaluated by charging/discharging at different current densities ranging between 0.2 to 1.6 A g^{-1} (Figure7.8b). The specific capacitance decreased from 260 to 95 F g^{-1} upon increasing current density from 0.2 to 1.6 A g^{-1}. The capacitive retention of PEDOP-Au@WO_3 was about 36% in the current loading range of 0.2 to 1.6 A g^{-1}. These observations revealed that the combination of PEDOP with WO_3 leads to improved rate performance and capacitance which can be explained by the synergic effect of the high surface area provided by the WO_3 fibers which not only allows for increased loading of PEDOP, but also affords more number of electrochemically addressable sites available for ion uptake upon application of electric voltage or current. The uniform coating of PEDOP on WO_3 fibers also prevents them from aggregating, resulting in improved accessibility for ingress of electrolyte ions. In a previous work, a SC of 115 F g^{-1} was achieved for PEDOT spheres [20] and in yet another study Szymanska et al. reported a SC of 205 mF cm^{-2} for a WO_3/PEDOT composite [19]. A WO_3/PANI composite film exhibited good pseudocapacitive performance over a wide potential range of −0.5 to 0.7 V *versus* SCE with a SC of 168 F g^{-1} at a current density of 1.28 mA cm^{-2} [21]. The cycling stability of the films recorded at a current density of 1 A g^{-1} is shown in Figure 7.8c. At the end of 100 cycles, the PEDOP-Au@WO_3 hybrid film showed a

capacitance of 90 F g^{-1} compared to much lower values of 10 and 4 F g^{-1} obtained for the WO_3 and PEDOP. The hybrid film retained 70% of its' original capacitance upon repetitive cycling, thus indicating the suitability of this film for supercapacitor applications.

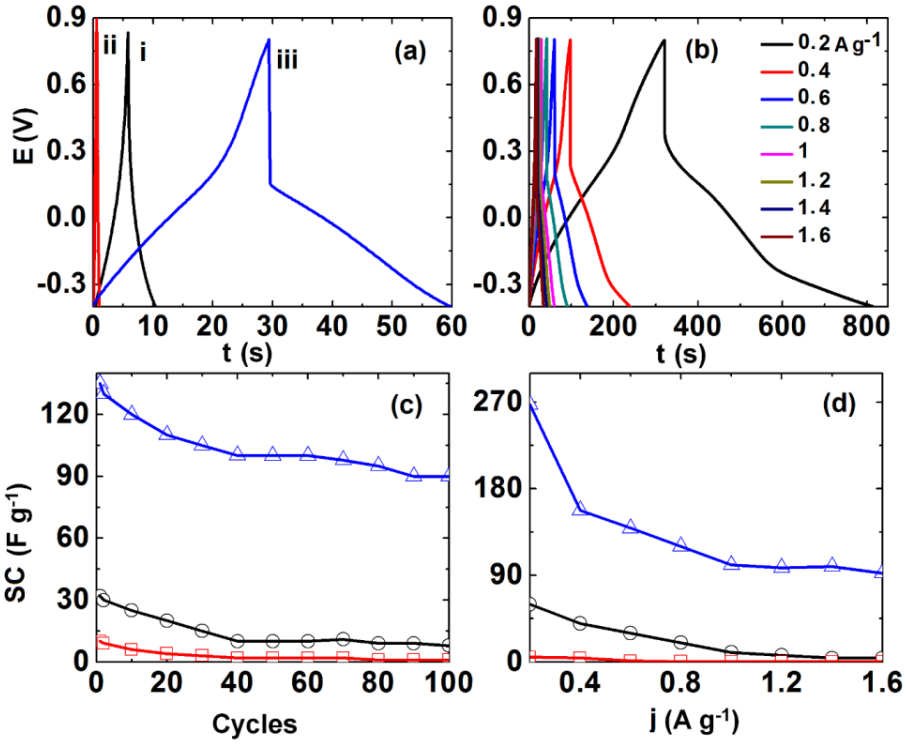

Figure 7.8: Galvanostatic charge-discharge curves of (i) WO_3, (ii)PEDOP and (iii) PEDOP-Au@WO_3 hybrid films at a current density of 1 A g^{-1}, (b) rate capability of PEDOP-Au@WO_3 hybrid film (at different current densities between 0.2 - 1.6 A g^{-1}), (c) cycling response (at 1 A g^{-1}) and (d) specific capacitance *versus* current density of WO_3 (○), PEDOP (□) and PEDOP-Au@WO_3 hybrid (△) films.

The SC of the three films was also calculated from CV plots(Figure 7.7) and they were found to be 44, 18 and 214 F g^{-1} at s = 5 mV s^{-1} and 13, 3 and 78 F g^{-1} at s = 100 mV s^{-1} for WO_3, PEDOP and PEDOP-Au@WO_3 hybrid electrodes. Values were calculated using equation (3).

$$SC = \int_{E1}^{E2} \frac{i(E)dE}{2(E2-E1)m\,v} \quad (3)$$

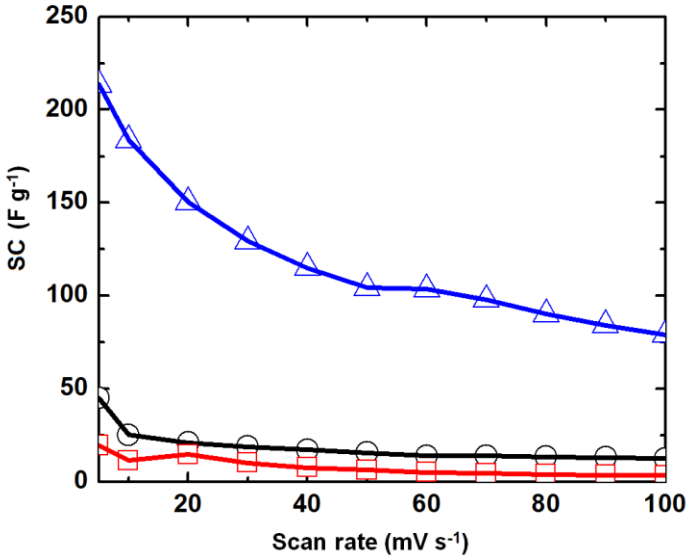

Figure 7.9: Specific capacitance *versus* scan rate of WO_3 (○), PEDOP (□) and PEDOP-Au@WO_3 hybrid (△) cells.

7.3.5 Electro-optical performance characteristics

The absorption spectra of as-fabricated films and Au colloid are shown in Figure 7.10a. The Au colloid shows an absorption peak at 531 nm which originates from the surface plasmon resonance of Au nanoparticles [22]. The absorption of Au on WO_3 fibers is affirmed from retention of this peak in the Au@WO_3 film, albeit a slight blue shift by 4 nm. Pristine WO_3 film does not show any absorption peaks in the visible region and pristine PEDOP shows a broad absorption wave above 700 nm attributed to bipolaronic transitions. The absorption profile of the PEDOP-Au@WO_3 hybrid film is akin to the absorption of curve of pristine PEDOP and is relatively featureless in the as-fabricated state.

The variation of absorbance a PEDOP film and transmittance of WO_3 and PEDOP-Au@WO_3 films under the influence of an applied bias in the range of +1.5 to –1.5 V as a function of wavelength are shown in Figure 7.10b, c and d. The measurements were performed *in-situ* in the IL: 1-butyl-3-methyl imidazolium triflate. For all the three films, the reduction potential was varied in steps of 0.1 V from –0.1 to –1.5 V and oxidation potentials were applied over longer intervals between +0.2 to +1.5 V. The transmission spectra of WO_3 films in their colored (under E = 0.2 to +1.5 V) and bleached (under E = –0.1 to –1.5 V) states in the 300 <λ< 1700 nm wavelength region are displayed. In the fully oxidized state (E = +1.5 V), the percent transmittance of WO_3 film varies between 70%-85% in the visible region and the film is colorless and transparent. Percent transmission decreases monotonically in the NIR region and it reaches a value of ~30% at 1650 nm. Transmittance in the visible and NIR region decreases systematically at less positive potentials (when E is decreased from +1.0 to –1.5 V) due to the formation of $[BmIm]_xWO_3$ which is blue in color. This absorptive modulation of WO_3 in the photopic region has been attributed to an intervalence charge transfer between W^{+5} and W^{+6} sites [23] or to small polaron absorption [24]. For the pristine polymer film, ΔOD is defined as the optical density change at a monochromatic wavelength: ΔOD (λ) = OD(λ, −x V) – OD(λ, +1.5 V), where x = –0.1 to –1.5 V. For the PEDOP film, the broad band observed in the NIR region under all oxidation potentials stems from bipolaronic transitions (Figure 7.10c). With increasing reduction potential, the broad NIR absorption loses intensity and paves way for a peak corresponding to π-π* transitions in the visible region which progressively gains intensity upon raising negative bias signaling the formation of neutral reduced polymer. When the film is fully reduced (at E = −1.5 V), the film is insulating and shows a λ_{max} at 500 nm. The PEDOP film has a transparent blue-black hue in the oxidized state and it is deep red in the reduced form. The

ΔOD_{max} value for PEDOP was deduced to be 2.33 at λ_{max} of 500 nm. The variation of transmittance with wavelength and applied bias in the PEDOP-Au@WO_3 hybrid is shown in Figure 7.10d. The significant dip in the transmittance curve with a T_{min} = 5.2% at 500 nm in the fully reduced/colored (reddish-blue) state of the hybrid especially in the 400 – 600 nm wavelength range achieved under E = –1.5 V is ascribed to the increased absorption due to π-π* transitions of PEDOP complemented by $[BmIm]_xWO_3$ formation. These two phenomena impart the film with an intense hue which cannot be achieved either in pristine PEDOP or WO_3 films. In the fully bleached/oxidized (transparent) state attained at E = +1.5 V, the hybrid retains good transmission characteristics in visible-NIR range with a T_{max} of about 78% (at 460 nm) primarily due to the good reversibility of the oxidation-reduction process. The transmittance in the fully bleached state is slightly less for the hybrid compared to WO_3, due to the presence of PEDOP which shows a pale color even in the oxidized state.

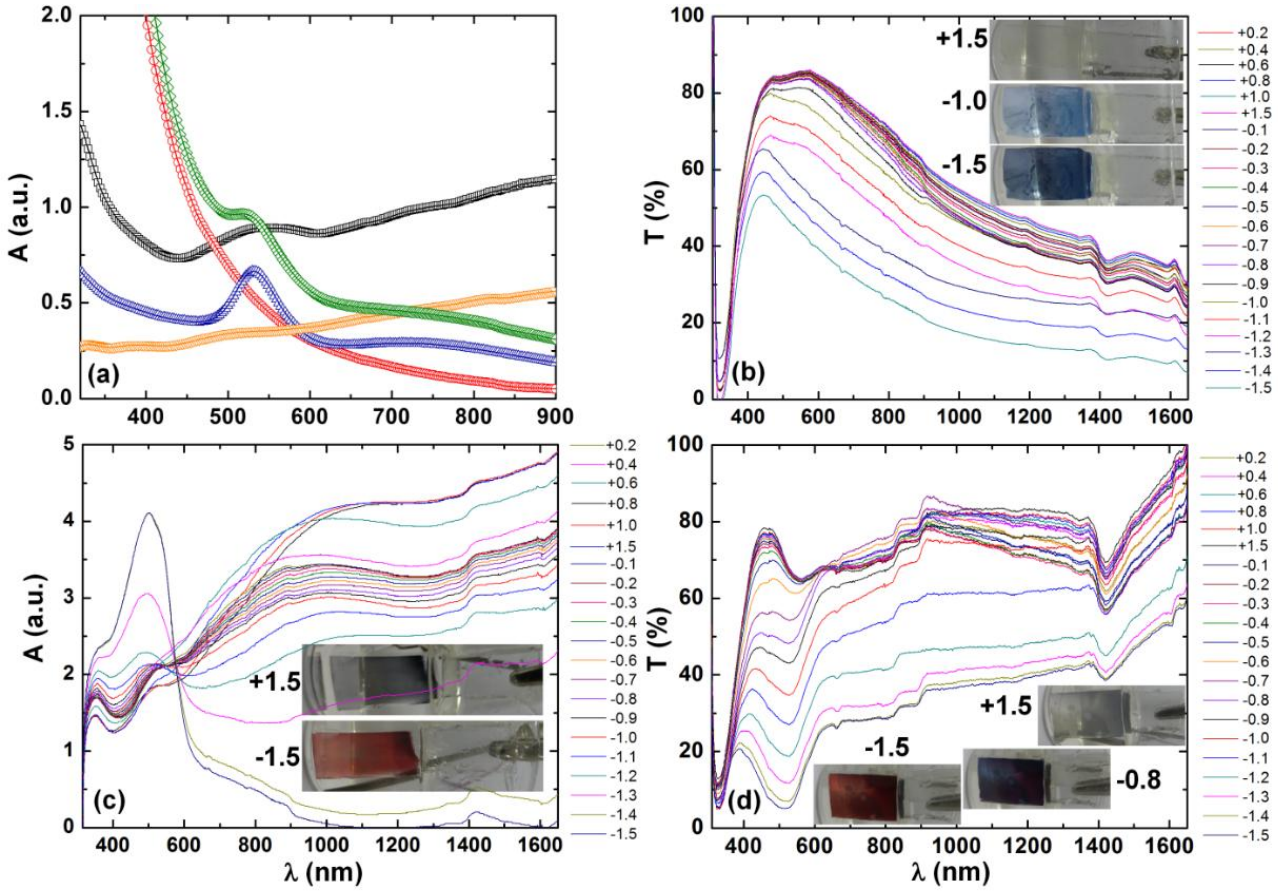

Figure 7.10: (a) Absorbance *versus* wavelength spectra of a WO_3 film (○), Au colloid (△), a PEDOP film (▽), an Au@WO_3 film (◇) and a PEDOP-Au@WO_3 film (□). *In-situ* optical spectra as a function of applied potential: (b) transmittance (%) *versus* wavelength of a WO_3 film, (c) optical density *versus* wavelength of a PEDOP film and (d) transmittance (%) *versus* wavelength of a PEDOP-Au@WO_3 film. In c-d, the electrolyte and the counter electrode were 1-butyl-3-methyl imidazolium triflate and Pt respectively and each potential was applied for a duration of 60 s. Insets of (b-d) show photographs of films under different bias.

Transmission modulation (ΔT), a parameter which determines the suitability of an electrode for electrochromic window applications was calculated for both WO_3 and PEDOP-Au@WO_3 films using the following equation: $\Delta T(\lambda) = T(\lambda, +1.5\ V) - T(\lambda, -x\ V)$, where x = –0.1/–1.5 V (Figure 7.11a). The hybrid shows a remarkably enhanced maximum transmission modulation of

71% at λ_{max} = 476 nm which is 1.5 times greater than the maximum modulation of 47% offered by WO_3 film at λ_{max} = 650 nm, for the same values of applied bias. In bulk of the spectral range under consideration, between 400 - 1650 nm, the maximum modulation offered by the hybrid is ≥ 50% which makes it an excellent candidate for electrochromic smart window applications. It is obvious that the hybrid film has greater electrochemical capacity than the pure oxide film and the additional optical modulation in the hybrid arises from the contribution of PEDOP to color change. Coloration efficiency (CE) at a given wavelength is the change in the optical density (ΔOD) for the charge (q) consumed per unit electrode area (A). It has been calculated in the present report for all films using the following equation (4).

$$CE\ (\eta) = \Delta OD(\lambda) / (q/A) = \log(T_b(\lambda) / T_c(\lambda)) / (q/A) \quad (4)$$

T_b and T_c are the transmittances of the film in the bleached and colored states respectively. CEs for the films were determined from the slopes of the ΔOD (for PEDOP) or $\log(T_b/T_c)$ (for WO_3 and PEDOP-Au@WO_3 hybrid) *versus* inserted charge density at different wavelengths (Figure 7.11b, c and d). The CEs plots for all films can be divided into one or two linear dependence regimes. At low values of inserted charge densities, CE is low, but in the higher charge density region, CE values are high. The CEs of pristine WO_3 in the visible region at λ_{max} of 441 and 572 nm are 66 and 88 $cm^2\ C^{-1}$. PEDOP shows a CE of 176 $cm^2\ C^{-1}$ at λ_{max} = 500 nm. Compared to the polymer and WO_3 films, the PEDOP-Au@WO_3 hybrid shows outstandingly high coloration efficiencies of 523 and 707 $cm^2\ C^{-1}$ at λ_{max} of 460 and 500 nm. The highest CE achieved for the PEDOP-Au@WO_3 hybrid is four- and eight-fold times greater than the CE maxima shown by pristineWO_3 and pristine PEDOP films, for the same values of applied bias. In fact the intercalated charge density range is much wider for WO_3 (0.65-7.0 mC cm^{-2}) compared

to PEDOP or PEDOP-Au@WO_3 hybrid (0.025-2.2 mC cm^{-2}). CE in hybrid is larger as the PEDOP-Au@WO_3 is a dual electrochrome electrode wherein both PEDOP and WO_3 undergo coloration concurrently when subjected to reduction potentials and bleach simultaneously when oxidation potentials are applied. A higher degree of coloration results in the fully reduced state and likewise an almost quasi-transparent hue is realized in the bleached state. In pristine PEDOP, the bleached state is dark and in pristine WO_3, in the fully reduced state (E = –1.5 V), the film does not darken significantly, it continues to be transmissive as can be judged from a high transmittance of 53% (λ_{max} = 441 nm). In the NIR region, at 1100 nm pristine PEDOP shows a slightly higher CE of about 407 cm^2 C^{-1} compared to 328 cm^2 C^{-1} obtained for the PEDOP-Au@WO_3 hybrid. In the hybrid, decreasing transmittance of WO_3 in the reduced states causes a drop in CE. However, the best trade-off between high CE in visible and NIR regions is attained only in the PEDOP-Au@WO_3 hybrid, which establishes its' suitability for smart window applications. In an earlier report, Wang et al. obtained a maximum optical modulation of ~66% after applying a voltage of –3.0 V for WO_3 nanorods [25] and in another study they achieved a contrast of ~33.9% after applying a 1.0 V voltage bias for 300 s [26]. In a report on a PEDOT film, a contrast of 71% was attained in a $LiBF_4$/PC solution [27]. In another report, the contrast for an electropolymerized PEDOT film was found to be 32% [28]. Our values for contrast and CE render the hybrid suitable for electrochromic applications.

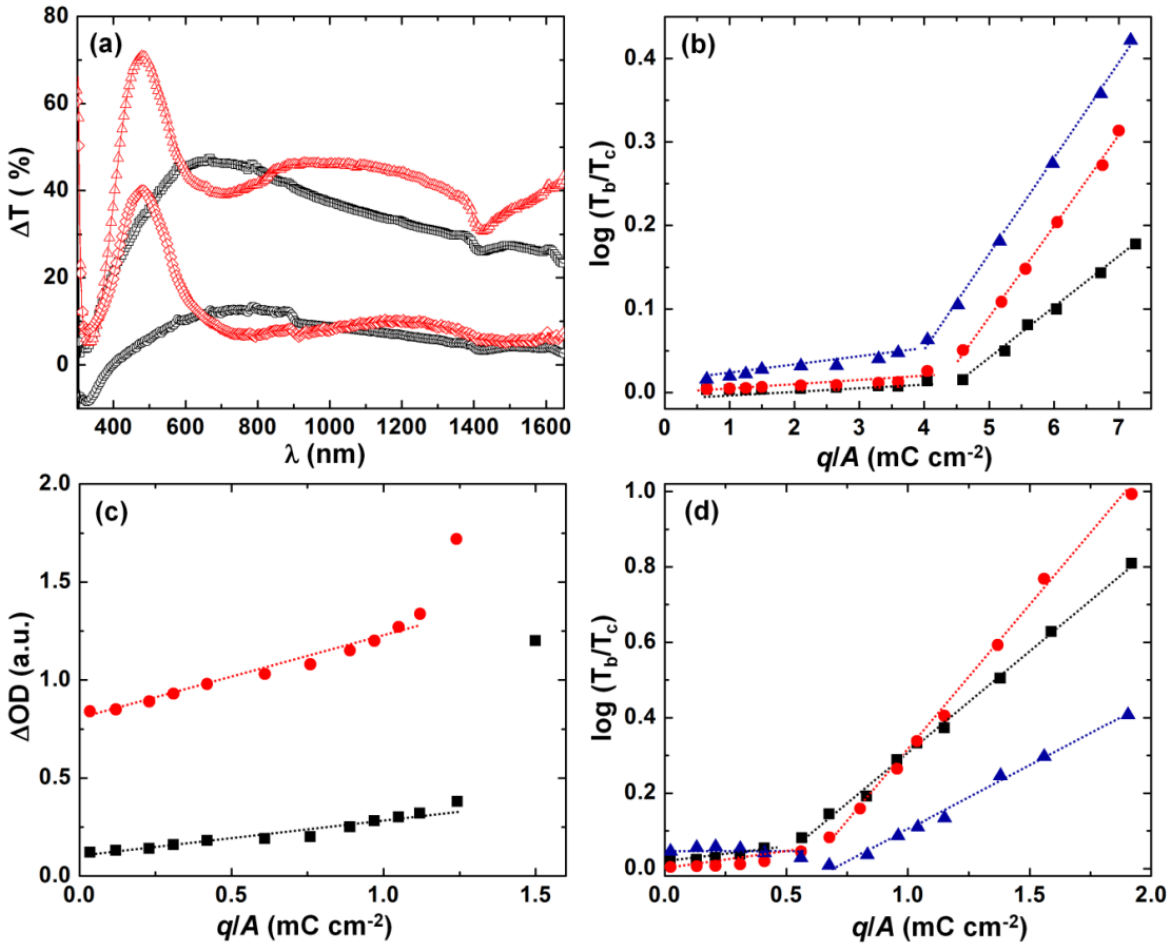

Figure 7.11: (a) Transmission modulation: ΔT (λ) = T (+1.5 V) – T (–1 V (○) or –1.5 V (□)) of a WO_3 film and ΔT (λ) = T (+1.5 V) – T (–1 V (◇) or –1.5 V (△)) of a PEDOP-Au@WO_3 hybrid film, (b) log (T_b/T_c) *versus* q/A of a WO_3 film at 441 (■), 572 (●) and 800 (▲) nm, (c) ΔOD *versus* q/A of a PEDOP film at 500 (■) and 1100 (●) nm and (d) log (T_b/T_c) *versus* q/A of a PEDOP-Au@WO_3 film at 460 (■), 500 (●) and 1100 (▲) nm. T_b at +1.5 V was taken as reference for WO_3 and PEDOP-Au@WO_3 films in (b) and (d) respectively and OD at +1.5 V was taken as reference for the PEDOP film in (c).

The coloration-bleaching kinetic plots of WO_3 (λ_{max} = 650 nm), PEDOP (λ_{max} = 500 nm) and PEDOP-Au@WO_3 hybrid (λ_{max} = 476 nm) films are shown in Figure 7.12 with half cycle times of 3 and 10 s respectively. The coloration and bleaching times are calculated as 7.4 and 1.7 s

respectively for the WO_3 film under a step time of 10 s and 2.1 and 1.6 s under step time of 3 s. Under a step time of 10 s, t_c and t_b of 6.6 and 5.9 s and under 3 s, t_c and t_b of 1.7 and 1.6 s were observed for PEDOP. The PEDOP-Au@WO_3 hybrid achieved a contrast considerably more than that of WO_3 and PEDOP for the same step times, under the same applied potential, thus reaffirming the cumulative contributions from PEDOP and WO_3 in increasing the color contrast. For the hybrid, under a step time of 10 s, t_c and t_b of 6 s and under 3 s, t_c and t_b of 2 s were obtained. In the past switching times of 5.1 s at 700 nm were obtained for a WO_3 nanosheets-based ECD [29]. For a PEDOP film, switch times of 2.14 and 1.37 s were observed at 490 nm [30]. Although there are no reports on a WO_3-PEDOP combination to date, nonetheless, our switching times are comparable to reported values for electrochromic PEDOP or WO_3.

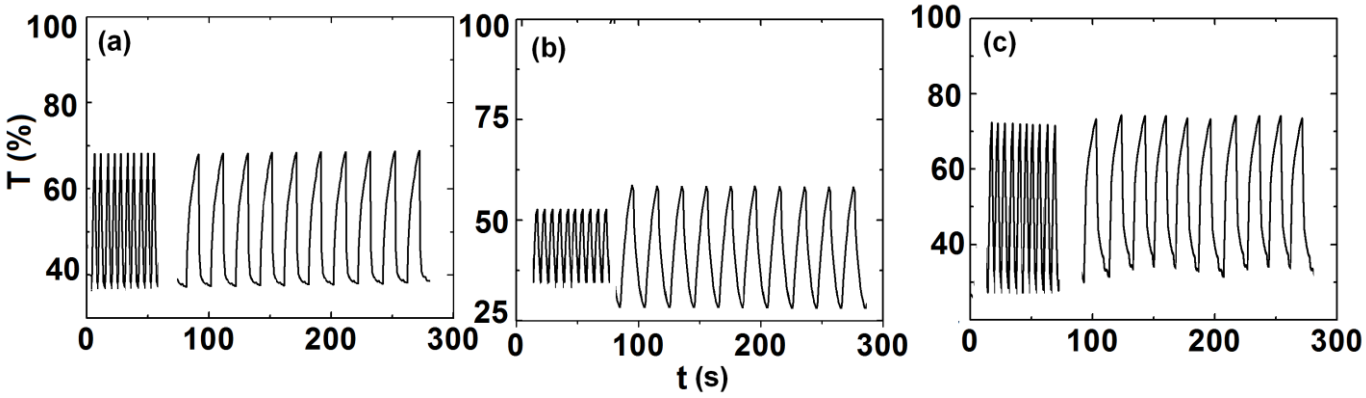

Figure 7.12: Transimitance *versus* time curves for (a) WO_3, (b) PEDOP and (c) PEDOP-Au@WO_3 hybrid films at λ = 650, 500 and 476 nm respectively under a square wave dc potential of ±1.5 V at different step times of 3 s and 10 s. The electrolyte and the counter electrode were 1-butyl-3-methyl imidazolium triflate and Pt respectively.

7.3.6 Electrochromic supercapacitor

To evaluate the potential of the PEDOP-Au@WO_3 hybrid as a dual function electrochromic supercapacitor electrode, a 3D visualization of variation of transmittance at a monochromatic

wavelength of 460 nm and potentiometric response is presented in Figure 7.13**.** At the onset, under a reduction potential of −1.5 V, the film is fully colored/reduced with a deep red-blue hue corresponding to the fully discharged state and upon linearly increasing the potential from −1.5 to +1.5 V through 0 V, the film undergoes oxidation or charging concomitant with a gradual optical transition from a red-blue color to a transparent blue-grey color. The progressive increase in transmittance from ~9% to 78% (λ = 460 nm), as E is raised from −1.5 to +1.5 V simultaneously accompanied by charging or intercalation of anions in the film is followed by a systematic drop in transmittance from 78% to 9% when potential is swept in the reverse direction from +1.5 to −1.5 V and this optical change is accompanied by discharging or ejection of anions from the film. The charge and discharge capacitances are almost ~130 F g^{-1} at a current density of 1 A g^{-1}. This plot clearly shows that the PEDOP-Au@WO_3 hybrid can easily work as an electrochromic supercapacitor as it can perform two linked functions of charging/discharging and optically modulating visible radiation at the same time.

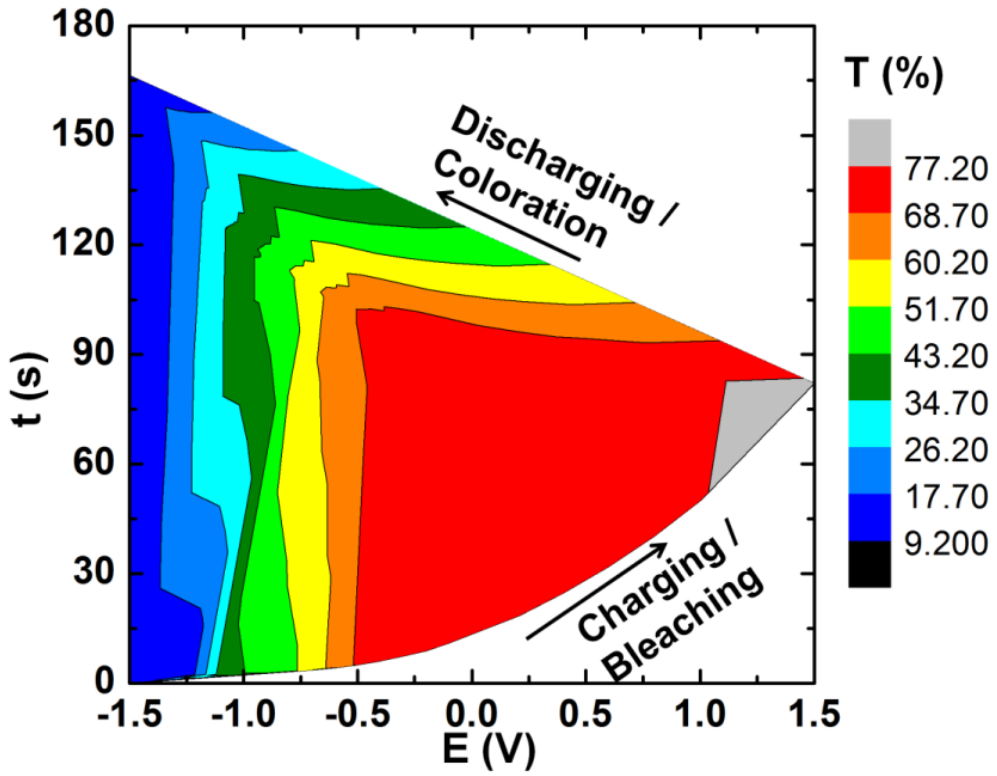

Figure 7.13: *In-situ* optical transmittance spectra as a function of applied potential and time for a PEDOP-Au@WO_3 film, illustrating simultaneous electrochromic and pseudocapacitve capabilities of this film.

7.4 Summary

A dual function PEDOP-Au@WO_3 hybrid film was prepared for the first time by firstly synthesizing WO_3 fibers with a monoclinic crystal structure by a hydrothermal route, followed by their electrophoretic deposition onto a conducting electrode. Citrate capped Au nanoparticles served as electrically conductive linkers between WO_3 and PEDOP wherein PEDOP was electropolymerized using poly(styrene sulfonate) as the dopant onto an Au@WO_3 film. The inclusion of Au in the PEDOP-Au@WO_3 hybrid film was confirmed by XRD, Raman, and EDX studies. The nanoscale electrical conductivity of the PEDOP-Au@WO_3 hybrid film was found to

be 0.88 S cm^{-1} and it was 60-fold and 1-fold times greater than that of the pristine polymer and WO_3. An exceptionally high maximum electrochromic color contrast of 71% (λ = 476 nm) was achieved in the hybrid, which underwent a color change from a transparent blue to bluish-red to a deep red hue as opposed to a maximum contrast of 47% (at 650 nm) obtained in pristine WO_3 which experienced a colorless to blue transition. The CE of the hybrid was 707 cm^2 C^{-1} (at 500 nm) and it also switched in about 6 s; both coloration efficiency and kinetics were substantially higher and faster than that achieved in pristine WO_3 or polymer. The specific capacitance of the PEDOP-Au@WO_3 hybrid film was 130 F g^{-1} (at 1 A g^{-1}) and it decreased by 30% after 100 cycles, indicating its' suitability for practical applications. Concurrent electrochromic cum pseudocapacitive roles of a PEDOP-Au@WO_3 hybrid filmhave been established and assessed with respect to pristine PEDOP and WO_3 films, thus opening up avenues to integrate this CP with other electroactive oxide nanostructures for the realization of electrochromic psuedocapacitors.

References

[1]. H. Jia, J. Wang, X. Zhang, Y. Wang, ACS Macro Lett. 3 (2013) 86–90.
[2]. K. Wang, H. Wu, Y. Meng, Z. Wei, Small 10 (2013) 14–31.
[3]. B. Weng, S. Ashraf, P. C. Innis, G. G. Wallace, J. Mater. Chem. C 10 (2013) 7430–7439.
[4]. R. Gracia, D. Mecerreyes, Polym. Chem. 4 (2013) 2206–2214.
[5]. D. Gupta, M. M. Wienk, R. A. J Janssen, Adv. Energy Mater. 3 (2013) 782–787.
[6]. J. Luo, Q. Zeng, Y. Long, Y. Wang, J. Nanosci. Nanotech. 13 (2013) 1372–1376.
[7]. M. Winter, R. J. Brodd. Chem. Rev. 104 (2004) 4245–4270.
[8]. M. Grätzel, Nature 409 (2001) 575–576.
[9]. P. M. Beaujuge, S. Ellinger, J. R. Reynolds, Nature Mater. 7 (2008) 795–799.
[10]. D. Wei, M. R. J. Scherer, C. Bower, P. Andrew, T. Ryhänen, U. Steiner, Nano Lett. 12 (2012) 1857–1862.
[11]. H. Wei, X. Yan, S. Wu, Z. Luo, S. Wei, Z. Guo. J. Phys. Chem. C 116 (2012) 25052–25064
[12]. X. Sun, H. Sun, H. Li, H. Peng, Adv. Mater. 25 (2013) 5153–5176.
[13]. L. X. Wang, X. G. Li, Y. L. Yang, Reactive Functional Polymers 47 (2001) 125–139.
[14]. Y. Jin, X. Kang, Y. Song, B. Zhang, G. Cheng and S .Dong, Anal. Chem. 73 (2001) 2843–2849

[15]. D. Y. Lu, J. Chen, H. J. Chen, L. Gong, S. Z. Deng, N.S. Xu, Y. L. Liu, Appl. Phys. Lett. 90 (2007) 041919–0411921.
[16]. S. Garreau, G. Louarn, J. P. Buisson, G. Froyer, S. Lefant, Macromolecules 32 (1999) 6807–6812.
[17]. X. Zou, E. Ying, S. Dong, Nanotech. 17 (2006) 4758–4764.
[18]. D. Susanti, R. Narendra, D. Wibawa, L. Tananta, H. Purwaningsih, R. Fajarin, G. E. Kusuma, Frontiers Mater. Sci. 7 (2013) 370–378.
[19]. D. Szymanska, I. A. Rutkowska, L. Adamczyk, S. Zoladek, P. J. Kulesza. J. Solid State Electrochem. 14 (2010) 2049–2056.
[20]. T. L. Kelly, K. Yano, M. O. Wolf, ACS Appl. Mater. Interfaces 1 (2009) 2536–2543.
[21]. B. X. Zoua, Y. Lianga, X. X. Liua, D. Diamond, K. T. Lau, J. Power Sources 196 (2011) 4842–4848.
[22]. S. Eustis, M. A. El-Sayed. Chem. Soc. Rev. 35 (2006) 209–217.
[23]. B. W. Faughnan, R. S. Crandall, P. M. Heyman, RCA Rev. 36 (1975) 117.
[24]. O. F. Schirmer, V. Wittiwer, G. Baur, G. Brandt, J. Electrochem. Soc. 124 (1997) 749–754.
[25]. J. Wang, E. Khoo, P. S. Lee, J. Ma, J. Phys. Chem. C 112 (2008) 14306–14312.
[26]. J. Wang, E. Khoo, P. S. Lee J. Ma, J. Phys. Chem. C 113 (2009) 9655–9658.
[27]. E. Poverenov, M. Li, A. Bitler, M. Bendikov, Chem. Mater. 22 (2010) 4019–4025.
[28]. S. Sindhu, K. N. Rao, S. Ahuja, A. Kumar, E. S. R. Gopal, Mater. Sci. Engg. B 132 (2006) 1–2.
[29]. L. Liang, J. Zhang, Y. Zhou, J. Xie, X. Zhang, M. Guan, B. Pan, Y. Xie, Sci. Rep. 3 (2013) 1–8.

Chapter 8

PEDOP/V_2O_5 nanobelts hybrid for photoelectrochromic and supercapacitor applications

8.1 Introduction

Transition metal oxides such as WO_3, MoO_3, NiO_x, IrO_2 etc owing to their ability to exist in two or more oxidation states enables their widespread usage in diverse applications. Among oxides, V_2O_5 is a well-established intercalation compound due to a layered crystalline structure and has been used in the past as an electrochromic material, as an electrode for supercapacitors and in Li ion batteries as well [1-3]. All these applications of V_2O_5 rely on its ability to intercalate and deintercalate charge by undergoing oxidation and reduction reactions. Nanostructures of V_2O_5 (rods, belts, wires, sheets) have been utilized in literature, owing to higher surface area offered by these morphologies compared to the particulate structure [4-7]. However, the electronic conductivity of V_2O_5 is low, which leads to sluggish ion insertion/extraction rates [8]. Approaches to alleviate this issue include integration of V_2O_5 with CPs such as PEDOT [9], poly(aniline) or PANI [10], or this oxide can be combined with carbon nanostructures like reduced graphene oxide [11] and improved performance characteristics either in terms of increased electrochromic contrast or increased charge storage capacity were attained.

In the present study, V_2O_5 nanobelts were synthesized by a hydrothermal route and the electrical conductivity of the oxide was improved by integrating it with PEDOP. PEDOP was electropolymerized onto an electrophoretically deposited V_2O_5 film. Here we used pristine

$V_2O_5$and PEDOP/V_2O_5 electrodes for constructing (a) photoelectrochromic cells, wherein we used a CdS/TiO_2 as the photoactive electrode and the composite/oxide as the counter electrode separated by an electrolyte. Under illumination, the photocurrent produced by the photoanode is channelized to the counter electrode via the external circuit and the oxide based electrode undergoes color change upon reduction. To date there are no reports on the use of either V_2O_5 or a PEDOP/V_2O_5 hybrid as photoelectrochromic electrodes in a quantum dot based solar cell. Further the ability of V_2O_5 or a PEDOP/V_2O_5 hybrid to function as psuedocapacitors is also demonstrated. We correlated the structure and electrical properties of the electrodes with their photoelectrochromic and charge storage characteristics and illustrate the high potential this PEDOP/V_2O_5 hybrid has for self-powered smart windows and energy storage devices.

8.2 Experimental

8.2.1 Syntheses of PEDOP films and V_2O_5 nanobelts

A clear solution of 0.1 M 3,4-EDOP and 0.1 M Lithium perchlorate in 20 mL of acetonitrile was prepared for fabricating PEDOP films. Electropolymerization of films was performed in a three electrode configuration. FTO coated glass plates were employed as working and counter electrodes, and Ag/AgCl/KCl was used as the reference electrode. Bluish-black colored films of perchlorate doped PEDOP films were deposited under potentiostatic conditions at room temperature in chronoamperometric mode by application of +1.5 V to the working electrode for 500 s. All films were washed in deionized water, dried in air for 2 h and stored in air.

V_2O_5 nanobelts were synthesized using a hydrothermal method. A solution of Na_2VO_4 (2.5 mmol) was prepared in 20 mL of deionized water. NaCl (0.02 mol) used as capping agent was added to above solution. The resulting solution was stirred for 10 min. The pH of the solution

was adjusted to 2 by adding 3 M HCl in a drop-wise manner. This solution was further stirred for another 10 min and then transferred to a 50 mL Teflon lined autoclave and heated at 180 ^{o}C for 12 h. A yellow colored precipitate was formed at the bottom of autoclave. The precipitate was cleaned with plenty of deionized water, dried in an oven and used for preparing pristine V_2O_5 and hybrid films.

8.2.2 Preparation of V_2O_5 and PEDOP/V_2O_5 films

V_2O_5 powder (~1 g) was transferred to a mortar and grinded for a few minutes alongwith a few drops of N-methyl pyrrolidine. A homogeneous deep yellow-brown colored paste of V_2O_5 was obtained which applied onto pre-cleaned FTO coated glass substrates using doctor blading to yield pristine $V_2O_5$and also applied onto PEDOP films to yield PEDOP/V_2O_5 hybrid films. Both pristine V_2O_5 and PEDOP/V_2O_5 films were heated at 80 ^{o}C for 1 h and the resulting dry films were used.

8.2.3 CdS/TiO_2 photoanode construction

A TiO_2 coating was made on FTO/glass by doctor blading from a paste of TiO_2 powder (P25, Degussa) prepared in ultrapure water (8 mL) and Triton X-100 (20 mg). The TiO_2 film was annealed at 500 ^{o}C for 30 min. The resulting film was kept immersed in an aqueous $TiCl_4$ (40 mM) solution for 30 min at 70 ^{0}C. The TiO_2 film was rinsed in distilled water and sintered at 500 ^{0}C for 30 min, cooled to ambient temperature and used for CdS deposition. CdS quantum dots (QDs) were deposited on the TiO_2 coated glass electrodes by successive ionic layer absorption and reaction (SILAR) method.The TiO_2/FTO electrode was sequentially immersed in four different beakers for about 30 s immersion time, in each solution. The first dipping solution contained aqueous $Cd(CH_3COO)_2$ (0.1 M, Merck) which, was followed by an ultrapure water

rinse to remove superfluous acetate. The film was then immersed in aqueous Na_2S (0.1 M, Merck), and again followed by a water dip to remove the surplus sulfide. The immersion cycle was repeated ten times. The resulting films were yellow and were referred to as CdS/TiO_2 electrodes. Quantum dot solar cells or photoelectrochromic cells were assembled by using a CdS/TiO_2 electrode as the photoanode, a PEDOP or V_2O_5 or PEDOP/V_2O_5 as the counter electrode and aqueous Na_2S (0.1 M) as the electrolyte. I-V characteristics were measured using a Newport Oriel 3A solar simulator with a Keithley model 2420 digital source meter. A 450 W Xenon arc lamp with an irradiance of 100 mW cm^{-2} of Air Mass (AM) 1.5 was used as the light source; the spatial uniformity of irradiance was confirmed by calibrating with a 2 cm × 2 cm Si Reference Cell and re-confirmed with a Newport power meter.

8.3 Structural analyses

8.3.1 FE-SEM analysis

FE-SEM images of pristine V_2O_5, PEDOP and PEDOP/V_2O_5 hybrid at different magnifications are shown in Figure 8.1. As can be judged from Figure 8.1a, b and c, pristine V_2O_5 have a predominant nanobelt like morphology; we refer to them as belts and not rods, as they are curved in some regions. The lengths of the belts extend over several tens of microns, and their widths lie in the range of 50 to 70 nm. The nanobelts are misaligned with respect to each other and they are overlapping. Upon coating the polymer, the resulting PEDOP/V_2O_5 hybrid continues to retain the nanobelt like morphology (Figure 8.1e and f), but the belts tend to aggregate, suggestive of the CP serving as glue which connects the V_2O_5 belts, which is advantageous for improving the electronic conductivity of the whole system. The porosity of the pristine V_2O_5 is such that it allows an intimate contact between the V_2O_5 nanobelts and PEDOP

during hybrid formation and therefore it is not just the uppermost layer but the entire cross-section of belts which PEDOP can anchor onto. Since there are no particles seen in the low magnification image of the composite, it is apparent that despite the polymer coating, the advantage of the elongated shapes such as high surface area which enables increased ion uptake from the electrolyte during electrochemical switching can be exploited. The SEM image of the pristine polymer shows a granular porous structure and therefore the V_2O_5 nanobelts can easily mix with the polymer when the paste is applied onto the polymer surface. The EDX plot of V_2O_5 shows two dominant signals from oxygen and vanadium, whereas the EDX plot of PEDOP/V_2O_5 shows signals from C, N, O and V, indicating the inclusion of the polymer in the V_2O_5.

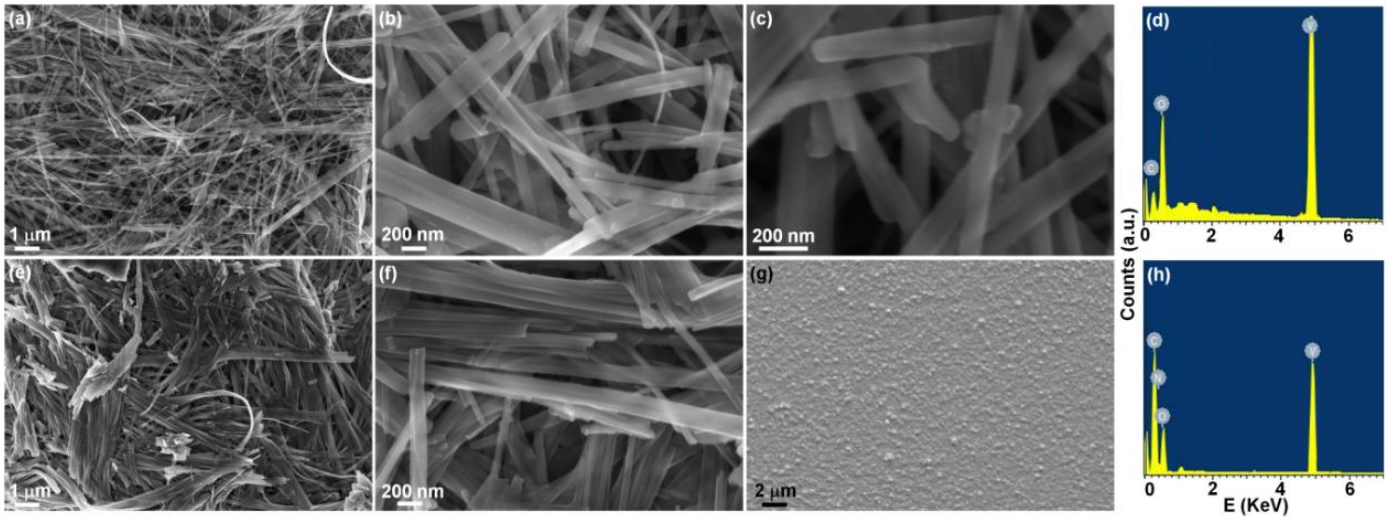

Figure 8.1: FE-SEM micrographs of (a,b,c) pristine V_2O_5 nanobelts and (e,f) PEDOP/V_2O_5 hybrid at different magnifications and (g) pristine PEDOP; (d,h) EDX plots of pristine V_2O_5 nanobelts and PEDOP/V_2O_5 hybrid respectively.

8.3.2 XRD and Raman analysis

The XRD pattern of V_2O_5 (Figure 8.2a) shows prominent diffraction peaks at d = 7.44, 3.47, 3.1, 2.9 and 1.8 Å which correspond to $(\bar{2}01)$, (500), $(\bar{1}12)$, $(\bar{6}01)$ and $(\bar{1}21)$ planes of the monoclinic crystal structure of V_2O_5, in concurrence with JCPDS file number 07-0332. Additional peaks with relatively lower intensities were also observed, and these were also indexed to the diffraction lines of monoclinic V_2O_5. The Raman spectra of pristine V_2O_5 nanobelts, PEDOP and PEDOP/V_2O_5 hybrid are shown in Figure 8.2b. Pristine V_2O_5 nanobelts show broad peaks at 763 and 472 cm^{-1} corresponding to the vibrational stretching modes of V–O linkages. A cluster of peaks is also seen at ~296 and 256 cm^{-1} which are assigned to the bending vibrational modes of V=O bonds. An intense peak observed at ~130 cm^{-1} is attributed the lattice vibrations. The Raman spectrum of pristine PEDOP shows a doublet of intense peaks at 1637 and 1584 cm^{-1}, which are ascribed to the asymmetric C=C stretching vibrations, followed by another set of twin peaks at 1427 and 1393 cm^{-1} corresponding to the symmetric C_α=C_β(–O) stretching and C_β–C_β stretch modes. An intense peak is also seen at 1202 cm^{-1} which arises from overlapping modes of C_α– $C_{\alpha'}$ (inter-ring stretching) and C_β–H bending vibrations. The PEDOP/V_2O_5 hybrid shows peaks from both V_2O_5 and PEDOP, slightly shifted with respect to the pristine moieties, thus confirming the formation of the hybrid. In the hybrid, three peaks cloistered with apexes at 1637, 1615 and 1585 cm^{-1} originate from the ν_{asym}(C=C) modes of PEDOP, a broad peak at 1415 cm^{-1} corresponds to C_α=C_β(–O) stretching vibration of PEDOP and the peak at 1193 cm^{-1} is due to the $\nu(C_\alpha–C_{\alpha'}) + \delta(C_\beta–H)$ modes. Strong, intense broad peaks are also observed at 762 and 470 cm^{-1} due to ν(V-O) stetch modes of V_2O_5 nanobelts. Peaks at 294 and 262 cm^{-1} correspond to δ(V=O) modes and the peak at 142 cm^{-1} arises from lattice

vibrational modes of V_2O_5, thus re-affirming the hybrid formation. The photoluminescence spectrum of V_2O_5 nanobelts, recorded at an excitation wavelength of 350 nm is shown in Figure 8.2c. The nanobelts show a broad emission ranging from 400 to 470 nm, indicating blue light emission. This broad peak is interspersed with several spikes, indicative of emission due to defect states in V_2O_5 which are typically caused by oxygen deficiency [12].

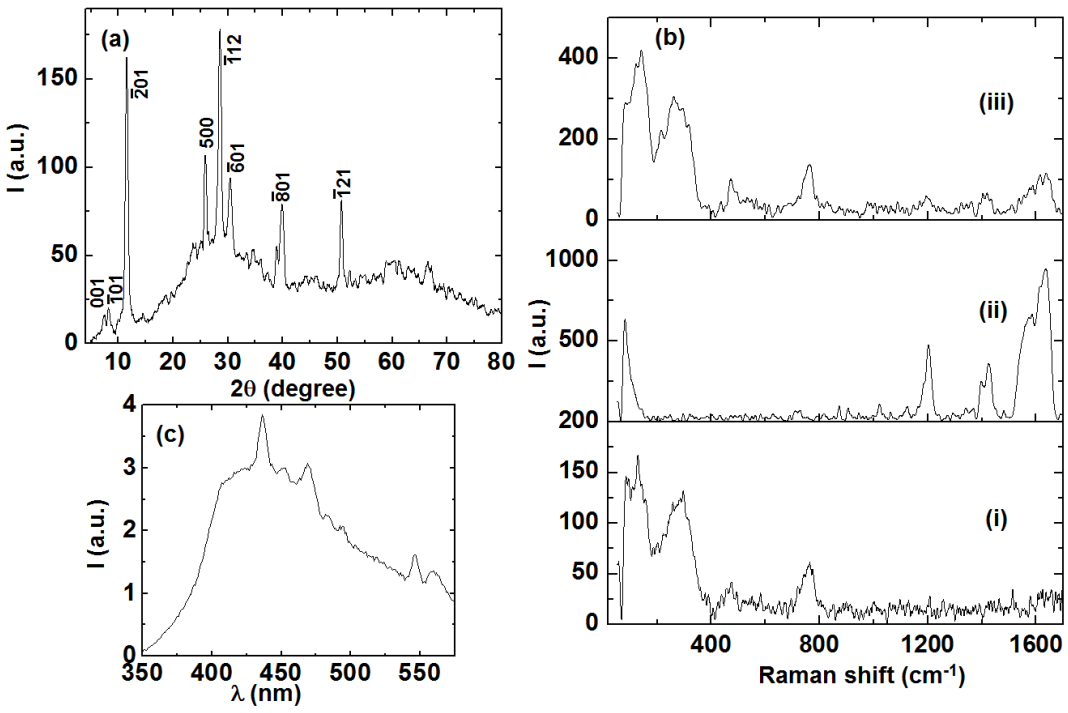

Figure 8.2: (a) XRD pattern of pristine V_2O_5 nanobelts, (b) Raman spectra of (i)V_2O_5, (ii) PEDOP and (iii) PEDOP/V_2O_5 and (c) photoluminescence (recorded at an excitation wavelength of 350 nm) of pristine V_2O_5 nanobelts.

8.3.3 Conductivity of films

The I-V characteristics of pristine V_2O_5 nanobelts, PEDOP and PEDOP/V_2O_5 hybrid recorded in the SnO_2:F/Film/SS configuration are displayed in Figure 8.3. A spring contact probe was used to ensure that there was no puncturing of the film during the measurement. Film

thickness (d) was deduced by running an AFM tip across a step of FTO/film, from the height profile. The films show linear variation of current with potential with different slopes in different domains of the –1 to +1 V measurement range at room temperature. The conductivities were calculated from the slopes using $\sigma = (I/V) \times d/A$, and averaged for a given film, where d is the thickness of the film and A is the area of contact of the probe with the film. Pristine V_2O_5 film exhibits the lowest current response in comparison to PEDOP and PEDOP/V_2O_5 hybrid in the same potential range, for the same geometric area and film thickness. As expected, pristine PEDOP exhibits the highest conductivity of 3.6 mS cm^{-1} and the conductivity of the PEDOP/V_2O_5 hybrid is slightly lower (1.6 mS cm^{-1}).

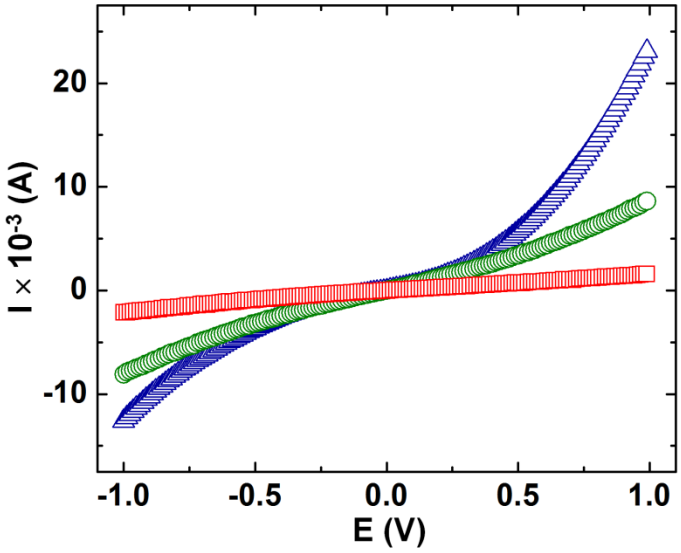

Figure 8.3: LSV plots of pristine V_2O_5 nanobelts (□), pristine PEDOP (△) and PEDOP/V_2O_5 hybrid (○) recorded in FTO/sample/SS configuration.

Conductivity of pristine V_2O_5 is the least (0.4 S cm^{-1}), for the conductivity is largely due to the defect states, and their concentration is small, not enough to induce a significant increase in

the electronic conductivity. Since the conductivity of the PEDOP/V_2O_5 hybrid is 4 times larger than that of pristine oxide, it is obvious that the polymer is effective in improving the electron conduction capability of V_2O_5.

8.3.4 Photoelectrochromic response

Photoelectrochemical cells were constructed with CdS/TiO_2 as the photoanode, 0.1 M Na_2S as the electrolyte and pristine V_2O_5 or PEDOP or the PEDOP/V_2O_5 hybrid as the counter electrode. The J-V characteristics were measured under one sun (100 mW cm^{-2}) irradiance and are displayed in Figure 8.4. Upon illumination electron-hole pairs are generated in the photoactive CdS layer, and electrons are injected from the conduction band of CdS to the conduction band of TiO_2 and to the current collector (FTO). A low concentration of CdS is maintained to keep the device transparent. The electrons reach the counter electrode vis-à-vis the external circuit. As in a conventional electrochromic device, the injection of sodium ions into the electrochromic layer causes it to color. Here, if pristine V_2O_5 or the hybrid is used as the counter layer, it will color according to following equation.

$$V_2O_5 + xNa^+ + xe^- \leftrightarrow Na_xV_2O_5 \quad (1)$$

(Yellow, Oxidized) (Green, Reduced)

Electrons are transferred to V_2O_5 (in the oxidized state) from the external circuit and Na^+ ions are inserted from the electrolyte for charge compensation; the yellow film turns green upon reduction. When sunlight is blocked or in dark, the charge stored in the electrochromic layer drives the process in reverse, releasing sodium ions from the electrochromic layer and triggering it to bleach. Thus, without an external control (in closed circuit), the photoelectrochromic device

will color in sunlight and bleach in its absence. The external circuit can also be employed to control the device, disconnection of the circuit will cause the device to remain in its current state irrespective of the presence or absence of sunlight. Moreover, an external voltage can be supplied to the device to drive the device to either the bleached or colored state. A typical configuration of a photoelectrochromic device, based on CdS/TiO_2 and V_2O_5 or $PEDOP/V_2O_5$ is shown in Figure 8.5. PEDOP is also a cathodically coloring electrochrome, but here the PEDOP film thickness or concentration is optimum, enough to enhance the electrical conductivity of V_2O_5, but at the same time (even when used in its' pristine form), insufficient to undergo a perceptible color transition.

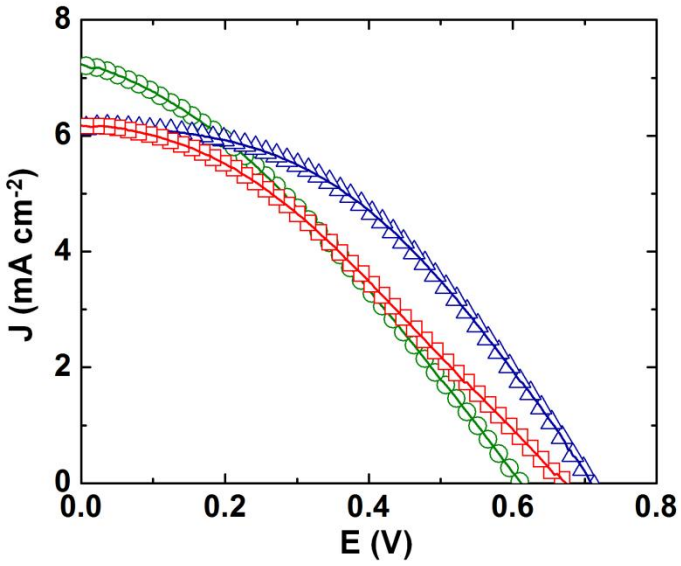

Figure 8.4: J-V characteristics of solar/photoelectrochromic cells with pristine V_2O_5 nanobelts (□), pristine PEDOP (△) and $PEDOP/V_2O_5$ hybrid (○) as counter electrodes under one sun illumination (λ> 300 nm, 100 mW cm^{-2}, AM1.5). A CdS/TiO_2 assembly was used as the photoanode and a 0.1 M Na_2S solution was employed as electrolyte.

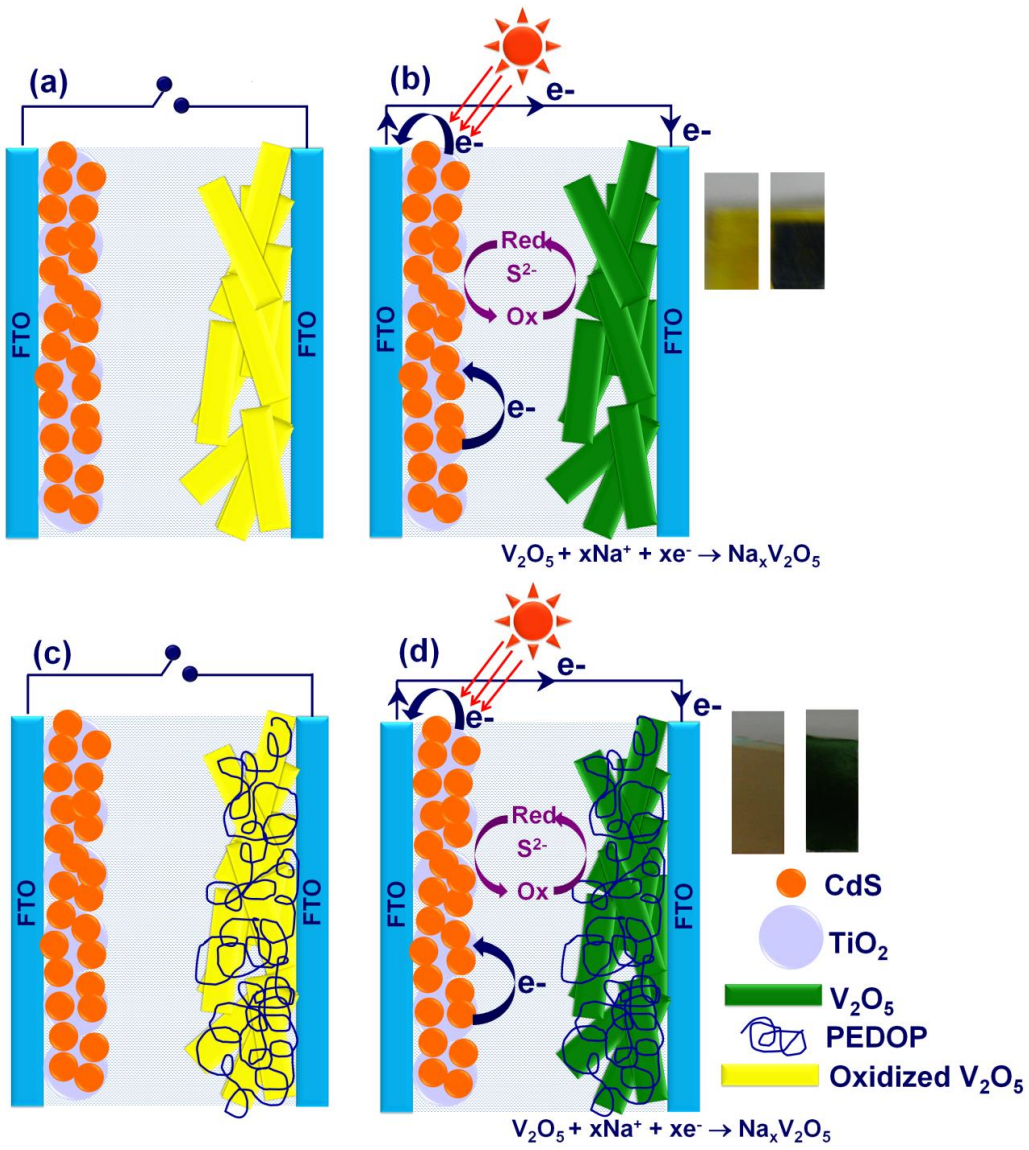

Figure 8.5: Photoelectrochromic cell configurations with (a,b) pristineV_2O_5 nanobelts and (c,d) PEDOP/V_2O_5 hybrid as the coloring counter electrodes. (a,c) show the electrochromes in their bleached (yellow, oxidized) states in dark or in light under open circuit and (b,d) show the electrochromes in their colored (reduced, green) states under illumination under closed circuit. Panels on right side show the photographs of the corresponding films in bleached and colored states.

The transmittance *versus* wavelength curves, obtained for the pristine V_2O_5 nanobelts and PEDOP/V_2O_5 hybrid films when used as counter electrodes with CdS/TiO_2 photoanodes, under

different durations of one sun illumination are shown in Figure 8.6. The time spans for which the device was subjected to 100 mW cm^{-2} light irradiance were fixed at 10, 20, 40, 50, 60 and 70 s. No external bias was applied to the cell during the measurement. The transmittance of the film was measured at the end of each of these time intervals over the visible region from 400 to 800 nm and over the near infrared (NIR) wavelength range of 1000 to 1900 nm. The films be it V_2O_5 or the hybrid showed excellent open circuit memory upon coloration by illumination (~3-4 h without color fading) and therefore %T plots were recorded easily under *ex-situ* conditions. Prior to exposure to one sun, the film (either V_2O_5 or PEDOP/V_2O_5) was oxidized and its' transmittance in this bleached state was found to lie in the range of 75 to 80% in the visible and NIR regions. Upon illumination, the transmittance of the electrochromic film decreased as a function of increasing period of illumination. Transmission modulation (ΔT) is a useful parameter for determining the suitability of a given material for electrochromic application. We define modulation as $\Delta T\ (\lambda) = T_b(\lambda) - T_c(\lambda)$, where T_b and T_c are transmittances in the bleached (as-fabricated) and colored (upon x min exposure of 1 sun illumination, x = 0, 10, 20, 40, 50, 60 and 70 s) states respectively. Transmission modulation as a function illumination time is displayed in Figure 8.7 for both V_2O_5 and PEDOP/V_2O_5 films. Transmission modulation offered by the PEDOP/V_2O_5 film for maximum contrast (achieved under an 8 min exposure to 1 sun) is 65.5% at a λ_{max} of 475 nm. The modulation at 550 nm for the same film is 55% and at NIR wavelengths of 1400 and 1900 nm, the ΔT values are 54 and 45% respectively. For the pristine V_2O_5 film, the magnitudes of transmission modulation are lower. At photopic wavelengths of 475 and 550 nm, the values are 36 and 31%. Even at NIR wavelengths, the modulation does not decrease much. Since both the hybrid and pristine oxide film are able to retain high values of optical modulation even in the NIR region, it is obvious that in addition to being capable of

modulating visible wavelengths, the films can modulate NIR or heat radiation also efficiently. The role of PEDOP in increasing the conductivity of the V_2O_5 film, tends to promote electron transport in the oxide which in turn, is responsible for a greater uptake of sodium ions from the electrolyte, thus leading to a larger optical contrast, for the same duration of illumination. The pristine PEDOP film did not exhibit any change in transmittance as a function of illumination, perhaps due to a low thickness, or an insufficient electronic current to trigger a color change.

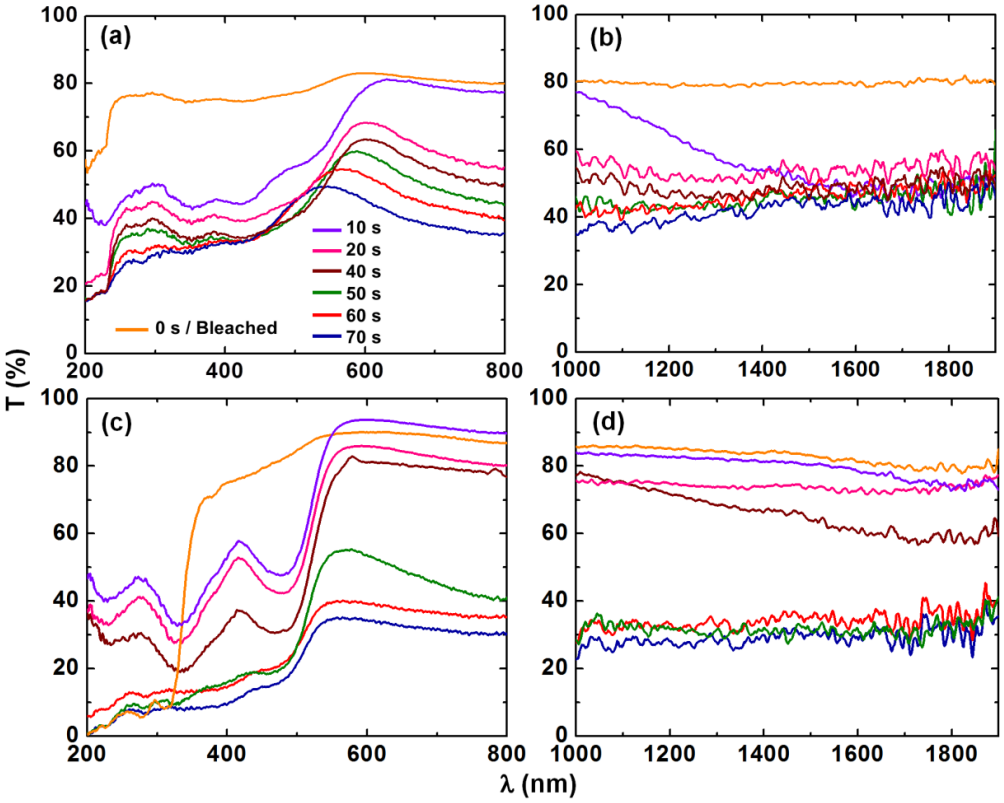

Figure 8.6: Transmittance variation as a function of wavelength for the (a,b) pristineV_2O_5 nanobelts and (c,d) PEDOP/V_2O_5 hybrid as the coloring counter electrodes in the visible and NIR regions. The %T variation was recorded upon x s exposure of 1 sun illumination, x = 0, 10, 20, 40, 50, 60 and 70 s states in the following configurations: CdS/TiO_2/Na_2S/V_2O_5 in (a,b) and in the CdS/TiO_2/Na_2S/PEDOP/V_2O_5 in (c,d).

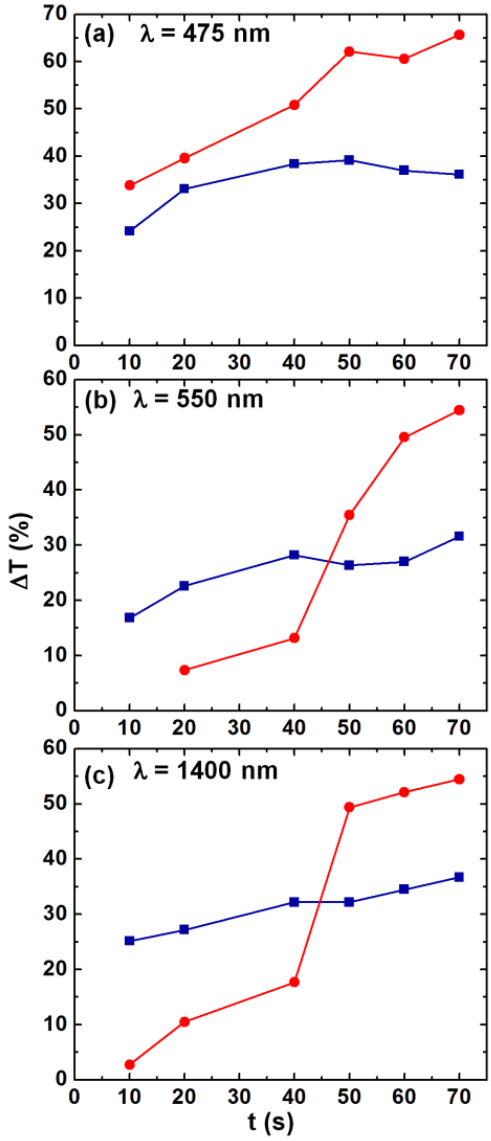

Figure 8.7: Comparison of transmission modulation of pristine V_2O_5 nanobelts (■) and PEDOP/V_2O_5 hybrid (●) films at monochromatic wavelengths of (a) 475, (b) 550 and (c) 1400 nm. ΔT values were calculated using the transmittance in the corresponding bleached states (x = 0 min or open circuit condition shown in Figure 8.6) as reference.

The solar cell parameters for the photovoltaic cells with the following configuration: CdS/TiO_2/Na_2S/V_2O_5 or PEDOP or PEDOP/V_2O_5 are provided in **Table 8.1.** We observed that the cell with pristine PEDOP as the counter electrode showed the highest efficiency, possibly

because of the highest electronic conductivity compared to pristine V_2O_5 or the PEDOP/V_2O_5composite. The large electronic conductivity of the counter electrode is beneficial for catalyzing the reduction of the oxidized electrolyte species, which leads to higher efficiency. Surprisingly, the cell with the hybrid as the counter electrode and the cell with V_2O_5 as counter show nearly equivalent efficiencies of 1.4%. The cell with hybrid shows a higher short circuit current density and a lower open circuit voltage compared to the cell with pristine V_2O_5 as counter electrode.

Table 8.1: Parameters of photoelectrochromic cells with CdS/TiO_2 as photoanode, 0.1 M Na_2S electrolyte, under 1 sun illumination (λ> 300 nm, 100 mW cm^{-2}); with different counter electrodes.

Counter Electrode	V_{OC}(V)	J_{SC}(mA cm^{-2})	FF	η (efficiency, %)
V_2O_5 nanobelts	0.672	6.15	32.65	1.43
PEDOP	0.714	6.14	43.01	1.88
PEDOP/V_2O_5 hybrid	0.611	7.21	48.79	1.44

8.3.5 Charge-discharge characteristics

Cyclic voltammograms of pristine V_2O_5 or PEDOP or the PEDOP/V_2O_5 hybrid as working electrodes and graphite (Gr) as a counter electrode in an IL: 1-butyl-3-methyl imidazolium trifluoromethanesulfonate in a two electrode configuration at scan rates of 10, 50 and 100 mV s^{-1} are shown in Figure 8.8. Pristine V_2O_5 showed a sharp well-defined peak at +0.003 V in the anodic branch at all the three scan rates, which arises from oxidation of V_2O_5. In the cathodic

sweep, a broad peak was observed at −0.88 V, which is assigned to the reduction of V_2O_5 to yield the deep green colored film formation.

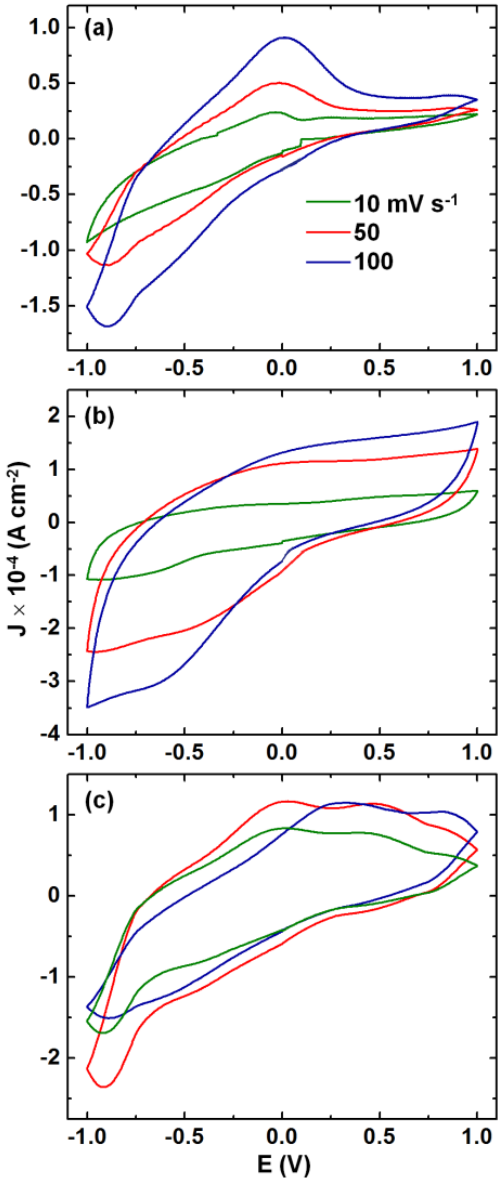

Figure 8.8: Cyclic voltammograms of (a) V_2O_5-Gr, (b) PEDOP-Gr and (c) PEDOP/V_2O_5-Gr based two electrode cells recorded at scan rates of 10, 50 and 100 mV s^{-1}.

The PEDOP/V_2O_5 hybrid shows two broad peaks at ~0 V and +0.35 V in the anodic branch, corresponding to oxidation of V_2O_5 and PEDOP respectively and in the reverse sweep, a broad

peak was observed at −0.92 V corresponding to reduction of V_2O_5 by simultaneous cation and electron intercalation. Pristine PEDOP showed featureless voltammograms at all the three scan rates, with no distinctive oxidation/reduction peaks, somewhat representing capacitive characteristics.

The galvanostatic charge-discharge curves of V_2O_5-Gr, PEDOP-Gr and PEDOP/V_2O_5-Gr cells obtained at a fixed current density of 0.1 A g^{-1} using a potential window of 0 – +1 V are shown in Figure 8.9. The charge/discharge times are different for each electrode, for a constant magnitude of applied current density, thus suggesting different specific capacitances. The specific capacitance of the cells was calculated from slope of the discharge curve and by using following equation.

$$SC = I \times \Delta t / \Delta V \times m \quad (2)$$

In equation (2), SC is the specific capacitance, I is the current applied for discharge, Δtis the time in seconds for discharge, ΔV is voltage window and m is mass of active material of the working electrode. The specific capacitance for the PEDOP/V_2O_5-Gr cell is 106 F g^{-1} in comparison to a SC of 6 and 67 F g^{-1} achieved for pristine V_2O_5 and pristine PEDOP based cells. The substantial difference in specific capacitance ongoing from the pristine polymer or V_2O_5 to the composite, shows that the synergistic effects of the two components are responsible for ameliorating the SC of the composite. The high electronic conductivity of PEDOP improves the electron propagation capability of the electrode and the ability of V_2O_5 to store and release charge by undergoing simultaneous oxidation and reduction reactions coupled with the large surface area of the V_2O_5 nanobelts that increases the number of electrochemically addressable sites on the oxide, results in a larger SC relative to the pristine polymer or oxide. The rate capability of the PEDOP/V_2O_5-Gr

cell was examined by recording the charge/discharge curves at different current densities of 0.02, 0.05 and 0.1 A g^{-1} (Figure 8.9).

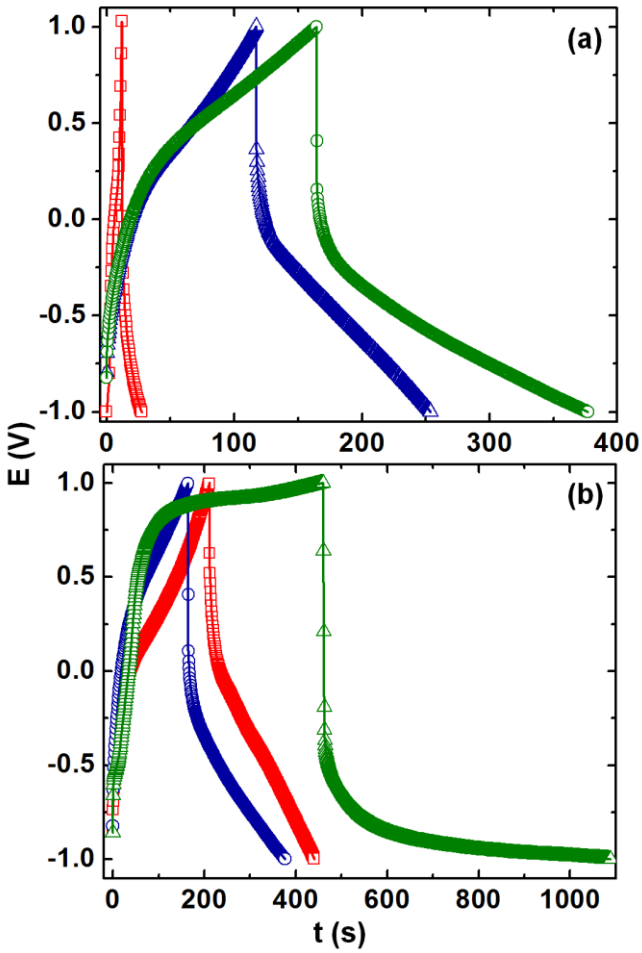

Figure 8.9: Galvanostatic charge-discharge characteristics of (a) V_2O_5-Gr (□), PEDOP-Gr (△) and PEDOP/V_2O_5-Gr (○) based two electrode cells recorded at a constant current density of 0.1 A g^{-1} and (b) rate capability of the PEDOP/V_2O_5-Gr cell obtained at current densities of 0.02 (△), 0.05 (□) and 0.1 (○) A g^{-1}.

The hybrid retained 60 % of its capacitance when the current density was increased from 0.02 to 0.1 A g^{-1}, thus indicating good rate performance. The cycling stability of the PEDOP/V_2O_5-Gr cell was determined by monitoring the variation of specific capacitance

(obtained from the charge/discharge curves, at a current density of 0.1 A g^{-1}), as a function of galvanostatic charge/discharge cycles. At the end of 1000 charge/discharge cycles, the PEDOP/V_2O_5-Gr cell retained 81% of its initial capacitance, thus confirming its' suitability for pseudocapacitors as well.

8.4 Summary

V_2O_5 nanobelts, 50 to 70 nm wide and several microns in length with a monoclinic crystalline structure, were synthesized by a hydrothermal route and deposited onto an electropolymerized PEDOP layer to yield a PEDOP/V_2O_5 hybrid film. The electronic conductivity of V_2O_5 nanobelts improved by 4-fold times upon integrating it with PEDOP. Photoelectrochromic cells were assembled with V_2O_5 nanobelts or PEDOP/V_2O_5 as counter electrodes and CdS/TiO_2 assembly as the photoactive electrode. The hybrid underwent deep coloration upon one sun illumination, with a maximum transmission modulation of 65% (λ = 475 nm) compared to a modulation of 36% at the same wavelength for the pristine V_2O_5 nanobelts, thus exemplifying the role of PEDOP in improving the optical contrast of V_2O_5. The hybrid was also able to retain this high optical modulation even at NIR wavelengths thereby validating its' suitability for self-powered smart windows, as the yellow to green switch is effected by photocurrent and not by an external bias. The suitability of the hybrid for pseudocapacitors was also demonstrated as it showed a specific capacitance of 106 F g^{-1}, which was 18 times greater than that shown by the pristine V_2O_5 nanobelts. Our study opens up possibilities of integrating PEDOP with other conducting polymers for similar dual function materials.

References

[1] Z. Tong, J. Hao, K. Zhang, J. Zhao, B. L. Su, Y. Li, J. Mater. Chem. C. (2014).
[2] M. Sathiya, A. S. Prakash, K. Ramesha, J. Tarascon, A.K. Shukla, J.Am. Chem. Soc. 113 (2011) 16291–16299.
[3] J. Liu, H. Xia, D. Xue, L. Lu, J. Am. Chem. Soc. 131 (2009) 12086–12087.
[4] H. Peng, W. Wu, C. Zhang, G. Li, K. Chen, Mater. Letts. 65 (2011) 3436–3439.
[5] C. Xiong, A. E. Aliev, B. Gnade, K. Balkus, ACS Nano 2 (2008) 293–301.
[6] Y. Wang, K. Takahashi, H. Shang, K. Lee, G. Cao, MRS Proceedings, Cambridge University Press 879 (2005) 7–8.
[7] G. Gu, M. Schmid, P. W. Chiu, A. Minett, J. Fraysse, G.T. Kim, S. Roth, M. Kozlov, E. Munoz, R. H. Baughman, 2 (2003) 316–319.
[8] K. Takahashi, Y. Wang, G. Cao, App. Phys. Letts. 86 (2005) 053102
[9] A. V. Murugan, C. W. Kwon, G. Campet, B. B. Kale, A. B. Mandale, S. R. Sainker, C. S. Gopinath, K. Vijayamohanan, J. Phys.chem. B 108 (2004) 10736–10742.
[10] L. Shao, J. W. Jeon, J. L. Lutkenhaus, Chem. Mater. 24 (2012) 181–189
[11] M. Li, G. Sun, P. Yin, C. Ruan, K. Ai, ACS Appl. Mater. Interfaces 5 (2013) 11462–11470.
[12] S. H. Leea, H. M. Cheongb, M. J. Seonga, P. Liua, C. E. Tracya, A. Mascarenhasa, J. R. Pittsa, S. K. Deb, Solid State Ionics 165 (2003) 111–116.

Chapter 9

Summary and conclusions

9.1 Summary and conclusions

Conducting polymers are widely used as electrodes in electrochemical devices such as electrochromic devices (smart windows, rear-view mirrors, elements of information displays etc.), supercapacitors, Li-ion batteries, chemical sensors, owing to ease of processability, ability to store and release charge by undergoing facile oxidation and reduction reactions, good electrochemical cycling stability and low cost. Further, large electro-optical contrasts and their ability to exhibit multiple colors under different applied potentials render them suitable especially for electrochromic applications. In this thesis, electrodes of **PEDOP** and its' composites were synthesized and were evaluated in terms of both fundamental and practical viewpoints. PEDOP is attractive due to its lower oxidation potential (compared to its' extensively investigated thiophene analogue, PEDOT), good stability in the oxidized state and since its' band gap is poised in the visible region of the electromagnetic spectrum, PEDOP is cathodically coloring and transparent and transmissive to visible light in the doped, bluish, conducting state (oxidized form) thus enabling its' use in electrochromic devices.

Considering the gamut of advantages offered by PEDOP, the present thesis dealt with the syntheses, characterization and application of PEDOP and its' composites to electrochromic devices and pseudocapcitors. The objective was to attempt and establish novel dopants for electropolymerizing PEDOP films and integrating it further with appropriate moieties to enhance the electrochemical and electro-optical performances. Conducting-AFM and KPFM were used

effectively to understand the charge transport dynamics and energetics in PEDOP based films/electrodes. Electrochemistry tools such as cyclic voltammetry, impedance spectroscopy, *in-situ* spectroelectrochemistry etc. were also used to furnish structure-property correlations in these films. Electrochromic devices and supercapacitors were successfully constructed using PEDOP based electrodes and their performance parameters were evaluated for practical applications.

Electrodes of a PEDOP composite comprising of PEDOP enwrapped by reduced graphene oxide/ionic liquid (RGO/IL) were compared in terms of microstructure, nanoscale conduction and electrochromic response with those of control PEDOP-IL electrodes (doped by the sole ionic liquid imide anion). The advantageous effect of functionalized RGO on the polymer, the structure, conduction properties and redox chemistry of the PEDOP-RGO/IL composite films was demonstrated. The PEDOP-RGO/IL film exhibited a reduced Fermi edge to valence band gap, an exemplary electrochromic coloring efficiency of 477 cm^2 C^{-1} (λ_{max} = 509 nm), a two-fold increment in dc electronic conductivity, improved switching kinetics, an amplified charge insertion-extraction capacity, as opposed to the control film which mirrored the role of RGO/IL in controlling the charge transport dynamics of PEDOP. The results showed that the entrapping of a conducting polymer by RGO based nanostructures affords tunable redox, electronic and optical properties, thus providing a paradigm for mapping the current distribution in similar nanocomposites.

The influence of counter ion on nanoscale conduction and work function of PEDOP films was further unraveled by synthesizing and comparing the properties of PEDOP films doped with electronically insulating- (a) triflate ions and (b) dodecyl sulfate ions and (c) electronically conducting- benzyl sulfonate functionalized multiwalled carbon nanotubes or (MWCNT)SO_3^-. The dynamic variation of local work function at the nanoscale was followed by KPFM and the

measure of heterogeneity of dopant distribution was assessed from the distinctive disparities in the current maps, using C-AFM. The experimentally observed increased electrochromic color contrast and improved charge storage capacity of the PEDOP-(MWCNT)SO_3^- film showed how the macroscopic properties of a conducting polymer are controlled by local charge propagation behavior. The combination of two powerful tools namely, KPFM and C-AFM aided in demystifying to some extent, the complex structure-function relationships in PEDOP films.

A practical demonstration of PEDOP films was achieved by fabricating "an all polymer" electrochromic device comprising PEDOP and poly(5-cyano indole) (PCIND) films as cathodic and anodic electrochromes, with a free standing ionic liquid based polymeric film as the electrolyte sandwiched in between. PCIND, an anodically coloring electrochrome, exhibited a reversible switching between a transmissive yellow and a saturated green hue, with an absorption maximum at 650 nm in the fully oxidized state. Prototype electrochromic devices were fabricated using PEDOP and PCIND as cathode and anode with a thermally stable ionic liquid based, free standing polymeric gel film with a high ionic conductivity of 1.19×10^{-3} S cm^{-1} as the electrolyte. The device showed large coloration efficiencies of 480 and 796 cm^2 C^{-1} at visible and NIR wavelengths of 475 and 1100 nm respectively which far exceeded the coloration efficiencies of the individual electrochromes, thereby demonstrating the synergy between the two colorants. The performance attributes of the device, which switched reversibly between red, green and blue hues, are an outcome of an interplay between the high nanolevel electron conduction capabilities (enable fast charge transport) and high ion storage capacities (increase optical contrast as more number of electrochemically addressable sites are accessed by the electrolyte ions) of the PEDOP and PCIND films. This particular study validated the

applicability of PEDOP and PCIND films as cathodic and anodic electrochromes in energy efficient windows.

The research work on PEDOP was further extended by applying it to supercapacitor applications. Composites of PEDOP enwrapped Sb_2S_3 nanorods were synthesized for the first time for use as supercapacitor electrodes. The remarkably high nanoscale (~5 S cm^{-1}) conductivity of the Sb_2S_3 nanorods enables facile electron transport in the composite. Asymmetric supercapacitors were constructed using the neat PEDOP or PEDOP/Sb_2S_3 and graphite as electrodes. High specific capacitance of 1008 F g^{-1} (at 1 A g^{-1}), enhanced power density (504 W kg^{-1}) and excellent cycling stability (88% capacitance retention at the end of 1000 cycles) are delivered by the PEDOP/Sb_2S_3 cell relative to the neat PEDOP cell. A demonstration of a light emitting diode illumination using a light-weight, flexible, supercapacitor fabricated with PEDOP/Sb_2S_3 and carbon-fiber cloth, further showed the applicability of Sb_2S_3 enwrapped conducting polymers as sustainable electrodes for ultra-thin supercapacitors.

Pseudocapacitive and electrochromic characteristics were concomitantly achieved in a PEDOP-Au@WO_3based hybrid electrode. Two cathodically coloring and pseudocapacitive materials such as WO_3 and PEDOP were combined to form a single electrode. WO_3 fibers, were first synthesized by a novel hydrothermal route and electrophoretically deposited on a conducting substrate. Au nanoparticles served as a bi-functional conductive linker, and they anchored to WO_3 via electrostatic attraction and also to the electropolymerized PEDOP:poly(styrene sulfonate) overlayer vis-à-vis the Au-sulfur affinity, thus yielding the PEDOP-Au@WO_3 hybrid film. The PEDOP-Au@WO_3 hybrid exhibited a greatly enhanced coloration efficiency of 707 cm^2 C^{-1} and a transmission contrast of 68% at 500 nm which was accompanied by a color transitions from a transmissive blue to a bluish-red to a fully red hue. In

comparison, pristine WO_3 and PEDOP electrodes showed coloration efficiencies of 88 and 176 $cm^2\ C^{-1}$ at λ_{max} of 572 and 500 nm respectively. The hybrid simultaneously showed a high specific discharge capacitance of 130 F g^{-1} during coloration which was 4 and 10 times greater than that achieved in WO_3 or PEDOP. The capacitance and redox switching capability of the hybrid decreased insignificantly with cycling thus establishing the viability of this hybrid for electrochromic psuedocapacitors for it underwent charge storage/release parallely with coloration/bleaching phenomena.

The ability of PEDOP to increase the photoelectrochromic response of another electrochrome (V_2O_5) was illustrated by preparing a PEDOP/V_2O_5 nanobelts hybrid for photoelectrochromic and supercapacitor applications. Pristine V_2O_5 and PEDOP/V_2O_5 electrodes were used for constructing (a) photoelectrochromic cells, wherein a CdS/TiO_2served as the photoactive electrode and the hybrid/oxide as the counter electrode, separated by an electrolyte. Under illumination, the hybrid underwent deep coloration, with a maximum transmission modulation of 65% (λ = 475 nm) in comparison to a modulation of 36% at the same wavelength for the pristine V_2O_5 nanobelts, thus exemplifying the role of PEDOP in improving the optical contrast of V_2O_5. The suitability of the hybrid for pseudocapacitors was also demonstrated as it showed a specific capacitance of 106 F g^{-1}, which was 18 times greater than that shown by the pristine V_2O_5 nanobelts. The structure and electrical properties of the electrodes were correlated with their photoelectrochromic and charge storage characteristics thus illustrating the high potential the PEDOP/V_2O_5 hybrid has for self-powered smart windows and supercapacitors.

Overall, in this thesis, by connecting fundamental aspects such as nanoscale conduction, localized work functions and structure with electrochemical and electro-optical behaviour of PEDOP films and its' composites, the enormous potential that this conducting polymer has for

various applications such electrochromic devices, supercapacitors, electrochromic pseudocapacitors, photoelectrochromic devices, and even photovoltaic cells has been demonstrated. Considering the excellent chemical compatibility of PEDOP with a variety of functional materials like transition metal oxides, carbon nanostructures, metal sulfides, metal nanoparticles, high performance composites of PEDOP can be easily processed and used in advanced next generation dual function devices.

List of publications included in the thesis

[1] Poly(3,4-ethylenedioxypyrrole) enwrapped by reduced graphene oxide: How conduction behavior at nanolevel leads to increased electrochemical activity, B. N. Reddy, M. Deepa, A. G. Joshi, A. K. Srivastava, *J. Phys. Chem. C***115** (2011) 18354-18365.

[2] Unraveling nanoscale conduction and work function in a poly(3,4-ethylenedioxypyrrole)/carbon nanotube composite by Kelvin probe force microscopy and conducting atomic force microscopy" B. N. Reddy, M. Deepa, *Electrochim. Acta***70**(2012) 228-240.

[3] Electrochromic switching and nanoscale electrical properties of a poly (5-cyano indole)-poly (3,4-ethylenedioxypyrrole) device with a free standing ionic liquid electrolyte, B. N. Reddy, M. Deepa, *Polymer***54**(2013) 5801-5811.

[4] Highly conductive poly(3,4-ethylenedioxypyrrole) and poly(3,4-ethylenedioxythiophene) enwrapped Sb_2S_3 nanorods for flexible supercapacitors, B. N. Reddy, M. Deepa, A. G. Joshi, *Phys. Chem. Chem. Phys.***16**(2014) 2062-2071.

[5] A poly(3,4-ethylenedioxypyrrole)–Au@WO_3-based electrochromic pseudocapacitor, B. N. Reddy, P. Naresh Kumar, M. Deepa, *ChemPhysChem*DOI: 10.1002/cphc.201402625.